Technical University of Munich
TUM School of Engineering and Design

Uncertainties in conceptual karst hydrological models and possible approaches to constrain them

Beatrice Richieri

Complete reprint of the dissertation approved by the TUM School of Engineering and Design of the Technical University of Munich for the award of the

Doktorin der Ingenieurwissenschaften (Dr.-Ing.)

Chair: Prof. Dr.-Ing. Markus Disse

Examiners:

1. Prof. Dr. Gabriele Chiogna
2. Prof. Dr. David Labat (University of Toulouse)
3. Priv.-Doz. Dr. Arno Rein

The dissertation was submitted to the Technical University of Munich on 01.07.2024 and accepted by the TUM School of Engineering and Design on 08.10.2024.

The only thing you should be afraid of is not trying.

(Wanda Rutkiewicz)

Abstract

Karst systems represent a major global source of freshwater, providing drinking water to nearly a quarter of the world's population. Hydrological models are crucial for understanding the functioning of karst systems and ensuring the sustainable use of karst groundwater resources. However, modeling karst systems is challenging due to the difficulties in observing subsurface flow and transport processes. Similarly, the complex interactions between the solid rock matrix and the karst conduits and cavities formed by rock dissolution are difficult to describe. Hydrological conceptual models are often used to conceptualize the hydrological processes of karst systems at the catchment scale due to their relatively easy implementation and low data requirements. Uncertainties in model outcomes arise from various sources, i.e., input, parametric, and structural uncertainties. Typically, model evaluation is performed using measured discharge time series at a monitoring site and computing performance metrics. Nonetheless, acceptable values of a model performance indicator do not necessarily imply that the model is reliable and capable of making predictions. This is due to the equifinality of the model, meaning that comparable results can be achieved with various model variants.

This dissertation aims to contribute to the current discussion on the investigation of the different kinds of uncertainties in hydrological karst conceptual models (in the sense of lumped-parameter and semi-distributed models), with a particular focus on using multi-objective approaches to reduce equifinality. The initial step focuses on the time-dependent relevance of model input uncertainties, defined as the uncertainties in the conceptualization of groundwater recharge processes, for the LuKARS hydrological conceptual model on a daily scale. Nine different input modeling approaches were considered, addressing interception, evapotranspiration, and snowmelt for the Kerschbaum karst system, Austria. Results indicate that evapotranspiration and snowmelt input uncertainties are higher than interception uncertainties and exhibit seasonal variability. Furthermore, the significance of a particular process in groundwater recharge can be inferred from its corresponding input uncertainties. Next, structural uncertainties were explored by considering model structures with varying complexities. Semi-distributed recharge models with an increasing number of land cover and land use (LCLU) were implemented at a daily scale for three forest-dominated karst watersheds: Kerschbaum in Austria, Baget and Oeillal in France.

To account for different conceptualizations of flow processes, two hydrological conceptual models, LuKARS and KarstMod, were used. It was found that a semi-distributed recharge improves model performance in some catchments but not in others, indicating the need for higher frequency data to capture dynamic recharge processes in heterogeneous systems. To address the issue of hydrochemical data availability, a method was developed to derive continuous solute concentrations from electrical conductivity (EC) measurements at karst springs. The concentrations of free ions and solute species

involved in complexes were computed separately using speciation calculations on PHREEQC. The methodology was applied to two karst catchments, Kerschbaum and Baget, showing that accurate solute concentration estimates need to account for complexation processes, especially for SO_4, Ca, Mg, and HCO_3. For the Baget catchment, the method shows significant uncertainty due to varying water contributions from different geological regions. In contrast, it accurately estimates solute concentrations in more homogeneous areas like the Kerschbaum watershed. Finally, high-temporal resolution hydrochemical data were used to verify and constrain the parametrization of the LuKARS 2.0 model at an hourly scale for the Baget karst system. The LuKARS model was modified to account for the interaction between matrix and conduit, as well as to represent the surface water bypassing the spring at peak flow conditions. The results highlight the importance of considering hydrochemical constraints when selecting hydrological models. Indeed, even if different model realizations simulate the spring discharge with a comparable KGE, not all of them are consistent with the dynamics of the measured SO_4^{2-} and HCO_3^- time series.

Zusammenfassung

Karstsysteme repräsentieren eine bedeutende globale Süßwasserressource und stellen Rohwasser für circa 25% der Weltbevölkerung bereit. Hydrologische Modelle sind relevante und effiziente Werkzeuge, um die Funktionsweise von Karstsystemen zu verstehen und um die nachhaltige Nutzung von Karstgrundwasserressourcen zu gewährleisten. Es ist jedoch eine Herausforderung, Karstsysteme mit Modellen darzustellen, da sich die unterirdischen Fließ- und Transportprozesse nur schwierig beobachten lassen. Ebenso lassen sich die komplexen Wechselwirkungen zwischen Festgesteinsmatrix und den aufgrund von Gesteinslösung entstandenen Karströhren und Hohlräumen nur schwierig beschreiben. Lumped-Parameter Modelle werden häufig verwendet, um die hydrologischen Prozesse von Karstsystemen im Einzugsgebiet zu konzeptualisieren und mathematisch zu beschreiben, da diese Modelle relativ einfach zu implementieren sind und relative geringe Anforderungen an die ntowendigen Daten stellen haben. Unsicherheiten in den Modellergebnissen ergeben sich aus verschiedenen Quellen, u. a. Eingangsdaten-, Parameter- und strukturelle Unsicherheiten. Typischerweise wird die Modellevaluation anhand gemessener Abflusszeitreihen an einer Messstelle durchgeführt. Dazu werden entsprechende Kennzahlen der Modellgüte berechnet. Eine akzeptable Modellgüte, ausgewiesen durch die entsprechenden Kennzahlen, impliziert jedoch nicht unbedingt, dass das Modell zuverlässig und prognosefähig ist. Dies begründet sich aus der Mehrdeutigkeit beziehungsweise Equifinalität des Modells, d. h. mit verschiedenen unterschiedlichen Modellvarianten lassen sich vergleichbare Ergebnisse erzielen.

Diese Dissertation liefert einen Beitrag zur aktuellen Diskussion in Hinblick auf die Untersuchung verschiedener Unsicherheiten in hydrologischen konzeptionellen Karstmodellen (im Sinne von Lumped-Parameter und semidistributiven Modellen). Dabei liegt der Fokus auf der Verwendung von multi-objektiven Ansätzen um die Mehrdeutigkeit der Modelle zu reduzieren. Im ersten Schritt wird die zeitabhängige Relevanz von Eingabeunsicherheiten in Bezug auf die tägliche Grundwasserneubildung als Eingangsinformation für das hydrologische konzeptionelle Modell LuKARS untersucht. Dabei wird die Eingabeunsicherheit bezüglich täglicher Daten der Grundwasserneubildung in Hinblick auf Unsicherheiten in der Konzeptualisierung von Grundwasserneubildungsprozessen betrachtet. Für die Eingabemodellierung werden neun verschiedene Ansätze betrachtet, welche die Interzeption, die Evapotranspiration sowie die Schneeschmelze für das Kerschbaum-Karstsystem (Österreich) berücksichtigen. Die Ergebnisse zeigen, dass die Unsicherheiten bei der Evapotranspiration und Schneeschmelze höher sind als bei der Interzeption und saisonale Schwankungen aufweisen. Darüber hinaus kann die Bedeutung eines bestimmten Prozesses bei der Grundwasserneubildung aus den entsprechenden Eingabeunsicherheiten abgeleitet werden. Anschließend wurden Strukturunsicherheiten untersucht, indem Modellstrukturen mit unterschiedlichen Komplexitätsgraden betrachtet wurden.

Semidistributive Neubildungsmodelle mit einer zunehmenden Anzahl von Landbedeckungs- und Landnutzungsklassen (LCLU) wurden im täglichen Maßstab für drei walddominierte Karsteinzugsgebiete implementiert: Kerschbaum in Österreich sowie Baget und Oeillal in Frankreich. Um verschiedene Konzeptualisierungen von Fließprozessen zu berücksichtigen, wurden zwei hydrologische konzeptionelle Modelle verwendet: LuKARS und KarstMod. Es wurde festgestellt, dass eine semidistributive Verteilung der Grundwasserneubildung die Modellleistung in einigen Einzugsgebieten verbessert, in anderen jedoch nicht. Dies deutet darauf hin, das höherfrequente Daten notwendig sind, um dynamische Neubildungsprozesse in heterogenen Systemen zu erfassen.

Um das Problem der Verfügbarkeit von hydrochemischen Daten zu untersuchen, wurde eine Methode entwickelt, welche die kontinuierliche Konzentration gelöster Stoffe an Karstquellen aus Messungen der elektrischen Leitfähigkeit (EC) ableitet. Die Konzentrationen freier Ionen und der an Komplexen beteiligten gelösten Stoffe wurden separat mit Hilfe von Speziationsberechnungen im hydrochemischen Modell PHREEQC berechnet. Die Methodik wurde auf zwei Karsteinzugsgebiete angewendet, Kerschbaum und Baget. Dabei wurde gezeigt, dass aufgrund der komplexen Prozesse genaue Schätzungen der Konzentration gelöster Stoffe berücksichtigt werden müssen, insbesondere für SO_4, Ca, Mg und HCO_3. Für das Baget Einzugsgebiet zeigt die Methode erhebliche Unsicherheiten aufgrund variierender Zuflüsse aus den verschiedenen geologischen Teilregionen. Im Gegensatz dazu liefert die Methode in homogeneren Gebieten wie dem Kerschbaum-Einzugsgebiet genaue Konzentrationen gelöster Stoffe.

Schließlich wurden hydrochemische Daten mit hoher zeitlicher Auflösung auf stündlicher Basis verwendet, um die Parametrisierung des LuKARS 2.0-Modells für das Baget-Karstsystem zu überprüfen und sinnvoll einzugrenzen. Das LuKARS-Modell wurde modifiziert, um die Interaktion zwischen Festgesteinsmatrix und Karströhren zu berücksichtigen. Ebenso wurde der Einfluss von Oberflächengewässern einbezogen, welche dazu führen können, dass die Karstquelle bei Spitzenabfluss umgangen werden kann. Die Ergebnisse unterstreichen die Bedeutung hydrochemischer Daten und Informationen, um die Auswahl geeigneter hydrologischer Modelle einzugrenzen. Es konnte letztendlich gezeigt werden, dass nicht alle verschiedenen Modellrealisierungen, die den Quellabfluss mit einem vergleichbaren KGE simulieren, mit den Dynamiken der gemessenen SO_4^{2-} und HCO_3^- Zeitreihen konsistent sind.

Acknowledgements

First, I want to thank the Chair of Hydrology and River Basin Management at the Technical University of Munich for providing a great research environment over the last three years. I am particularly thankful to my supervisor Prof. Dr. Gabriele Chiogna, for giving me the opportunity to engage in international research collaborations and teaching experiences. He always guided my research and encouraged the development of my professional and personal skills. Special thanks go to my mentor, Dr.-Ing. Daniel Bittner, who introduced me to the fascinating world of research and shared with me his passion and love for karst aquifers.

I would especially like to thank Prof. Dr. David Labat from the Géosciences Environnement Toulouse for supervising me during my three research stays in Toulouse. He shared with me his knowledge about karst systems and modelling approaches and provided essential assistance during several days in the field.

This research is part of the ROCKAT project (RObust Conceptualisationof KArst Transport), funded by Deutsche Forschungsgemeinschaft (DFG), CH 981/6-1 and HA 8113/6–1. Special thanks to the co-authors and project partners, especially Prof. Dr. Andreas Hartmann and Dr. Vianney Sivelle, who supported my integration into the karst community. Furthermore, I want to thank PD Dr. Arno Rein for agreeing to be one of the examiners of my dissertation, as well as Prof. Dr.-Ing Markus Disse for taking over the role as chairman for my PhD defense.

I want to express my gratitude to the entire team of the Chair of Hydrology and River Basin Management. In particular, I am thankful to Michael Tarantik for helping me set up the instrumentations for measurements in France and Austria, and to Alice Spadina who assisted during the fieldwork and laboratory analyses in the framework of her master's thesis. Furthermore, I would like to extend my special thanks to the Laboratoire Gosciences Environnement Toulouse, the Erftverband laboratory in Bergheim, and the CFEA laboratory in Dresden for their help with the chemical analyses.

My deepest thanks go to my friends, who supported and encouraged me throughout my research, to Thomas, who was there in the most difficult moments, and to my parents, without whom I would not be where I am today.

Research articles and author contributions

Presented research articles

The presented cumulative dissertation is based on four research articles, all of which are peer-reviewed and published in relevant international journals. The works of Richieri et al. (2023) and Richieri et al. (2024) are first author publications. The works of Bittner et al. (2021) and Sivelle et al. (2022) are co-author publications, which were added to fully address the research questions of the dissertation. All articles are presented in Chapters 3 to 6. The data used in the first author publications can be downloaded from the Hydroshare repository at the link
http://www.hydroshare.org/resource/fb92daaffced415fb7a991747e73adfa

Article 1

Bittner, D., **Richieri, B.**, and Chiogna, G. (2021). Unraveling the time-dependent relevance of model input uncertainties for a lumped hydrologic model of a pre-alpine karst system. Hydrogeology Journal, 29(7): 2363–2379. https://doi.org/10.1007/s10040-021-02377-1

- Co-author publication
- Chapter 3
- Author contributions: All authors conceived the research idea. Daniel Bittner developed the methodology. Beatrice Richieri performed the simulations. All authors analyzed the results. Daniel Bittner and Beatrice Richieri wrote the article. All authors reviewed the article. Gabriele Chiogna supervised this study.

Article 2

Sivelle, V., Jourde, H., Bittner, D., **Richieri, B.**, Labat, D., Hartmann, A., and Chiogna, G. (2022). Considering land cover and land use (LCLU) in lumped parameter modeling in forest dominated karst catchments. Journal of Hydrology, 612, Part C, 128264. https://doi.org/10.1016/j.jhydrol.2022.128264

- Co-author publication
- Chapter 4
- Author contributions: All authors conceived the research idea. Vianney Sivelle (KarstMod model) and Daniel Bittner (LuKARS model) developed the methodology and software. Vianney Sivelle wrote the original draft of the paper. All authors reviewed the article and wrote its final version. Hervé Jourde and Gabriele Chiogna supervised this study.

Article 3

Richieri, B., Bittner, D., Hartmann, A., Benettin, P., Van Breukelen, B. M., Labat, D., and Chiogna, G. (2023). Using continuous electrical conductivity measurements to derive major ion concentrations in karst systems. Hydrological Processes, 37(6), e14929. https://doi.org/10.1002/hyp.14929

- First author publications (core publication)
- Chapter 5
- Author contributions: All authors conceived the research idea. Beatrice Richieri developed the methodology and performed the simulations. All authors analyzed the modelling results. Beatrice Richieri wrote the article. All authors reviewed the article. Gabriele Chiogna supervised this study.

Article 4

Richieri, B., Bittner, D., Sivelle, V., Hartmann, A., Labat, D., and Chiogna, G. (2024). On the value of hydrochemical data for the interpretation of flow and transport processes in the Baget karst system, France. Hydrogeology Journal. https://doi.org/10.1007/s10040-024-02801-2

- First author publications (core publication)
- Chapter 6
- Author contributions: Beatrice Richieri and Gabriele Chiogna conceived the research idea. Beatrice Richieri developed the software (LuKARS 2.0 model), tested the method, and performed the simulations. All authors analyzed the results. Beatrice Richieri wrote the article. All authors reviewed the article. Gabriele Chiogna supervised this study.

Further scientific contributions

Peer-reviwed articles

- Özdemir Çallı1, K., Chiogna, G., Bittner, D., Sivelle, V., Labat, D., **Richieri, B.**, Çallı, S.S., and Hartmann, A. (2024). Karst Water Resources in a Changing World: Review of Solute Transport Modelling Approaches. [Manuscript submitted for publication]. Reviews of Geophysics.

Book chapter

- **Richieri, B.**, Bittner, D., Hartmann, A., Benettin, P., Van Breukelen, B. M., Labat, D., and Chiogna, G. (2023). Deriving Major Ion Concentrations at High Resolution from Continuous Electrical Conductivity Measurements in Karst Systems. In: Andreo, B., Barberá, J.A., Durán-

Valsero, J.J., Gil-Márquez, J.M., Mudarra, M. (eds) EuroKarst 2022, Málaga. Advances in Karst Science. Springer, Cham. https://doi.org/10.1007/978-3-031-16879-6_14

Oral presentation

- Sivelle, V., Jourde, H., Bittner, D., **Richieri, B.**, Labat, D., Hartmann, A., and Chiogna, G. (2022, May 23-27). A lumped parameter modeling approach considering land-cover and land-use for the simulation of karst spring hydrological functioning. EGU General Assembly 2022, Vienna, Austria. https://doi.org/10.5194/egusphere-egu22-2637

- **Richieri, B.**, Bittner, D., Hartmann, A., Benettin, P., Van Breukelen, B. M., Labat, D., and Chiogna, G. (2022, June 22-24). Deriving major ion concentrations at high resolution from continuous electrical conductivity measurements in karst systems. Eurokarst 2022, Malaga, Spain.

- **Richieri, B.**, Bittner, D., Sivelle, V., Hartmann, A., Labat, D., and Chiogna, G. (2024, June 10-14). Coupling PEST and LuKARS 2.0: Merits and limits of automatic parameter optimization. Eurokarst 2024, Roma, Italy. http://dx.doi.org/10.13140/RG.2.2.21320.12807

Posters

- **Richieri, B.**, Bittner, D., Sivelle, V., Hartmann, A., Labat, D., and Chiogna, G. (2023, December 11-15). On the Importance of Hydrochemical Data for the Interpretation of the Dynamics of Karst Systems Characterized by Varying Contributions of Water from Different Geological Areas. AGU Annual Meeting 2023, San Francisco, USA.

Contents

List of figures

List of tables

Chapter 1

Introduction

1.1 General motivation

Groundwater is the most important source of fresh water providing almost half of the world´s drinking water demand (Smith et al., 2016). In the last decades, the vulnerability of groundwater systems to anthropogenic activities has drastically increased due to growing demand of fresh water for irrigation (Aeschbach-Hertig and Gleeson, 2012; Siebert et al. 2010) and growing exposure to contaminants (Foley et al., 2011; Menció et al. 2016). The impact of anthropogenic activities on different kinds of groundwater resources have been intensively studied (Luo et al., 2016; Narany et al., 2017; Zipper et al., 2019).

Karst systems cover 10-15% of the emerged Earth's surface and 35% of Europe's continental area (Goldscheider et al., 2020). They are a crucial source of freshwater, providing drinking water to nearly a quarter of the world's population (Ford and Williams, 2007; Stevanović, 2019). Sustainable management of karst systems is essential to maintain sufficient quantity and quality of groundwater for societal needs (De Stefano et al., 2012; Wada et al., 2016). The degradation of karst resources, in terms of both quantity and quality, results from climate change and increasing anthropogenic pressures such as unsustainable water abstraction and changes in land cover and use (Gleeson et al., 2012; Gutiérrez et al., 2014; Hartmann et al., 2014; Katz, 2019; Taylor et al., 2013; Vilhar et al., 2022; Zhang et al., 2023). Studies have documented reductions in karst groundwater capacity in regions like the Mediterranean (Charlier et al., 2015; Smiatek et al., 2013), North America (Chen et al., 2005; Lóaiciga et al., 2000), and Asia (Hao et al., 2009; Wu et al., 2017). Additionally, karst water contamination is increasingly causing serious quality issues (Reberski et al., 2022; Savio et al., 2018; Selak et al., 2023). Karst aquifers are particularly vulnerable to contamination (Katz et al., 2009) due to the possible reversal of flow from karst conduits into the surrounding rock matrix during high flow events, causing a subsequent long-lasting release of contaminants from the rock matrix into karst conduits (Faulkner et al., 2009). In addition, preferential flow paths facilitate rapid pollutant spread (Bakalowicz, 2005; Stevanović, 2018; Quinn et al., 2006; Field, 2018; White, 2018) and thin soils allow direct pollutant release into the aquifers (Sinreich, 2014; White, 2019).

Consequently, there is the need to investigate and better understand karst flow and transport dynamics, which requires, due to the karst subsurface heterogeneity, special considerations and aquifer specific characterization. Hydrological models support the understanding of karst system functioning and are fundamental to ensure the sustainable water management of karst water resources (Hartmann et al.,

2014) as well as to investigate the potential evolution of karst groundwater availability under different climate change (Chen et al., 2018; Nerantzaki et al., 2020) and management scenarios (Hartmann et al., 2012; Sivelle et al., 2021). However, modelling of karst systems is affected by large uncertainties, which can derive from the conceptualization of complex internal dynamics of the system (Chen et al., 2017; Enemark et al., 2019), the scarce availability of hydrochemical data at high temporal resolution (Pinza et al. 2024) and from the quality/quantity of driving input time series (Bhanja et al., 2023; Oudin et al., 2006). There is therefore the need to investigate possible approaches for multi-objective calibration to reduce the uncertainties affecting hydrological karst models. Multi-objective calibration involves optimizing a model against multiple criteria simultaneously, allowing for a more comprehensive and balanced assessment of model performance across various aspects of the system being studied (Efstratiadis and Koutsoyiannis, 2010; Seibert and McDonnell, 2002).

1.2 An overview of karst systems

Karst systems originate from the weathering of water-soluble rocks, such as limestone (consisting in the mineral calcite $CaCO_3$) and dolostone (consisting in the mineral dolomite $CaMg(CO_3)_2$). Typically, karst develops in carbonate rocks, but can also appear in other soluble rocks such as halite and gypsum; however, carbonate sedimentary rocks represent the most important karstifiable rocks for water resources management (Ford and Williams, 2007; Hartmann et al., 2014). Karst aquifers and related land surface features develop due to water-rock interaction over a long period of time. Although the solubility of carbonate rocks in pure water is low, the presence of carbon dioxide (CO_2), which reacts with water leading to the formation of carbonic acid (H_2CO_3), strongly increases this solubility. The carbon dioxide contained in water originates both from the atmosphere (Ford and Williams, 2007) and from biological processes in the soil, such as plant decomposition or plant roots respiration (Liu et al., 2007). The chemical equilibriums in Eq 1.1 and Eq 1.2 (Ulloa-Cedamanos et al., 2020) represent the dissolution of calcite (Eq 1.1) and dolomite (Eq 1.2), respectively, by carbonic acid. Carbonate dissolution processes affect the chemical composition observed at karst springs, which in the case of dolostone is dominated by Ca^{2+}, Mg^{2+}, and HCO_3^- and therefore belong to Ca–Mg–HCO_3 (alkaline-earths-carbonatic) groundwater type (Narany et al., 2019). The carbonate dissolution kinetics are strongly influenced by water temperature and pCO_2 partial pressure (Ulloa-Cedamanos et al., 2020). Thermodynamically, carbonate solubility decreases with increasing temperature (Parkhurst and Appelo, 2013). However, high temperatures enhance biological activity and decomposition of soil organic matter, causing the increase in pCO_2 and carbonic acid and, consequently, an acceleration in carbonate dissolution (Calmels et al., 2014).

$$CaCO_3 + H_2CO_3 \rightarrow Ca^{2+} + 2HCO_3^- \quad (1.1)$$

$$CaMg(CO_3)_2 + 2H_2CO_3 \rightarrow Ca^{2+} + Mg^{2+} + 4HCO_3^- \quad (1.2)$$

The process of formation of karst systems is called karstification and is controlled by dissolution kinetics. Initially, water rich in CO_2 enters narrow fractures and within a few meters dissolves calcite/dolomite at a high dissolution rate up to 75% calcite/dolomite dissolution. After this threshold, the dissolution rate drops to very low levels (Berner and Morse, 1974; Dreybrodt, 1990; Plummer and Wigley, 1976). This slightly undersaturated water causes the initial karstification to be at a very slow rate. On the contrary, the karstification process becomes much faster when dissolution causes wider fractures, which allow a larger flow and thus more calcite/dolomite dissolution. The difference in dissolution rates in narrow and wide fractures leads to the development of a hierarchically organized network of conduits, fractures, and caves, which are hydraulically connected to each other and often drain to a single large karst spring (Worthington and Ford, 2009). The presence on the land surface of karst landforms, such as karrens, dolines, sinkholes, and dry valleys indicate the presence of subsurface karstification processes (Hartmann et al., 2014).

Karst systems are characterized by the coexistence of three types of porosities (Bakalowicz, 2005). The first porosity, also called continuous porosity, refers to the intergranular pore space; the second porosity to small fissures that developed due to tectonic processes; the third porosity to large conduits and fractures that developed due to karstification processes. This triple porosity results in heterogeneous and anisotropic hydraulic parameters with hydraulic conductivities that can vary by several orders of magnitude over short distances (Kuniansky et al., 2012). The presence of large conduits and fractures causes the characteristic rapid response of karst springs, whose discharge can vary by one order of magnitude within hours or days (Hartmann et al., 2014). Moreover, the strong karstic heterogeneity governs both the flow and transport at multiple spatial scales, i.e., regional scale, aquifer scale, local scale, and single fracture scale.

Fig. 1.1 provides a description of the functioning of karst groundwater systems. On the catchment scale, the recharge of karst systems can be classified as autogenic, i.e., internal runoff and diffusive infiltration, and allogenic, i.e., external runoff and sinking streams (Hartmann et al., 2014). Karst systems can be conceptualized by means of three compartments, i.e., epikarst, matrix (first and second porosity) and conduits (third porosity). The epikarst is the uppermost layer underneath the upper soil, which results from rapid dissolution (Williams, 2008), and plays an important role in regulating flow and transport processes (Perrin et al., 2003) as well as the storage of karst aquifers (Klimchouk, 2000; Sauter, 2000). The water is then routed downward either through rapid (direct) discharge in the conduits or slow (diffuse) infiltration into the matrix. Gradients in water pressure can then cause the transfer of water from the matrix to the conduit or the other way around (Faulkner et al., 2009). The coexistence of matrix and conduits results in the characteristic dual behavior of karst systems (Kavousi et al., 2020):

- Duality of recharge processes: direct localized recharge into conduits through, e.g., sinkholes and diffuse distributed recharge into the matrix (Geyer et al., 2008).

- Duality of flow fields: fast turbulent flow in the conduit and slow laminar flow in the matrix (Kiraly, 1998; Hauns et al., 2001).
- Duality of storage: major storage in the matrix, and minor storage in the conduits (Sauter, 1992).
- Duality of discharge conditions: during precipitation events the karst spring discharge is dominated by the flow through the conduit and thus shows high temporal variability, whereas during dry periods the baseflow is typically fed by water from the matrix (Hartmann et al., 2014).

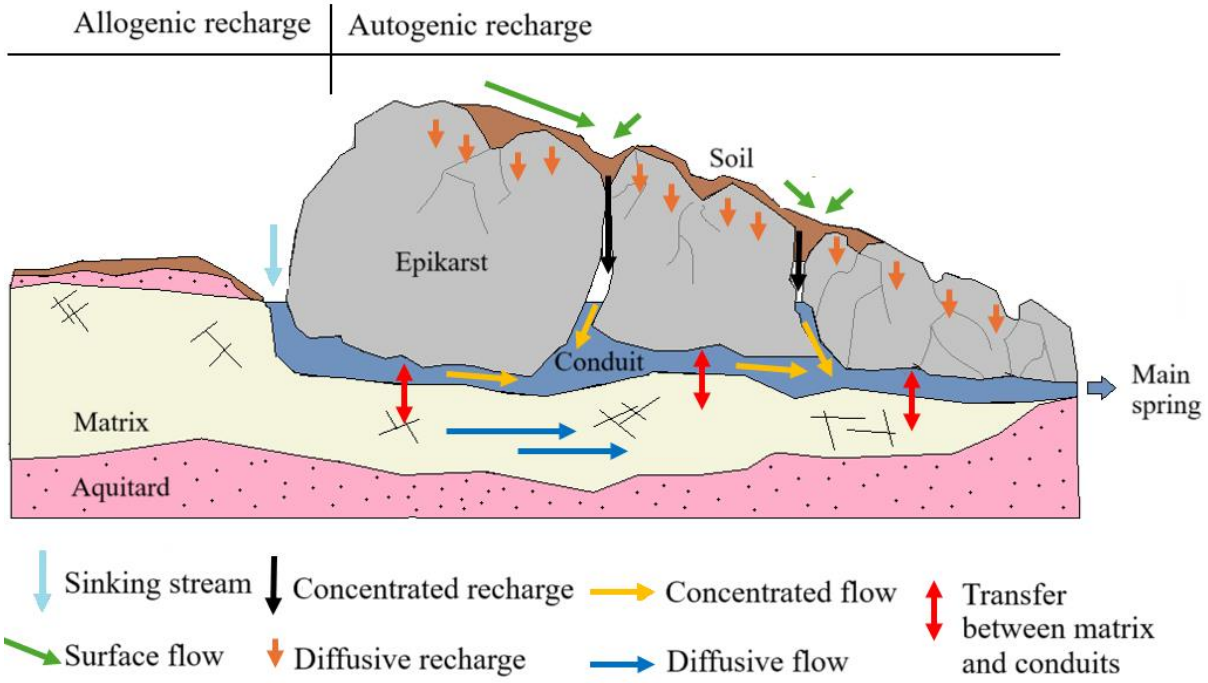

Fig. 1.1 Conceptualization of karst groundwater systems functioning including all characteristic karst processes.

The high temporal variability, spatial heterogeneity, and anisotropy of flow fields in karst systems result in complex transport phenomena and a highly transient (e.g., hourly) chemical signal at the spring (Dagan, 1988). The variability in the chemical signature at karst springs results from the variability in relative water contributions from the matrix and conduits (Ewers et al., 2012; Field, 2018) and relative water contributions from different geological areas of the aquifer (Richieri et al, 2023). Moreover, the chemical composition at karst springs depends on the recharge processes (Filippini et al., 2018; Wang et al., 2020) as well as on storage and residence time, which ranges from hours to decades (Jourde and Wang, 2023). Karst systems dominated by diffusive recharge processes typically display a piston and flushing effect of the elements stored in the saturated zone, meaning that the increase in discharge and electrical conductivity at the spring are simultaneous. Indeed, the rainwater pushes out water which had been stored in the system and thus rich in ionic content due to prolonged water-rock interaction.

Contrary, karst systems dominated by concentrated recharge/point infiltration are characterized by a rapid and direct transfer of the recharge water to the spring through large conduits causing a reduction in ionic content observed at the spring. Thus, in case of dilution, the increase in spring discharge is followed by a decrease of electrical conductivity. The same karst system can display different responses to precipitation events close in time, underlining the importance of the initial condition of the system especially in terms of water storage (Perrin et al., 2003; Richieri et al., 2023).

Understanding these chemical and flow dynamics at karst springs requires a detailed examination of the transport processes within both the karst matrix and conduits. The transport processes in the matrix at the pore scale are controlled by advection (mainly transport along the main flow direction), pore diffusion (driven by a concentration gradient) and mechanical dispersion (random velocity variations). Generally, the advective velocity in the matrix is laminar with a Reynolds number smaller than one (Bear, 1972). In karst conduits flow can become turbulent when the Reynolds number exceeds 500 to 2000 (Reimann et al., 2011; Shoemaker et al., 2008; White, 2002). When the ratio between the product of the groundwater flow velocity and the grain size over the aqueous diffusion coefficient (grain Pèclet number) is smaller than one, pore diffusion is the dominant transport process in the karst matrix; whereas if the grain Pèclet number is larger than one, advection is the dominant transport process (Bear, 1972). Transport processes in karst conduits show similarities, depending on the degree of saturation, with free surface flow or with saturated pipe flow under pressurized conditions (Liedl et al., 2003; Reimann et al., 2014). The solute transport in conduits is mainly controlled by advection and aqueous diffusion. However, being the typical flow velocity such to lead to turbulent flow in the conduit, the role of turbulent diffusion becomes relevant for the mass dispersion (Hauns et al., 2001; Taylor 1954, Birk et al. 2005).

At the karst aquifer scale, the transport mechanisms can be overall described by (1) transport along the main flow direction controlled by advection and dispersion processes, (2) matrix diffusion and mechanical dispersion along the conduit surfaces in and out of the matrix (matrix acts as a sink and/or source depending on the hydraulic head and concentration gradient of the system) , and (3) matrix exchange between flowing water and matrix via sorption, ion exchange, and chemical reactions (Field and Liej, 2014; Field and Pinsky, 2000; Sinreich, 2011). Solutes, which are neither affected by sorption nor chemical reactions, are defined as conservative. Sorption is the process through which solutes move from the dissolved aqueous phase to an immobile sorbed phase in the matrix causing an initial reduction in solute concentration and a retardation effect. Ion exchange is a specific type of sorption process, which occurs when ions in a solution are replaced by ions of similar charge from the solid phase. Sorption and ion exchange occur at the conduit walls and within the surrounding carbonate matrix (Geyer et al., 2007; Morales et al., 2010) and are generally relevant at local scale (Hauns et al., 2001). Retardation is the delay of the solute transport with respect to the groundwater flow and is generally negligible in karst systems due to the quick flow in the conduits (Kresic and Stevanovic, 2009). Finally,

(biogeo)chemical reactions (i.e., degradation, nitrification, dissolution, mineralization, weathering) occur when the reactants are mixed and degrade with consequent formation of the reaction products. In the matrix, reaction processes are limited by transport mechanisms due to slow diffusion and dispersion processes; whereas in the conduit by the reaction rate constants (Spiessl et al., 2007).

1.3 Characterization of flow and transport processes in karst systems

The characterization of flow and transport processes in karst systems requires specific investigation techniques which need to be able to capture the duality of karst dynamics (Goldscheider and Drew, 2014). Tracers are commonly used to investigate and quantify flow and transport processes and parameters in karst systems (Goldscheider et al., 2008; Martín-Rodríguez et al., 2023; Mudarra et al., 2014). Tracers can be categorized in natural tracers, artificial tracers, and physical quantities.

Natural tracers, such as major ions, stable isotopes (oxygen-18, deuterium, and tritium), trace elements, dissolved organic carbon DOC and natural fluorescence, are naturally present in karst groundwater (Hartmann et al., 2014). Natural tracers are used to determine proportion and mixing of water contributions from different sources or recharge areas (Barbieri et al., 2005, Đurović et al., 2022; Gil-Márquez et al., 2017), and to investigate the internal system functioning, i.e, variability of relative importance of the saturated/unsaturated zones and/or of quick/slow flow components under different flow conditions (Aquilina et al., 2006; Barbera´ and Andreo, 2011; Frank et al., 2019; Hartmann et al., 2013; Hartmann and Andreo, 2017; Mudarra and Andreo, 2011; Ravbar et al., 2011; Torresan et al., 2020). In addition, stable water isotopes are widely used, due to their conservative behavior, to investigate the residence time and origin of karst waters (Batiot et al., 2003; Long and Putnam, 2004; Wang et al.,2021; Winston and Criss, 2004). The residence time indicates the time between the water entering and leaving the system and provides insight into the system's mixing, storage, and transport characteristics (i.e., piston flow, complete mixing) (Bailly-Comte et al., 2011). Karst springs typically show rapid reactions to precipitation events both in terms of flow and transport processes, with discharge variation commonly by factors of 10 to 100 within hours or days (Hartman et al., 2014). Therefore, continuous monitoring (e.g., hourly) is required to characterize the dynamics and variability of karst systems. However, the collection at high temporal resolution of water samples is limited by high cost and time requirements (Charlier et al., 2012; Richieri et al., 2023). On the contrary, physical properties of water, such as electrical conductivity and temperature, are often used as natural tracers due to easy and cheap monitoring (Hartmann et al., 2014).

Artificial tracers are substances, which are added to the system at specific injection points and allow the estimation of the travel flow paths and times through the system. An artificial tracer is considered ideal if it is highly soluble, detectable at low concentrations, conservative and nontoxic to humans and the environment (Käss, 2004). Artificial tracers widely used due to their behavior close to the ideal are

fluorescent dyes, such as uranine, sulforhodamine, eosin, or naphthionate (Leibundgut et al., 2009). Artificial tracers are applied to estimate karst systems´ hydraulic properties (e.g., hydraulic conductivity, porosity), geometric properties (e.g., conduit volumes and diameters) and transport parameters (e.g., dispersion, mass exchange rate) (Mudarra et al., 2019; Lauber and Goldscheider, 2014; Peely et al., 2021). Moreover, they allow the delineation of subsurface connections and karst spring recharge area (Luhmann et al., 2012) as well as the identification of the origin and destination of contaminants (Goldscheider et al., 2008). The breakthrough curve (BTC) is the principal result of artificial tracer tests. The BTC shows the tracer concentration over time and thus allows the determination of the recovery time (Labat and Mangin, 2015).

1.4 Modelling approaches for karst systems

Hydrological models are representations of the hydrodynamic processes governing the movement and distribution of water within the hydrological cycle. Hydrological models support the assessment of the system functioning and are fundamental to perform sustainable water management of karst water resources (Hartmann et al., 2014). The first models for the investigation of karst systems were developed in the 1960s (Castany, 1968; Forkasiewicz and Paloc, 1967; Schoeller, 1962) and since then several conceptual ideas have been developed including a wide variety of types of mathematical models (Jeannin et al., 2021, Kovács and Sauter, 2007). The simplest approach to model a karst system is the application of the so called black-box models, which transfer input to output without accounting for any physical process. Black-box models can be based on analytical transfer functions (Labat et al. 2000a; Jukic and Denic-Jukic, 2008) or neural networks (Kurtuluş and Razack, 2007). However, black-box models are not reliable outside the specific hydrological conditions of the calibration period (Hartmann et al., 2014). Therefore, distributed models and hydrological conceptual models are required for proper characterization of karst systems functioning and for predictions (Jeannin et al. 2021). In this thesis the terminology hydrological conceptual model is used for lumped and semi distributed models.

Distributed models represent the spatial variability of the hydrological parameters by discretizing the karst system in a two- or three-dimensional grid, assigning at each grid cell characteristic parameters and system states, and solving governing equations for each grid cell. They ensure the representation of the complexity and spatial heterogeneity of karst internal dynamics and provide the temporal and spatial evolution of groundwater levels. Different subtypes of distributed modeling approaches can be found in the literature (Jeannin et al., 2021; Kuniansky, 2016). Generally, distributed models describe the flow in the matrix with the groundwater flow equation based on Darcy´s law (Eq 1.3), where S_S (1/L) is the specific storage coefficient, K (L/T) is the hydraulic conductivity, H (L) is the hydraulic head, t is the time (T), and ∇ is the Nabla operator (Bear, 1972). These parameters are defined over a Representative

Elementary Volume (REV) to ensure they accurately represent the average properties of the porous medium.

$$S_S \frac{\partial H}{\partial t} = \nabla(K \nabla H) \tag{1.3}$$

The specific storage S_S is a measure of the volume of water that a porous medium can store per unit volume of saturated material and per unit change in hydraulic head. Hydraulic conductivity K represents the ability of a porous medium to transmit water, and it is defined as the volume of water that flows through a unit cross-sectional area of the porous medium per unit time under a unit hydraulic gradient.

On the contrary, the flow in the conduits is often represented by the one-dimensional Darcy-Weisbach equation (Eq. 1.4), as function of the friction coefficient μ (-), conduit diameter d (L), the mean flow velocity q (L/T), the flow length along the path x (L), the gravitational acceleration g (L/T^2), and time t (Liedl et al., 2003; Munson et al., 2021; Reimann et al., 2011).

$$\frac{\partial H}{\partial x}(t) = -\mu \frac{q(t)^2}{2gd} \tag{1.4}$$

Different approaches have been investigated to include karst heterogeneity in distributed model (Jeannin et al., 2021; Kuniansky, 2016), e.g., equivalent porous medium approach (EPM) (Rodríguez et al., 2013; Worthington, 2009), double continuum approach (DC) (Kordilla et al.,2012; Maréchal et al.,2008) and combined discrete-continuum approach (CDC) (Liedl et al. 2003, Reimann et al., 2011; Shoemaker et al., 2008). Despite allowing the representation of karst complexity, the application of distributed models to karst systems is restricted to well-explored study areas (e.g., Birk et al., 2005; Doummar et al., 2012). This is caused by the high data requirement of distributed models together with the large uncertainty characterizing the subsurface structure of karst systems which cannot be directly observed (Berthelin and Hartmann, 2020). Distributed models are here presented to provide a general overview of karst modelling approaches. However, as they are not the focus of the present dissertation thesis, they will not be further discussed.

Hydrological conceptual models do not explicitly consider the spatial distribution of hydro(geo)logical properties and include both fully lumped and semi-distributed models. Lumped models conceptualize physical processes at the scale of the entire karst system, whereas semi-distributed models divide the catchment into hydrological response units (Bittner et al., 2018; Ladouche et al., 2014). Hydrological conceptual models conceptualize the karst system functioning using different buckets, i.e., model compartments, and transfer functions, each of them representing a specific hydrological process (Azimi et al., 203; Bancheri et al., 2019; Mazzilli et al., 2019; Tritz et al., 2011). For a single bucket model, the discharge Q is often computed as linear on nonlinear function of the stored water volume S (Eq. 1.5),

with a and b model parameters that depend on system properties, t the time, P the precipitation and ET the evapotranspiration (Rimmer and Hartmann, 2012).

$$Q = -\frac{dS}{dt} - ET + P = \text{a}\, S^b \tag{1.5}$$

A large variety of hydrological conceptual models have been developed to represent karst processes from the infiltration into the soil to the spring discharge considering different levels of complexity (e.g., Bancheri et al., 2019; Bittner et al., 2018; Hartmann et al., 2013; Le Moine et al., 2007; Rimmer and Salingar, 2006). More complex lumped models allow the representation of a larger variety of hydrological processes for which simpler models would not be sufficient. However, introducing more complex model structures could result in overparameterization and overfitting due to the large number of model parameters (Engelhardt et al., 2014; Hartmann et al., 2014).

Hydrological conceptual models are widely used for the investigation of karst systems. Despite the relatively easy implementation, the parameters of hydrological conceptual models cannot be directly measured in the field, and thus need to be estimated during the calibration process (Wagener and Gupta, 2005). Moreover, model parameters need to be validated to access models' reliability and usefulness for further applications (Andréassian, 2023; Klemeš, 1986). Typically, model evaluation generally involves assessing both the structure and parameters of the model, along with calibrating and validating these parameters, using measured discharge time series at the karst spring and computing performance metrics. Among the several existing metrics, commonly used metrics in hydrological studies are the Nash-Sutcliffe efficiency NSE (Nash and Sutcliffe, 1970) and the Kling-Gupta efficiency KGE (Gupta et al., 2009). For a comprehensive description of the existing performance metrics, one can refer for instance to the works of Bennett et al. (2013), Ferreira et al. (2020) and Moriasi et al. (2007). Given the inherent uncertainties in parameter estimation, global sensitivity analysis and uncertainty quantification should be performed when applying hydrological conceptual models (Bittner, 2020).

1.5 Multi-objective calibration

A single metric is generally insufficient for a comprehensive evaluation of all aspects of hydrological model performance (Gupta et al. 2008; Leins et al. 2023). Due to the problem of equifinality (Cinkus et al. 2022), i.e., the existence of multiple optimal parameter sets that reproduce the observed values (Beven and Freer, 2001; Chiogna et al., 2024), acceptable values of a model performance indicators do not necessarily mean that the model is reliable. Studies have demonstrated that when validated using data from a single spring monitoring site, different models with varying structures or parameter values can produce satisfactory simulated spring discharge (Mudarra et al., 2019). However, these models often fail to adequately capture the internal dynamics of the karst system, leading to significant equifinality

(Hartmann et al., 2017). Multi-objective calibration approaches can be used to reduce the problem of equifinality and related modeling uncertainties (Seibert and McDonnell, 2002). In this context, the model results should not only be able to reproduce a discharge time series measured at the karst spring but also further relevant hydrological processes, e.g., water contributions from different compartments of the systems and transport processes (Wang et al., 2017). This requires the calibration of the hydrological model with more than a single objective function and the incorporation of additional information beyond the measured discharge time series at the karst spring (Gupta et al., 2008; Leins et al. 2023). Multi-objective approaches can consist in calibrating the input models used to generate driving input time series (e.g., evapotranspiration, interception), in extracting more information from the available data (i.e., discharge data), or in considering additional data (i.e., hydrochemical data). Some of the existing approaches are presented in the following subsections.

1.5.1 Input time series analysis

The input of any hydrological model is the groundwater recharge time series, which is controlled, for the case of pre-alpine karst catchments, by precipitation, evapotranspiration, interception, and snowmelt processes (Bittner et al., 2021). While precipitation time series are generally recorded at meteorological stations, other driving forces are difficult to measure. Therefore, additional input models are often applied to compute input time series for hydrological models (Hartmann et al., 2014b; Mazzilli et al., 2012; Ollivier et al., 2020). For instance, evapotranspiration can be modeled using temperature-based parametrizations (Oudin et al. 2005; Thornthwaite 1948) or energy balance methods (Colaizzi et al. 2012; Penman 1948); interception using mechanistic (Gash et al. 1995; Liu 2001) and stochastic modeling approaches (Calder 1996; Hall 2003); snow processes using degree-day-factor methods (Girons Lopez et al. 2020; Martinec 1960) or energy balance methods (Herrero et al. 2009; Marks et al. 1999). Parameters related to physical properties like vegetation characteristics and soil properties can often be measured directly or estimated from remote sensing data (Mohanty et al., 2017; Thenkabail et al., 2011). However, other parameters within these models, such as proportionality constants, are not measurable with field experiments and thus need to be calibrated. This is particularly true for input models relying on (semi)empirical relationships and for hydrological conceptual models, which conceptualize the recharge processes at the scale of the entire catchment.

In a multi-objective calibration approach, the model's performance on the output discharge time series can be assessed in conjunction with the calibration of the parameters of the input models. Observations of input time series can be either measured in the field or obtained from satellite images/gridded data (Ollivier et al., 2020). This approach can lead both to a more realistic representation of the recharge processes and to a reduction in the model output uncertainty starting from the analysis of the input data which are independent from the discharge.

1.5.2 Spring discharge time series analysis

In karst systems, there is usually only one monitoring point at the spring outlet, providing typically solely discharge measurements. In this case, multi-objective calibration approaches rely on the intensive use of the information contained in discharge time series (Moussu et al., 2011). The extraction of additional information from the available data can be achieved, for instance, by comparing multiple performance metrics (Li et al., 2017; Pölz et al., 2024; Rudolph et al., 2023; Sivelle et al., 2022), or by means of auto-correlation analysis of spring discharge (Lorette et al., 2018; Moussu et al., 2011; Sivelle and Jourde, 2020, Sivelle et al., 2022), cross-correlation between discharge and precipitation (Sivelle et al., 2022) and wavelet multiresolution analysis (Labat et al., 2000b; Mallat, 1989; Sivelle, 2019; Sivelle et al., 2022).

Combination of multiple performance metrics

Several performance metrics are used to quantify model errors (Ferreira et al., 2020; Hauduc et al., 2015; Jackson et al., 2019). Each metric could be more or less suitable to capture specific aspects of flow conditions and model performance. For instance, the Nash-Sutcliffe Efficiency (NSE) tends to give more importance to peak flow conditions and the Root Mean Square Error (RMSE) is sensitive to outliers (Mizukami et al., 2019). NSE and RMSE are computed as shown in Eq. 1.6 and Eq. 1.7 (Bennett et al., 2013), where $y_{obs,i}$ is the observed variable at time i, $y_{sim,i}$ the observed variable at time i, $\overline{y_{obs}}$ the mean of the observed values, and n the total number of time steps.

$$\mathrm{NSE} = 1 - \frac{\sum_{i=1}^{n}\left(y_{obs,i} - y_{sim,i}\right)^2}{\sum_{i=1}^{n}\left(y_{obs,i} - \overline{y_{obs}}\right)^2} \tag{1.6}$$

$$\mathrm{RMSE} = \sqrt{\frac{1}{n}\sum_{i=1}^{n}\left(y_{obs,i} - y_{sim,i}\right)^2} \tag{1.7}$$

On the contrary, the Kling-Gupta Efficiency (KGE), is considered suitable for capturing the entire flow regime (Gupta et al., 2009). Eq. 1.8 shows the equation for the computation of KGE, with r_c the linear correlation between the observations and simulations, σ_{sim} the standard deviation in simulations, σ_{obs} the standard deviation in observations, μ_{sim} the simulation mean and μ_{obs} the observation mean (Knoben et al. 2019).

$$\mathrm{KGE} = 1 - \sqrt{(r_c - 1)^2 + \left(\frac{\sigma_{sim}}{\sigma_{obs}} - 1\right)^2 + \left(\frac{\mu_{sim}}{\mu_{obs}} - 1\right)^2} \tag{1.8}$$

To ensure a comprehensive analysis of the model performance, a multi-objective approach accounting for a combination of different performance metrics is recommended (Huo and Liu, 2020; Monteil et al., 2020). In this sense, KGE could be already considered as a multi-objective model performance criterion since it combines information about linear correlation between the observations and simulations with mean and standard deviation of the simulations and observations (Knoben et al., 2019).

Several studies have considered multiple performance metrics (Li et al., 2017; Pölz et al., 2024; Rudolph et al., 2023; Sivelle et al., 2022). For instance, Sivelle et al. (2019) defined a new objective function as the weighted sum of Nash-Sutcliffe Efficiency (NSE) and balance error (BE) to avoid important mass balance errors between observed and simulated data caused by the overestimation at low flow conditions. Zhao et al. (2023) used five different performance metrics, including NSE (Nash and Sutcliffe 1970), KGE (Gupta et al. 2009), flood peak relative error (FPRE), flood volume relative error (FVRE), and root mean square error (RMSE) to evaluate the model performance. For the mathematical description of the existing performance metrics, one can refer for instance to the works of Bennett et al. (2013).

Auto-correlation and cross-correlation analyses

The auto-correlation and cross-correlation functions are widely used in hydrological studies to characterize the temporal structure of hydrological signals under the linear-stationary hypotheses (Labat, 2000a). The auto-correlation function is a normalized measure of the linear dependence among successive values of a single time series (rainfall or discharge) and allows to quantify the memory effect of a system (Labat et al., 2000a; Mangin, 1984; Panagopoulos and Lambrakis, 2006). The auto-covariance function $C(k)$ is calculated as shown in Eq. 1.9, with k the lag time, n the length of the time series, x_t the value of the studied variable at time t, $\bar{x}$ the mean value of the studied variable (Labat, 2000a). The auto-correlation function $ACF(k)$ is then equal to $C(k)$ normalized respect to the auto-covariance for a lag time equal to zero ($C(0)$), which corresponds to the variance (Eq. 1.10, Delbart et al., 2014).

$$C(k) = \frac{1}{n}\sum_{t=1}^{n-k}(x_t - \bar{x})(x_{t+k} - \bar{x}) \tag{1.9}$$

$$ACF(k) = \frac{C(k)}{C(0)} \tag{1.10}$$

As proposed by Mangin (1984) and later applied in different hydrological studies (Lorette et al., 2018; Sivelle and Jourde, 2020), the memory effect of a karst aquifer can be defined as the lag time value at which the ACF of the spring discharge time series reaches the value of 0.2 (also called decorrelation time). From the hydrogeological point of view, the shape of the correlogram, i.e., ACF over lag time,

gives information on the degree of karstification and storage capacity of a karst system (Panagopoulos and Lambrakis, 2006). For instance, well-developed karst systems with limited water storage are characterized by a low memory system, meaning steeper decreasing slope of the correlogram and shorter decorrelation time. On the contrary, poorly developed karst systems with relevant water storage show high memory system with ACF values above 0.2 over a long-time lag (Panagopoulos and Lambrakis, 2006).

The cross-correlation function quantifies the statistical relation between, for instance, the precipitation and discharge time series (Panagopoulos and Lambrakis, 2006). Assuming the precipitation to be a random process (white noise), the shape of the cross-correlation function gives insights into the impulse response of the system: the higher the peak, the more the system acts as a piston; the smaller the lag time to reach the maximum value of cross-correlation, the faster the response time of the system (Mangin, 1984). Being x_t and y_t input (precipitation) and output (discharge) time series, respectively, k the lag time, n the length of the time series, $\bar{x}$ and $\bar{y}$ the mean values, the cross-covariance function $C_{xy}(k)$ is computed as shown in Eq. 1.11 (Labat, 2000a). Finally, the cross-correlation function $CCF_{xy}(k)$ is obtained by dividing $C_{xy}(k)$ by the product of the standard deviations $\sigma_x$and σ_y as shown in Eq. 1.12 (Delbart et al., 2014).

$$C_{xy}(k) = \frac{1}{n}\sum_{t=1}^{n-k}(x_t - \bar{x})(y_{t+k} - \bar{y}) \tag{1.11}$$

$$CCF_{xy}(k) = \frac{C_{xy}(k)}{\sigma_x \sigma_y} \tag{1.12}$$

Both the auto-correlation and cross-correlation functions can support the assessment of hydrological model performance in addition to numerical performance criteria such as NSE and KGE. For instance, to compare the performance of different model structures or parametrizations, the autocorrelation calculated on the observed discharge can be compared with the autocorrelation calculated on the simulated discharge of each model realization. Similarly, cross-correlation functions can be calculated between precipitation and both observed and simulated discharges of each model realization (Sivelle et al., 2022). However, when applying auto- and cross-correlation analyses, one should consider that both the memory effects and response time can be affected by the sampling frequency of precipitation and discharge time series (Sivelle and Jourde, 2020). This results from the coexistence of several processes with characteristic frequencies that can vary over several orders of magnitudes (Blöschl and Sivapalan, 1995).

Wavelet analysis

To account for non-stationarities, several studies showed that the wavelet analysis can be used to decompose the discharge time series observed at karst springs into different signals each of which characterized by its specific frequency scale (Labat et al., 2001, Labat, 2005, Labat, 2010, Hao et al., 2012, Miao et al., 2014). Contrary to the Fourier analysis, which fails to determine frequency time-dependence, the wavelet analysis allows not only the identification of signals with different frequency scale but also their temporal variation (Labat, 2005). Therefore, the wavelet analysis is suitable in case of signals characterized by localized high frequency events or by large numbers of scale-variable processes (Labat et al., 2000b). Signals characterized by different frequency scales provide relevant information about different hydrological processes, e.g., conduit and matrix flow, and transfer between them. Each frequency scale in which the discharge signal can be decomposed thus can be considered as an individual time series that is representative for different (sub)processes in a defined karst aquifer (Labat et al., 2000b). The investigation of these individual time series can support model performance assessment (Chiogna et al., 2018; Rathinasamy et al., 2014), model calibration (Duran et al., 2020; Schaefli and Zehe, 2009) and model parameter sensitivity analysis (Bittner et al., 2021b; Chiogna et al., 2024).

The continuous wavelet transform was introduced by Grossmann and Morlet (1984). The approach involves shifting a mother wavelet function $\psi(t)$ along the signal and computing the corresponding spectrum at each location. As shown in Eq. 1.13, a mother wavelet $\psi(t)$ is transformed into a wavelet function $\psi_{\tau,s}(t)$ through dilation or compression of the mother wavelet, along with a time shift.

$$\psi_{\tau,s}(t) = \frac{1}{\sqrt{|s|}} \psi\left(\frac{t-\tau}{s}\right) \tag{1.13}$$

The parameter s represents a dilation ($s > 1$) or a contraction ($s < 1$) factor of the mother wavelet $\psi(t)$, and corresponds to different scales of observation; the parameter τ represents the temporal translation of the wavelet $\psi(t)$ which allows to study the signal $x(t)$ locally around the time τ (Labat et al., 2000b).

In the case of the Continuous Wavelet Transform (CWT), the convolution of the signal $x(t)$ with the wavelet function determines the wavelet coefficients $C_x(\tau, s)$ (Eq. 1.14), which indicate the strength of each frequency scale component s at each time τ and position x (Labat et al., 2000b). The 2D plot of the wavelet coefficients as a function of the scale s and time τ is called scalogram and allows to graphically identify the strength of frequency components at specific scales and positions/times. Patterns and structures in the scalogram can provide insights into the dominant frequency components and their evolution over time or space (Chiogna et al., 2018; Schuler et al., 2021).

$$C_x(\tau, s) = \int_{-\infty}^{+\infty} x(t)\ \psi_{\tau,s}(t)\, dt \tag{1.14}$$

The results of the wavelet analysis of a signal are strongly affected by the choice of the mother Wavelet function $\psi(t)$. In continuous time applications, the most frequently used wavelets are the Haar wavelet and the complex Morlet wavelet (Labat et al., 2000b).

Since the CWT is not orthogonal (Mallat, 1999), the original signal cannot be reconstructed as the sum of all the decomposed signal components. For multiresolution analysis in hydrological studies, it is therefore more convenient to adopt an orthogonal wavelet transformation. The discrete wavelet and coefficients are defined in Eq. 1.15 and Eq. 1.16, respectively, where j is the scale factor and $k\tau_0$ is the translation factor (Labat et al., 2000b). To reconstruct a scale in power of two (dyadic scale) the parameters are fixed such as s_0 = 1 and τ_0 = 2 (Mallat, 1989).

$$\psi_{j,k}(t) = s_0^{\frac{j}{2}}\,\psi\left(s_0^j t - k\tau_0\right) \tag{1.15}$$

$$C_x(j,k) = \int_{-\infty}^{+\infty} x(t)\;\psi_{j,k}(t)\,dt \tag{1.16}$$

Being the DWT orthogonal, the original signal $x(i)$ at the discrete time i can be obtained as a linear combination of translates and dilates of orthonormal wavelets (Eq. 1.17) (Labat et al., 2000b).

$$x(i) = \sum_{j=0}^{+\infty}\sum_{k=-\infty}^{+\infty} C_{j,k}^{x}(i)\;\psi_{j,k}(t) \tag{1.17}$$

In the context of multiresolution analysis for model performance assessment, the DWT can be applied to both the discharge model realizations as well as to the observed time series. Standard performance metrics can be computed for each decomposed signal components allowing to quantify the ability of the model to represent processes characterized by different frequency scales (Sivelle et al., 2022).

1.5.3 Hydrochemical time series analysis

The use of hydrochemical data in addition to hydrometric information like spring discharge allows for a better understanding of the spatial and temporal variability in the hydrological response of karst systems (Barbieri et al., 2005; Chang et al., 2021; Gil-Márquez et al., 2017). Typical natural tracers used for the investigation of karst springs are major ions, electrical conductivity, dissolved organic carbon DOC, and water isotopes (Goldscheider and Drew, 2007; Leibundgut et al., 2009). For example, they allow to differentiate between the contribution from the critical zone, conduit and matrix compartments under varying hydrometeorological conditions (Dreiss, 1989; Frank et al., 2019; Liu et al., 2004; Ravbar et al., 2011; Torresan et al., 2020). They can also be used to estimate the fractions and mixing of water from different sources (Aquilina et al., 2006; Plummer et al., 1998), assess the functioning of karst

systems (Barberá and Andreo, 2011; Mudarra and Andreo, 2011), and determine the origin and residence times of karst waters (Batiot et al., 2003; Long and Putnam, 2004).

The integrated use of discharge time series and hydrochemical data (Li et al., 2022, Zhang et al., 2021) can address the problem of equifinality and thus support the increase in model reliability (Hartmann et al., 2013b; Khatami et al., 2019, Sarrazin et al., 2022). The use of hydrochemical data has been applied to test the realism of hydrological flow model structures and parameter uncertainty reduction (Hartmann et al., 2013a, Chang et al., 2021). In addition, Hartmann et al. (2013c) used hydrological and hydrochemical signals for model calibration, by combining discharge autocorrelation with $\delta^{18}O$ variability, Q–NO_3^- cross-correlation and Q–SO_4^{2-} regression. The model performance of coupled flow- and transport models over the parameter space can be quantified by computing performance metrics (e.g., KGE), which consider both the computed spring discharge and hydrochemcial time series (Hartmann et al., 2017; Çallı et al., 2023). Oehlmann et al. (2015) shows how the combination of groundwater flow and transport simulations can be used to reduce model ambiguity and to get insights into the karst network geometries.

The hydrochemical data particularly relevant for this dissertation are the electrical conductivity EC and the major ions, which are the cations calcium Ca^{2+}, magnesium Mg^{2+}, sodium Na^+, and potassium K^+, and the anions bicarbonate HCO_3^-, sulfate SO_4^{2-}, nitrate NO_3^-, and chloride Cl^-. These major ions originate from various sources, including geogenic sources, atmospheric deposition, and anthropogenic activities (Goldscheider and Drew, 2014; Ulloa-Cedamanos et al., 2020). In karst waters, Ca^{2+}, Mg^{2+} and HCO_3^- originate mainly from the weathering of carbonate rocks, following the dissolution reactions of calcite and dolomite shown in Eq 1.1 and Eq 1.2, respectively. SO_4^{2-} can originate, for instance, from geogenic sources, such as gypsum dissolution or pyrite oxidation, or from anthropogenic compounds and contaminants, including fertilizers and pesticides. NO_3^- can be related to natural sources, such as soil organic matter decomposition, or to agricultural and industrial activities. Na^+ and Cl^- can originate from silicate rocks and halite, respectively, as well as from anthropogenic sources, such as road deicing and agricultural practices. K^+ can be released into water by the dissolution of minerals such as feldspar (orthoclase), mica, and clay minerals, or be the result of industrial discharges and use of fertilizers. In minor concentrations, Ca^{2+}, Mg^{2+}, Na^+, K^+, SO_4^{2-}, NO_3^-, and Cl^- can originate from atmospheric decomposition (Goldscheider and Drew, 2014). Based on the concentration of major ions, the dominant water type can be visualized by means of a piper diagram (Piper, 1944). Karst waters dominated by calcite and dolomite usually belong to Ca–HCO_3 and Ca–Mg–HCO_3 groundwater type, respectively (Narany et al., 2019). Those ions which do not undergo significant chemical reactions or transformations are defined as conservative. The major ions considered conservatives are Na^+ and Cl^-, which can serve as tracers for studying the movement of water and mixing of water in hydrological studies. On the contrary, non-conservative ions, e.g., HCO_3^- and SO_4^{2-}, can be involved in processes such as weathering of minerals and dissolution of carbonate rocks (Hartmann et al., 2014).

Electrical conductivity (EC) in water refers to the ability of water to conduct an electrical current (µS/cm). The total electrical conductivity EC of water (Eq. 1.18) results from the sum of the contributions EC_i (µS/cm) of the individual ions i (Eq. 1.19) (Parkhurst and Appelo, 2013).

$$EC = \sum_{\mathrm{i}} \mathrm{EC_i} \tag{1.18}$$

$$EC_i = \Lambda^{\circ}_{\mathrm{m}} * m * \gamma_{\mathrm{EC}} \tag{1.19}$$

Where $\Lambda^{\circ}_{\mathrm{m}}$ is the molar conductivity (µS m^2/mol), m the molar concentration (mol/m^3) and γ_{EC} the electrochemical activity coefficient (-) of the individual ion. The molar conductivity of an ion is related to its diffusion coefficient D_{W} (m^2/s) at 25 °C (Eq. 1.20) (Parkhurst and Appelo, 2013).

$$\Lambda^{\circ}_{\mathrm{m}} = \frac{z^2 * \mathrm{F}^2}{\mathrm{R} * T} D_{\mathrm{W}} \tag{1.20}$$

Where z is the charge number (-) of the ion, F the Faraday´s constant (96485.333 Coulomb/mol), R the gas constant (8.315 J/°K/mol) and T the absolute temperature (°K). For temperatures different from 25 °C, the diffusion coefficient needs to be corrected based on the viscosity of water η (Pa s) at the specific temperature (Eq.1.21) (Parkhurst and Appelo, 2013).

$$(D_{\mathrm{W}})_T = (D_{\mathrm{W}})_{298} * \frac{T}{298} * \frac{\eta_{298}}{\eta_T} \tag{1.21}$$

The electrochemical activity coefficient γ_{EC} (-) of the individual ion *i* is function of the charge number z (-) and the Debye-Hückel activity coefficient γ_{DH} (-). For an ionic strength $I < 0.36\,|z|$, γ_{EC} is calculated es shown in Eq. 1.22 (Parkhurst and Appelo, 2013). To remove the temperature effect on $\Lambda^{\circ}_{\mathrm{m}}$ and γ_{EC}, EC measurements are normally given at the standard temperature of 25°C.

$$\log(\gamma_{\mathrm{EC}}) = \log(\gamma_{\mathrm{DH}}) * \frac{0.6}{|z|^{0.5}} \tag{1.22}$$

As proposed by Benettin and van Breukelen (2017), the chemical properties of each ion i can be grouped in a single coefficient a_i ((µS/cm) /(mg/L)) with M the solute molar mass (g/mol) (Eq. 1.23).

$$a_i = \frac{\Lambda^{\circ} * \gamma_{\mathrm{EC}}}{M} \tag{1.23}$$

Finally, Eq. 1.18 and Eq. 1.19 can be written as function of the coefficients a_i, concentration C_i (mg/L) and time t (Eq. 1.24).

$$EC(t) = \sum_i EC_i(t) = \sum_i a_i(t) * C_i(t) \tag{1.24}$$

Equations 1.18 to 1.24 are included in the supplementary material B.1.3 and are crucial for the section of this dissertation that focuses on the enhanced insights provided by high-temporal-resolution hydrochemical data in the investigation of karst systems. (Chapter 5).

As further discussed in Chapter 5, the high ion content and the complex hydrogeochemical interactions between water and the matrix often result in a karst spring discharge with intricate water speciation, characterized by complexation processes. Complexation processes involve the formation of complexes between two or more molecules or ions. These complexes are formed through coordination bonds, which involve the sharing of electron pairs between a central atom or ion (usually a metal) and surrounding ligands (atoms, ions, or molecules) known as complexing agents or ligands. Given the relevance of complexation processes within this dissertation (Chapter 5), the following nomenclature is introduced here and adopted throughout the thesis. The total concentration of a solute species (e.g., Ca, Mg, HCO_3) is the sum of the corresponding free ion (e.g., Ca^{2+}, Mg^{2+}, HCO_3^-) and the solute species involved in aqueous complexes.

1.6 Challenges in karst hydrological conceptual models

Uncertainties on model outcomes arise from different sources, i.e., structural (Enemark et al., 2019; Fandel et al., 2020; Henson et al., 2018), parametric (Mazzilli et al., 2012; Moussu et al., 2011), and input uncertainties (Liu et al., 2018; Nerantzaki et al., 2020). Structural uncertainties result from the simplifications required to create a conceptual model of a natural system (Butts et al., 2004; Gupta and Govindaraju, 2019; Lee et al., 2011; Rojas et al., 2008). Parametric uncertainties derive from the fact that the exact values of model parameters, such as storage capacity and discharge coefficients, are often unknown (Ahmadi et al., 2019; Hu et al., 2019). Finally, input uncertainties arise from missing or uncertain input and from the simplification of the processing resulting in the input boundary conditions, i.e., groundwater recharge (Breinl, 2016; McMillan et al., 2012). Due to the conceptualization of hydrological processes at the catchment scale and due to the impossibility to constrain the parameters by means of field experiments, hydrological conceptual models of karst systems are particularly prone to uncertainties (Wagener et al., 2003). *Hence, there is the need to carefully assess the impact of the different kinds of uncertainties on the performance of karst hydrological conceptual models, accounting for driving input times series, model structure, and parametrization.*

To account for the complexity and spatial heterogeneity of karst internal dynamics, karst hydrological conceptual models can be developed by including, for instance, a semi-distributed recharge and thus subareas of the catchment characterized by uniform hydrological properties (Bittner et al., 2018). However, considering more buckets introduces a higher degree of complexity in the modeling approach and consequently a larger uncertainty (Hartmann et al., 2014; Sivelle et al., 2022), opening the discussion about the trade-off between hydrological model complexity and hydrological model

performance. *Hence, the implications of considering semi-distributed recharges in hydrological conceptual models need to be further studied.*

The use of hydrochemical data provides insights into the internal dynamics of karst aquifers and thus supports the understanding of the system functioning. Karst systems exhibit intricate hydrological behaviors with significant fluctuations in discharge that may change by one order of magnitude within hours or days (Hartmann et al., 2014). To maximize the utility of hydrochemical data to reflect the variability of the internal response of a system more accurately, the hydrochemical sampling frequency should be comparable to the time scale of the hydrological response of the system (i.e., hours at peak flow conditions). However, continuous monitoring is often constrained to water level, discharge, temperature, and electrical conductivity (EC), whereas obtaining high-frequency time series of major solute species is hindered by the prohibitive analysis costs and time requirement (Charlier et al., 2012). *Consequently, new approaches are needed to retrieve high temporal resolution hydrochemical data without the need for intensive field measurements.*

Typically, model evaluation as well as parameter calibration and validation are done using measured discharge time series at a spring and computing performance metrics. Various models, characterized by diverse structures or parameter values, can produce satisfactory simulated spring discharge (Mudarra et al., 2019). Hence, prior studies have demonstrated that solely evaluating models based on spring discharge may not fully capture the internal dynamics of karst systems and can result in significant equifinality (Hartmann et al., 2017). To address the problem of equifinality and to constrain karst conceptual model structure and parametrization, multi objective approaches aim to couple hydrological (e.g., spring discharge) and hydrochemical (e.g., high resolution ion concentration time series) information data. In addition, to capture the internal variability of karst systems, conceptual models should have a temporal resolution that aligns with the time scale of the hydrologic response of the system, which, for karst systems with high temporal variability, is on an hourly scale. However, karst hydrological conceptual models calibrated solely on the time series of spring flow rates are generally implemented on a daily scale (Bakalowicz, 2005; Bittner et al., 2018; Sivelle et al., 2019). *Hence, there is the need to investigate how high-temporal resolution hydrochemical data can be used for the verification of karst hydrological conceptual model structure and parametrization at hourly scale.*

Chapter 2

Research framework

2.1 Previous works

2.1.1 Framework-specific modelling approaches

The models used in this thesis have been developed starting from two karst hydrological conceptual models, i.e., LuKARS (Bittner et al., 2018) and KarstMOD (Mazzilli et al., 2019). Here, a brief description of their model structure is presented. The equations of LuKARS and KarstMOD are reported in appendix A.2 and in the supplementary materials B.2.1 and B.2.2.

LuKARS

LuKARS (Land use change modeling in KARSt systems) is a semi-distributed model developed by Bittner et al. (2018) that lumps the predominant hydrotopes in a karst catchment as independent non-linear units. Each hydrotope represents an area of the catchment characterized by similar land use and soil type and by homogeneous hydrological behavior. Fig. 2.1a shows the schematic conceptualization of LuKARS for the case of two hydrotopes. The epikarst zone is represented by the specific responses of each hydrotope. To account for the duality of karst systems, each hydrotope contributes to the spring discharge (Q_{spring}) with a slow flow (Q_{is}) through the matrix and a fast flow (Q_{hyd}) through preferential flow paths directly to the spring. Infiltration through the matrix is implemented as a linear function of the water level in the corresponding bucket. The fast flow starts when the hydrotope-specific maximum storage capacity (E_{max}) is reached and stops once the storage volume drops below the hydrotope-specific minimum storage capacity (E_{min}). The saturated zone consists of a single linear storage B which is recharged independently by each hydrotope. Finally, to represent secondary springs, part of the water is moved out of the catchment (Q_{sec}) once a hydrotope-specific threshold (E_{sec}) is exceeded.

KarstMOD

KarstMod is a modeling platform, which allows a flexible implementation of different conceptual reservoir models and thus flexible representation of karst hydrological processes (Jourde et al., 2015; Mazzilli et al., 2019). Among the different structures available within the platform, Fig. 2.1b shows the model structure relevant in the context of this thesis. It consists of a two-level structure, i.e., epikarst routine (E) and groundwater routine (Matrix (M), and Conduit (C) components). The upper level represents the infiltration zone, whereas the lower level is the saturated zone where compartment M and C stand for the different sub-systems of the saturated zone. The water in the epikarst is transferred to the lower compartments either by a slow infiltration to the matrix (Q_{EM}) or fast flow to the conduits (Q_{EC}).

Both the matrix and conduit then provide water to the spring (Q_{MS} and Q_{CS}, respectively). Based on the pressure head in the lower compartments, a transfer of water can occur from the conduit to the matrix or vice versa (Q_{MC}). Finally, the hysteretic response of the epikarst is represented by accounting for both the discharge from compartment E to compartment C (Qhy_{ES}) and the discharge from compartment E directly to the spring (Qhy_{ES}). All the discharge components are implemented as exponential functions of the water levels in the buckets. (Mazzilli et al., 2019)

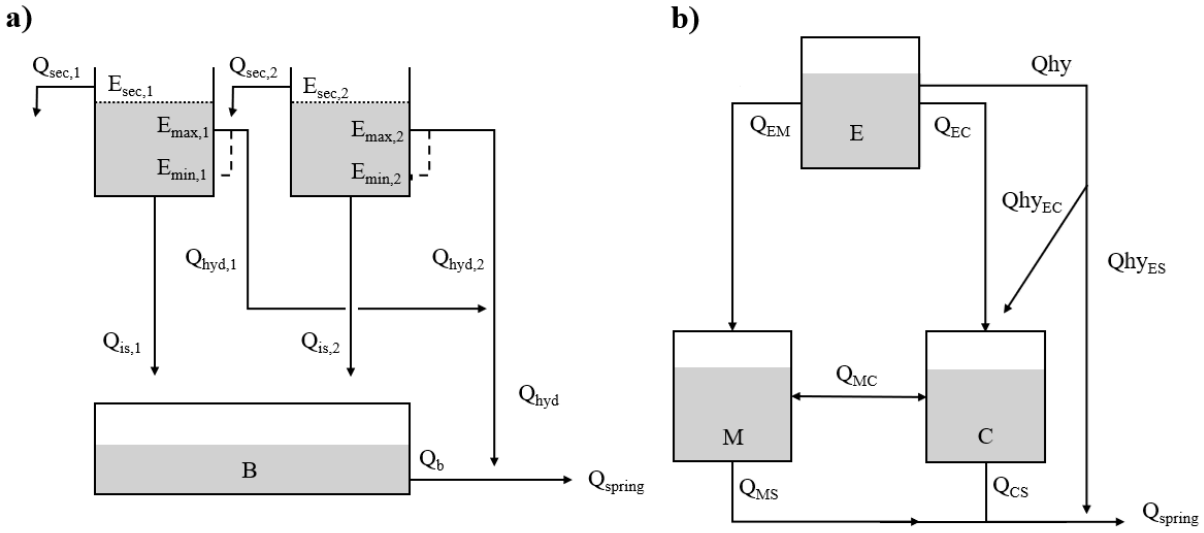

Fig. 2.1 Schematic representation of the model concept of **a** LuKARS and **b** KarstMod.

2.1.2 Experimental recharge areas

In this work, three karst systems in Europe were investigated, i.e., the Las Hountas spring and the Oeillal spring in southern France, as well as the Kerschbaum spring in Austria (Fig. 2.2). The three selected recharge areas show similarities in catchment size (2.5 – 43.2 km^2) and land cover (dominated by forest), and differences in geological and climate properties. In particular, they are characterized by different degree of karstification and accordingly show differences in discharge variability. In the following, a brief description of each selected karst system is provided. More information about the study areas is provided in Chapters 3–6.

The Las Hountas spring

The Baget recharge area (13 km^2) is located 10 km southwest of the city of Saint-Girons (French Pyrenees). It is a binary karst system with heterogeneous geology and intermittent overflow. The recharge area is characterized by the coexistence of calcareous formations with a mineralogical composition dominated by calcite (Jurassic and Lower Cretaceous) and an outcrop impermeable formation of black flysch (Ulloa-Cedamanos et al., 2021). Las Hountas is the only perennial spring of

the recharge area, and it is representative of a part of the total response of the system. Indeed, during high flood events, the water from the upper part of the recharge area bypasses the spring and directly reaches the catchment outlet (Mangin, 1975; Ulloa-Cedamanos et al., 2021) (Fig. 2.2 a). The Baget recharge area is predominantly covered by fir-beech forests (Fig. 2.2 a). The region is characterized by the Atlantic oceanic climate with an average annual air temperature of 12.3°C and mean annual precipitation of approximately 1700 mm (period from 1970 to 2020). The average annual discharge at the catchment outlet is 0.48 m^3/s with no influence of snow melt processes (Ulloa-Cedamanos et al., 2020).

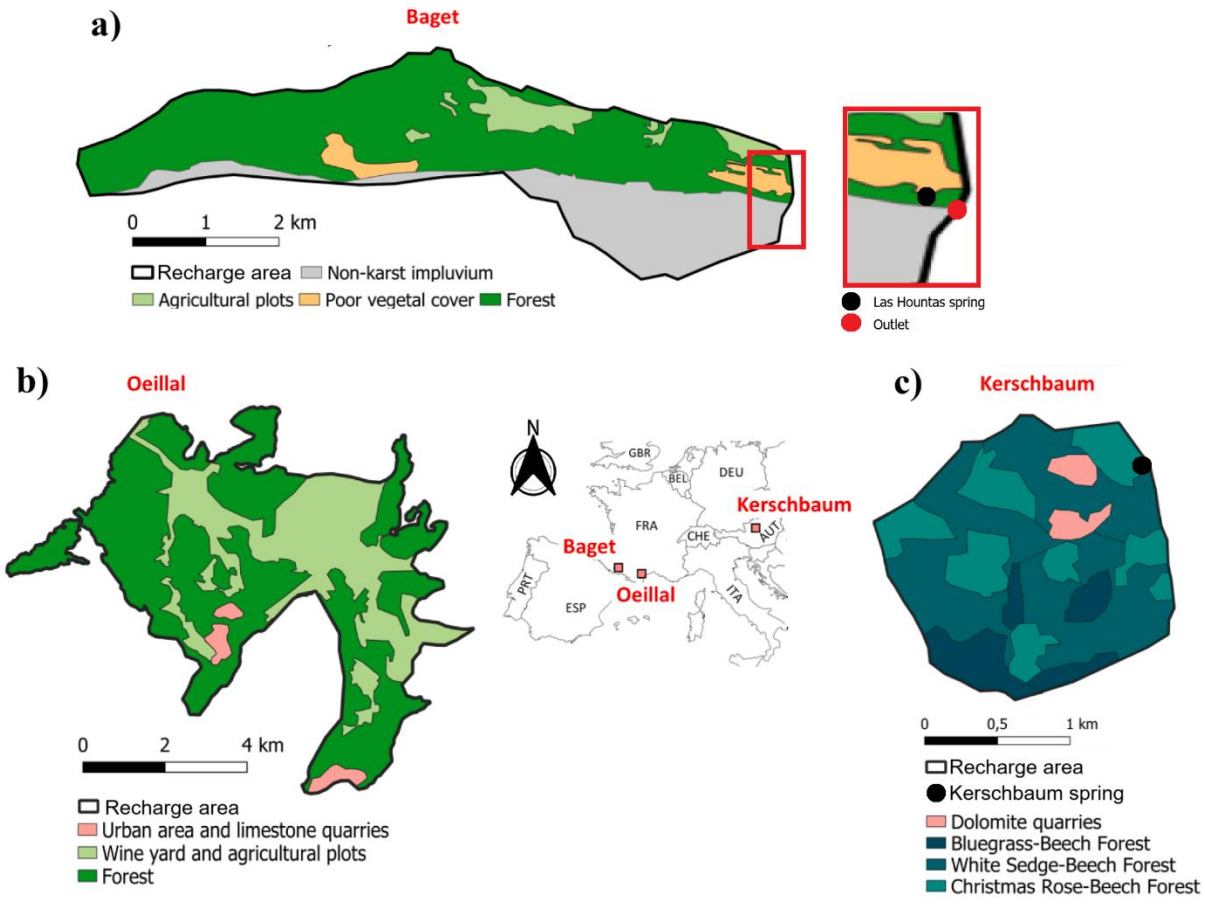

Fig. 2.2 Land use maps of the recharge areas of **a** Baget (France), **b** Oeillal (France), and **c** Kerschbaum (Austria) (modified after Sivelle et al., 2022). Note that the Oeillal spring is outside its recharge area (Sivelle and Jourde, 2020; Sivelle et al., 2021).

Météo-France provided precipitation data recorded at the meteorological station of Antichan, approximately 8 km northeast of the Baget spring, for the period 1970–2022. The French Karst National Observatory Service (SNO KARST) and French Geological Survay (BRGM) supplied daily discharge time series at the recharge area outlet (Fig. 2.2a) for the period 1970–2022. In addition, as part of the experimental work of this thesis, the Las Hountas spring (Fig. 2.2a) was instrumented in October 2021 with an In-Situ Aqua TROLL 200 device (In-Situ Inc., United States), recording continuous water level,

specific EC, and water temperature every 15 minutes (Fig. 2.3a). The observed discharge time series at the Las Hountas spring was derived from the recorded water levels by applying the rating curve from Mangin (1975), which was adjusted to account for the current cross-sectional state based on additional field measurements conducted in 2021 and 2022. To collect water samples for analysis of ions, a 6712 ISCO sampler (Teledyne ISCO, United States) was installed at the spring inside a shelter always in the shade and linked to the EC probe (Fig. 2.3b). For efficient sampling during storm conditions, the sampler was programmed to automatically initiate sampling when the water level exceeded a 30 cm threshold. Four precipitation events were sampled: from 4 October 2021 to 14 October 2021, from 1 November 2021 to 7 November 2021, from 30 March 2022 to 7 April 2022, and from 20 November 2022 to 26 November 2022. During these events, the sampling temporal resolution was 1 hour during the rising limb of the hydrograph and 2 hours during the recession phase. To capture baseflow following each precipitation event, composite samples were collected, integrating 8-hour intervals.

Fig. 2.3 Experimental site at the Las Hountas spring in the Baget catchment. Installation of **a** the In-Situ Aqua TROLL 200 probe and **b** the 6712 ISCO sampler (on the left side).

The samples were collected daily in LDPE plastic vials with zero headspace, filtered through 0.22 µm membrane filters, and stored in a refrigerator at 4°C for approximately one week before analysis. For each sample, an aliquot designated for cation analysis was acidified with nitric acid (HNO_3) to prevent complexation and precipitation (Weiss, 2020; Ulloa-Cedamanos et al., 2020). All samples were analyzed for major solute concentrations. Inductively coupled plasma optical emission spectrometry (ICP-OES) was used to quantify Ca, Mg, Na, and K; ion chromatography to quantify NO_3, SO_4, and Cl; and titration analysis to quantify HCO_3. Detailed specifications of the laboratory analysis are provided in the supplementary material B.1.2. During data preprocessing, the software PHREEQC was used to ensure that the charge balance error of each sample was within ±5% (Parkhurst and Appelo, 2013).

The Oeillal spring

The Oeillal spring is located north of the city of Narbonne, southern France, and drains water from the limestone terrain of the Fonfroide-Monredon massif (Fig. 2.2b). The primary aquifer in this region resides within a calcareous formation, supplying water to the Oeillal spring, which emerges in the western part of the Narbonne-Sigean sedimentary basin at four distinct spring pools (Padilla et al., 1994). Additionally, in the northern part of the area, there is an alluvial aquifer located within the Quaternary formation of the Aude river terrace. The recharge area covers around 43.2 km^2 with a potential additional 10 km^2 contributing zone (Sivelle and Jourde, 2020). The recharge area is characterized by Mediterranean climate with mean annual temperature of 14.7°C, annual precipitation of 570 mm, and mean annual discharge around 0.14 m^3/s (1980–2020) (Sivelle and Jourde, 2020).

Daily precipitation was measured at the Narbonne meteorological station and provided by Météo-France for the period 1987–2020. Daily discharge time series were computed starting from rating curves by Sivelle and Jourde (2020)

The Kerschbaum spring

The Kerschbaum spring is located 10 km south of the city of Waidhofen a.d. Ybbs, Austria. It has a recharge area of approximately 2.5 km^2 (Fig. 2.2c) and belongs to the eastern foothills of the Northern Calcareous Alps, showing a homogeneous dolomitic geology. Despite the dominance of carbonate bedrocks, the study area does not show significant sinkholes and therefore the spring discharge is controlled by diffusive infiltration (Narany et al., 2019). The recharge area is primarily covered with forests (Fig. 2.2 c) and is characterized by continental climate with a mean annual temperature of 8°C, mean annual precipitation of 1379 mm, and average annual spring discharge of 0.034 m^3/s (period from 1981 to 2014) (Bittner et al., 2018).

Most of the hydrochemcial data used in the framework of this thesis were recorded in the Kerschbaum spring recharge area by the water works in Waidhofen a.d. Ybbs, who provided

- daily discharge, precipitation and air temperature for the period 2006 – 2007;

- EC and dissolved major solutes (i.e., Ca, Mg, HCO_3, SO_4, NO_3, Cl, Na, K) for the periods 2000–2016 and 2018–2019 at different temporal resolutions (quarterly and weekly, respectively).

In addition, as part of the experimental work of this thesis, water samples were collected every 5 hours by means of a 6712 ISCO sampler during the period from 23 January 2022 to 28 January 2022. The specific EC was measured in the field using a conductivity meter (HT Hydrotechnik, Typ 575-LTC) and

reported at 25°C. Fig. 2.4 shows the installation at the Kerschbaum spring. The specifications of the laboratory analysis are reported in the supplementary material B.1.1.

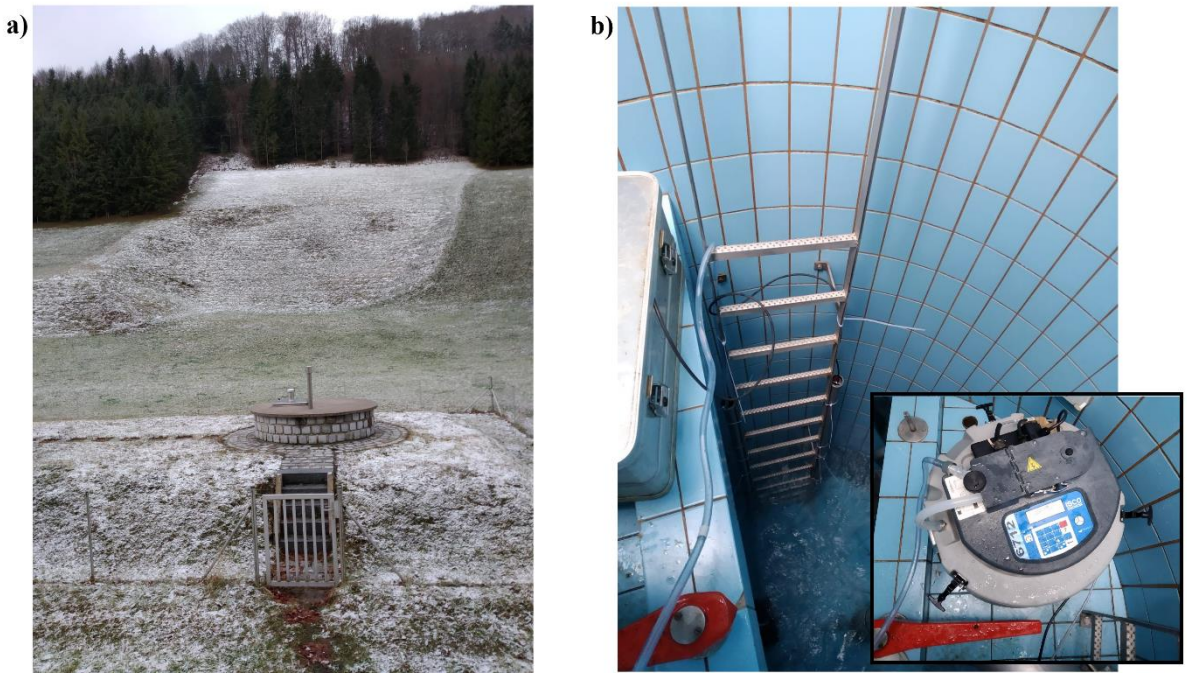

Fig. 2.4 Experimental site at the Kerschbaum spring. View from **a** outside and **b** inside the spring chamber where the ISCO sampler is located (see lower right corner in the right figure).

2.2 Research objectives

In the context of the challenges described in Subchapter 1.6, this dissertation aims to contribute to the current discussion related to the investigation of uncertainties in hydrological conceptual karst models and how to constrain them. In particular the following hypotheses will be evaluated.

1) Model input uncertainties show temporal variations depending on how much the groundwater recharge and the modeled spring discharge are controlled by one specific process, e.g., snowmelt or evapotranspiration.
2) The systematic consideration of a semi-distributed recharge does not necessarily lead to an increase in model performance in case of hydrological conceptual karst models at a daily scale.
3) Using continuous electrical conductivity measured at a karst spring, solute concentration time series can be retrieved at the same temporal resolution of the observed electrical conductivity.
4) Hydrochemical data at high temporal resolution can be used to conceptualize and select hourly event-based karst model concepts as well as to properly constrain the model parameter ranges.

Each hypothesis was addressed in an individual peer-reviewed publication. Fig. 2.5 gives an outline of the presented cumulative dissertation, by summarizing the hypothesis, main contents, and related article as well as indicating the chapter of this dissertation that deals with it. For each article, a summary abstract will be presented in Subchapters 2.3.

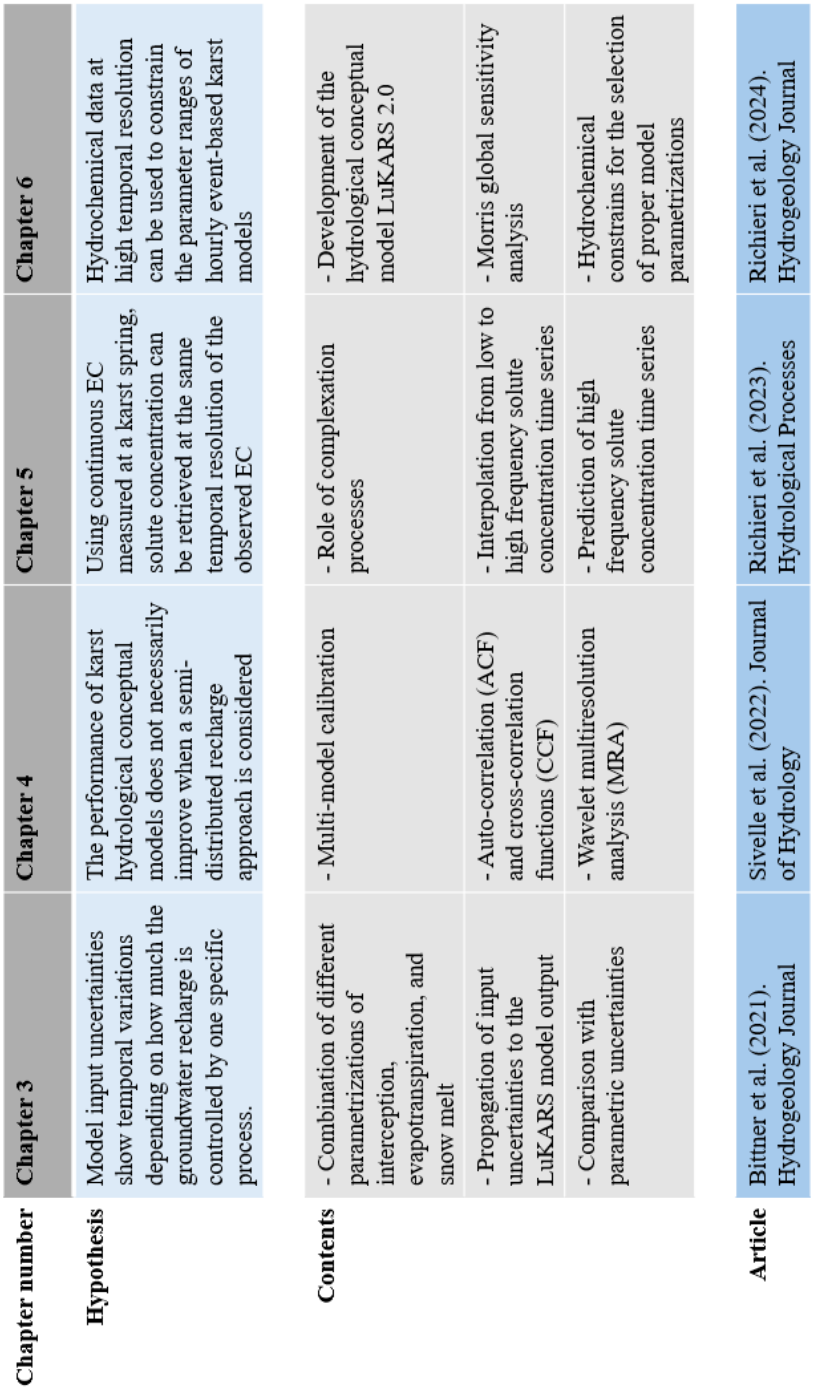

Fig. 2.5 Outline of this cumulative dissertation.

2.3 Research components and specific objectives

2.3.1 Hypothesis 1

Hydrological models simplify the subsurface heterogeneity and complex hydrodynamic processes typical of karst systems (Guinot et al., 2015; Sivelle et al., 2021; Sivelle and Jourde, 2020). Therefore, to assess the reliability of a model, different sources of uncertainty and their impact on the model output should be investigated (Sarrazin et al. 2018). The uncertainties in the model output can arise from different sources, i.e., structural (Enemark et al., 2019; Fandel et al., 2020; Henson et al., 2018), parametric (Mazzilli et al., 2012; Moussu et al., 2011) and input uncertainties (Liu et al., 2018; Nerantzaki et al., 2020). Structural uncertainties are related to the simplification necessary during the development of a conceptual model, potentially resulting in the underrepresentation of significant hydrodynamic processes (Butts et al., 2004; Gupta and Govindaraju, 2019; Lee et al., 2011; Rojas et al., 2008). Parametric uncertainties are the consequence of the unknown exact values of model parameters which need to be calibrated (Ahmadi et al., 2019; Hu et al., 2019). Input uncertainties arise from uncertain input data (Breinl 2016; McMillan et al. 2012), as well as from the simplifications of groundwater recharge processes (Patil et al. 2011; Vrugt et al. 2008). For the specific case of pre alpine karst systems, the groundwater recharge is controlled by interception, evapotranspiration and snowmelt processes, whose time series are often computed by applying additional models rather than measured in the field (Mazzilli et al., 2012; Ollivier et al., 2020).

The study presented in Chapter 3 explores the input uncertainties, arising from the representation and parameterization of processes relevant to groundwater recharge, i.e., interception, evapotranspiration, and snow melt processes, for the case of the semi-distributed karst model LuKARS (subchapter 2.1.1). This study hypothesizes, firstly, that *input uncertainties may fluctuate seasonally*, and secondly, that *the specific contribution of individual processes to groundwater recharge can be determined from the uncertainties in the model output.* The research questions are as follows.

1. To what extent do the input uncertainties of each individual recharge process affect model predictions compared to parametric uncertainties?
2. Are input uncertainties affected by seasonality?
3. Do input uncertainties show temporal variations depending on how much the groundwater recharge is controlled by one specific process?
4. How do the input uncertainties change when considering more processes to be unknown?

These research hypotheses and questions are addressed in the article Bittner et al. (2021) presented in Chapter 3. To study the time-dependent relevance of model input uncertainties, nine input models were selected to compute the input recharge time series: three to compute interception (DVWK, Gash and Liu), three to compute evapotranspiration (Thornthwaite, Hamon and Oudin) and three to compute snow

processes (Martinec, Girons Lopez and Magnusson) (Fig. 2.6a). All the input model combinations were tested at the pre alpine karst spring Kerschbaum, for which the hydrological conceptual LuKARS model was implemented by Bittner et al. (2018) (Fig. 2.6b). To focus on input uncertainties, only the parameters of the input models were considered as uncertain, while the model parameters were taken constant and equal to those previously calibrated for the same study area by Teixeira Parente et al. (2019). The findings of this study indicate that input uncertainties exhibit seasonal variations (Fig. 2.6c). Furthermore, the uncertainties associated with evapotranspiration and snowmelt inputs are greater than those related to interception (Fig. 2.6c). These results suggest that the significance of a particular process in groundwater recharge can be inferred from its corresponding input uncertainties. Finally, the results show that two or more uncertain processes can compensate for each other.

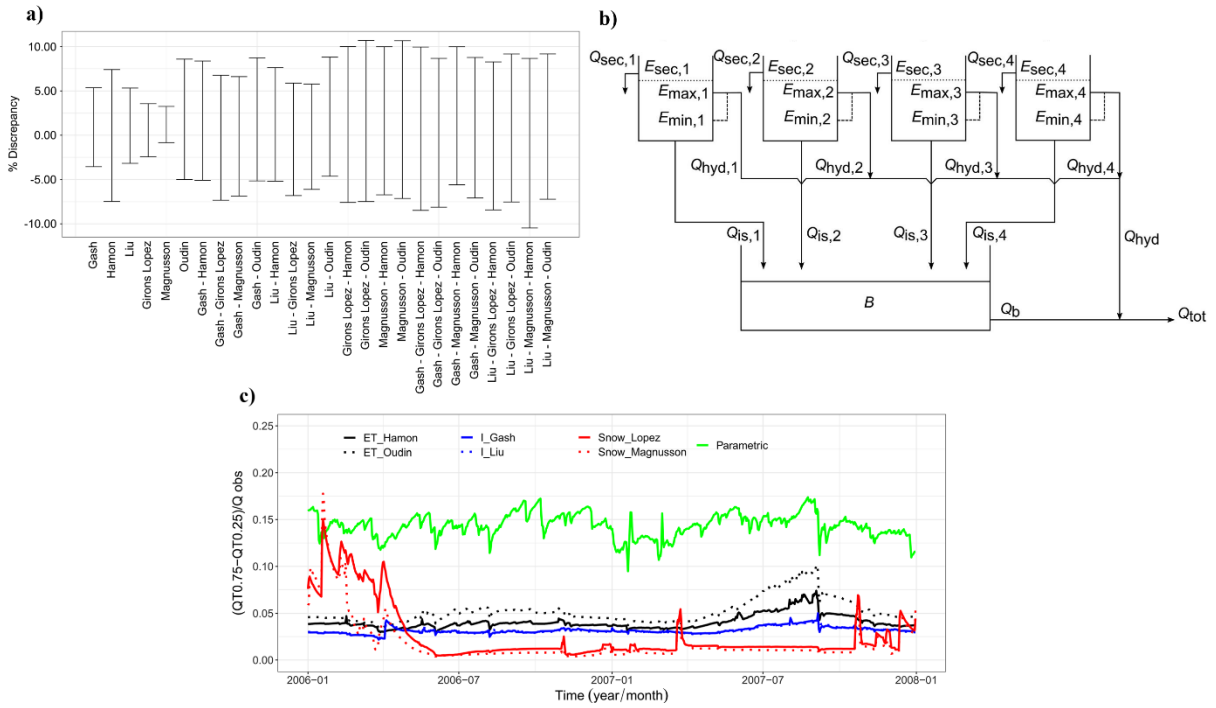

Fig. 2.6 a Minimum and maximum percentage discrepancies between computed spring discharge from each input model combination and the observed spring discharge. **b** Model structure of LuKARS for the Kerschbaum system. **c** Interquartile ranges of LuKARS model outputs normalized by the observed discharge when considering uncertain the single processes with the different input models, in comparison to the parametric uncertainties computed by Teixeira Parente et al. (2019) (modified after Bittner et al., 2021). Please refer to Chapter 3 for further details.

2.3.2 Hypothesis 2

Hydrological conceptual models have been used to assess the impact of climate change and anthropogenic activities on karst systems (Brenner et al., 2018; Chen et al., 2018; Doummar et al., 2018; Nerantzaki et al., 2020; Hartmann et al., 2012; Sivelle et al., 2021). However, only a few models have considered the influence that land-cover and land-use (LCLU) changes have on karst groundwater resources (Bittner et al., 2018; Sarrazin et al., 2018). As shown in former studies, it can be of interest to consider a semi-distributed recharge to improve the representation of flow spatial dynamics in karst systems (Bittner et al., 2018; Ollivier et al., 2020). On the one hand, a semi-distributed recharge approach is relevant for capturing the impact of land cover and land use (LCLU) on flow dynamics; on the other hand, it introduces more complexity into the modeling process. Therefore, it is necessary to assess the implications of considering a semi-distributed recharge in lumped parameter models. The aim of the study presented in Chapter 4 is to perform multiple hydrological model calibrations, focusing on the uncertainty arising from the model structure. The hypothesis of this study is *that the performance of karst hydrological conceptual models does not necessarily improve when a semi-distributed recharge approach, based on LCLU, is considered*. Therefore, *it is essential to identify the levels of model complexity that result in the best performance in terms of simulated spring flows*. The research questions are as follows.

1. How does a semi-distributed recharge affect the flow dynamics of a hydrological conceptual karst model, particularly the infiltration toward the saturated zone?
2. How can we evaluate the trade-off between hydrological model complexity and hydrological model performance?
3. Does considering a more complex conceptualization of recharge processes always result in better performance of hydrological conceptual karst models?

These research hypothesis and questions are addressed in the article Sivelle et al. (2022) presented in Chapter 4. The semi-distributed recharge is conceptualized based on the definition of hydrotopes (Bittner et al., 2018), which are individual units in the recharge area characterized by similar soil and land use, resulting in homogeneous response to precipitation events and different contribution to the groundwater. Two hydrological conceptual models, LuKARS and KarstMod (subchapter 2.1.1), were implemented to account for different conceptualizations of the flow processes. Three forest-dominated recharge areas were chosen for this investigation: Baget, Oeillal, and Kerschbaum (Fig. 2.2). A multi-model calibration, considering different levels of complexity in the upper model layer, was conducted by testing different configurations in the upper level (ranging from 1 to 4 hydrotopes) for each recharge area (Fig. 2.7a). To focus on the infiltration toward the saturated zone, the configuration of the lower level remains consistent with previous studies (Bittner et al., 2018; Sivelle et al., 2019; Sivelle et al., 2021).

The evaluation of the models was carried out using seven numerical performance criteria (Fig. 2.7b, pag. 68) and time series analysis, including auto-correlation function ACF (Fig. 2.7c), cross-correlation function CCF (Fig. 2.7d), and wavelet multiresolution analysis MRA (Fig. 2.7e). The results indicate that the consideration of a semi-distributed recharge does not necessarily lead to an increase in model performance. A more complex conceptualization of recharge processes results in better performance for both Kerschbaum and Oeillal, while no improvement is observed for the Baget catchment. The Baget catchment is characterized by a high degree of karstification and significant temporal variability in spring discharge. Therefore, recharge processes are difficult to capture using a daily lumped parameter hydrological model as applied here, and investigations at higher temporal resolutions are recommended.

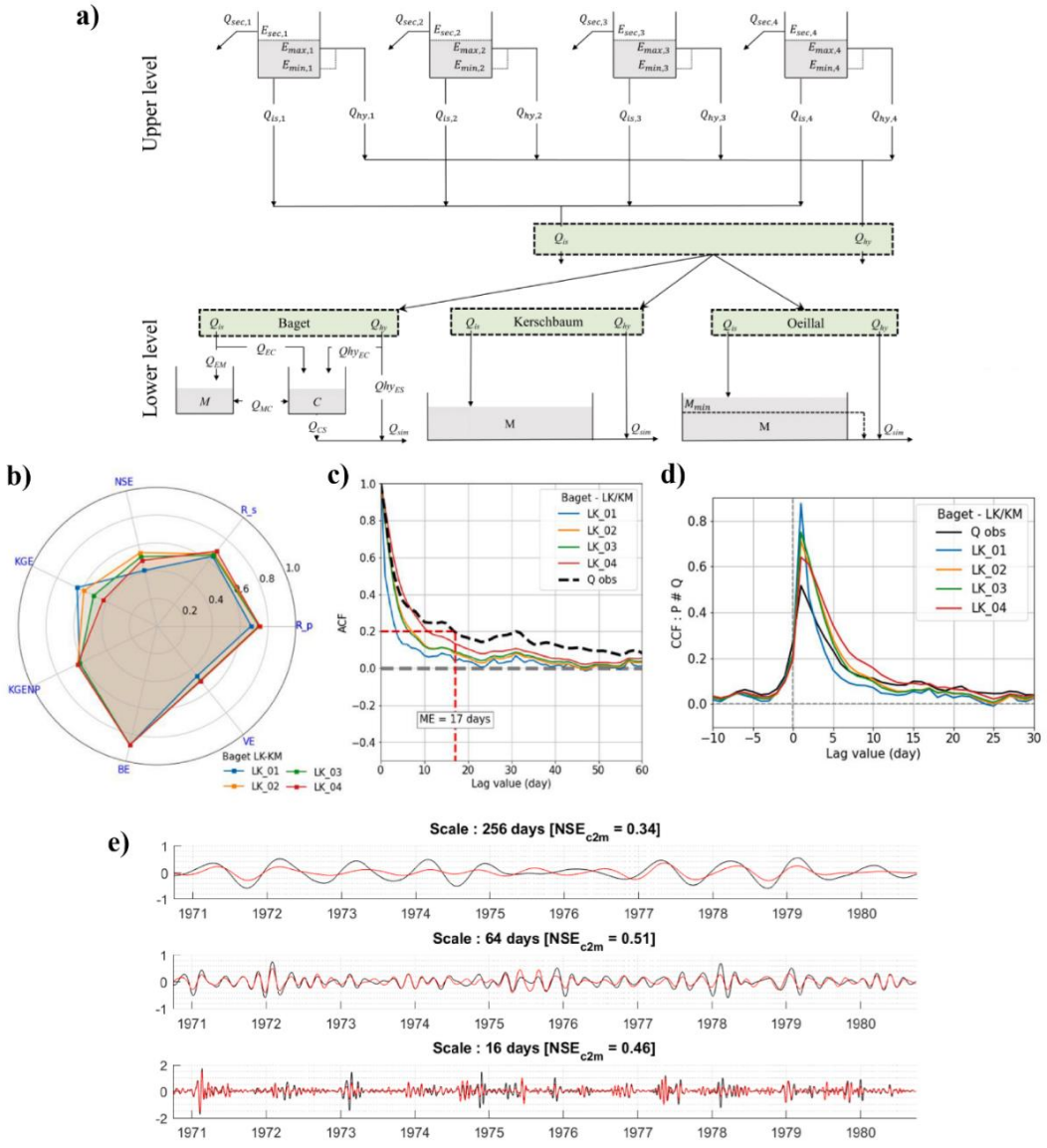

Fig. 2.7 a Structure of the hydrological conceptual models for the three catchments. Evaluation of model performance by means of **b** multiple numerical performance criteria, **c** auto-correlation function (ACF), **d** cross-correlation function (CCF) and **e** wavelet multiresolution analysis (MRA) (modified after Sivelle et al. (2022)). Please refer to Chapter 4 for further details.

2.3.3 Hypothesis 3

Hydrochemical data at high temporal resolution (e.g., hourly) at a karst spring can support the understanding of the subsurface hydrodynamical functioning (Hartmann et al., 2014). However, the continuous monitoring at karst springs is restricted to discharge, electrical conductivity and temperature, whereas the collection of solute concentration at high frequency is limited by high analysis costs and time requirement (Charlier et al., 2012). On the contrary, the EC signal is easy and cheap to measure by automatic instruments and therefor has been intensively used for the investigation of karst systems (Cano-Paoli et al., 2019; Chang et al., 2021; Hayashi et al., 2012; Jourde et al., 2018; Meus et al., 2014). Recently, continuous EC signal and point ionic measurements at a river gauge were used by Benettin and van Breukelen (2017) to derive the individual ion concentration at the same temporal resolution as the observed EC. Benettin and van Breukelen (2017) tested this approach for the Upper Hafren river catchment, United Kingdom, which shows low EC values of on average 29 µS/cm and total ion content dominated by Na^+ and Cl^-, which have no or little tendency to form complexes. Due to the high ion content with EC values up to 500 µS/cm and non-negligible concentrations of aqueous complexes in karst systems (Chang et al., 2021; Hilberg and Schneider, 2011; Narany et al., 2019), we had the necessity to modify the methodology proposed by Benettin and Van Breukelen (2017) to account for aqueous complexation processes. Thus, in the study presented in Chapter 5, we derived the concentrations of solute species present as free ions and as part of complexes separately (Fig. 2.8a). The concentration of free ions were derived from the linear interpolation of the relative contribution of each ion to the total measured EC (called weight factors). The contribution of each individual ion was computed with Eq. 1.18 – Eq. 1.24. On the contrary, the solute species involved in complexes were obtained by means of speciation calculations with PHREEQC as difference between the total molality of a solute (mol/kgw) and the molality of the solution (mol/kgw).

In this work, we hypnotize *that it is possiblt to retrieve high-temporal resolution solute concentration at a karst spring if complexation processes are explicitly considered by performing additional speciation calculation with PHREEQC.* The research questions are as follows.

1. Is it possible to retrieve solute concentration time series from EC measurements at a karst spring?
2. Can the method be used to interpolate from low to high frequency concentration time series?
3. Can the method be used to predict high frequency concentration time series?
4. Can the method be applied equally to a catchment with rather homogeneous and heterogeneous geology and different temporal resolution of the available datasets?

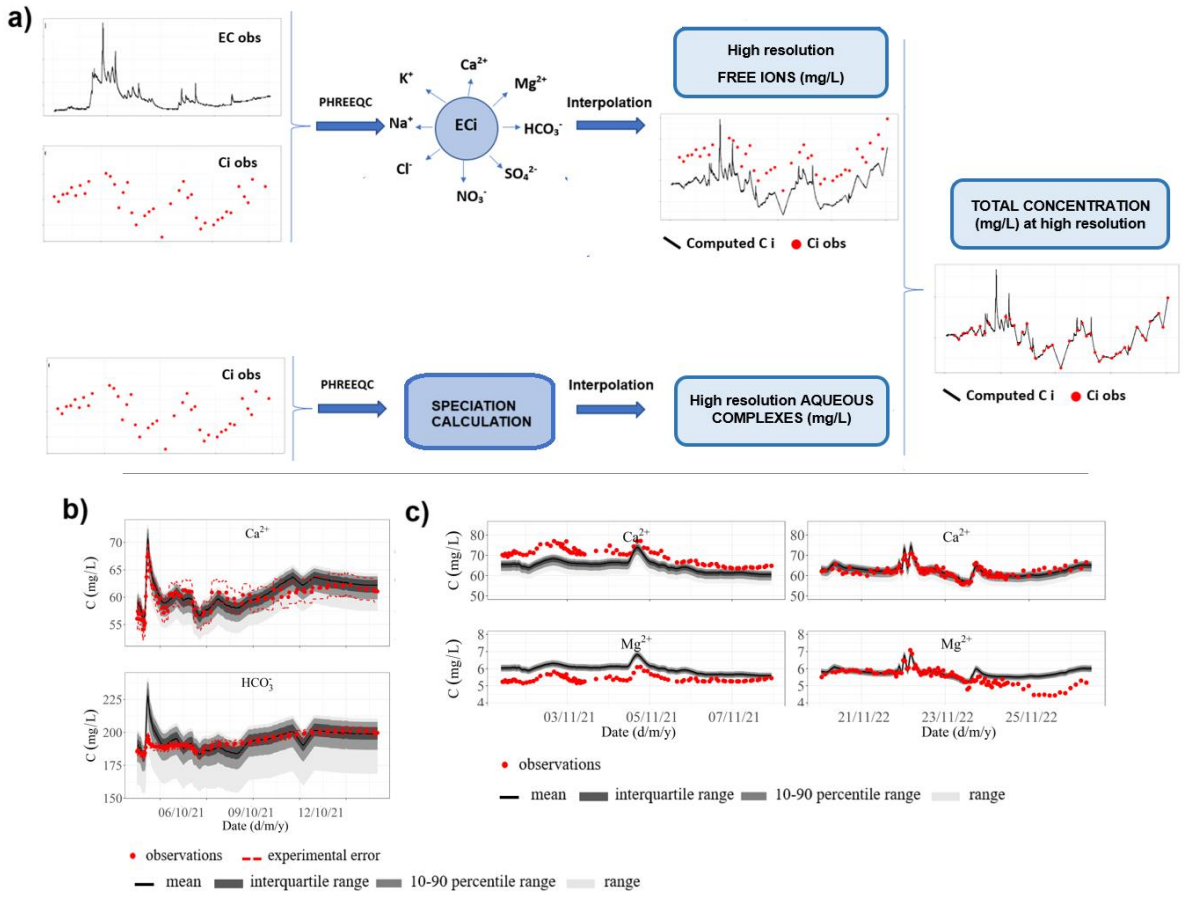

Fig. 2.8 a Schematic representation of the EC decomposition approach used to derive the individual solute species at high temporal resolution starting from continuous EC and point ionic measurements at karst springs. **b** Uncertainty quantification of the individual solute species concentrations in case of interpolation. **c** Predictive model based on the frequency of occurrence of the weight factors. Please refer to Chapter 5 for further details.

These research hypothesis and questions are addressed in the article Richieri et al. (2023) presented in Chapter 5. Two karstic catchments with differing geologies and temporal resolutions of available hydrochemical datasets are considered, i.e., the Kerschbaum dolostone system (Fig. 2.2c) and the Baget limestone system (Fig. 2.2a). The results show that complexation processes should be considered for accurately estimating total solute concentrations, particularly for SO_4, Ca, Mg, and HCO_3. The EC signal of a karst spring can effectively be used to retrieve the dynamics of those solutes significantly contributing (approximately > 6%) to the total EC, i.e., HCO_3, Ca and Mg. For the case of Baget, the method shows substantial uncertainty due to the varying water contributions from different geological regions. In addition, the temporal variability of the weight factors of the free ions SO_4^{2-} and HCO_3^- provides insight into the variability of the water contributions from different areas in the catchment. On the contrary, the proposed method can estimate solute concentrations in karst systems with stationary and hydrogeochemical homogeneous contributing areas, as is the case of the Kerschbaum watershed.

2.3.4 Hypothesis 4

Hydrological models need to be calibrated due to the lack of knowledge in process understanding and model parameter values (Le Moine et al., 2008). This is particularly true in the case of hydrological conceptual model of karst systems since model parameters cannot be determined by means of field observations (Hartmann et al., 2014). Generally, the model performance is evaluated by considering the discharge observed at the karst spring and by computing performance metrics (Bennett et al., 2013; Ferreira et al., 2020). However, calibrating the model solely against the spring discharge is considered not reliable since different model structures and parameters can result in satisfactory simulated spring discharge (Mudarra et al., 2019). Thus, multi-objective approaches based on the use of additional data can be applied to reduce the problem of equifinality, i.e., multiple parameter sets reproducing the observed discharge (Chiogna et al., 2024). As described in subchapter 1.5.3, major ions and EC allow to investigate the spatial and temporal variability in the hydrological response of karst systems (Barbieri et al., 2005; Chang et al., 2021; Gil-Márquez et al., 2017; Hartman et al., 2013).

In the study presented in Chapter 6, we aim to verify the model parametrization of a conceptual event-based karst model by coupling hydrological data (spring discharge) and hydrochemical data (high resolution solute concentration time series), which were collected in the Baget karst watershed during the field campaign in April 2022. Due to the high temporal variability of the hydrochemical signal observed at the spring (hourly), the semi-distributed model LuKARS 2.0, based on the original model from Bittner et al. (2018) (subchapter 2.1.1), was implemented for the first time at hourly scale. LuKARS 2.0 allows a flexible conceptualization of karst systems by accounting for the water contributions draining from the main geological areas (hydrotopes) in the watershed. In addition, a transfer between matrix and conduit was implemented in the lower compartment of the model (Fig. 2.9a) following the approach proposed in the model KarstMod (Mazzilli et al., 2023; Sivelle et al., 2023).

The hypothesis of this work is that *hourly hydrochemical data can be used for the selection of proper model parametrization for a hydrological conceptual event-based karst model*. The research questions are as follows.

1. When considering a set of model realizations covering the parameter space, do the realizations simulating the spring discharge with comparable Kling-Gupta Efficiency (KGE) also capture the internal dynamics of a karst system?
2. Can high resolution ion concentration time series be used to select proper model parametrizations for hydrological conceptual event-based models?
3. When coupling hydrological and hydrochemical information, can hydrological conceptual models capture the response of water contributions from different geological areas in the catchment to different flow conditions?

4. Is sensitivity analysis considering solely the spring discharge time series reliable for the identification of sensitive parameters?

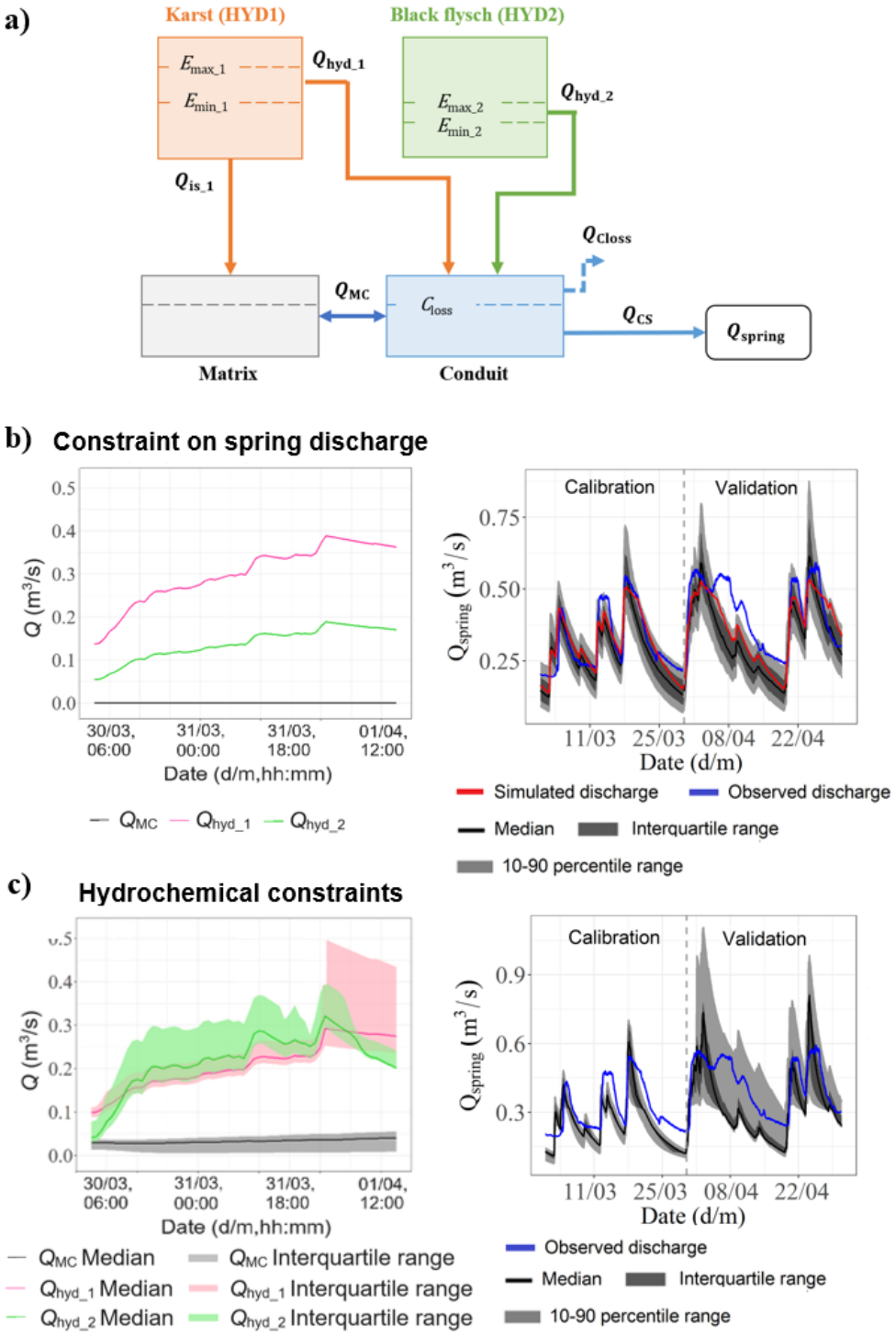

Fig. 2.9 a LuKARS 2.0 model concept. **b** Internal fluxes (left) and spring discharge (right) of the selected Morris´ simulation based on the constraint on the spring discharge. **c** Internal fluxes (left) and spring discharge (right) of the subset of simulation respecting the hydrochemical constraints (modified after Richieri et al., (2024)). Please refer to Chapter 6 for further details.

These research hypothesis and questions are addressed in the article Richieri et al. (2024) presented in Chapter 6. The model was tested on the Baget karst system (Fig. 2.2a), characterized by a heterogeneous geology combining karst (limestone) and non-karst (black flysch) areas. The Morris screening method was used to investigate parameter sensitivity by considering 9,000 parameter sets, each corresponding to a model run, i.e., a Morris realization. First, the model was evaluated by selecting an envelope of Morris´ realizations simulating spring discharge with a certain accuracy (KGE < 0.5) (Fig. 2.9b). Then, time series at hourly resolution of the contributions of the free ions HCO_3^- and SO_4^{2-} to the total EC, called weight factors (Richieri et al. (2023)), were used to define hydrochemical constrains and thus to identify a subset of realizations respecting both the temporal variability at the spring and the variability of the internal fluxes of the system (Fig. 2.9c). The results show that high resolution ion concentration time series can be effectively used to constrain model parametrization for an hydrological conceptual event-based karst model.

Chapter 3

Impact of input model uncertainties on hydrological conceptual karst modelling

Bittner, D., **Richieri, B.**, and Chiogna, G. (2021). Unravelling the time-dependent relevance of model input uncertainties for a lumped hydrologic model of a pre-alpine karst system. Hydrogeology Journal, 29(7): 2363–2379. https://doi.org/10.1007/s10040-021-02377-1

Abstract

Uncertainties in hydrologic model outputs can arise for many reasons, such as structural, parametric and input uncertainty. Identification of the sources of uncertainties and the quantification of their impacts on model results are important to appropriately reproduce hydrodynamic processes in karst aquifers and to support decision-making. The present study investigates the time-dependent relevance of model input uncertainties, defined as the conceptual uncertainties affecting the representation and parameterization of processes relevant for groundwater recharge, i.e. interception, evapotranspiration and snow dynamic, on the lumped karst model LuKARS. A total of nine different models are applied, three to compute interception (DVWK, Gash and Liu), three to compute evapotranspiration (Thornthwaite, Hamon and Oudin) and three to compute snow processes (Martinec, Girons Lopez and Magnusson). All the input model combinations are tested for the case study of the Kerschbaum spring in Austria. The model parameters are kept constant for all combinations. While parametric uncertainties computed for the same model in previous studies do not show pronounced temporal variations, the results of the present work show that input uncertainties are seasonally varying. Moreover, the input uncertainties of evapotranspiration and snow melt are higher than the interception uncertainties. The results show that the importance of a specific process for groundwater recharge can be estimated from the respective input uncertainties. These findings have practical implications as they can guide researchers to obtain relevant field data to improve the representation of different processes in lumped parameter models and to support model calibration.

Keywords: Conceptual models, Input uncertainties, Groundwater recharge, Karst, Rainfall-runoff

3.1 Introduction

Hydrologic models serve as important tools for the assessment of dominant hydrodynamic processes in karst systems (Hartmann et al., 2013a; Sivelle et al., 2019). In those models, subsurface heterogeneity and the resulting complex hydrodynamic processes typical for karst aquifers are often represented in a simplified way (Fleury et al., 2007; Guinot et al., 2015; Sivelle et al., 2021; Sivelle and Jourde, 2020). The assessment of the reliability of a model output is therefore an important step towards an improved description of the karst system (Hartmann et al., 2014). This assessment is usually done by uncertainty quantification techniques, which investigate the likelihood of a model outcome while considering the unknowns in a hydrologic model (Sarrazin et al., 2018; Teixeira Parente et al., 2019). These unknowns arise from different sources of uncertainties, i.e. structural (Fandel et al., 2020; Henson et al., 2018), parametric (Mazzilli et al., 2012; Moussu et al., 2011) and input uncertainties (Liu et al., 2018; Nerantzaki et al., 2020).

Structural uncertainties evolve from the simplifications required while creating a conceptual model of a real world system (Gupta and Govindaraju, 2019; Rojas et al., 2008). This conceptualization often neglects certain parts of the natural system due to a lack of knowledge, which can lead to an underrepresentation of important hydrodynamic processes (Butts et al., 2004; Lee et al., 2011). Parametric uncertainties arise from the fact that the exact values of model parameters, such as discharge coefficients and storage thresholds, are often not known (Ahmadi et al., 2019; Hu et al., 2019). This is particularly true for lumped conceptual models, whose parameters cannot often be constrained by physical field experiments (Wagener et al., 2003). Hence, for each parameter, a reasonable parameter range needs to be defined in which the true parameter value is located (Seibert, 1997). Finally, input uncertainties exist due to missing and/or uncertain input data (Breinl, 2016; McMillan et al., 2012) as well as due to simplifications of the processes that finally represent the model input, e.g., the groundwater recharge (Kavetski et al., 2006; Patil et al., 2011; Vrugt et al., 2008).

More recent studies highlighted that groundwater recharge in systems with strong subsurface heterogeneities, such as karst systems, exhibits a high sensitivity to changes in climatic forcings (Hartmann et al., 2017b). In the specific case of pre-alpine karst catchments, these forcings controlling groundwater recharge are interception, evapotranspiration and snow melt processes. Garrigues et al. (2015) and Sarrazin et al. (2018) showed that the sensitivity of groundwater recharge with respect to vegetation related processes, i.e. interception and evapotranspiration, mainly results from the spatial variability of soil properties. Moreover, Ollivier et al. (2021) underline that this sensitivity is further related to often missing information about spatially distributed and vegetation-dependent evapotranspiration dynamics. In cases where snowmelt represents a controlling factor in the water balance of karst areas, Doummar et al. (2018) showed that groundwater recharge estimations are most sensitive to temperature variations. That is mainly due to the importance temperature has for the timing

of snow accumulation and melt and the resulting control on a spring's discharge behavior (Liu et al., 2021).

As it is difficult to measure interception, evapotranspiration and snow melt, additional models are often applied to compute input time series for hydrologic models (Hartmann et al., 2014b; Mazzilli et al., 2012; Ollivier et al., 2020). Interception can be modeled using mechanistic (Gash et al., 1995; Liu, 2001) and stochastic modeling approaches (Calder, 1996; Hall, 2003). Data demanding energy balance methods (Colaizzi et al., 2012; Penman, 1948) or simple temperature-based parametrizations (Oudin et al., 2005; Thornthwaite, 1948) provide evapotranspiration time series. Snow processes, which were recently shown to play a major role for groundwater recharge in pre-alpine and alpine areas (Jódar et al., 2020; Lucianetti et al., 2020), can be modeled using energy balance methods (Herrero et al., 2009; Marks et al., 1999) or simpler degree day factor methods (Girons Lopez et al., 2020; Martinec, 1960). Reliable time series of interception, evapotranspiration and snowmelt are a prerequisite for a proper description of the water balance for distributed, semi-distributed and conceptual models.

An example for a conceptual model applied to a pre-alpine karst system is the LuKARS model, which was developed by Bittner et al. (2018) for the Kerschbaum springshed in Austria. Given the natural characteristics of the springshed (forested catchment, elevation between 415 and 969 m a.s.l., annual mean temperature of 8°C), evapotranspiration, interception and snow melt representations are expected to have an important influence on the modeled spring discharge (Bittner et al., 2018). However, since no direct measurements for these input data are available, simple algorithms have to be applied for computing the input time series for the LuKARS model (Bittner et al., 2020a).

While previous studies investigated the parametric uncertainties of LuKARS for the Kerschbaum springshed (Teixeira Parente et al., 2019), the presented article aims to investigate how much the input uncertainties affect model predictions. The hypotheses, which we want to test in this study, are, first, that the input uncertainties can vary seasonally, then, that it is possible to derive the specific importance of a single process, e.g., snow melt, for groundwater recharge from its related uncertainties in the model output. This is of particular importance, as it serves as a practical example which is beneficial to guide researchers and decision-makers in favoring field experiments and data collection differently during different seasons to improve the output of a karst aquifer model. To study the uncertainty propagating to the spring discharge, three different modeling approaches are applied for each of the considered hydrological processes, i.e. interception, evapotranspiration and snow processes. In particular, the methods of DVWK (1996), Gash et al. (1995) and Liu (2001) are applied to compute interception, the methods of Hamon (1961), Oudin et al. (2005) and Thornthwaite (1948) to calculate evapotranspiration and the methods of Girons Lopez et al. (2020), Magnusson et al. (2014) and Martinec (1960) to model snow melt and accumulation. The selection of lumped approaches is driven by data availability in the study area and in particular by the lack of radiation data. Then, all possible model combinations are run varying the parameters of the input models and by using the sampling algorithm of the Fourier

Amplitude Sensitivity Test (FAST) (Pianosi et al., 2015). Finally, the study investigates the impact of the input model parametrization on the LuKARS model output and how this changes over time. To conclude, the input uncertainties are compared with the parametric uncertainties, which were computed in an earlier study (Teixeira Parente et al., 2019).

3.2 The study area

The Kerschbaum springshed is located close to the city of Waidhofen a.d. Ybbs (Fig. 3.1a), about 100 km west of the city of Vienna (Austria) (Fig. 3.1b). The study site covers an area of 2.5 km². This pre-alpine recharge area forms part of the eastern foothills of the Northern Calcareous Alps and is dominated by a lithologic sequence of dolomitic basement rocks (Fig. 3.1c). The study area shows karst features such as springs, dry valleys and caves. Due to the absence of significant sinkholes, the groundwater recharge can be assumed barely influenced by point-infiltration processes. Moreover, according to the study of Narany et al. (2019), the Kerschbaum springshed is characterized by a deep karstified groundwater system with a well-connected network of fractures and conduits.

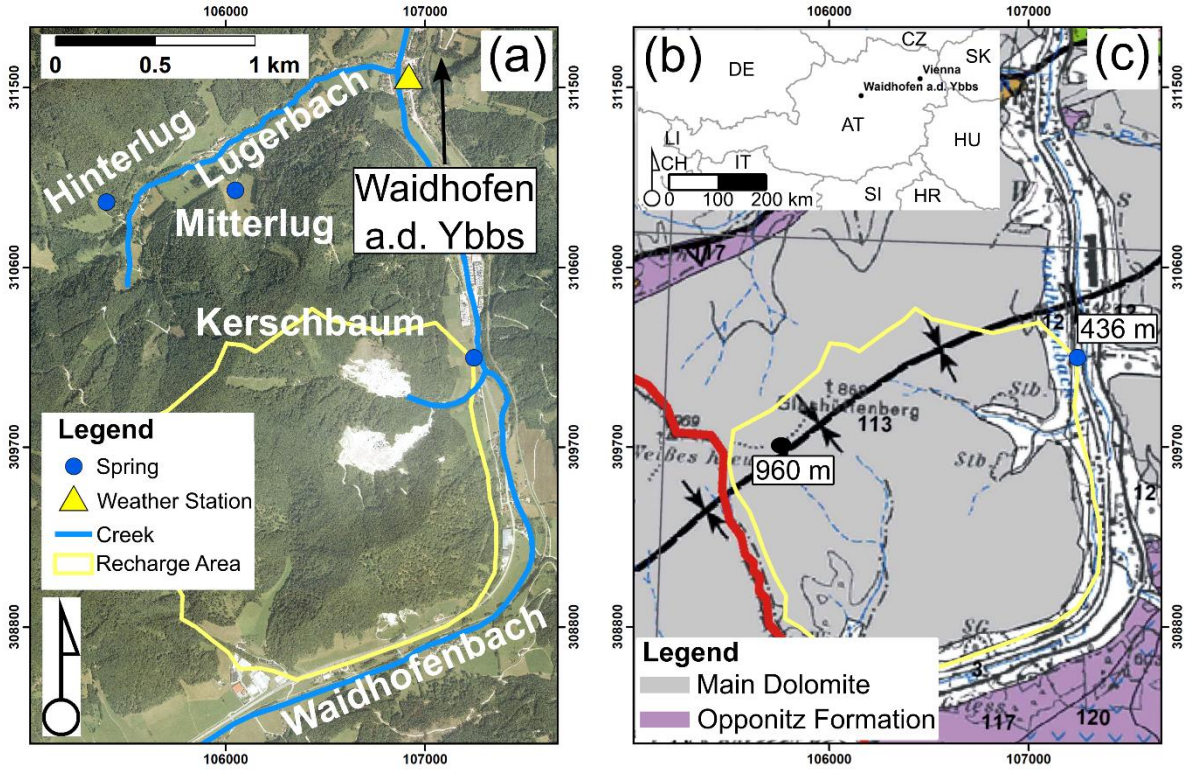

Fig. 3.1 Overview of the study area close to Waidhofen a.d. Ybbs and the LuKARS model implementation. **a** The orthophoto of the study area including the delineated recharge area of the Kerschbaum spring. **b** The location of Waidhofen a.d. Ybbs seen from a European perspective. **c** The geological map of the study area (GBA 2021).

The land cover is dominated by beech forests. Its spring provides a mean discharge of 34 l/s to the regional water supply and shows a quick reaction time to precipitation and snow melt events of 1 day

(Bittner et al., 2021). Fig. 3.2 shows the available precipitation, temperature, snow depth and discharge time series for the period from 01 January 2006 to 31 December 2007. These time series were measured at the weather station whose location is shown in Fig. 3.1a. For more information about the study area, the interested reader could refer to the publication of Narany et al. (2019).

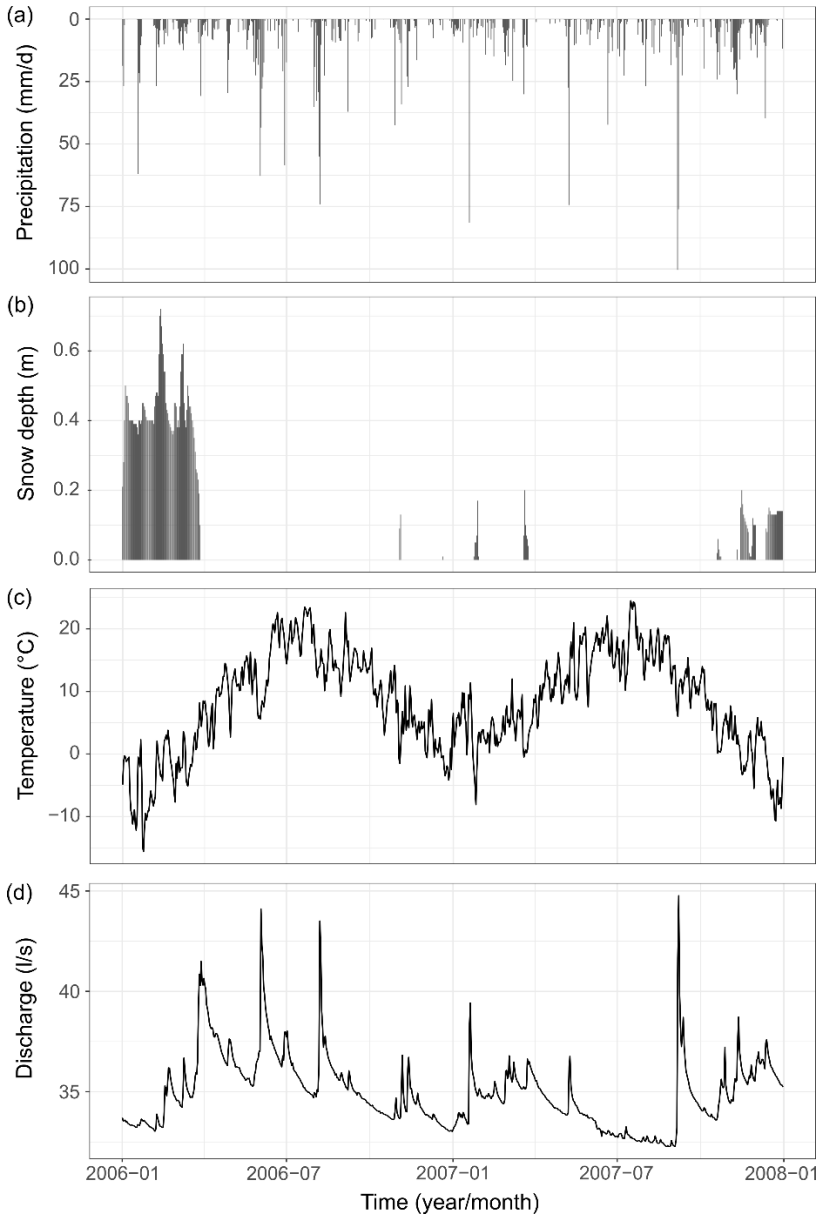

Fig. 3.2 Data time series used in the presented study. **a** Daily precipitation (mm), **b** daily snow depths (m), **c** daily air temperature (°C) and **d** daily discharge of the Kerschbaum spring (L/s).

3.3 Methodology

The paper briefly describes the lumped karst hydrological model LuKARS of the Kerschbaum springshed. For more information about the model the reader could refer to the publication of Bittner et al. (2020b). The paper then focuses on the description of both commonly applied and recently proposed

parameterizations for interception, evapotranspiration and snow processes. Since precipitation and air temperature are the only meteorological parameters measured in the study area, temperature-based methods are used to compute evapotranspiration and snowmelt. Finally, the method used to quantify the uncertainty of all investigated model combinations is described.

3.3.1 The LuKARS model

The LuKARS model is a lumped parameter model developed by Bittner et al. (2018) that considers the dominant hydrotopes in a recharge area as distinct response units. Hydrotopes are defined as landscape units with similar soil and land use characteristics (Arnold et al., 1998). Each hydrotope is characterized by a specific retention capacity. As Figure 3.3a shows, shallow and coarse-textures soils lead to low soil storage and high quickflow intensity. In contrast, thick and fine-textured soils lead to high soil storage and low quick flow intensity. The conceptual model considers the hydrotopes to represent the vadose zone (soil-epikarst-infiltration zone) and to be directly connected to the saturated zone, which consists of a single linear storage recharged by each hydrotope independently. The duality of flow behavior is implemented by considering for each hydrotope both the fast flow component through the conduits and the slow diffusive discharge in the matrix. Each hydrotope simulates three different types of flow, i.e. the quickflow (Q_{hyd}), the matrix infiltration (Q_{is}) that feeds the baseflow storage (B), and the secondary spring discharge (Q_{sec}) (Fig. 3.3b). Q_{hyd} represents the discharge that is directly moved to the outlet of the catchment through preferential flow paths, such as subsurface conduits, and factors that are responsible for the fast reaction of the spring discharge to rainfall and snowmelt events. Q_{hyd} is implemented considering the hysteretic behavior of the soil-epikarst system that starts after a constant hydrotope specific storage value (E_{max}) was exceeded and stops after a lower constant threshold (E_{min}) was reached. Q_{is} is the water that infiltrates into the lower reservoir B (Fig 3.3) and, thus, represents the groundwater recharge. Q_{sec} is the flow that discharges outside the investigated recharge area and is activated only when the threshold for secondary spring discharge (E_{sec}) was exceeded. Q_{is}, Q_{sec} and Q_b (the baseflow) are implemented using linear transfer functions. Finally, Q_{tot} is the discharge at the spring. The mathematical equations and a graphical user interface for the model are provided in Bittner et al. (2018) and Bittner et al. (2020a), respectively.

3.3.2 Interception

The approach applied by Bittner et al. (2018) was based on the percentages for interception of beech forest stands proposed by DVWK (1996). This study further considers the methods proposed by Gash et al. (1995) and Liu (2001).

DVWK (1996) suggests that 11% of precipitation is intercepted from beeches in the winter season (21 December, d_w), whereas 17% of precipitation is intercepted in the summer season (21 June, d_s). A linear interpolation is applied between these values following Eq. 3.1 and Eq. 3.2, which compute daily

time series of interception I (mm/d) for the time between 21 December and 21 June and the time between 21 June and 21 December, respectively. The maximum interception is limited to 5 mm/d.

$$\text{if } I < 5 \text{ mm/d},\ I = 11 + \left(\frac{17-11}{d_s - d_w}\right)(d - d_w),\ \text{else } I = 5 \text{ mm/d} \qquad \text{from Dec 21 to June 21} \qquad (3.1)$$

$$\text{if } I < 5 \text{ mm/d},\ I = 17 + \left(\frac{11-17}{d_w - d_s}\right)(d - d_s),\ \text{else } I = 5 \text{ mm/d} \qquad \text{from June 21 to Dec 21} \qquad (3.2)$$

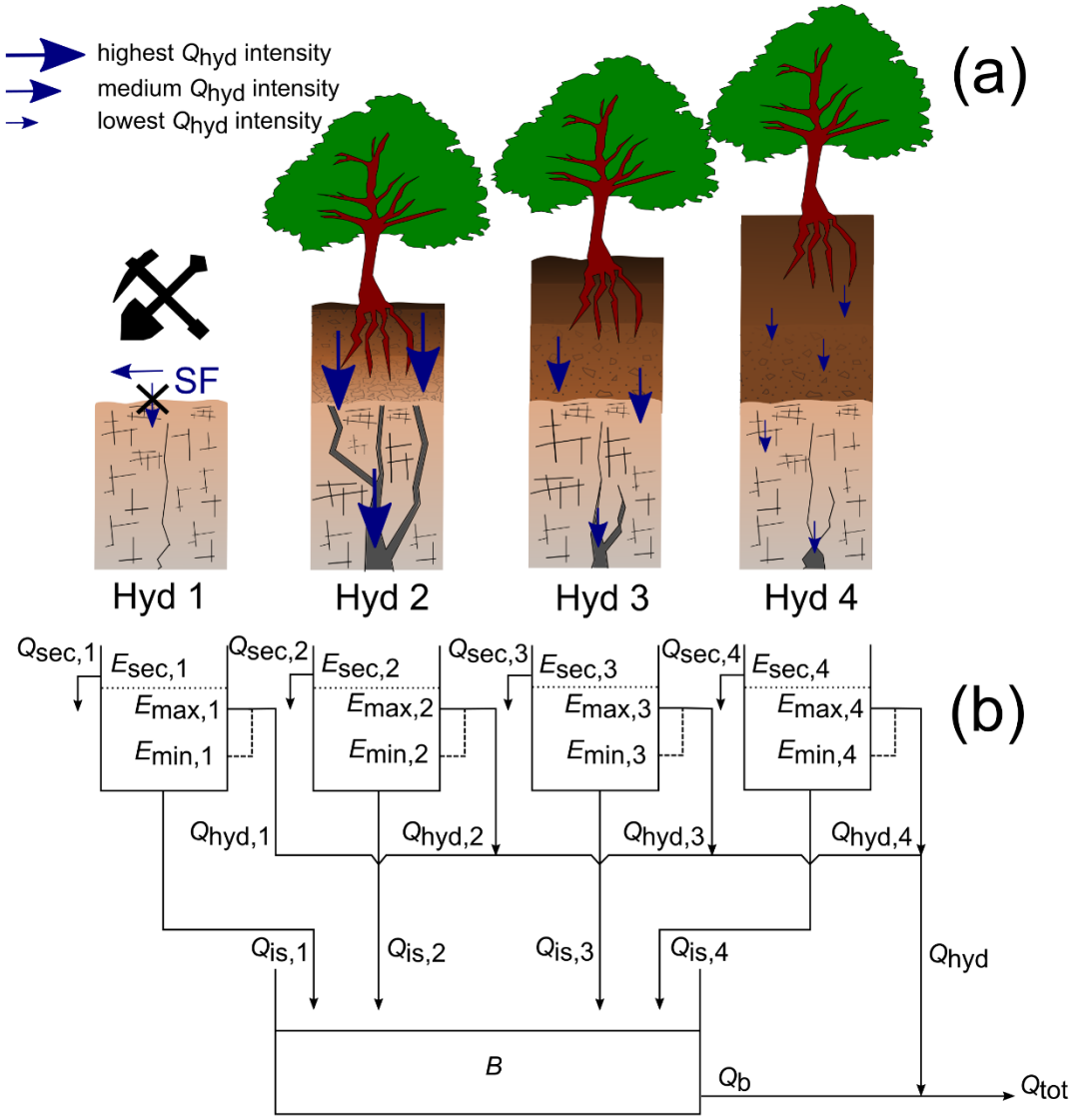

Fig. 3.3 The conceptual modeling approach of LuKARS. **a** Conceptual representation of the four implemented hydrotopes. Hyd 1 indicates the dolomite quarries with no groundwater recharge and the dominance of surface runoff (SF). Hyd 2 and Hyd 4 represent coarse-textured and fine-textured soils, respectively. **b** The bucket-type model implementation of dominant hydrotopes. Q_{sec} is the secondary spring discharge, Q_{hyd} the quickflow, Q_{is} the matrix infiltration feeding the baseflow storage B, Q_b the baseflow and Q_{tot} the discharge at the spring. E_{sec}, E_{max} and E_{min} are thresholds storage values regulating the activation of the discharge components.

The approach by Gash et al. (1995) is based on the calculation of a gross rainfall that is needed to saturate the canopy, i.e. P'_g (mm). P'_g is calculated using Eq. 3.3.

$$P'_g = -\left[\frac{C_m}{ER\,(1-p)}\right] \ln(1 - ER) \tag{3.3}$$

where C_m is the stand storage capacity (mm), ER (-) is the ratio between the mean evaporative rate E and the mean rainfall rate of the event for saturated canopy conditions R. The parameter p represents the free throughfall coefficient (-). For a daily time step, if the precipitation P (mm/d) is larger than P'_g (mm/d), I (mm/d) can be calculated with Eq. 3.4.

$$I = (1 - p)\,P'_g + (1 - p)\,ER\,(P - P'_g) \tag{3.4}$$

If $P < P'_g$, I is computed following Eq. 3.5.

$$I = (1 - p)\,P \tag{3.5}$$

The method proposed by Liu (2001) requires the definition of the same parameters as in the method of Gash et al. (1995). However, instead of differentiating between the cases in which precipitation P is greater or smaller than the gross rainfall that is needed to saturate the canopy (P'_g), the exponential function in Eq. 3.6 is defined to compute daily interception amounts (I).

$$I = C_m\left[1 - e^{\left(-\frac{(1-p)}{C_m}P\right)}\right]\left[1 - \frac{ER}{(1-p)}\right] + ER \cdot P \tag{3.6}$$

Liu (2001) investigated the parameter sensitivities of Eq. 3.4 and 3.6 and showed that an overestimation of either C_m or ER results in an overestimation of interception, whereas *large values* of p cause an underestimation of interception. Moreover, the parameter sensitivities depend on the magnitude of a considered rainfall event and the type of canopy. For example, ER is most sensitive in areas dominated by intense rainfall events, whereas ER and C_m are most sensitive in areas characterized by small rainfall events. The parameter p is sensitive when the models are applied to areas with small rainfall events and open canopies.

3.3.3 Evapotranspiration

The Thornthwaite (1948) evapotranspiration model was used to calculate the potential evapotranspiration (ET_{pot}) in the original LuKARS model of the Kerschbaum spring (Bittner et al., (2018). In this work, the simulation approaches proposed by Hamon (1961) and Oudin et al. (2005) are additionally applied. It is important to note that Bittner et al. (2018) and Teixeira Parente et al. (2019) used ET_{pot} as actual evapotranspiration (ET_{act}), since the results obtained for the annual ET_{pot} losses were in good agreement with ET_{act} computed in previous studies for the same study area (Markart et al.

2006). Specifically, for the years 2006 – 2007, Bittner et al. (2018) calculated a total of 45% ET_{pot}, which is in good agreement with the 43% ET_{act} presented in Markart et al. (2006). In the presented study, ET_{act} is hence considered to be equal to the ET_{pot} to be able to compare the different model configurations under the same conditions.

Thornthwaite (1948) provides estimates for monthly ET_{pot} and assumes that once the mean monthly temperature becomes larger than 0 °C, ET_{pot} becomes 0. In this method, the hours of daylight are assumed to be 12 and each month is 30 days long. Then, ET_{pot} (mm/month) is calculated as shown in Eq. 3.7,

$$\mathrm{ET_{pot}} = k_{\mathrm{TH}} \left(10 \, \frac{T_{\mathrm{Mean}}}{H}\right)^{r} \tag{3.7}$$

where k_{TH} (mm/month) is a proportionality constant, T_{Mean} (°C) the mean monthly temperature and H (°C) is the heat index defined in Eq. 3.8,

$$H = \left(\frac{T_{\mathrm{Mean}}}{5}\right)^{1.514} \tag{3.8}$$

with r an exponent given by Eq. 3.9.

$$r = 6.75e^{-7} \, H^3 + 7.71 \, e^{-5} \, H^2 + 1.792 \, e^{-2} \, H + 0.49239 \tag{3.9}$$

As proposed by Bittner et al. (2018), the monthly ET_{pot} are divided by the number of days and the resulting daily ET_{pot} are to be representative for the 15th day of a month. In order to obtain daily ET_{pot} (mm/d) from this method, a linear interpolation is applied between these representative ET_{pot} values.

Oudin et al. (2005) derived an empirical equation to estimate daily ET_{pot} (mm/d) as input for lumped rainfall-runoff models. They tested various ET_{pot} modeling approaches for numerous catchments in France, Australia and the United States. Their goal was to identify those atmospheric variables which provide the best streamflow predictions when being used as input for ET_{pot} models. The equation they derived is shown in Eq. 3.10,

$$\mathrm{ET_{pot}} = [0.408 \; H_{\mathrm{O}}] \, [k_{\mathrm{OU}} \, (T_{\mathrm{Mean}} + 5)] \tag{3.10}$$

where H_{O} is the extraterrestrial solar radiation (MJ/ (m^2 d)), k_{OU} (m^3 kg/ (1000 MJ^2 °C)) is a proportionality constant, T_{Mean} is the mean daily temp (°C), and 0.408 is an approximation for the latent heat flux (MJ/kg). It is important to note that $\mathrm{ET_{pot}}$ is 0 (mm/d) if $T_{\mathrm{Mean}} \leq 5$ (°C).

The third method applied to calculate $\mathrm{ET_{pot}}$ was proposed by Hamon (1961), who derived a simple procedure to be used in water balance estimations. The goal was to use readily available data, i.e. daily

air temperature (T_{Mean}), for $\mathrm{ET_{pot}}$ estimations. The derived methodology is based on the saturated water vapor concentration at T_{Mean}, i.e. $e^0(T_{\mathrm{Mean}})$ (kPa) and is expressed by Eq. 3.11,

$$\mathrm{ET_{pot}} = k_{\mathrm{HA}} \frac{N}{12} \left[216.7\, e^0\, (T_{\mathrm{Mean}})/(T_{\mathrm{Mean}} + 273.3)\right] \tag{3.11}$$

where k_{HA} (mm/d) is a proportionality constant and N is the maximum number of daylight hours. $e^0(T_{\mathrm{Mean}})$ was approximated using the modified Magnus equation proposed by Alduchov and Eskridge (1996) that is shown in Eq. 3.12.

$$e^0(T_{\mathrm{Mean}}) = 6.1094\, e^{17.625\, T_{\mathrm{Mean}}/(243.04 + T_{\mathrm{Mean}})} \tag{3.12}$$

3.3.4 Snow melt

Bittner et al. (2018) used the method proposed by Martinec (1960) to model snow melt and storage for the Kerschbaum spring recharge area. This study additionally considers the methods described by Girons Lopez et al. (2020) and Magnusson et al. (2014). All snow routines considered in this framework assume that the energy available for snow melt is proportional to air temperature. This means that below a certain threshold temperature T_{T}, precipitation falls as snow, whereas rainfall occurs for temperatures above this threshold. The proportionality of snow melt (M) is controlled by the degree-day factor C_0 (mm/ (d °C)) and the daily mean temperature T_{Mean} (°C). Moreover, all the considered snow models neglect sublimation processes, which is often the case in degree-day methods.

The degree-day method proposed by Martinec (1960) simulates M (mm/d) using Eq. 3.13.

$$M = C_0 \max(0,\ T_{\mathrm{Mean}} - T_{\mathrm{T}}) \tag{3.13}$$

While Martinec (1960) considers C_0 to be constant, Braun and Renner (1992) argue that this factor should be changing over time, since environmental conditions, e.g., solar inclination and snow albedo, vary seasonally. Girons Lopez et al. (2020) describe a seasonally varying degree-day factor, i.e. $C_{0,\mathrm{n}}$, based on a sine function. The intensity by which C_0 varies is controlled by an amplitude factor $C_{0,\mathrm{a}}$ (mm/ (d °C)). Then, $C_{0,\mathrm{n}}$ is computed as shown in Eq. 3.14, where n is the time (d).

$$C_{0,\mathrm{n}} = C_0 + \frac{1}{2}\, C_{0,\mathrm{a}}\, sin\frac{2\pi(n - 81)}{365} \tag{3.14}$$

Finally, Magnusson et al. (2014) approach the calculation of snow melt with the exponential function shown in Eq. 3.15,

$$M = C_0 \, M_{\mathrm{M}} [\frac{T_{\mathrm{Mean}} - T_{\mathrm{T}}}{M_{\mathrm{M}}} + \ln\left(1 + e^{-\frac{T_{\mathrm{Mean}} - T_{\mathrm{T}}}{M_{\mathrm{M}}}}\right)] \quad (3.15)$$

where M_{M} represents a snowmelt transition (°C). This method allows for melting to occur even below freezing temperature.

According to the investigation of Girons Lopez et al. (2020), who tested a variety of modifications to different temperature-based snow routines, the most sensitive parameters in the models applied in this study are the snowmelt transition M_{M} and the temporally varying degree-day factor $C_{0,\mathrm{n}}$.

3.3.5 Parameter sampling and investigated model combinations

Appropriate parameter ranges are defined for all unknown parameters in the equations describing interception, evapotranspiration and snow melt. The parameter ranges selected for the nine considered calibration parameters, i.e. C_{m}, p, ER, k_{OU}, k_{HA}, C_0, T_{T}, $C_{0,\mathrm{a}}$ and M_{M}, are shown in Table 3.1. The specific range of values for each parameter is based on previous studies, which are indicated in Table 3.1.

This study considers the model configuration from Bittner at al. (2018) as the reference model, whose results are used to evaluate the performance of all the considered model combinations. All investigated model combinations are shown in Table 3.2. The name given to each model combination indicates the input algorithms which have been changed from Bittner et al. (2018). Each simulation is run with daily time steps for a warm-up period between 2001 and 2005 and an evaluation period from 2006 – 2007. The selection of these two particular years was driven, firstly, by the fact that the original LuKARS model from Bittner et al. (2018) was calibrated and validated for the years 2006 and 2007, respectively. Secondly, the relevant contrast in snow accumulation and evaporative demand between 2006 and 2007 makes it possible to account for the climatic variability between different years. Indeed, as Fig. 3.2b shows, the winter in 2006 is characterized by snow depth values up to 0.72 m, whereas almost no snow accumulation occurred in 2007 (max snow depth = 0.2 m).

The sampling algorithm of the Fourier Amplitude Sensitivity Test (FAST), which was developed by Cukier et al. (1978) and implemented in the SAFE toolbox (Pianosi et al., 2015), is used in this study to obtain for each model combination a set of values that covers the full parameter space of each parameter. To avoid unrealistic water budgets, the model input time series computed with each parameter sample of each model combination are compared with the computed input time series of Bittner et al. (2018) for the hydrological year 2006. All parameter samples leading to an annual model input that differs more than 15% from the water volume computed by Bittner et al. (2018) are discarded. Then, the remaining 2673 parameter samples are used to investigate all possible model combinations, i.e. 26, which are evaluated and compared with the results of Bittner et al. (2018) for the period 2006 and 2007. For the input algorithms of the original Kerschbaum spring LuKARS model, i.e. DVWK (1996), Thornthwaite

(1948) and Martinec (1960), rather than defining parameter ranges and samples, this study keeps the parameters fixed and equal to those found in Bittner et al. (2018) (Table 3.1). The model combinations including the total number of investigated samples are summarized in Table 3.2. For the sake of completeness, Appendix A.1 shows the calibrated LuKARS model parameters found in Bittner et al. (2018). The hydrotope specific parameters control the behavior of the soil-epikarst system, of the matrix infiltration and of the quickflow through the conduits, while the baseflow storage parameters determine the response of the saturated zone.

Table 3.1 Overview of the calibration parameter used in the presented methodology, including their respective parameter range, their description and the reference. The parameters marked with $^{(*)}$ are taken fixed and correspond to the input algorithms used in Bittner et al. (2018).

Parameter	**Parameter range**	**Description**	**Reference**
C_{m}	0.1–5	Stand storage capacity (mm)	Liu (2001)
p	0.01–0.6	Free throughfall coefficient (-)	Liu (2001)
ER	0.01–0.4	Ratio between mean evaporative rate and mean rainfall rate for saturated canopy conditions (-)	Liu (2001)
k_{OU}	0.006–0.012	Proportionality constant in Oudin's method (m³ kg/ (1000 MJ² °C))	Almorox et al. (2015)
k_{HA}	0.1–0.2	Proportionality constant in Hamon's method (mm/d)	Almorox et al. (2015)
C_0	1–10	Degree-day factor (mm/ (d °C))	Bittner et al. (2018)
T_{T}	-2–2	Threshold temperature (°C)	Bittner et al. (2018)
$C_{0,\mathrm{a}}$	1–10	Amplitude factor (mm/ (d °C))	Hottelet et al. (1994)
M_{M}	1–10	Snowmelt transition (°C)	Magnusson et al. (2014)
$k_{\mathrm{TH}}{}^{(*)}$	16	Proportionality constant in Thornthwaite's method (-)	Bittner et al. (2018)
$C_0{}^{(*)}$	4	Degree-day factor (mm/ (d °C))	Bittner et al. (2018)
$T_{\mathrm{T}}{}^{(*)}$	0.5	Threshold temperature (°C)	Bittner et al. (2018)

Table 3.2 Overview of the 26 investigated model combinations including the total number of investigated parameter samples.

Name of model combination	Samples	I model	ET model	M model
Gash	17	Gash	Thornthwaite	Martinec
Liu	11	Liu	Thornthwaite	Martinec
Oudin	24	DVWK	Oudin	Martinec
Hamon	19	DVWK	Hamon	Martinec
Girons Lopez	105	DVWK	Thornthwaite	Girons Lopez
Magnusson	105	DVWK	Thornthwaite	Magnusson
Gash – Hamon	48	Gash	Hamon	Martinec
Gash – Girons Lopez	63	Gash	Thornthwaite	Girons Lopez
Gash – Magnusson	64	Gash	Thornthwaite	Magnusson
Gash – Oudin	59	Gash	Oudin	Martinec
Liu – Hamon	34	Liu	Hamon	Martinec
Liu – Girons Lopez	51	Liu	Thornthwaite	Girons Lopez
Liu – Magnusson	52	Liu	Thornthwaite	Magnusson
Liu – Oudin	45	Liu	Oudin	Martinec
Girons Lopez – Hamon	232	DVWK	Hamon	Girons Lopez
Girons Lopez – Oudin	281	DVWK	Oudin	Girons Lopez
Magnusson – Hamon	238	DVWK	Hamon	Magnusson
Magnusson – Oudin	285	DVWK	Oudin	Magnusson
Gash – Girons Lopez – Hamon	114	Gash	Hamon	Girons Lopez
Gash – Girons Lopez – Oudin	153	Gash	Oudin	Girons Lopez
Gash – Magnusson – Hamon	113	Gash	Hamon	Magnusson
Gash – Magnusson – Oudin	150	Gash	Oudin	Magnusson
Liu – Girons Lopez – Hamon	84	Liu	Hamon	Girons Lopez
Liu – Girons Lopez – Oudin	121	Liu	Oudin	Girons Lopez
Liu – Magnusson – Hamon	83	Liu	Hamon	Magnusson
Liu – Magnusson – Oudin	122	Liu	Oudin	Magnusson

3.4 Results

The results of this study are presented in the following sections. First, the uncertainties of single processes in relation to the parametric uncertainties of the Kerschbaum spring LuKARS model which were computed in an earlier study (Teixeira Parente et al., 2019). Notice that this comparison is mainly qualitative, since the parameter uncertainty was estimated using only the combination DVWK –

Thornthwaite – Martinec with fixed input parameters. Then, section *'Evaluation of all model combinations'* focuses on the comparison of the results of all evaluated model combinations and highlights how the input uncertainties change when considering more processes to be unknown, i.e. interception, evapotranspiration and snow melt. The analyses focus on the comparison of the interquartile range of the LuKARS model outputs as an indicator for model uncertainty. Moreover, the interquartile ranges are normalized with the observed spring discharge to make the interpretation of input uncertainties independent of high and low flow periods, occurring during snow melt and snow accumulation periods, respectively.

Fig. 3.4 shows the cumulative input values generated with all parameter samples for each applied algorithm. As the analyses focus on the interquartile range of model outputs, also the generated cumulative recharge values of that range are shown. Cumulated sums allow a better visualization through continuous plots. It is observed that the inputs computed with the different algorithms are well distributed around the input time series used in the original Kerschbaum spring LuKARS model. Slight deviations are only visible for ET_{pot} in 2006, where the method of Hamon (1961) partially overshoots the inputs generated with the method of Thornthwaite (1948), and in 2007, where the Thornthwaite (1948) method overshoots the interquartile range of inputs computed with the method of Oudin et al. (2005). These deviations are related to the linear interpolation which is applied to derive daily values from the monthly ET_{pot} ,which are obtained with the methodology of Thornthwaite (1948).

3.4.1 Model input uncertainties related to single hydrological processes

In this section, the focus is on the uncertainties related to single hydrological processes, i.e. interception, evapotranspiration and snow melt, how these uncertainties change in different periods of the year and how they compare to the parametric uncertainties previously computed by Teixeira Parente et al. (2019). The model parameters, which were considered in the evaluation of the parametric uncertainties of the LuKARS model, are highlighted with an asterisk (*) in Appendix A.1 and are the discharge coefficients and exponents, minimum and maximum storage capacities, and activation level of secondary spring discharge for hydrotopes Hyd 2, Hyd 3 and Hyd 4 (Teixeira Parente et al., 2019).

Fig. 3.5 shows that the interquartile ranges resulting from uncertainties in interception (model combinations Gash and Liu) are generally smaller than the evapotranspiration and parametric uncertainties. Moreover, the uncertainties related to interception do not show a distinct seasonal variation in 2006. However, a slight seasonal variation with increasing interception over the summer period can be observed in 2007. Moreover, both Gash and Liu model follow the same temporal dynamics and lead to very similar interquartile ranges, showing that the choice of the interception model is not very significant for this case study.

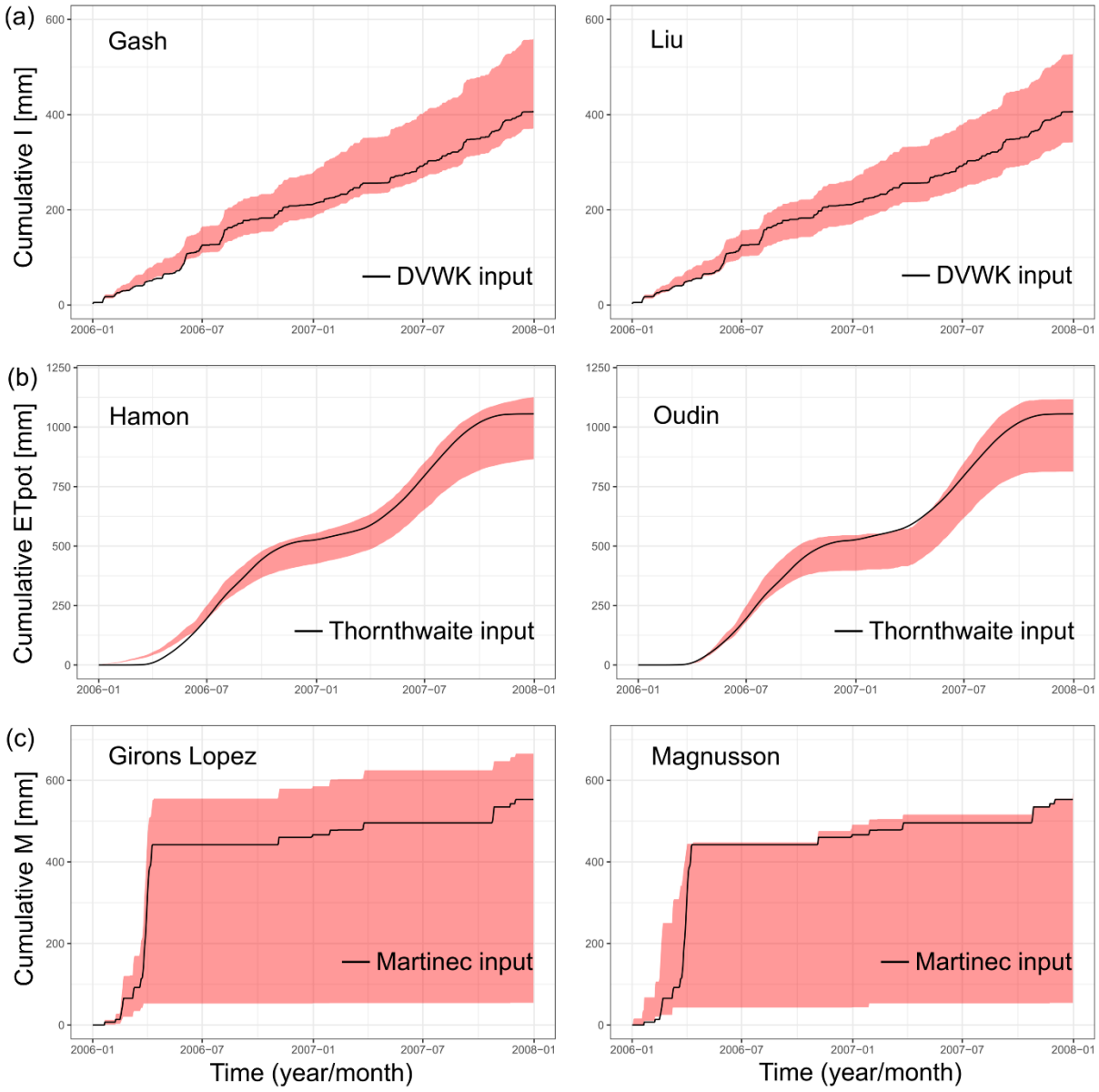

Fig. 3.4 The plots show the interquartile range of the cumulative input values for each applied algorithm. For comparison, the black lines highlight the inputs used in the study of Bittner et al. (2018). **a** The interception inputs, **b** the potential evapotranspiration inputs and **c** the potential snowmelt inputs.

Regarding the interquartile ranges resulting from the use of the Oudin et al. (2005) and Hamon (1961) methods, it is noted that the uncertainties related to evapotraspiration are characterized by a clear seasonal variability. The method of Oudin et al. (2005) brings the largest difference in the normalized interquartile range, which increases over the summer seasons in 2006 from 0.03 (29 March) to 0.06 (2 August) and in 2007 from below 0.04 (21 January) to 0.1 (5 September) and decreases again in the winter seasons. Overall, the normalized interquartile range of evapotranspiration is smaller than the parametric uncertainties. Moreover, most of the time the uncertainties of evapotranspiration are higher than the snow melt uncertainties, even over the winter period 2006–2007. The uncertainties in snow melt are higher than the evapotranspiration uncertainties for an extended period only in the early year

2006. Also in this case, as it was observed for interception, the difference in the normalized interquartile range between the Hamon and the Oudin models is rather small, reaching a maximum value of 0.04 on 4 September 2007.

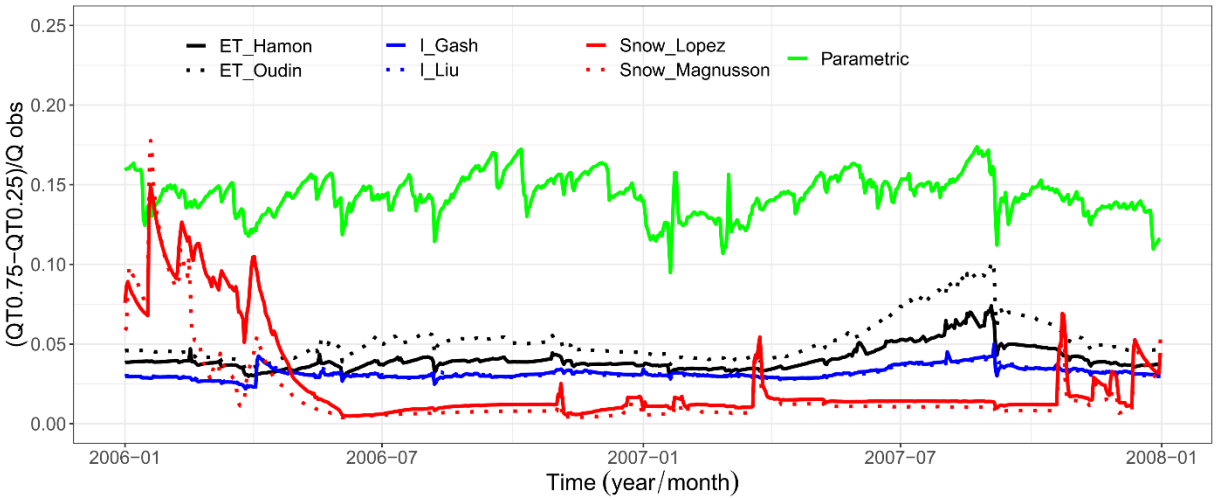

Fig. 3.5 Interquartile ranges of LuKARS model outputs normalized by the observed discharge. Single processes, i.e. interception, evapotranspiration and snowmelt, are considered as uncertain. For comparison, the parametric uncertainties of the Kerschbaum LuKARS model computed by Teixeira Parente et al. (2019) are also shown. A clear seasonal dependence of uncertainties related to snowmelt and evapotranspiration can be identified.

Fig. 3.5 also shows that the uncertainties in snow melt have the highest temporal variability of all investigated hydrological processes. Here, the method of Magnusson et al. (2014) bears the largest variation in normalized interquartile range, i.e. between 0.18 on 19 January 2006, and 0.003 on 6 November 2006. Moreover, similar to the normalized interquartile ranges of model results considering uncertainties in evapotranspiration, the results show a seasonal dependence of uncertainties in snow melt. The normalized interquartile range of LuKARS results considering snow melt to be uncertain exceeds all other normalized interquartile ranges in January 2006. In contrast, the snow melt related uncertainties are even smaller than the uncertainties related to interception during the winter season 2006–2007. Moreover, the normalized interquartile range of LuKARS results considering snow melt to be uncertain almost becomes 0 (< 2% of the measured discharge) in summer time in 2006 and 2007.

In case of snow processes, the choice of the model appears to be more relevant than for evapotranspiration and interception. On the one hand, the mean of the differences in the normalized interquartile range between both ET models, i.e. 0.011, is higher than the mean of the normalized interquartile range differences between the snow models, i.e. 0.008. On the other hand, the maximum difference in the normalized interquartile range is identified between the Girons Lopez and Magnusson models, i.e. is 0.06 on 21 March 2006. This is reasonable, since snow processes do not play a role over the whole time of a year, whereas ET does.

3.4.2 Evaluation of model combinations

The minimum and maximum percentage discrepancies between the simulated and observed spring discharge for each model combination are shown in Fig. 3.6.

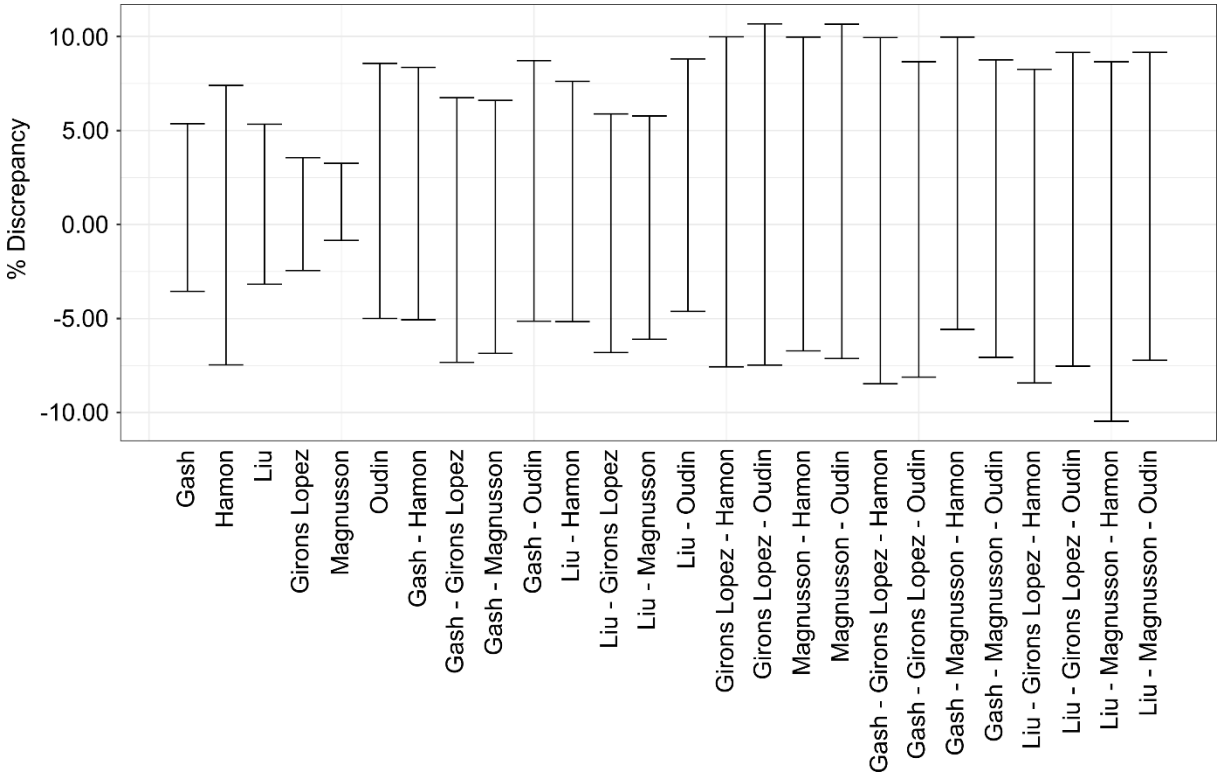

Fig. 3.6 The bars show the minimum and maximum percentage discrepancies between each model combination and the observed spring discharge.

Fig. 3.7 shows the interquartile ranges of all model evaluations, including the results of the parametric uncertainty study performed in Teixeira Parente et al. (2019) and the simulated spring discharge obtained from the original Kerschbaum LuKARS model. Comparing the interquartile ranges of the different model combinations (Fig. 3.7), it is seen that including more uncertain hydrological processes does not necessarely lead to an increase in the output variance. As an example, Fig. 3.8a and 3.8b show two different cases, characterized by an increase and a decrease in output variance with increasing process complexity, respectively. Fig. 3.8a compares the model combinations Liu, Liu–Magnusson and Liu–Magnusson–Oudin, therefore introducing progressive uncertainties in interception, snow melt and evapotranspiration. Here, the normalized interquartile ranges increase with the number of hydrological inputs considered as uncertain. Fig. 3.8b considers the model combinations Magnusson, Magnusson–Oudin and Gash–Magnusson–Oudin. In contrast to the previous case, the model combination considering snow and evapotranspiration as uncertain input (Magnusson–Oudin) shows larger output variability than the model considering uncertainties in all the three processes (Gash–Magnusson–Oudin). Looking at all model combinations in Fig. 3.7, the highest normalized interquartile ranges are noted for model combinations considering snow melt and evapotranspiration to be uncertain.

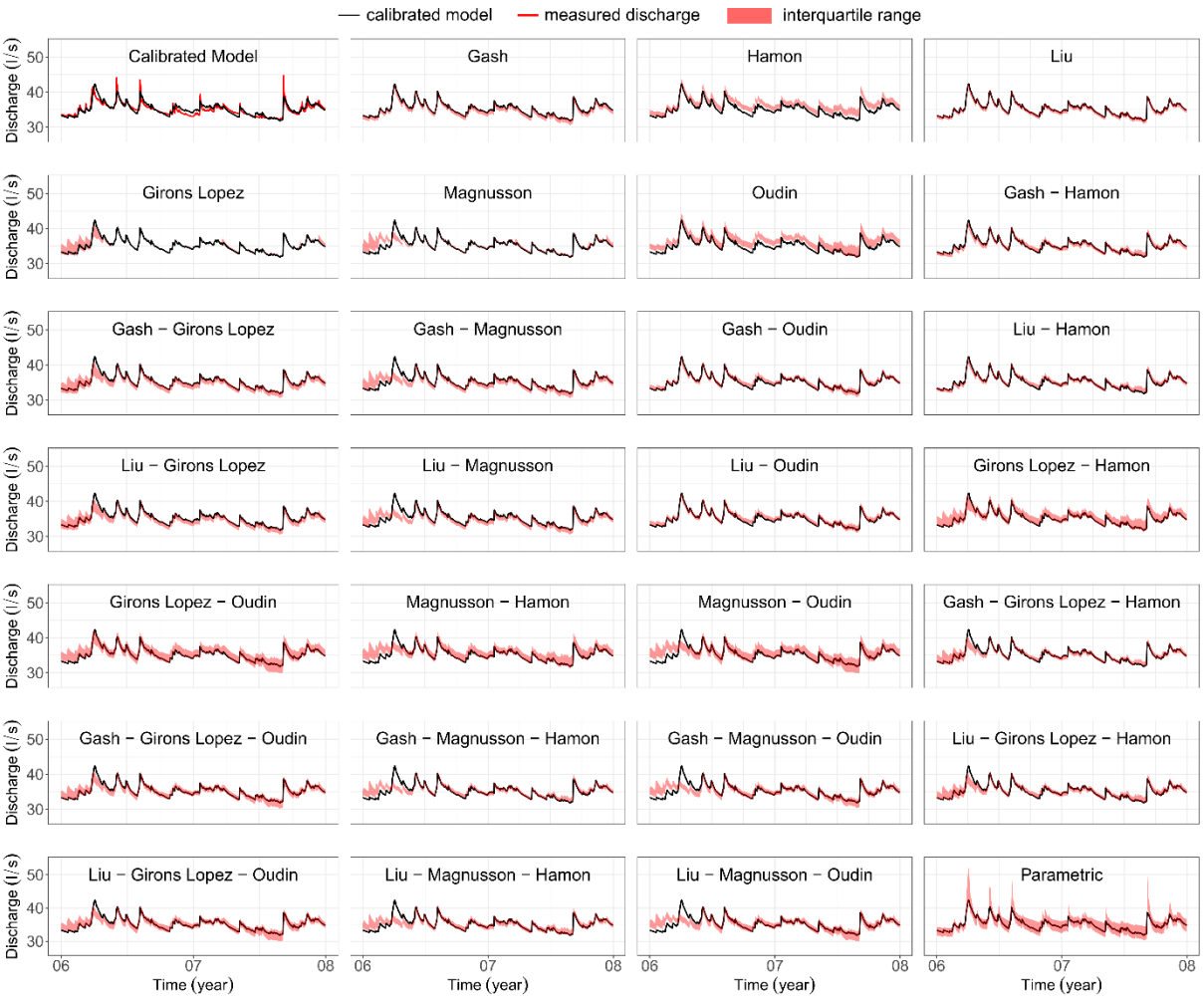

Fig. 3.7 Interquartile ranges of each model combination (red bands), including the results of the calibrated model from Bittner et al. (2018) (black line) and the parametric uncertainties obtained from Teixeira Parente et al. (2019), which are shown in the bottom-right graph. The results of the calibrated model from Bittner et al. (2018) (black line) are also compared to the measured discharge (red line) in the top-left graph.

3.5 Discussion

When considering the uncertainties related to single processes, no significant seasonal variation is observed in the normalized interquartile range related to uncertainties in interception. In the particular case of a broadleaf forest, in Waidhofen/Ybbs beech forest, a more pronounced seasonal variation should be expected due to the higher interception capacity of the leafs in the summer period. This change in canopy cover is, however, not considered in the modeling approaches of Gash et al. (1995) and Liu (2001). In order to obtain more realistic interception estimates, future works should represent variable canopy cover by considering the gross rainfall needed to saturate the canopy, i.e. P'_g, to be changing

over time rather than constant. This could be achieved by a temporally varying stand storage capacity (C_{m}).

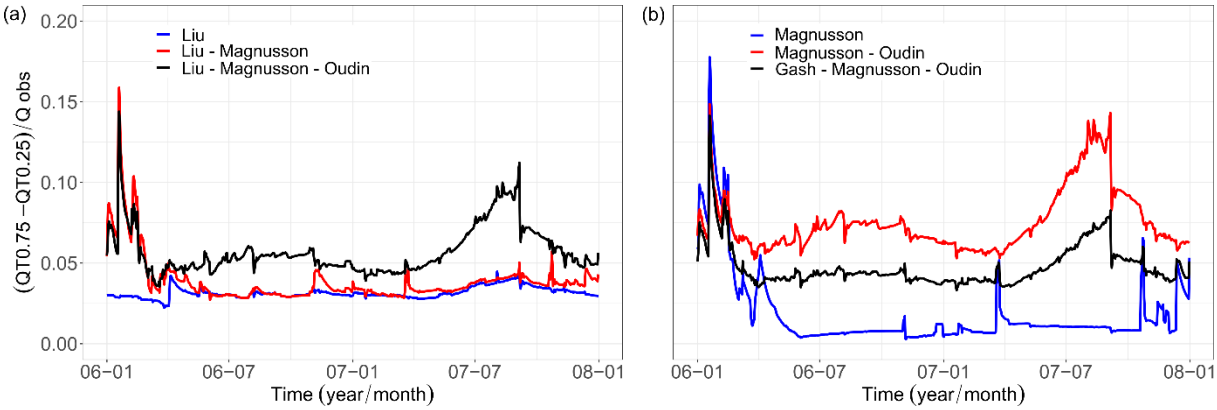

Fig. 3.8 Two examples to highlight that model input uncertainties do not necessarily increase with increasing hydrological process complexity. **a** Shows a case in which the input uncertainties increase with increasing process complexity. **b** Shows a case in which the input uncertainties can also partially decrease with increasing process complexity.

In contrast to uncertainties related to interception, a pronounced seasonal variation characterises the uncertainties related to evapotranspiration. The reason why the uncertainties in evapotranspiration are higher in summer 2007 as compared to summer 2006 can be found in the mean summer temperatures of both years (Fig. 3.2). The mean temperature between April and September in 2006 was 13.17 °C. In comparison, a mean temperature of 14.16 °C was observed in the same period in 2007. This difference of 1 °C leads to the observed increased uncertainties in $\mathrm{ET_{pot}}$. Thus, the results using temperature-based approaches for computing $\mathrm{ET_{pot}}$ show that the uncertainties of ET_{pot} increase with the available temperature for evapotranspiration. Given the fact that evapotranspiration related uncertainties can even reach the range of parametric uncertainties, e.g., in summer 2007, an appropriate representation of evapotranspiration is crucial to reasonably calculate the groundwater recharge as input for modeling a karst spring discharge in pre-alpine karst systems. Given the seasonal variation of uncertainties related to evapotranspiration, a reasonable representation of evapotranspiration for computing groundwater recharge is even more important during the summer period. This specific knowledge can guide researchers in gathering better field data when specific discharge conditions, e.g., mean and low flow conditions in summer, should be favored in model calibration. As recent studies highlighted the specific role of snow melt for groundwater recharge in alpine and pre-alpine catchments, this study further investigates if this specific importance is also reflected in increased uncertainties in modeled spring discharge when snow melt is relevant. Similar to evapotransipiration, the results show a clear seasonal pattern of snow melt related uncertainties. The differences in snow melt uncertainties are more pronounced than for evapotranspiration. Large uncertainties in snow melt are found in the winter 2005/2006, whereas snow melt related uncertainties are even smaller than those related to interception

in winter 2006–2007. Fig. 3.2b shows that in the winter season 2005–2006 the snow cover stayed for several months. Whereas, no longlasting and pronounced snow cover was observed in the winter season 2006–2007. The same pattern of uncertainties can also be identified when considering snow melt to be uncertain in combination with other processes, i.e. interception and evapotranspiration. Fig. 3.9 shows the maximum interquartile range for all model combinations including uncertainties in snow processes, i.e. 18 model combinations, and for those which do not include these uncertainties, i.e. 8 model combinations. In case of uncertain snow melt, the overall interquartile range significantly changes when snow melt controls groundwater recharge and, thus, the modeled spring discharge (e.g., from January 2006 to May 2006). Moreover, while only considering snow melt estimations to be uncertain does not lead to a significant increase in model output uncertainties in the evaporative season (Fig. 3.5), Fig. 3.9 shows that snow melt estimations increase model output uncertainties in cases when snow melt, interception and evapotranspiration are uncertain, e.g., in summer 2007. This can be explained by the fact that different processes can compensate for over- or underestimated water budgets of other processes. For example, an overestimation of the snow melt can be compensated by an underestimation of the evapotranspiration.

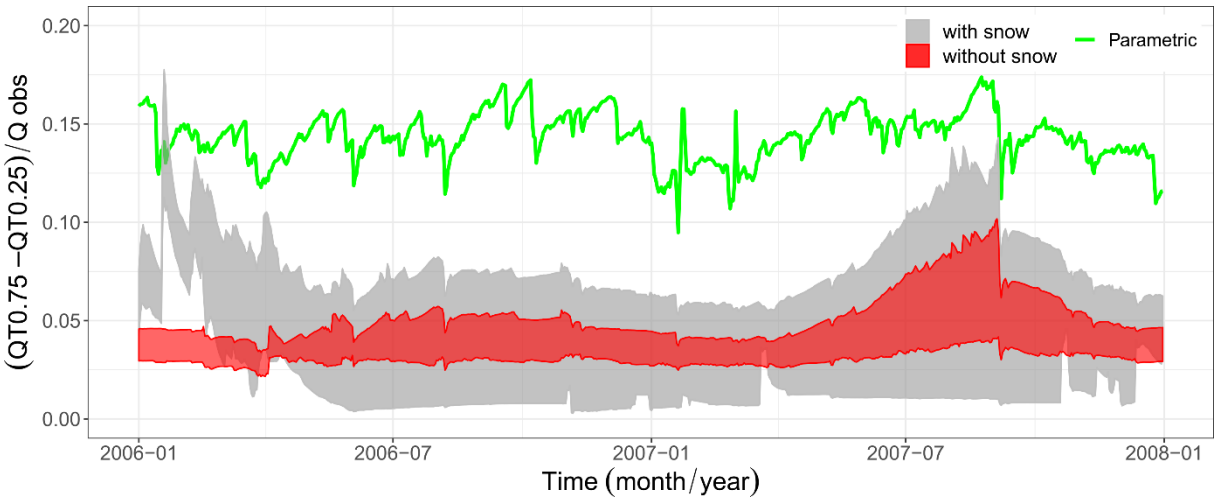

Fig. 3.9 Contribution of uncertainties related to snowmelt to the total LuKARS model input uncertainties. The two bands show the maximum interquartile ranges of the investigated model combinations that include uncertainties in snowmelt (grey) and of those which do not (red). An effect of snow process uncertainties can be observed throughout the years with a more pronounced impact during the winter.

Summarizing, the results show that the higher uncertainties in snow melt occur when the simulated spring discharge is controlled by snow processes. This highlights that the specific importance of snow melt for groundwater recharge can be identified in the snow melt related uncertainties when modeling a karst spring discharge. Hence, an erroneous assessment of snow melt related groundwater recharge can negatively affect the simulated spring discharge. On the contrary, the results do not exhibit a clear impact of uncertainties in snow melt on the spring discharge during the evaporative season in summer, when

the snow melt related uncertainties are not significant (< 2% of the observed discharge, Fig. 3.5). In the specific case of the Kerschbaum LuKARS model, the baseflow storage of the dolomite-dominated aquifer has a high storage capacity and is not immediately affected by changing hydrometeorological conditions. However, this can be different in more limestone-dominated karst systems and requires further investigations.

Finally, the results of all model combinations highlight that considering more processes to be uncertain does not necessarily lead to an increase of the normalized interquartile range of modeled spring discharge. This is particularly true when considering evapotranspiration and snow melt to be uncertain compared to considering also interception to be uncertain. These results highlight once more that two uncertain processes can compensate each other, leading to a reduction of the interquartile range of model outputs.

3.6 Conclusion

This study investigated how the input uncertainties of a lumped parameter model, i.e. LuKARS, vary temporally when applying the hydrologic model in a pre-alpine recharge area. Therefore, snow melt, evapotranspiration and interception were computed with three different algorithms each. The resulting groundwater recharge was used as input for LuKARS considering each possible model combination and focusing on the uncertainties of each single process. Moreover, the input uncertainties imposed by each process were compared to the parametric uncertainties obtained in previous studies (Teixeira Parente et al., 2019).

No clear tendency towards increasing model output uncertainties can be identified when more hydrological input time series are considered to be uncertain. Indeed, it was found that with increasing number of uncertain input the interquartile range of the LuKARS model outputs can even decrease. This shows that two or more uncertain processes can compensate each other.

The results of this study further show that model input uncertainties show temporal variations depending on how much the groundwater recharge and the modeled spring discharge is controlled by one specific process, e.g., snow melt and evapotranspiration. Thus, the results highlight that the importance of a specific process for groundwater recharge can be derived from the respective input uncertainties. Further, this research identified that uncertainties in snow processes can even be higher than parametric uncertainties.

This study investigated the time-dependent relevance of the model input uncertainties for pre-alpine conditions typical of Central Europe. A similar approach should be applied to extend these results to karst catchments with different climate conditions and land uses. An intercomparison study could be based on the recently developed WoKaS database (Olarinoye et al., 2020). Moreover, it is of particular

interest to apply the presented methodology to karst catchments characterized by different recharge processes. Thus, a comparison between catchments dominated by diffusive recharge, as the Kerschbaum springshed, and those dominated by point infiltration is suggested.

The knowledge gained from investigating temporally varying model input uncertainties can guide researchers and water managers in gaining relevant data needed for improving the reliability of hydrologic model results. In this case, e.g., the uncertainties in snow melt could be reduced by implementing snow measurement stations in the recharge area. Moreover, the information on the temporal variability of model input uncertainties helps to derive which data are needed to improve the reliability of model output results during different times of a year.

Chapter 4

Impact of semi-distributed recharge on hydrological conceptual karst modelling

Sivelle, V., Jourde, H., Bittner, D., **Richieri, B.**, Labat, D., Hartmann, A., and Chiogna, G. (2022). Considering land cover and land use (LCLU) in lumped parameter modeling in forest dominated karst catchments. Journal of Hydrology, 612, Part C, 128264. https://doi.org/10.1016/j.jhydrol.2022.128264

Abstract

Lumped parameter modeling approach has been widely applied in karst hydrology for, among other applications, groundwater availability assessment in a context of global change. Nonetheless, such approach generally does not account for land-cover land-use (LCLU) and its impacts on recharge processes. Then, considering a semi-distributed recharge constitutes a relevant approach to capture the impacts of LCLU on flow dynamics but also introduce more complexity in the modeling approach. The present study consists of a multiple hydrological model calibration to assess the implication of considering a semi-distributed recharge in a lumped parameter model and focuses on the uncertainty originating by the model structure. The modeling results are discussed to evaluate the trade-off between hydrological model complexity and hydrological model performance. The study focuses on forest dominated karst areas with three karst catchments: Kerschbaum (Lower Austria), Baget (French Pyrenees) and Oeillal (southern France). Considering a semi-distributed recharge gives better performance for both Kerschbaum and Oeillal catchments hydrological models, while no improvement is obtained for Baget catchment. Systematic consideration of LCLU is thus not necessarily worthwhile in karst environments as it can bring contradictory results in terms of hydrological model performance.

Keywords: Karst hydrology, Lumped parameter modeling, Land Cover Land Use, Recharge

4.1 Introduction

One-quarter of the world's population depends on freshwater from karst aquifers (Ford and Williams, 2013). Ensuring a sustainable karst freshwater supply constitutes a major challenge in a context of increasing imbalance between freshwater supply capacity and the needs of a growing population (Stefano et al., 2012; Wada et al., 2016). Moreover, both climate change and anthropogenic pressures, including an increase in water abstraction or changes in land cover and land use (LCLU), may have a strong impact on the future availability of karst water resources (Gleeson et al., 2012; Taylor et al., 2013). A decreasing karst groundwater availability has already been observed in various regions around the world such as in the Mediterranean area (Charlier et al., 2015; Fiorillo and Guadagno, 2012; García-Ruiz et al., 2011; Smiatek et al., 2013), North America (Loáiciga et al., 2000), and Asia (Guo et al., 2005; Hao et al., 2009; Ma et al., 2004; Wu et al., 2017). Moreover, many studies have investigated the potential evolution of karst groundwater resources under various climate change assumptions (Brenner et al., 2018; Chen et al., 2018; Doummar et al., 2018; Nerantzaki et al., 2020) or various future anthropogenic scenarios (Andreas Hartmann et al., 2012; Sivelle et al., 2021). Nonetheless, only a few studies consider the impact of LCLU changes such as urban area expansion or vegetation adaption to climate change in the assessment of global change impacts on karst groundwater (Sarrazin et al., 2018).

Zhao et al. (2020) highlighted on a global scale that vegetation in the karst regions can be more sensitive to changes in precipitation regimes than to temperature. Ellison et al (2012) stated that “forest–water interactions play a crucial role in supplying the atmospheric moisture that becomes precipitation in the hydrologic cycle” and so forest may have a noticeable influence on the rainfall regime on a large scale. Also, forest coverage around the world is in evolution with an estimated loss of around 2.3 million kilometers square and a gain of around 0.8 million kilometers square from 2000 to 2012 (Hansen et al., 2013). Under changing climatic conditions, the vegetation can show an adaption and consequently modify the land-atmosphere exchanges (Bussotti et al., 2014; Klausmeyer and Shaw, 2009; Llorens and Domingo, 2007), which could at the end cause a modification in the recharge processes (Tramblay et al., 2020). Finally, LCLU changes may constitute a first-order factor in the evolution of groundwater resources, since they may strongly impact the recharge processes. The assessment and prediction of the effects of LCLU changes on groundwater resources require information on the heterogeneities of the recharge processes and thus the implementation of hydrological models that include a distributed or semi-distributed recharge.

One common approach for hydrodynamic modeling in karst systems consists of considering different combinations of the dominant flow components as distinct conceptual buckets (Bittner et al., 2018; Butscher and Huggenberger, 2008; Fleury et al., 2007; Guinot et al., 2015; Mazzilli et al., 2019; Tritz et al., 2011). Such a model can be useful for the long-term assessment of the flow dynamics and groundwater resources evolution. Sivelle et al., (2019) highlighted a decrease of more than 10 % in the water level during spring periods since the 1960s on Aliou and Baget karst systems in the French

Pyrenees. Hartmann et al. (2012) show that the discharge could decrease by 30% by the end of the 21st century at the Faria spring in Palestine. Nerantzaki and Nikolaidis (2020) highlighted an increased dryness in terms of frequency, duration and intensity for three Mediterranean karst springs located in Greece. Sivelle et al. (2021) proposed a methodology to assess the relative impact of climate changes and anthropogenic forcing on spring discharge and highlighted climate change as the main factor causing a decrease in the predicted Oeillal´s spring discharge, in southern France. In these former studies, the proposed conceptual lumped-parameters models consider homogeneous recharge processes at the catchment scale. Depending on land use, heterogeneities in soil properties, heterogeneities in climate inputs (e.g., convective events, altitudinal gradient), and catchment size, it can be of interest to consider a semi-distributed recharge as shown in former studies (Bittner et al., 2018; A. Hartmann et al., 2012; Ollivier et al., 2020).

The first purpose of this study is to investigate how considering a semi-distributed recharge, depending on LCLU, affects the flow dynamics of a lumped parameter model and more especially the infiltration toward the saturated zone. The second purpose is to identify the appropriate levels of model complexity that allows obtaining the best performance in terms of spring discharge simulations. For that purpose, the study will focus on forest dominated karst areas to avoid bias due to significant differences in terms of the dominant type of LCLU in the recharge area. Therefore, three karst catchments characterized by recharge areas lower than 50 km^2 were chosen to run a multi-model calibration considering different levels of complexity in the upper level of the model (i.e. the compartment can be subject to evapotranspiration and so reproduce the land-atmosphere exchanges). Also, the evapotranspiration is supposed independent of the LCLU to avoid uncertainties related to the estimation method as well as the introduction of cultural coefficient. In this way, the study is more related to the impact of model structure rather than input uncertainty.

4.2 Study sites and data

Fig. 4.1 shows the location and the land-use for the three selected catchments: Kerschbaum (Bittner et al., 2018), Oeillal spring (Sivelle et al., 2021; Sivelle and Jourde, 2020) and Baget (Sivelle et al., 2019). To avoid misinterpretations due to significant differences in terms of dominant land-use, the study focuses on forest dominated karst areas. Table 4.1 summarizes the main characteristic of the three catchments in terms of climate, geology/lithology and LCLU.

The Kerschbaum spring is located 10 km south of the city of Waidhofen a.d.Ybbs, Lower Austria. Its recharge area covers approximately 2.5 km^2 and is characterized by a mean annual temperature of 8 °C and annual precipitation of 1405 mm (2001 - 2014). The small-scale recharge area is predominantly covered by beech forests and parts of it by dolomite quarries (Table 4.1). With a mean annual discharge of 34 $l.s^{-1}$, the Kerschbaum spring is part of the regional water supply and shows a response time to rainfall events of 1 day (Bittner et al., 2021). The recharge area belongs to the eastern foothills of the

Northern Calcareous Alps and consists of a sequence of dolomitic basement rocks, which result in a deep karstified groundwater system. Despite the well-connected network of conduits, the recharge area does not present significant sinkholes and the recharge processes can be assumed to be mainly diffusive (Bittner et al., 2018).

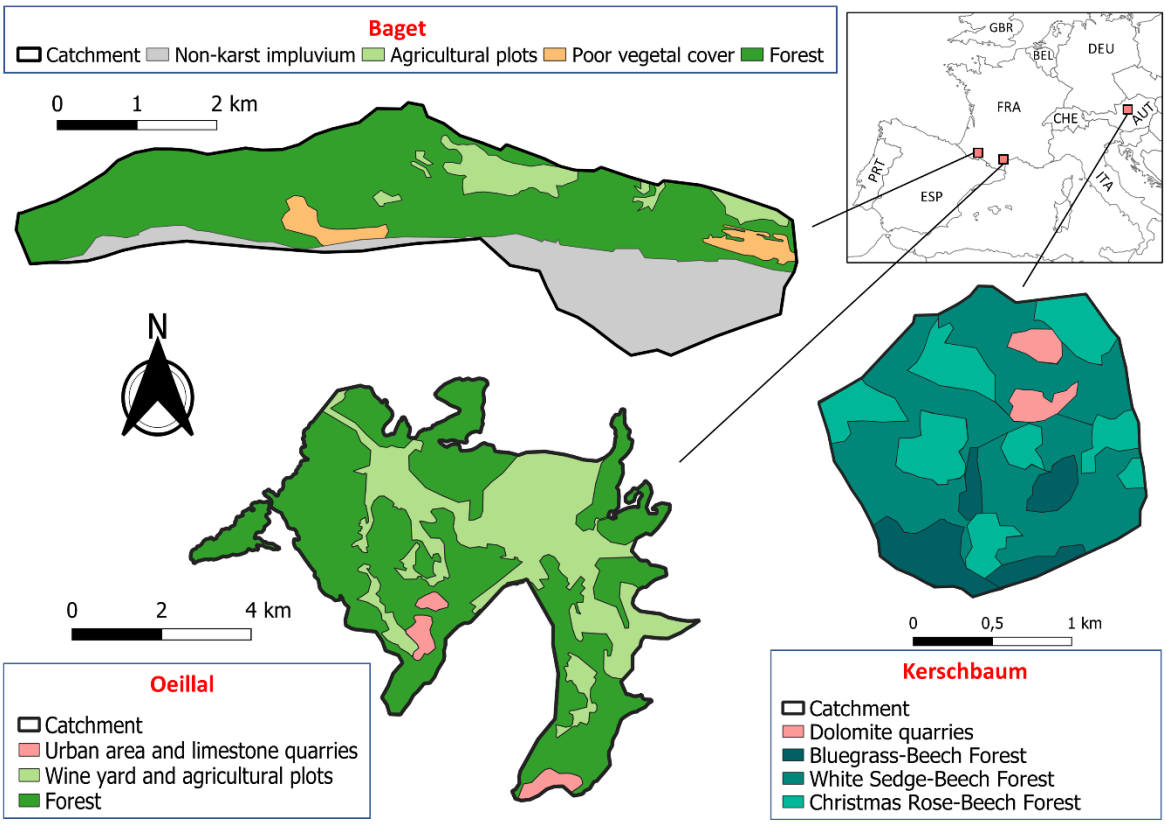

Fig. 4.1 Land use in the recharge area **a** Kerschbaum, **b** Oeillal and **c** Baget. The land use is determined based on field investigation and the CORINE Land Cover - CLC12.

The Oeillal spring is located north of the city of Narbonne (southern France) and drains water from the limestone terrain of the Fonfroide-Monredon massif. The main aquifer in the area runs within the calcareous formation and fed the Oeillal spring, which is located in the Western part of the Narbonne-Sigean sedimentary basin and rises at four spring pools. In the Northern part of the area, there is also an alluvial aquifer which is contained in the Quaternary formation of the Aude river's terrace. The recharge area covers around 43.2 km^2 with a potential additional 10 km^2 contributing zone (Sivelle and Jourde, 2020) and is characterized by a Mediterranean climate with a mean annual temperature of 14.7 °C and annual precipitations of 570 mm (1980-2020). The mean annual discharge is estimated to be around 0.14 m^3/s.

The Baget catchment is located 10 km southwest of the city of Saint-Girons (French Pyrenees). Its recharge area covers approximately 13.2 km^2 and is characterized by a mean annual temperature of 11.8 °C and annual precipitation of 1000 mm (1970 - 2020). The mean annual discharge is estimated to be around 0.45 m^3/s. The karstified part of the basin is characterized by metamorphic Jurassic to Cretaceous

dolomites, limestones and calcareous marls. These formations deep 70 to 90° southwards, under the slaty Albian-Cenomanian Ballongue flysch that constitutes the southern boundary of the catchment. The contact between karstified formation and non-karstifiable rocks give the west-east direction of the main drainage system. The northern limit of the Baget drainage basin consists of a secondary fault from the North Pyrenean fault, the Alas fault.

Table 4.1 Information about the karst catchments

			Climate		**Geology**	**LCLU**
	Recharge Area (km^2)	Mean annual discharge (m^3/s)	Mean Annual Precipitation (mm)	Mean Annual ET (mm)		
Kerschbaum	2.5	0.034	mean = 1405 from 1040 to 1820	mean = 814 from 723 to 984	Dolostone Triassic	Dolomite quarries – 4% Bluegrass-Beech Forest – 13% White Sedge-Beech Forest – 56% Christmas Rose-Beech Forest – 27%
Oeillal	43.2	0.14	mean = 570 from 300 to 1150	mean = 1380 from 875 to 1540	Limestone Upper and Lower Jurassic	Urban area and limestone quarries – 6.5% Wine yard and agricultural plots – 30.8% Coniferous forest – 62.7 %
Baget	13.2	0.45	mean = 1000 from 650 to 1350	mean = 810 from 680 to 940	Limestone and dolostone Jurassic to Cretaceous	Non-karstic impluvium - 20% Agricultural plots - 3% Poor vegetal cover - 5% Hardwood trees forest - 72%

Both Kerschbaum and Oeillal catchment are impacted by the presence of quarries and Oeillal catchment is also impacted by the presence of urban areas. The Baget catchment differs from other catchments due to the presence of non-karstic impluvium that represent 20 % of the total recharge area. This part of the watershed consists of the slaty Albian-Cenomanian Ballongue flysch, considered an impervious

formation. The orientation of the main drainage system in the area is given by the contact between the Ballongue flysch and the karstified part of the basin in the west-east direction (Debroas, 2009; Sivelle et al., 2020). This part of the watershed contributes to the spring discharge through surface runoff rather than infiltration in the main aquifer.

The three selected catchments are characterized by a small recharge area (< 50 km^2) and with a LCLU dominated by forest that represents 96% of the total recharge area for Kerschbaum, 62.7% of the total recharge area for Oeillal and 72% of the total recharge area for Baget (Fig. 4.1). The catchments are chosen based on their dominant LCLU and their comparable size of recharge areas to avoid bias related to LCLU and scale effects. Regarding Kerschbaum and Baget, the two systems show similar catchment size and land cover characteristics but different geological and climate properties. The Kerschbaum springshed is a dolostone karst system with a mean annual temperature of 8 °C. On the contrary, the geology of Baget is dominated by limestones and the climate is characterized by a mean annual temperature of 12.2 °C. Moreover, the Kerschbaum and Baget springs have a mean discharge of 34 and 450 $l.s^{-1}$, respectively.

4.3 Methodology

4.3.1 Hydrological models

4.3.1.1 Semi-distributed recharge in lumped parameter modeling

A semi-distributed recharge can be implemented in lumped parameter model at the catchment scale employing two distinct approaches which consist of either increasing the model complexity (and so adding more parameters) or considering distributed meteorological data (precipitation, land-surface temperature, evapotranspiration) as input in the model. Such approaches have proved their efficiency in improving karst aquifers hydrological modeling:

Ollivier et al. (2020) propose the KaRaMel model with several lumped model units running in parallel. The structure of the model is based on a three-compartments model: the upper compartment collects precipitation, hosts evapotranspiration, and governs infiltration toward a slow discharge compartment (M) and a rapid discharge compartment (C). The outlet discharge consists of the sum of discharge from the slow and rapid compartments. Such model structure is widely used in karst hydrology (Baudement et al., 2017; Moussu, 2012; Pinault et al., 2001; Schmidt et al., 2014). The modeling is performed over the Fontaine de Vaucluse aquifer (southern France) showing a large watershed area (about 1600 km^2). The model structure allows accounting for both slow matrix flows and fast conduit flows (Fleury et al., 2007; Mazzilli et al., 2019) considering there is no exchange between these two flow components, although exchanges flow can be observed in the non-saturated zone (Dal Soglio et al., 2020). The input data consists of gridded data set with a spatial resolution of several kilometers that cannot be considered as valuable input for hydrological modeling on karst aquifers with recharge areas lower than 50 km^2.

Such an approach allows to better assess the recharge distribution, with heterogeneities due to environmental factors such as geology, LCLU or even meteorological forcing (precipitation, evapotranspiration). In large karst catchments such as Fontaine de Vaucluse, the recharge distribution explains a large part of the discharge variation at the outlet (Ollivier et al., 2020).

Another approach relies on the introduction of hydrotopes, which were considered in the LuKARS model (Bittner et al., 2018). Each hydrotope is characterized by land use and soil type and conceptually represents the vadose zone. The model structure consists of a compartment contributing to the recharge of the saturated zone, including also a loss function flowing to secondary springs and a hysteresis function (Tritz et al., 2011) flowing directly to the spring. In the LuKARS model, each hydrotope is exposed to effective precipitation depending on interception, evapotranspiration and, when applicable, snow processes. The hydrotopes consist of several lumped parameter models running in parallel, in a similar way as the KaRaMel model (Ollivier et al., 2020). Each hydrotope contributes to recharge, loss and fast flow depending on their relative area, their distance from the spring as well as the land use and soil properties. The use of such "hydrotopes" relies on the assumption of a hydrophysical uniqueness of each hydrotope (Bittner et al., 2018).

4.3.1.2 Model structures

Two lumped parameters models are implemented in this study to account for a different conceptualization of the flow processes. The first model corresponds to the original LuKARS model (Bittner et al., 2018) and the second model corresponds to a coupled model with the concept of hydrotopes implemented in the LuKARS model in the upper level of a model structure with two interconnected compartments in the lower level of the model structure, as proposed in the KarstMod modeling platform (Mazzilli et al., 2019). A detailed description of LuKARS and KarstMod and their underlying equations are provided in appendix A.2.1 and appendix A.2.2, respectively. Fig. 4.2 summarizes the different model structures for each catchment concerning both the upper and lower level of the model structures and a description of the associated parameters is given in Table 4.2. In this study, the different configurations in the upper level are tested, considering 1 up to 4 hydrotopes, bringing also more uncertain parameters for the model calibration. Conversely, the lower level is chosen for each catchment based on former studies for Oeillal (Sivelle et al., 2021), Kerschbaum (Bittner et al., 2018) and Baget (Sivelle et al., 2019). The present study focuses on the characterization of the infiltration processes through two fluxes denoted Q_{is} and Q_{hy} that flow from the upper level toward a compartment in the lower level or directly to the spring (Fig. 4.2). In this study, the original "Linear baseflow storage" from Bittner et al, (2018) is referred to as a compartment with linear discharge law for notation consistency with the use of coupled LuKARS and KarstMod model structures. Also, this compartment is denoted M (Fig. 4.2) and represent the baseflow as suggested in the original KarstMod model (Baudement et al., 2017; Mazzilli et al., 2019; Sivelle et al., 2019).

In this study, the lower level in the model structure for Kerschbaum corresponds to a compartment with linear discharge law implemented in the original LuKARS model (Bittner et al., 2018) whereas a model structure considering matrix-conduit exchanges in the lower level is applied within the Baget catchment (Sivelle et al., 2019). Concerning the Oeillal spring, a threshold effect in lower level of the model structure (i.e. compartment with linear discharge law) allows reproducing the change in flow dynamics during the period of low water table elevation (Sivelle et al., 2021).

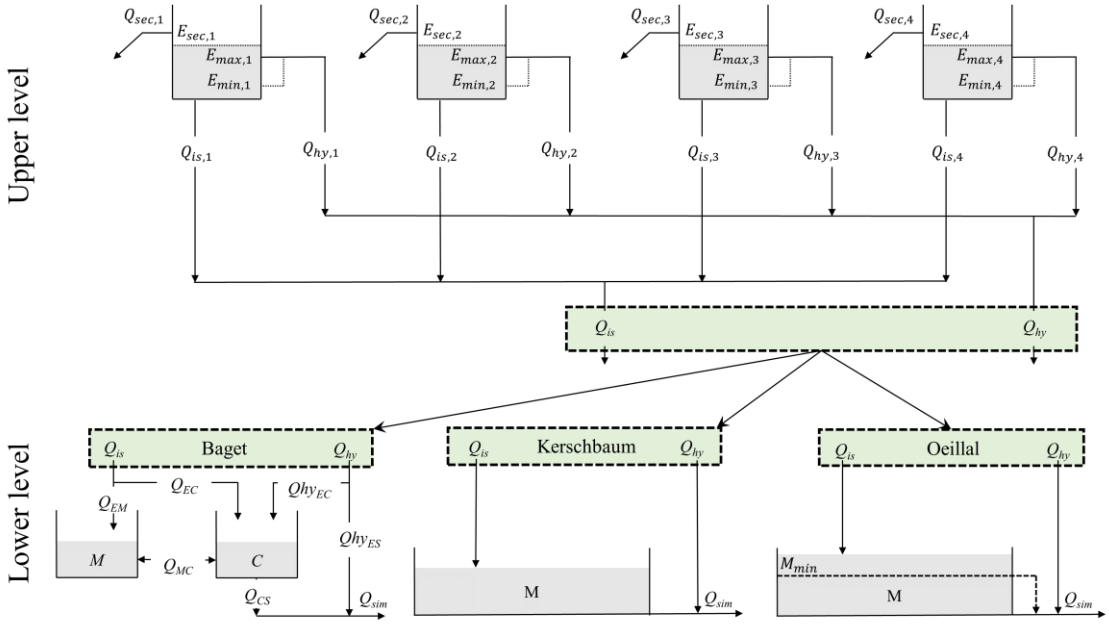

Fig. 4.2 Structure of the lumped parameter model for the three catchments. The upper level is based on the LuKARS model (Bittner et al., 2018) for each catchment whereas the lower level is based on former studies for Baget (Sivelle et al., 2019), Kerschbaum (Bittner et al., 2018) and Oeillal (Sivelle et al., 2021).

The upper level of the model structure consists of four lumped model units running in parallel, denoted 'hydrotopes', characterized by different land uses and soil types. It conceptually represents the vadose zone compartment (higher level with the continuum soil-epikarst-infiltration zone). A hydrotope is analogous to a bucket that has three discharge components with different flow directions: [1] the quickflow component Q_{hy} (L^3 T^{-1}) is characterized with a hysteresis function (Tritz et al., 2011) and is directly transferred to the spring outlet, [2] the secondary spring discharge Q_{sec} (L^3 T^{-1}) is transferred out of the system and do not contribute to the spring discharge or the lower compartment recharge and [3] the recharge Q_{is} (L^3 T^{-1}) is transferred to the lower compartment.

The lower level of the model structure in the LuKARS model consists of one compartment with linear discharge law. The recharge of the compartment consists of the sum of the intra-storage flow Q_{is} from each hydrotope. The outlet discharge of the lower compartment is transferred to the spring. The total

spring discharge consists of the sum of the fluxes flowing from the compartment with linear discharge law Q_{MS} (L^3 T^{-1}) and the fluxes from the hydrotopes Q_{hy} (L^3 T^{-1}) with a hysteretic behavior.

Table 4.2 Information about the model structures tested along with the three-karst catchment (Baget, Oeillal and Kerschbaum). Some of the mode structure were already published in former studies.

			Upper level				Lower level
Catchment	**Model**	**Ref.**	**Hyd. 1**	**Hyd. 2**	**Hyd. 3**	**Hyd. 4**	
Oeillal	LK_01	-	Complete recharge area				1 compartment with linear discharge law
	LK_02	Sivelle et al., (2021)	Impervious zone	Infiltration zone	-	-	
	LK_03	-	Impervious zone	Wine yard Agricultural lots	Forest	-	
Kerschbaum	LK_01	-	Complete recharge area				1 compartment with linear discharge law
	LK_02	-	Quarries	Infiltration zone	-	-	
	LK_03	-	Quarries	White Sedge-Beech Forest	Christmas Rose-Beech Forest + Wood Barley-Beech Forest	-	
	LK_04	Bittner et al., (2018)	Quarries	White Sedge-Beech Forest	Christmas Rose-Beech Forest	Wood Barley-Beech Forest	
Baget	LK_01	-	Complete recharge area				1 compartment with linear discharge law
	LK_02	-	Non-karstic impluvium	Karstic impluvium	-	-	
	LK_03	-	Non-karstic impluvium	Poor vegetation cover	Agricultural plot + Forest	-	
	LK_04	-	Non-karstic impluvium	Poor vegetation cover	Agricultural plot	Forest	
	LK-KM_01	-	Complete recharge area				1 compartment with linear discharge law
	LK-KM_02	-	Non-karstic impluvium	Karstic impluvium	-	-	
	LK-KM_03	-	Non-karstic impluvium	Poor vegetation cover	Agricultural plot + Forest	-	
	LK-KM_04	-	Non-karstic impluvium	Poor vegetation cover	Agricultural plot	Forest	
	KM	Sivelle et al., (2019)	1 compartment with 2 different discharge law through the compartments of the lower level				2 interconnected compartments M and C with nonlinear discharge laws

Concerning the coupled LuKARS-KarstMod model, the lower level of the model structure consists of two interconnected compartments denoted M (representative of slow linear flow dynamics that mainly

occurs in the matrix) and C (representative of quick non-linear flow dynamics that may occur in conduits and/or unclogged fractures). Then compartment M corresponds to the capacitive function of the aquifer, whereas compartment C is more related to the transmissive function of the aquifer. Both M and C can be filled with water flow from the upper compartment, which are the intra-storage flow Q_{is} and the quick-flow component Q_{hy}. The flow partition is made through a portioning coefficient for both Q_{is} flowing to M or to C and Q_{hy} flowing to C or to the spring. One should note that the original KarstMod modeling platform also implemented such flow partition from the compartment in the upper level to the different compartment of the lower level. The difference for the coupled LuKARS/KarstMod model relies on the use of several buckets running in parallel rather than a single bucket with different discharge coefficients toward the bucket in the lower level of the model. Such conceptualization brings more complexity to the model structure and increases the number of uncertain parameters for the model calibration.

Finally, the two proposed models (Fig. 4.2) consist of modular "bucket-style" model of lumped parameters that enable to build of interconnected compartments, depending on different levels of complexity in both upper and lower levels of the models. In this study, it should be noticed that hydrotopes can be activated/deactivated depending on the levels of complexity considered in the upper level of the model to run the fluxes contributing either to the recharge of the lower level or directly to the spring discharge. So, the number of hydrotopes varies depending on how the heterogeneity in the upper level is considered. Table 4.2 summarizes the model structures in terms of flow conceptualization in the upper and lower level of the model for the three catchments

4.3.1.3 Model calibration

The hydrological models were implemented in the Python environment (Summerfield, 2010) while the parameter estimation was performed using a particle swarm optimization (PSO) procedure (Eberhart and Kennedy, 1995) implemented in the "pyswarm" package (Lee, 2014). This approach leads to the definition of a unique optimal parameter set for each model configuration and therefore this study does not address parametric uncertainty and model equifinality since the study focuses on the uncertainty originating by the model structure. The data set for the calibration and validation of the hydrological model depends on the available data and the calibration procedure is performed on the same time intervals considered in the former studies to avoid bias due to the calibration period on the parameter estimation (Mazzilli et al., 2012). The calibration is made on a period of 1 year for the Kerschbaum spring, 18 months for the Oeillal spring and 10 years for the Baget. The calibration and validation periods are presented in Table 4.3. The calibration is made on a period where the required data are available on a daily time step. Regarding the Oeillal spring, validation data consists of sparse temporal discharge time series, measured before installation of probes for continuous hourly measurement (Sivelle and Jourde, 2020). Also, adding BE in a weighted function with KGE was required to give more

importance of the water balance in the calibration procedure and to better reproduce the significant flow decrease during the summer period.

Table 4.3 Calibration periods, validation periods and objective function (Wobj) for hydrological models. Calibration and validation periods and objective function are based on former references. BE: Balance Error, NSE: Nash-Sutcliffe Efficiency, KGE: Kling-Gupta Efficiency and Q: spring discharge

	Period	Calibration	Validation	Wobj	Reference
Baget	from to	01/10/1970 30/09/1980	01/10/1980 31/12/2016	$0.9 \times NSE(Q) + 0.1 \times BE(Q)$	(Sivelle et al., 2019)
Kerschbaum	from to	01/01/2006 31/12/2006	01/01/2007 31/12/2007	$NSE(Q)$	(Bittner et al., 2018)
Oeillal	from to	19/09/2018 25/04/2020	01/01/1987 31/12/2017	$0.75 \times KGE(Q) + 0.25BE(Q)$	(Sivelle et al., 2021)

4.3.2 Model evaluation

4.3.2.1 Model evaluation using performance criteria

The metrics used for hydrologic model calibration and evaluation are mainly based on the comparison between observed and simulated streamflow. According to Hauduc et al. (2015) model errors can be calculated in different ways and expressed as performance criteria, allowing to evaluate model performance numerically. Several studies have proposed number of performance criteria (Bennett et al., 2013; Ferreira et al., 2020; Hauduc et al., 2015; Jackson et al., 2019). To assess different aspects of the model performance, it is recommended to adopt a multi-objective model evaluation with a combination of different performance criteria (Huo and Liu, 2020; Monteil et al., 2020).

In this paper, the hydrological models are evaluated with some performance criteria widely used in karst hydrology: the Nash-Sutcliff efficiency NSE (Nash and Sutcliffe, 1970), the Kling-Gupta efficiency KGE (Gupta et al., 2009), the non-parametric Kling-Gupta efficiency KGENP (Pool et al., 2018). To evaluate the model performance in terms of volume of transit, the modified balance error BE (Perrin et al., 2001) and the volumetric error VE (Criss and Winston, 2008) are also considered. The correlation coefficient of Pearson Rp as well as Spearman Rs are also considered. Then, hydrological model evaluation is performed using an ensemble of seven performance criteria, allowing to account with different aspect of the model performance. For more information, the reader may refer to some literature review (Bennett et al., 2013; Ferreira et al., 2020; Jackson et al., 2019). Given that the model structures are characterized by a different number of parameters, the Akaike Informative Coefficient (AIC) is computed such as $AIC = 2k + Nln(RSS)$, where k is the number of model parameters, N the number of observations and RSS is the sum of the squared residuals. The AIC penalizes the model structures with large number of parameters and gives information on how the performance may evolve with the number of uncertain parameters.

The various performance criteria are plotted according to a “radar chart”, which consists of a polygon where the position of each point from the center gives the value of the performance criteria. One should note that all the performance criteria used in this study are given with a perfect model fitting when the value is equal to 1. Then, plotting several models in the same radar plot allows a quick comparison of the model performance according to the various criteria.

4.3.2.2 Model evaluation using time series analysis

In karst hydrology, the auto-correlation function (ACF) is frequently used to characterize the temporal structure of hydrological signals under the linear-stationary hypothesis (Labat et al., 2000a; Larocque et al., 1998; Mangin, 1984; Padilla and Pulido-Bosch, 1995; Panagopoulos and Lambrakis, 2006). Mangin (1984) proposed to determine the memory effect of karst aquifers as the lag time value where the ACF of the spring discharge time series reaches the value of 0.2. This approach is commonly used to characterize hydrodynamics in karst aquifers (Lorette et al., 2018; Sivelle and Jourde, 2020). In addition, the cross-correlation function (CCF) between rainfall and spring discharge provides an approximation of the impulse response (Mangin, 1984) when assuming the rainfall consists of a random process (white noise). Also, it describes the capacity of a system to transform the rainfall into discharge. The higher the CCF peak, the more the system acts as a piston. Moreover, the lag time for the occurrence of the maximum value in CCF corresponds to the time of response. Due to high heterogeneities in karst aquifers, the response time can be dependent on the seasonal variability in rainfall intensity (Delbart et al., 2014). Both memory effects and response time can be dependent on the sampling frequency of the rainfall-discharge time series (Sivelle and Jourde, 2020) because of the occurrence of several processes with characteristic time covering several orders of magnitudes (Blöschl and Sivapalan, 1995). Lumped parameter modeling can show bias such as underestimation of the memory effect and overestimation of CCF peak (Sivelle, 2019) and may testify the importance of considering low frequencies component in the simulated impulse response since the high frequencies processes appear to be predominant. Such time series analysis can provide information about the hydrological model performance in addition to the performance evaluation through numerical performance criteria such as NSE, KGE or KGENP.

In addition, the wavelet multiresolution analysis (MRA) is applied to project the spring discharge time series on an orthogonal basis of wavelet and scale functions (Labat et al., 2000b; Mallat, 1989). The basis is generated from a filter band following a dyadic scale. The projection allows building for each level of this scale the component of the signal that explains the variability at this scale. The decomposition is orthogonal and therefore the sum of all components (details and residue or smooth) give back the initial signal. For a deeper hydrological model evaluation, Sivelle (2019) runs MRA on both observed and simulated spring discharge time series and calculate the goodness of fit with the NSE criteria for each scale. Application on highly karstified watersheds such as Aliou and Baget karst systems shows the weakness of a daily rainfall-discharge model for the high frequency (scale < 8 days) and for the 8-months scale (scale = 256 days). Such an approach can be useful to evaluate hydrological model

performances, in addition to ACF and CCF, since it gives a deeper description of the model bias. Indeed, since the usual performance criteria consider the mean errors it does not capture how the model errors can be structured in time and frequency and so how the model can be biased in forecasting purposes.

4.4 Results and discussion

4.4.1 Hydrological models´ calibration and validation

The calibrated model parameters set for LuKARS model on Baget, Oeillal and Kerschbaum catchments are reported in Table 4.4 whereas the performance criteria for both the calibration and the validation periods are shown in Fig 4.3. The performance criteria are color scaled from red for bad values to blue for good values, where the closer the value to 1 the better the fit between observed and simulated spring discharge. The simulated spring hydrographs are reported in Fig 4.4 and the radar chart for model performance evaluation are given in Fig 4.5.

Table 4.4 Model parameters for LuKARS model over Kerschbaum, Oeillal and Baget and the coupled LuKARS/KarstMod model for the Baget catchment. Parameter description is given in Table 4.2.

		Kerschbaum				Oeillal			Baget - LuKARS				Baget - Coupled LuKARS/KarstMod			
		1	2	3	4	1	2	3	1	2	3	4	1	2	3	4
Hydrotope 1	Ra	2,5	0,1	0,1	0,1	42,3	2,7	2,7	13,2	2,64	2,64	2,64	13,2	2,64	2,64	2,64
	L	1000	550	550	550	7300	7300	5600	5000	2000	2000	2000	5000	2000	2000	2000
	khy	320,817	0	0	0	426,80	0	0	1840100	593920	1727320	1083560	0	0,965	0	0
	Emin	38,242	0	0	0	117,85	0	0	762,65	894,76	632,54	570,49	0	95,78	31,36	31,36
	Emax	160,075	1	1	1	191,63	1	1	1127,94	1194,28	1496,22	1157,98	1	179,74	495,75	495,75
	alpha	0,547	0	0	0	0,28	0	0	1,98	1,34	1,015	1,25	1	5,81	2,61	2,61
	kis	0,003	0	0	0	0,02	0	0	0,0001	0	0	0	1	0	0	0
	ksec	0,488	0	0	0	5,35	3,9	3,9	0	0	0	0	0	0	0	0
	Eloss	233,109	0	0	0	162,76	0	0	10000	100000	100000	100000	100000	100000	100000	100000
Hydrotope 2	Ra		2,35	0,325	0,325		39,6	13,0		10,56	1,056	0,396		10,56	1,056	0,396
	L		971	1600	1600		5900	6200		5000	3000	2000		5000	3000	2000
	khy		118,77	517,86	684,21		919,15	224,87		1483800	1605420	2429460		0	0	0
	Emin		2,98	14,09	34,89		110,16	69,70		744,07	195,32	104,48		0	0	0
	Emax		62,83	55,55	73,65		193,42	148,99		1652,6	640,97	140,08		1	1	1
	alpha		1,44	1,47	1,54		0,38	0,44		1,25	1,21	1,04		1	1	1
	kis		0,04	0,03	0,12		0,02	0,29		0,0001	7,6	7,22		0,302	0,46	0,46
	ksec		0,28	0,77	0,92		16,08	14,60		0	0	0		0	0	0
	Eloss		35,00	27,83	64,10		177,17	16,29		100000	100000	100000		100000	100000	100000
Hydrotope 3	Ra			2,075	1,4			26,5			9,504	0,66			9,504	0,66
	L			920	900			6800			5000	3100			5000	3100
	khy			99,9284	105,1630			740,60			3413900	2116618			0	0
	Emin			46,6049	8,0584			97,94			532,55	432,55			0	0
	Emax			148,9139	114,7194			159,40			1357,07	1153,07			1	1
	alpha			0,8078	0,9812			1,81			1,25	1,25			1	1
	kis			0,0035	0,0033			0,04			1,02	1,02			0,31	0,35
	ksec			0,0298	0,0465			87,34			0	0			0	0
	Eloss			211,2942	171,7668			118,10			100000	100000			100000	100000
Hydrotope 4	Ra				0,675							9,504				9,504
	L				960							5000				5000
	khy				167,593							3413900				0
	Emin				100,676							532,55				0
	Emax				224,941							1357,07				1
	alpha				0,489							1,25				1
	kis				0,001							1,02				0,21
	ksec				0,024							0				0
	Eloss				419,301							100000				100000
Lower level	kMS_bot	0,00099	0,00098	0,00092	0,00092	0,06134	0,02880	0,06670	0,00774	0,04050	0,09233	0,04032				
	kMS_top					0,00844	0,00886	0,00822								
	M_min					2,38138	4,93496	2,57138								
	XEC												0,75	0,87	1	1
	Xhy												1	0,78	0,626	0,626
	aMS												1	1	1	1
	kCS												0,0001	0,00483	0,00676	0,00676
	aCS												4	4	4	4
	kMC												0,39	0,559	0,634	0,634
	aMC												1	1	1	1

The LuKARS model shows quite satisfactorily performance criteria for both Kerschbaum and Oeillal and provides lower performance criteria on the Baget catchment. In comparison, the coupled LuKARS/KarstMod model provides higher performance criteria values although it appears to be quite close to the performance criteria with the KarstMod model (Sivelle et al., 2019) where NSE = 0.59, BE = 0.94 and KGE = 0.61 within the same calibration period.

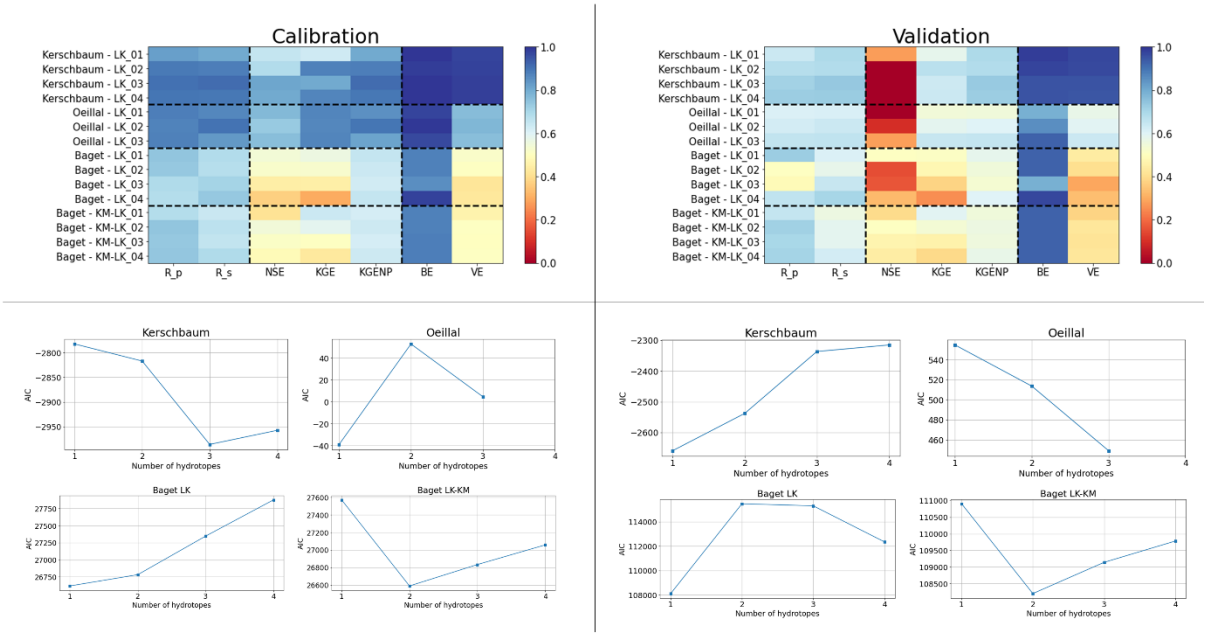

Fig. 4.3 (top) Hydrological models' performance criterion between observed and simulated spring discharge for both the calibration and validation periods. R_p: Pearson correlation coefficient, R_s: Spearman correlation coefficient, NSE: Nash Sutcliff Efficiency, KGE: Kling Gupta Efficiency, KGE_prime: modified KGE, KGENP: Kling Gupta Efficiency Non-Parametric, _c2m: bounded version for NSE, KGE, KGE_prime and KGENP, BE: Balance Error and VE: Volume Error, IOA: Index of Agreement. The performance criteria are color scaled from red for bad values to blue for good value, up to 1 when perfect fit between observed and simulated discharge time series. (bottom) Akaike Informative Criterion (AIC) as a function of number of hydrotopes, and so number of parameters.

The first LuKARS application on the Kerschbaum catchment counts 4 hydrotopes and shows satisfactorily performance criteria (Bittner et al., 2018). Here, the LuKARS model application with a lower number of hydrotopes shows lower performance criteria values but is still quite satisfactorily. Indeed, the LK_01 and LK_04 model structures show tiny close BE and VE values. Conversely, other performance criteria show significant differences when the model structure considers at least two hydrotopes in the upper level. Both LK_03 and LK_04 outperforms with the NSE, KGENP, R_s and R_p and share close performance. Thus, a comparison of the different combinations of hydrotopes may allow assessing the trade-off between model complexity (i.e. number of calibration parameters) and the model performance. Analysis of the simulated spring hydrograph (Fig 4.4) shows that whatever the number of active hydrotopes, the LuKARS model allows capturing the complete spring hydrograph in

a quite satisfactorily way. Moreover, increasing the number of hydrotopes allows to better capture the recession part. Indeed, the LK_01 model structure shows an important misfit during recession periods, with a quite permanent offset (while the recession dynamics appears to well reproduced) and underestimates the flood peaks. LK_02 model structure produces a better fit for the recession periods but overestimates the flood peaks (Fig 4.4). Finally, LK_03 and LK_04 model structures seem to provide a satisfactorily fit during both flood and recession periods of the spring hydrograph. All LK model structures show very good BE and VE errors and both LK_03 and LK_04 model structure outperforms other LK model structures considering most of the performance criteria (Fig. 4.5). The AIC shows a lower value when considering the LK_03 model structure within the calibration period compared with the other LK model structures. Then the model performance increase does not compensate for the introduction of additional parameters for Kerschbaum when moving from LK_03 to LK_04. Nonetheless, a higher number of hydrotopes gives higher performance for both the calibration and validation periods (Fig. 4.3). Considering the NSE criteria one should note a significant decrease in the performance criteria between calibration and validation periods, whereas the other criteria show quite satisfactorily agreement. It may testify significant errors on flood peaks estimation within the validation period while the model correctly reproduces water balance (VE and BE) and correlation (R_p and R_s).

Concerning the Oeillal spring's catchment, the total landcover consists of four types of land use: (i) quarries covering 2% of the total area, (ii) urban areas covering 4.5% of the total area, (iii) vineyards and agricultural plots covering 30.8% of the total area, and (iv) forests and natural plots covering 62.7% of the total area (Fig. 4.1). The first LuKARS application within the Oeillal spring's catchment consists of two hydrotopes that represent an impervious zone (quarries and urban area) and an infiltration zone (Sivelle et al., 2021). Here, the LK_03 model structure is introduced to consider different LCLU in the infiltration zone with a distinction between wine yard and agricultural plots, covering 30.8% of the total recharge area, and forest, covering 62.7 % of the total recharge area. In a general way, the different LK model structures shows close performance considering KGE, BE, VE and R_p whereas LK_02 model structure outperforms considering the KGENP. Thus, the different LK model structures gives satisfactorily results for the different performance criteria, although some minor changes can be observed within the different LK model structures. Elsewhere, the model structures include a threshold effect in the lower compartment with linear discharge law, where all LK_01, LK_02 and LK_03 model structures show quite similar values for both the height of the threshold M_{min} around 2 to 5 mm and the discharge parameter for the upper fluxes out of the compartment *kMS_top* around 0.008 mm.day^{-1}. Conversely, hydrotope 2 and hydrotope 3 within the LK_03 model structure shows contrasted discharge coefficient values for the fast flow going directly to the spring, with *hyd2_khy* around 224 m mm^{-1}.day^{-1} and *hyd3_khy* around 740 m mm^{-1}.day^{-1}. The discharge coefficient for the slow flow going to the lower level of the model structure also shows contrasted values with *hyd2_kis* around 0.29 m mm^{-1}.day^{-1} and *hyd3_is* around 0.04 m mm^{-1}.day^{-1}. It testifies that the LK model, whatever the number of active hydrotopes, allows to capture the slow recession dynamics of the karst system associated with the

Oeillal's spring. Then, considering a different number of hydrotopes only affects the flow dynamics from the upper to the lower level and allow to correctly reproduce the spring hydrographs (Fig. 4.4). The AIC criteria show the lower value for the LK_01 within the calibration period (Fig. 4.3). It may call into question the interest of considering a pseudo-distributed recharge for calibration purpose only. The decrease of the performance criteria within the validation period might be the consequence of the sparse temporal resolution of discharge time series during the validation period (i.e. monthly gauging). Indeed, such discrepancy in performance criteria between periods with continuous monitoring and period with sparse temporal measurement was already experienced in the former study (Sivelle and Jourde, 2020). Nonetheless, the LK_03 model structure shows higher performance criteria within the validation period.

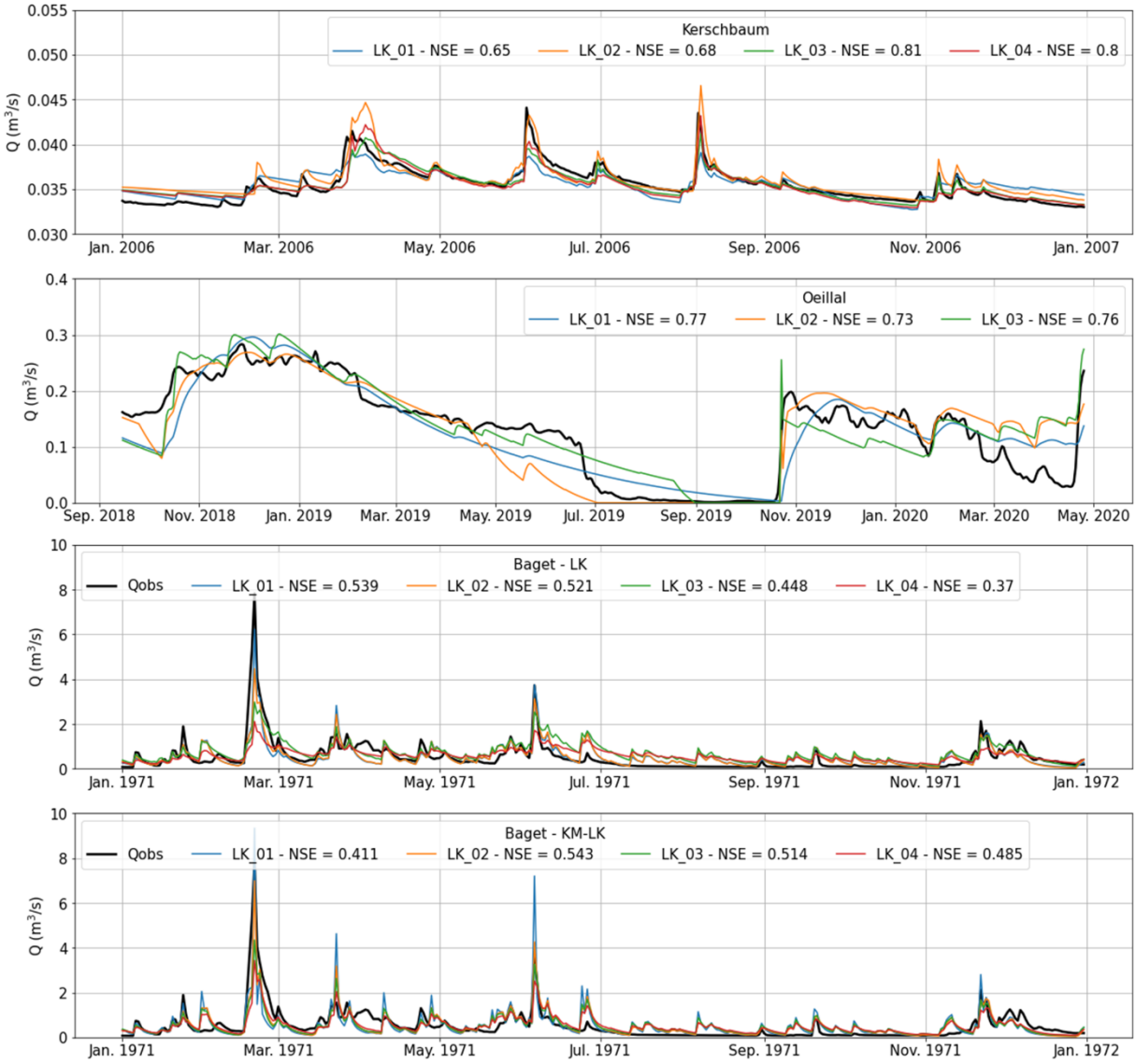

Fig. 4.4 Observed and simulated spring discharge time series within the calibration for the LuKARS model on Kerschbaum, Oeillal and Baget and for the coupled LuKARS/KarstMod model on the Baget. For a better comparison of spring discharge dynamics, only one year of the Baget discharge time series is shown during the calibration periods (10 years). The NSE is estimated for the whole calibration period.

Considering the Baget catchment, Sivelle et al. (2019) proposed a conceptualization of the hydrodynamic behavior based on the KarstMod model (Mazzilli et al., 2019) without any consideration for LCLU and so considers a homogeneous recharge at the catchment scale. To assess the impact of considering a semi-distributed recharge in the model structure, the original compartment E is replaced by the LuKARS model conceptualization with 4 hydrotopes within the upper level of the model structure. The model then corresponds to the coupled LuKARS and KarstMod model (Fig. 4.2), denoted LK-KM. As a comparison, the classical LuKARS model, denoted LK, is also calibrated considering 1 up to 4 hydrotopes. The LK_01 and LK_02 model structures show poor performance criteria regarding the NSE and KGE both lower than 0.5 which is also significantly lower than the performance observed with the original KarstMod model where NSE = 0.59 and KGE = 0.61 (Sivelle et al., 2019). The LK_03 and LK_04 model structures show performance criteria closer to the original KarstMod model although the value for both NSE and KGE is still lower.

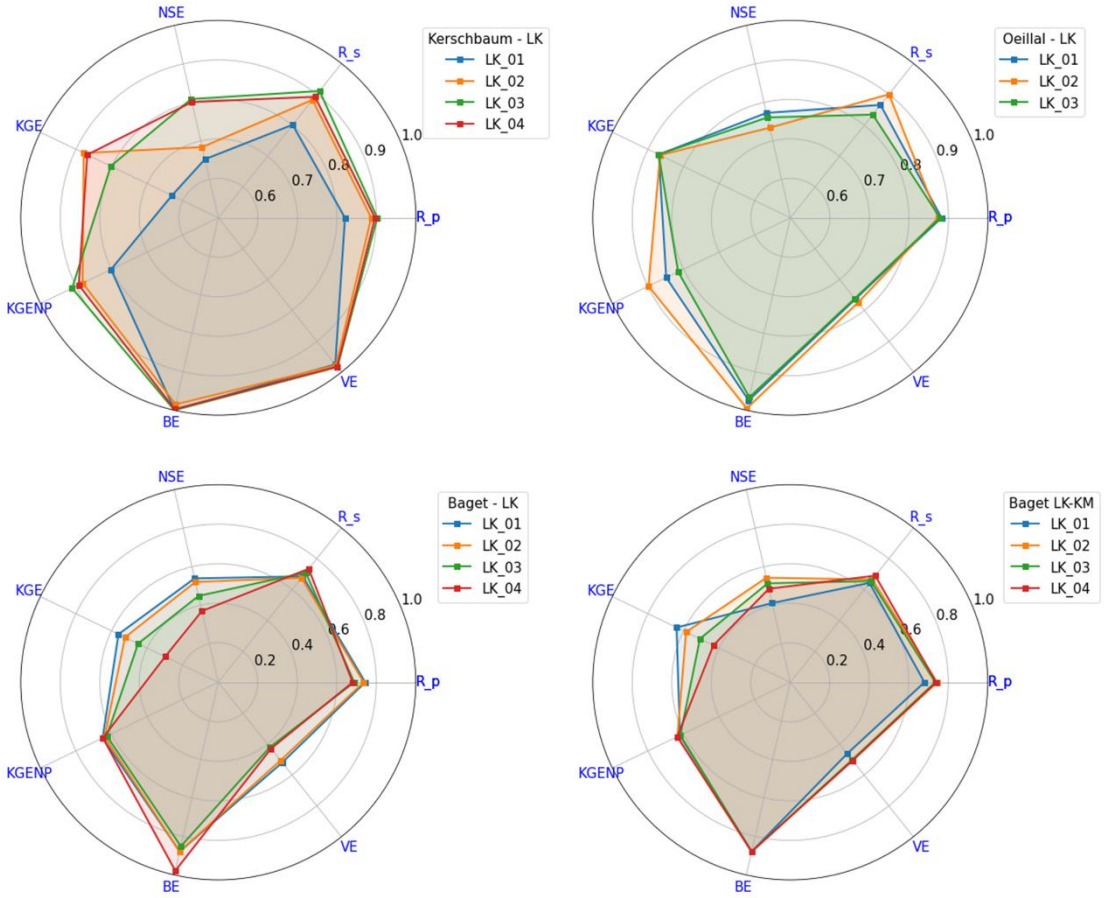

Fig. 4.5 Radar chart of the performance criteria for the calibration period within the Kerschbaum, Oeillal, and Baget catchments. The closer the point is to the outside of the radar chart, the better the model performs.

Analyses of the simulated spring hydrograph together with the observed one (Fig 4.4) show that increasing the number of hydrotopes leads to dramatically underestimating the discharge peaks, whereas all the LK model structures, with 1 up to 4 hydrotopes, provides quite comparable flow dynamics during

recession periods. In a general way, one should note a spring discharge overestimation during significant recession periods such as July to September 1971, with both LK and LK-KM models. Also, the LK-KM model simulates higher discharges during floods, which is following the model structure that includes a compartment with nonlinear discharge law in the lower level of the model structure contrary to the LK model structures that consider one compartment with linear discharge law. Considering the LK_03 model structure, *hyd3_kis* is around 1 mm.day^{-1} whereas concerning LK_04 model structure both *hyd3_kis* and *hyd4_kis* are also around 1 mm.day^{-1}. Then, the introduction of a fourth hydrotopes (when moving from LK_03 to LK_04 model structure) does not allow to differentiate the dynamics for the intra-storage fluxes from the upper level to the lower level. Moreover, *hyd2_kis* is still in the same range of values when moving from LK_03 to LK_04 model structures with a value around 7.6 mm.day^{-1} and 7.2 mm.day^{-1} respectively. It might show that the recharge dynamic from hydrotope 2, corresponding to poor vegetation cover, is well contrasted with the hydrotopes 3 and 4 corresponding to agricultural plots and forests respectively. Conversely, hydrotopes 3 and 4 cannot be separated in terms of recharge dynamics and brings back into question the assumption of hydrophysical uniqueness as well as the need of considering an additional hydrotope in the model structure. Finally, both LK and LK-KM models within the Baget catchment provide contradictory results with the above application within the Kerschbaum and the Oeillal spring catchments. Indeed, a higher number of hydrotopes do not necessarily provide a better model performance criterion (Fig. 4.3 and Fig. 4.5). Also, the AIC criteria confirms such analysis since the lower value concerns the model structure with 1 hydrotope for LK model and with 2 hydrotopes for LK-KM model and so the gain in model performance does not compensate for the penalization due to the introduction of additional parameters. Also, such observations within the calibration periods are consistent with the performance criteria calculated within the validation periods for which the lowest AIC values are obtained for LK with 1 hydrotope and LK-KM with 2 hydrotopes, as observed within the calibration period.

4.4.2 Model evaluation using time series analysis

4.4.2.1 Autocorrelation and crosscorrelation function analysis

The ACF is calculated on both observed and simulated spring discharges within the different model structures for the three karst catchments (Fig. 4.6). The ACF calculated on observed and simulated spring discharges for the Oeillal spring with the LK model structures look very closely. The memory effect appears to be well estimated at around 80 to 90 days. Conversely, the ACF calculated on simulated discharge for Kerschbaum seems to systematically underestimate the memory effect of 40 days. The second peak for a lag value around 65 days appears to be reproduced by the LK models, although the peak appears less frankly with the LK_01 model structure. Concerning the Baget catchment, the LK models generally estimate very poorly the memory effect of 17 days. Indeed, LK_01 and LK_02 model structures provide a lower value around 9 days whereas LK_03 and LK_04 model structures overestimate the memory effect, all the more with the LK_04 model structure that gives a memory effect

of around 45 days. The LK-KM models provide an underestimation of the memory effect although the higher the number of hydrotopes the closer the ACF on simulated discharge to ACF on observed discharge. One should note that such misfit considering the ACF was already investigated within the Baget catchment considering daily rainfall-discharge lumped parameter modeling (Sivelle, 2019) due to a short response time that may require a higher sampling frequency (Labat et al., 2000a).

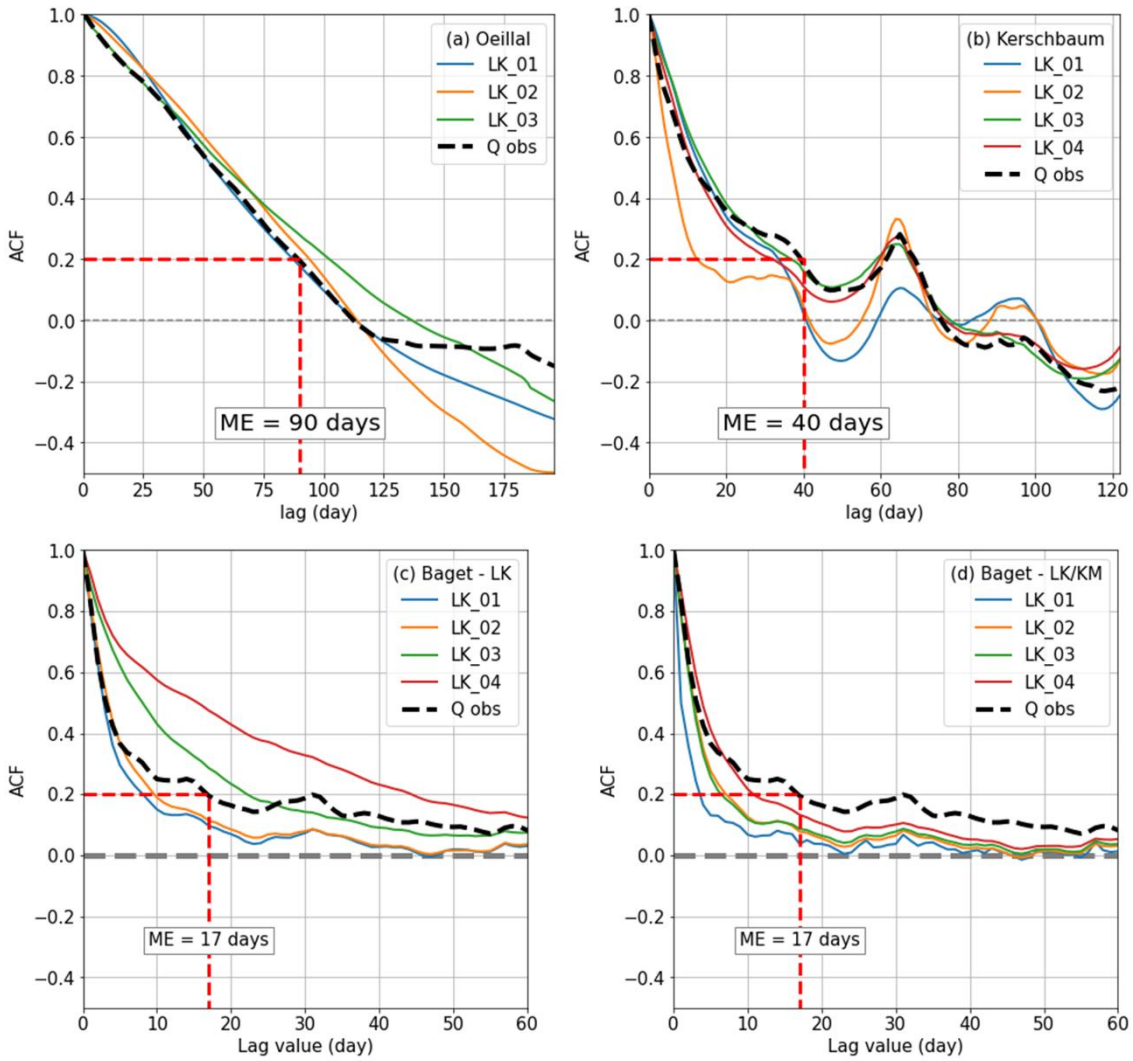

Fig. 4.6 Auto-correlation function (ACF) on spring discharge for each hydrological model during the calibration period. The memory effect ME is calculated based on ACF on the observed spring discharge measured during the calibration period.

In the same way, CCF is calculated between rainfall and both observed and simulated spring discharge within the different model structures for the three karst catchments (Fig 4.7).

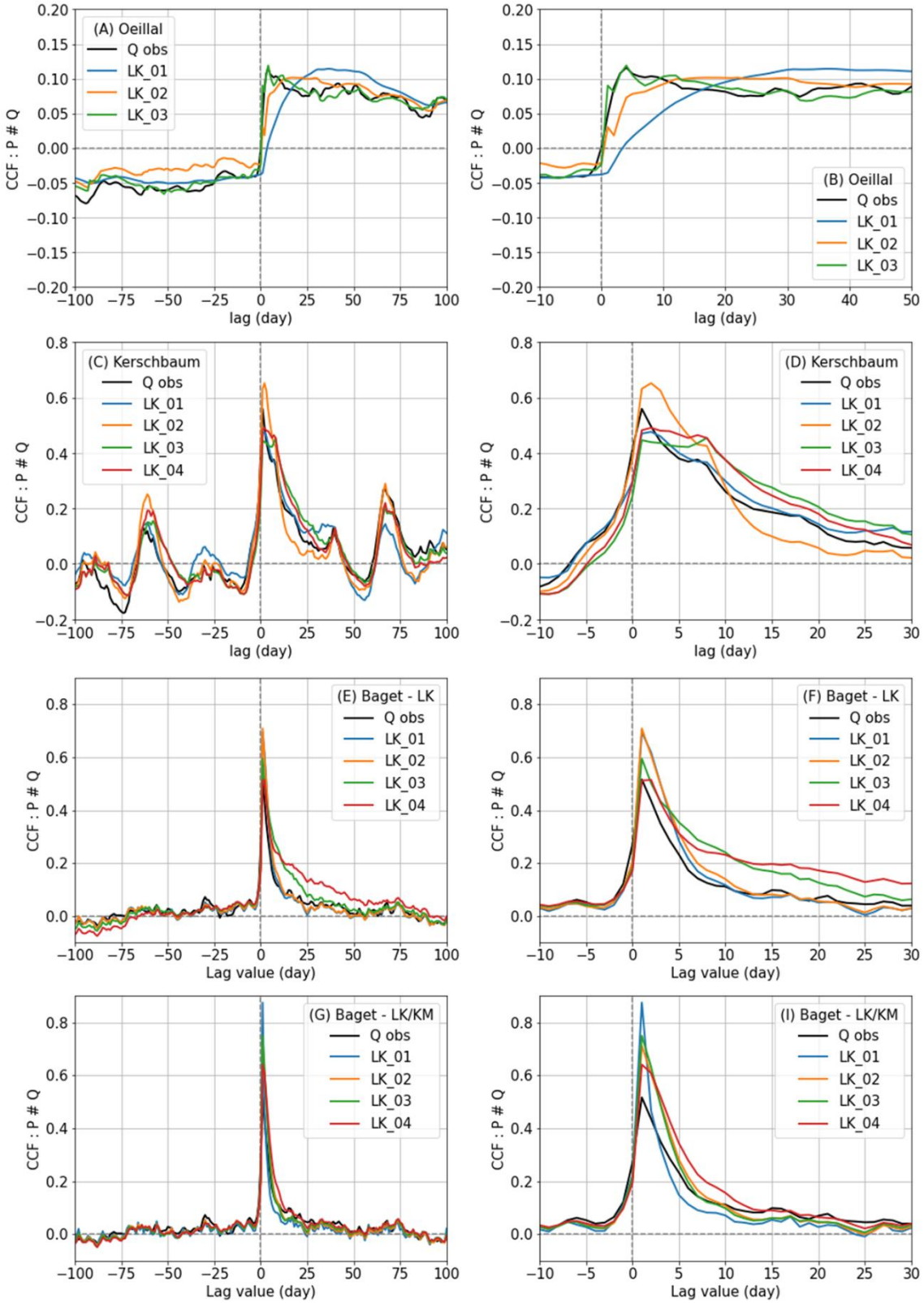

Fig. 4.7 Cross-correlation function (CCF) between rainfall and spring discharge within the calibration period for each hydrological model

Concerning the Oeillal spring, CCF based on observed and simulated discharge appears very close when considering LK_03 model structure. Then, the impulse response of the karst system with a slow

recession dynamic appears well reproduced with both the LK_02 and LK_03 model structures whereas the LK_01 model structure fails to reproduce the quick time of response. Concerning Kerschbaum, the LK_02 model structure seems to overestimate the CCF peak amplitude and to under estimate the persistence of correlation for lag values larger than 10 days. Also, the second peak around 65 days is well reproduced although the LK_01 model structure gives a lower CCF peak amplitude. Such a second peak in the rainfall-discharge CCF can be the consequence of the existence of the slow flow dynamics, which may have a delayed contribution with an important response time. Such observation can be consistent with the lithology of the Kerschbaum catchment dominated by dolostones, and a low value of the discharge coefficient for the compartment with linear law with an order of magnitude of 10^{-4} $m.day^{-1}$. This value is in contrast with values around 10^{-2} $m.day^{-1}$ for both Baget and Oeillal, dominated by limestones. Then the LK models allow capturing both short-term and mid-term responses although the short-term response with LK_04 model structure appears delayed. Within the Baget catchment, both LK and LK-KM models seem to overestimate the CCF peak value although the LK_04 and LK_04-KM model structure show lower peak value of the CCF and so closer to the CCF based on observed data. Such overestimation of the CCF peak was already observed with the KarstMod model (Sivelle, 2019).

4.4.2.2 Orthogonal wavelet decomposition

Application of orthogonal wavelet decomposition on both observed and simulated spring discharges allows to calculate the performance criteria according to a dyadic scale (Fig. 4.8) and to evaluate the model performance across different temporal scales. Here, the performance criteria consist of the bunded version of the NSE criteria (Mathevet et al., 2006), denoted NSE_c2m. It allows to reduce the amplitude of variation between -1 and 1. One should note that, the bounded version of NSE criteria keeps the same meaning with a comparison of the model errors with a "naïve" predictor (i.e. the mean of the observed spring discharge time series) where positive values mean the model is a better predictor and a NSE_c2m value of 1 corresponds to a perfect fit between the model prediction and the observation.

Fig. 4.9 shows the performance criteria (i.e. the bounded version of NSE) as a function of the scale. Concerning the Kerschbaum catchment, both le LK_03 and LK_04 seems to outperforms for the various scales, excepted for the 16 days scale, where all the LK model structures gives lower NSE_c2m values. Considering the periods larger than 32 days the LK_02, LK_03 and LK_04 models shows close performance, larger than the LK_01 model structure. Concerning the Oeillal spring, LK_02 and LK_03 model structures outperform the LK_01 model structure for the scales from 2 days to 128 days whereas as considering the larger periods all LK model structures show quite close performance. Also, all the LK model structures show poor performance criteria for the high frequency (periods lower than 8 days) whereas the low frequencies (period larger than 64 days) give much higher NSE_c2m values. Due to the slow recession dynamics of the Oeillal spring system, and the important contribution of the lower compartments in the spring discharge, it is difficult to well capture the fast flow dynamics. This is also observed with the rainfall-discharge CCF that shows a low peak value and testify of an important

smoothing effect operated by the karst system. Such results may testify to the importance of considering several flow dynamics from the non-saturated zone to the capacitive function of the aquifer. Then, since most of the effective rainfall flows toward the lower level of the model structure (Fig. 4.2) a suitable characterization of the recharge toward the capacitive function of the aquifer may constitute an important step for the assessment of groundwater resource variability.

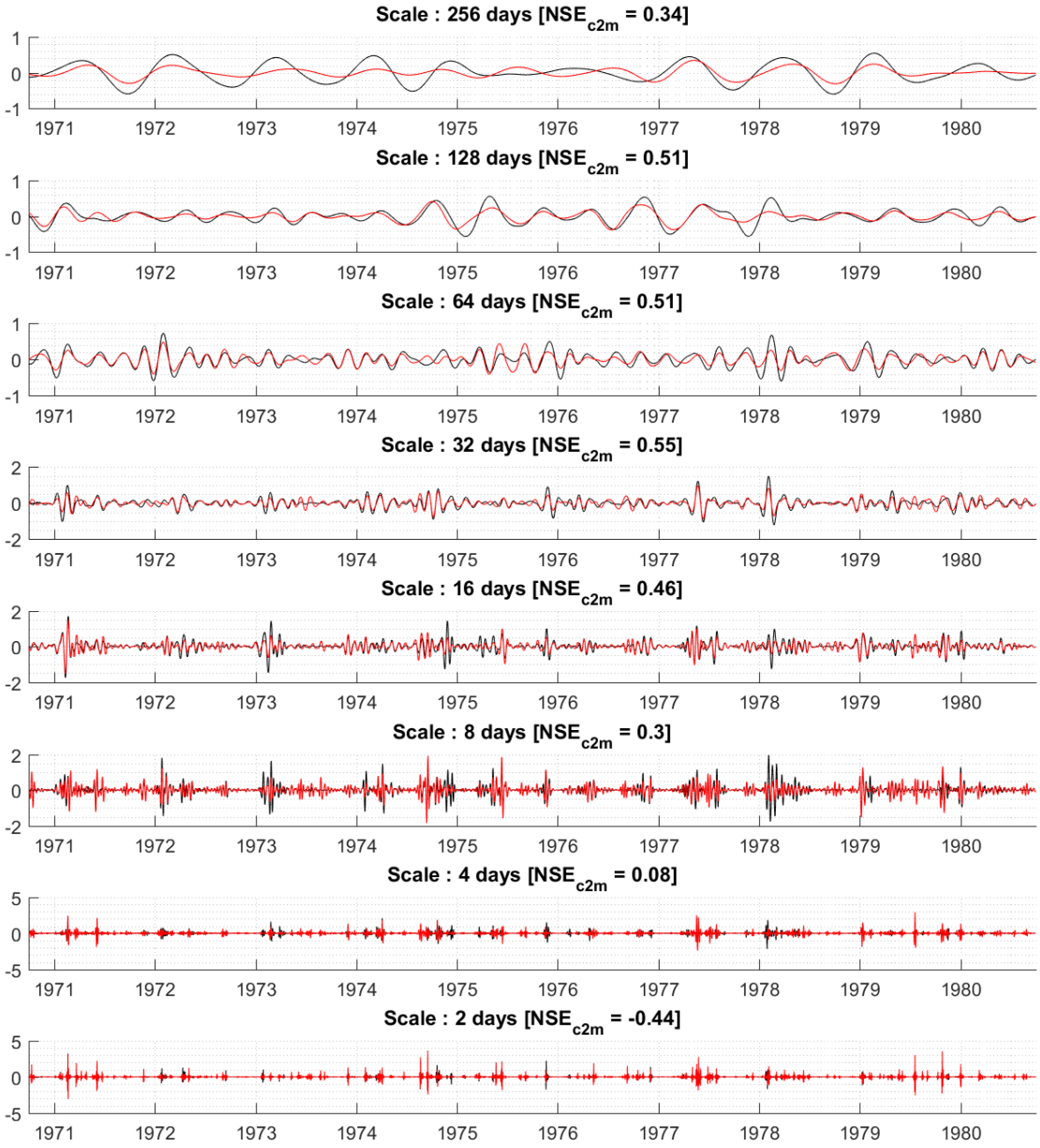

Fig. 4.8 Orthogonal wavelet decomposition of measured (black) and simulated (red) spring discharge over the calibration period for the Baget catchment with the coupled LK_01/KM model.

Concerning the Baget system, all the LK model structures present close performance criteria for the temporal scale above 128 days whereas the performance for the smaller scale can show a significant difference. This may indicate that for a reactive karst system such as Baget, the high-frequency processes can be better reproduced by considering homogeneous recharge at the catchment scale. Indeed,

increasing the number of hydrotopes seems to degrade the performance criteria for periods lower than 100 days. This is observed when the lower level is supposed to be a compartment with linear discharge law, and so the saturated zone consists of a unique flow dynamic. Over the Baget area, former studies have shown the existence of a well-developed drainage system (Mangin, 1975; Marsaud, 1996), with efficient quick flow evidenced by artificial tracer tests (Labat and Mangin, 2015; Sivelle and Labat, 2019) and highlighted the interest of considering two flow dynamics with exchange flow (Sivelle et al., 2019). Then, considering a lower level of the model structure with a more complex structure highlight that whatever the number of hydrotopes the model performance is comparable, scale by scale. In the end, increasing the number of hydrotopes does not bring better performance either in the high frequency or the low frequencies.

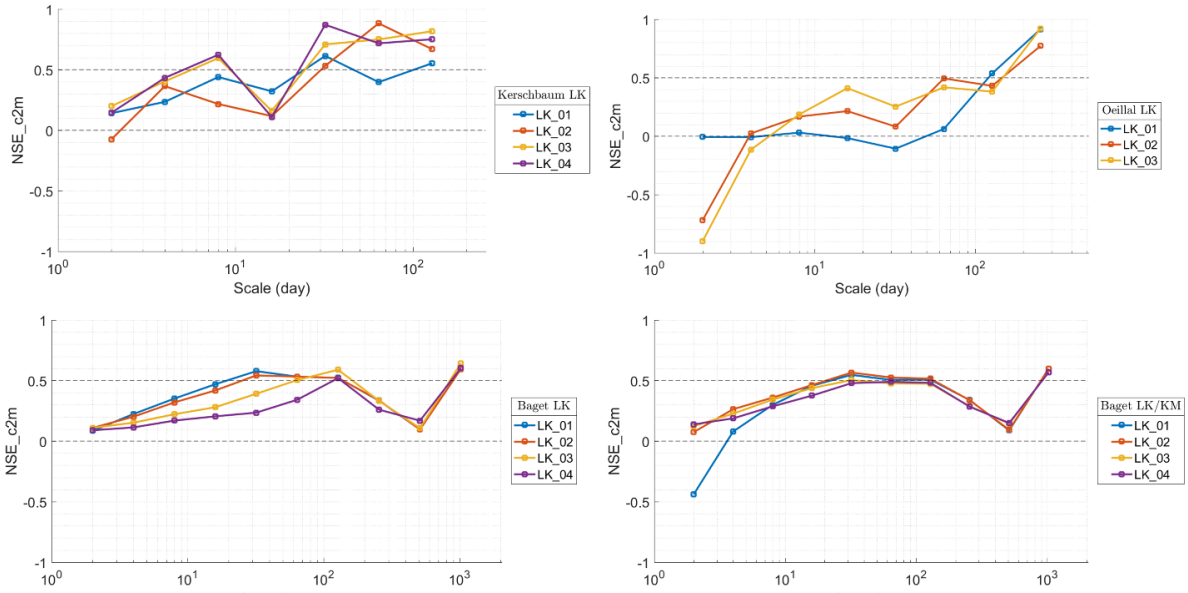

Fig. 4.9 Decomposition of the performance criteria on the calibration period.

4.4.3 Effect of hydrotopes on hydrodynamics

To quantify the impact of considering a different number of hydrotopes on the flow dynamics, the monthly mean intra-storage flow Qis (discharge from the hydrotopes in the upper level to the lower level of the model structure, considered as a proxy of the recharge) is calculated within the month of the year (Fig. 4.10). It gives an overview of how the recharge may occur along with the hydrologic cycle. Due to the bad performance of the modeling approach within the Baget karst system, the analysis is made only within the Kerschbaum spring and the Oeillal's spring, where considering several hydrotopes helped improving the hydrological model performance. To perform a preliminary assessment of the influence of parametric uncertainties, the estimation of the mean Qis is made on the 0.99 percentile ensemble of simulated hydrographs using the Latin Hypercube Sampling (LHS) procedure implemented in the SAFE toolbox (Pianosi et al., 2015). Then, the simulation with the highest objective function is

reported in solid line, while the confidence interval is given through a colored envelope (Fig. 4.10). The simulated spring hydrograph is given within the calibration period while the recharge is estimated on periods of 10 years, considering the hydrological model can be used out of calibration periods due to acceptable performance within the validation period (Fig. 4.3). The estimation is made on the 2010-2020 periods for Oeillal and 2006-2016 periods for Kerschbaum. Kerschbaum and Oeillal's spring catchments show very different pattern in the proxy of recharge along the hydrological cycle. Indeed, Qis appears quite constant along with the month of the year on Kerschbaum while Qis shows significant temporal variation with period of important recharge during spring and autumn, and low recharge during the summer period. Such discrepancy is a consequence of the exposition to different climate which is warm-moderate regional climate for Kerschbaum against Mediterranean climate for the Oeillal's spring catchment. Within the Oeillal's spring the regime of recharge follow the main Mediterranean precipitation pattern with two rainy seasons, in spring and autumn periods.

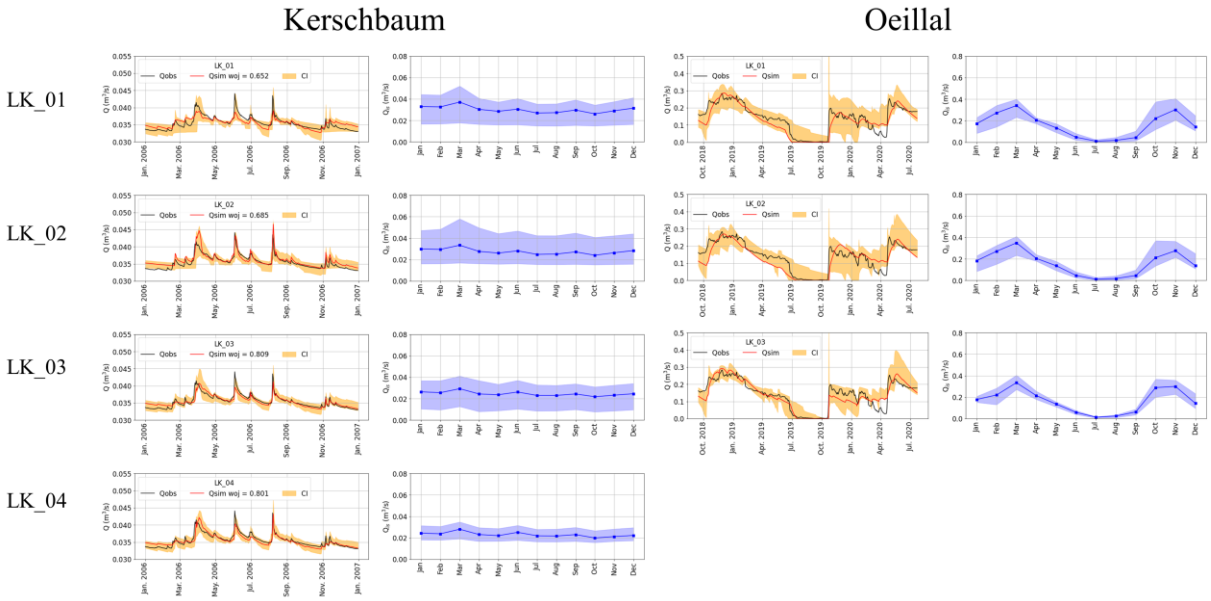

Fig. 4.10 Proxy of the effective recharge in the lower level compartments along with the month in the year. The estimation is made on simulated internal fluxes within periods of 10 years: from 2006 to 2016 for Kerschbaum and from 2010 to 2020 for Oeillal.

The analyses show that for both Kerschbaum and Oeillal's spring catchment the confidence interval on the variation of Qis along with the month of the year appears to reduce when considering a higher number of hydrotope. Such results are consistent with the analysis of the estimated parameters (Table 4.4). Indeed, for both Kerschbaum and Oeillal's spring catchment, the parameter values related to the lower compartment appears well constrained, whatever the number of hydrotopes in the upper part of the model structure. Then, considering infiltration heterogeneities through a semi-distributed model seems to better capture the infiltration processes from the upper level to the lower level compartments on both Kerschbaum and Oeillal's spring karst systems.

4.5 Conclusions

This study investigated how considering LCLU, and thus a semi-distributed recharge impacts the performance of a lumped parameter hydrological model as well as the recharge dynamics in forest dominated karst system. The model performances are compared using numerical performance criteria, time series analysis (i.e. auto-correlation analysis, cross-correlation analysis and wavelet multiresolution analysis) and analysis of the simulated recharge dynamics. Considering a semi-distributed recharge gives better performance for both Kerschbaum and Oeillal catchments hydrological models, while no improvement is obtained for Baget catchment. Kerschbaum and Oeillal karst springs are characterized by slower recession dynamics than the Baget spring. The results within the Baget catchment show that considering a more complex conceptualization of recharge processes does not bring better hydrological model performance. The Baget is characterized by a high degree of karstification, an important spring discharge variability as well as an important role of matrix-conduit exchanges. The heterogeneities in recharge processes are difficult to capture considering a daily lumped parameter hydrological model. A deeper investigation considering a higher frequency base might be needed to better assess the impact of LCLU on recharge processes. Also, considering a semi-distributed recharge seems to reduce the uncertainty in the quantification of the internal fluxes, flowing from the upper level to the lower level of the model structure. The main results of the study consist of a first step in the assessment of the trade-off between hydrological model complexity and hydrological model performance, in a framework of lumped parameter modeling dedicated to karst hydrology. Systematic consideration of LCLU is thus not necessarily worthwhile in karst environments as it can bring contradictory results in terms of hydrological model performance. Further work should investigate both structural and parametric uncertainties related to the inclusion of LCLU in lumped parameter modeling in karst hydrology since LCLU changes mays have strong impact on recharge processes as well as strong implications on groundwater vulnerability.

Chapter 5

Retrieve solute concentrations at high temporal resolution from electrical conductivity measurements in karst systems

Richieri, B., Bittner, D., Hartmann, A., Benettin, P., Van Breukelen, B. M., Labat, D., and Chiogna, G. (2023). Using continuous electrical conductivity measurements to derive major ion concentrations in karst systems. Hydrological Processes, 37(6), e14929. https://doi.org/10.1002/hyp.14929

Abstract

Hydrochemical data of karst springs provide valuable insights into the internal hydrodynamical functioning of karst systems and support model structure identification. However, the collection of high-frequency time series of major solute species is limited by analysis costs. In this study, we develop a method to retrieve the individual solute concentration time series and their uncertainty at high temporal resolution for karst springs by using continuous observations of electrical conductivity (EC) and low-frequency ionic measurements. Due to the large ion content and non-negligible concentrations of aqueous complexes in karst systems, the concentration of each solute species occurring as free ion and as part of aqueous complexes are computed separately. The concentration of species occurring as free ions are computed considering their contributions to the total EC, whereas the concentration of the species as part of complexes are obtained from speciation calculations. The pivotal role of the complexation processes for the reconstruction of ion concentration time series starting from the EC signal is investigated in two karstic catchments with different geologies and temporal resolution of the available hydrochemical datasets, i.e., the Kerschbaum dolostone system in Austria and the Baget limestone system in France. The results show that complexation processes are significant and should be considered for the estimation of the total solute concentration in case of SO_4, Ca, Mg and HCO_3. The EC signal of a karst spring can be used to interpolate and quantify the dynamics of those solutes characterized by large contribution (approximately >6%) to the total EC and low relative variability, i.e., HCO_3, Ca and Mg. Moreover, the presented method can be used to estimate concentrations of solutes when applied to karst systems with stationary and hydrogeochemical homogeneous contributing area. On the contrary, the method is affected by large uncertainty in case of dynamic systems characterized by varying contributions of water from different geological areas. This study aims to contribute to the problem of hydrogeochemical data availability and to support future works on karst systems conceptualization.

Keywords: Electrical conductivity decomposition, High-resolution hydrochemical data, Hydrochemical modeling, Karst

5.1 Introduction

The use of multiple data sources to improve our understanding of the karst hydrological functioning is getting more and more attention. For example, hydrochemical data of karst springs provide valuable insights into the internal hydrodynamical functioning, e.g., to characterize different kinds of karst systems or to differentiate between the contribution from the vadose and the phreatic zones under varying hydrometeorological conditions (Aquilina et al., 2006; Dreiss, 1989; Frank et al., 2019; Hartmann et al., 2013b; Hartmann et al., 2017; Liu et al., 2004; Mudarra and Andreo, 2011; Ravbar et al., 2011; Torresan et al., 2020). Therefore, it is important to collect and analyze hydrogeochemical information in karst systems.

Karst systems are characterized by a complex hydrologic response and discharge variations that may change by one order of magnitude within hours or days (Hartmann et al., 2014). To investigate flow and transport processes in such systems, the hydrochemical sampling frequency should be comparable to the time scale of the hydrological response of the system, that is hours to days. However, high-frequency monitoring is generally restricted to continuous measurements of water level, discharge, temperature, and electrical conductivity (EC), whereas the collection of high-frequency time series of major solute species e.g., Ca, Mg and HCO_3, is limited by high analysis costs (Charlier at al., 2012).

Recently, few studies investigated methods to derive continuous time series of major ions without the need of continuous measurements of these ions. Mewes et al. (2020) tested the ability of different machine learning algorithms to interpolate time series of natural tracer concentrations in karstic environment and to predict SO_4^{2-} and NO_3^- concentrations from discharge data. While the study showed that machine learning algorithms are valuable to fill gaps between point measurements of ionic concentrations, these algorithms cannot predict the tracers' temporal variability (Mewes et al., 2020).

Benettin and van Breukelen (2017) proposed a method to derive the individual ion concentration from the total ion content information embedded in the EC signal measured at a river gauge. The approach is based on the decomposition of the EC into the specific contributions of the major free ions that conduct electrical current in water. EC can be easily and cheaply measured by means of automatic instruments and thus shows a huge potential in model development and evaluation (Cano-Paoli et al., 2019; Chang et al., 2021; Hayashi et al., 2012; Jourde et al., 2018; Meus et al., 2014). Starting from continuous EC data and ionic point measurements, the method of Benettin and Breukelen (2017) makes it possible to estimate ionic concentration time series at the same temporal resolution as the EC signal. The approach was tested on data from the Upper Hafren river catchment in the Plynlimon area, mid-Wales, U.K., characterized by low EC values (average of 29 µS/cm) and by a total ion content dominated by Cl and Na, which have no or little tendency to be involved in complexation processes. The approach proved to give a better representation of the ion dynamics than a direct linear interpolation of the concentration point measurements. Similar approaches were used to first establish regressions between ionic concentrations and laboratory measurements of EC and then to decompose the EC measured at river gauges into the major ion contributions (Lechuga-Crespo e al., 2020).

Differently from the Upper Hafren river catchment, karstic environments can be characterized by large content of solutes that could form complexes and EC values around 500 μS/cm (Chang et al., 2021; Hilberg and Schneider, 2011; Narany et al., 2019). The large ion content and the complex hydrogeochemical interactions between water and the matrix cause the discharge of a karst spring to often show an intricate water speciation. Due to the non-negligible concentrations of aqueous complexes in karst systems, there is the necessity to modify the methodology proposed by Bennettin and van Breukelen (2017) to account for aqueous complexation processes. The aim of the present work is hence to develop a method to retrieve individual solute species concentration time series at high resolution from continuous EC measurements in karst springs, by explicitly accounting for complexation processes. Indeed, some solute species, like SO_4, Ca and HCO_3, have high tendency to form complexes, which thus need to be considered in the reconstruction of the total concentration, despite not having a significant influence on the total EC of the water. Moreover, we investigate the uncertainties related to the quantification of each individual solute species both for interpolation and prediction of high-resolution concentration time series. Since different geological structures and rock types of a system determine the flow regime and aqueous chemistry (Odeh et al., 2009), we consider two karstic watersheds with different types of bedrock and temporal resolution of the available hydrochemical datasets, i.e., the Kerschbaum dolostone system in Austria (quarterly, weekly and 5-hour sampling temporal resolutions) and the Baget limestone system in France (sampling temporal resolution from 1 to 4 hours). Thus, by testing the approach on karst systems characterized by different geology and different sampling frequency, we evaluate the relevance of complexation processes in karst systems characterized by different degrees of complexity.

5.2 Materials and methods

5.2.1 Study areas

We consider two study areas, that is the Kerschbaum dolostone karst system in Austria and the Baget limestone karst system in France (Fig. 5.1a). The different geological formations characterizing the two spring watersheds (Fig. 5.1b, c) result in different degree of karstification, discharge variability and solute transport processes.

The Kerschbaum spring is located 10 km south of the city of Waidhofen a.d. Ybbs, Austria (Fig. 5.1a, b). The pre-alpine springshed covers approximately 2.5 km^2 and is part of the eastern foothills of the Northern Calcareous Alps, showing a homogeneous dolomitic geology. The Kerschbaum spring aquifer is characterized by a complex small-scale groundwater karst system with a deep and developed network of fractures and conduits (Hacker 2003; Narany et al., 2019). Despite the dominance of carbonate bedrocks, the study area does not show significant sinkholes. Therefore, we assume that point infiltration and concentrated recharge processes scarcely contribute to the groundwater recharge and, thus, that the spring discharge is controlled by diffusive infiltration. Consequently, the response of the spring

discharge to precipitation events is characterized by a piston and flushing effect of the dissolved elements stored in the saturated zone. The recharge area is primarily covered with forests and is characterized by a mean annual temperature of 8°C and mean annual precipitation of 1379 mm (period from 1981 to 2014). The annual rainfall distribution is bimodal with a peak in the summer (June and July) and a peak in the winter (December and January) (Bittner et al., 2018). The Kerschbaum spring is an important source of fresh water providing a mean discharge of 34 l/s to the regional water supply and shows a fast reaction time to precipitation events of one day (Bittner et al., 2021).

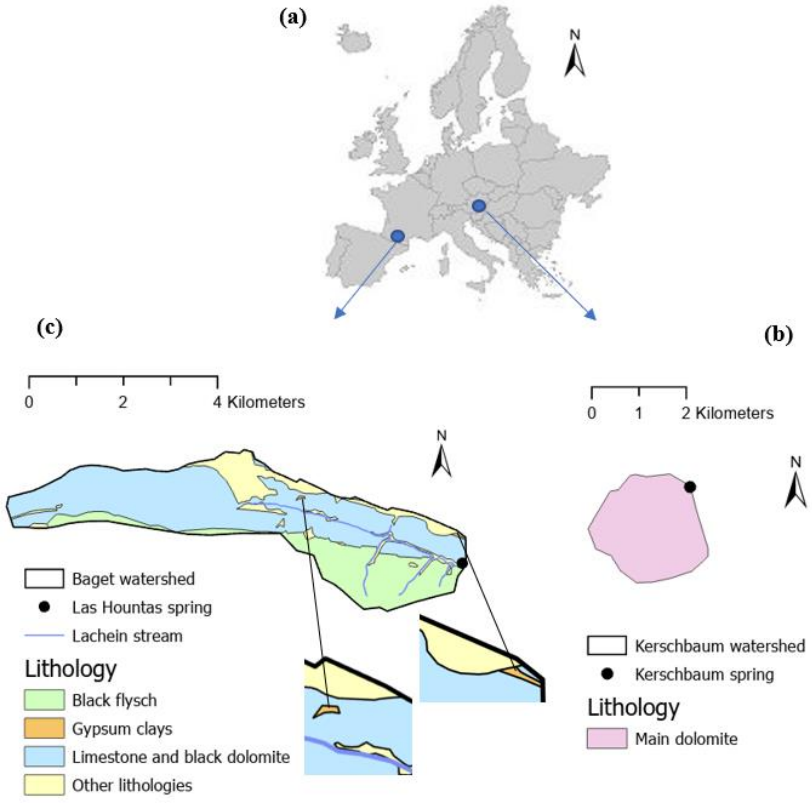

Fig. 5.1 Lithological maps of the study areas showing the location of the springs and recharge areas. **a** The locations of the study areas in Europe. **b** Kerschbaum dolostone karst system in Austria. **c** Baget limestone karst system in France.

The Baget karst system (13 km^2) is located in the Pyrenees, in the Ariege administrative department (Fig. 5.1a, c). The main perennial spring of the Baget catchment, called Las Hountas, is mainly recharged by the calcareous formation of the Jurassic and Lower Cretaceous, with a mineralogical composition dominated by calcite. Despite the large occurrence of limestone bedrocks, the catchment is also characterized by an outcrop impermeable formation of black flysch, which strongly influences the hydrochemical composition of the spring discharge due to pyrite oxidation and consequent formation of strong acids, that is sulfuric acid. Minor gypsum and dolomitic rocks are also observed in the watershed. The different geologies present in the area affect the temporal variability of the spring discharge displaying a complex response characterized by different mechanisms, i.e., dilution processes during

high discharge periods, piston and flushing effects after long dry periods and varying contributions of water draining different areas of the watershed (Ulloa-Cedamanos et al., 2020). The water from calcareous formations feeds the subsurface karst system through seepage or water losses of the Lachein stream, which is usually dry and gets activated only at high flow conditions. Las Hountas is the only perennial spring of the Baget catchment and it is representative of a part of the total response of the karstic watershed. Indeed, during high flood events, when the upper part of the catchment is active, there is water bypassing the spring (Mangin 1975; Ulloa-Cedamanos et al., 2021). The Baget catchment is mainly covered by fir-beech forest and is under the influence of the Atlantic oceanic climate with an annual air temperature of 12.3 °C and an average annual rainfall close to 1700 mm. The annual rainfall distribution is bimodal with a first peak in December and a second one in February. The average annual discharge is 477 l/s with no influence of snow melt processes (Ulloa-Cedamanos et al., 2020).

5.2.2 Datasets

Tables 5.1 and 5.2 show the temporal resolution, number of samples and the statistics of the measured EC (µS/cm) and major solute species of interest, i.e., Ca, Mg, HCO_3, SO_4, NO_3, Cl, Na and K (mg/L), for both the studied areas and available data periods.

Table 5.1 Summary of the datasets characteristics, including: temporal resolution (TR), number of samples (n), mean, standard deviation (Sd), minimum (Min) and maximum (Max) values of the electrical conductivity EC (µS/cm) and major solute species (mg/L) measured at the Kerschbaum spring for the periods 2000–2016, 2018–2019, and 23 January 2022–28 January 2022.

	EC (µS/cm)	Ca (mg/L)	Mg (mg/L)	HCO_3 (mg/L)	SO_4 (mg/L)	NO_3 (mg/L)	Cl (mg/L)	Na (mg/L)	K (mg/L)
Kerschbaum spring 2000–2016									
TR	Quarterly	Quarterly	Quarterly	Quarterly	Quarterly	Quarterly	Quarterly	Quarterly	Quarterly
n	64	62	62	62	62	62	62	62	62
Mean	474.4	58.8	26.6	294.8	8.2	5.4	6.3	3.5	0.7
SD	20.9	3.5	1.2	10.9	1.3	0.4	3.2	1.1	0.1
Min	430	49	24.7	230.7	5.8	4	3	1.9	0
Max	550	74	31	322	11	6.6	23.3	9.5	0.9
Kerschbaum spring 2018–2019									
TR	Hourly	Weekly	Weekly	Weekly	Weekly	Weekly	Weekly	Weekly	Weekly
n	8423	41	41	41	41	41	41	41	41
Mean	481	60.1	26.3	297.9	6.1	5.5	5.9	3.6	0.1
SD	11.9	1.8	0.7	3.5	0.7	0.3	1.4	0.7	0.3
Min	468	56.3	24.9	292.3	5.1	4.8	4.6	2.8	0
Max	565	64.9	27.6	307.1	7.6	6	11.7	5.8	1.1
Kerschbaum spring 23/1/2022–28/1/2022									
TR	Quarte- hour	5-h	5-h	5-h	5-h	5-h	5-h	5-h	5-h
n	461	24	24	24	24	24	24	24	24
Mean	506.8	67.9	28.2	319.3	8.4	7	9.6	4.7	1.1
SD	1.9	1.4	0.7	2.9	0.03	0.1	0.5	0.1	0.1
Min	503.4	65.2	27	317.3	8.3	6.8	8.6	4.3	0.9
Max	509.6	70.5	29.5	323.4	8.4	7.2	10	4.9	1.3

Table 5.2 Summary of the datasets characteristics, including: temporal resolution (TR), number of samples (n), mean, standard deviation (Sd), minimum (Min) and maximum (Max) values of the electrical conductivity EC (µS/cm) and major solute species (mg/L) measured at the Las Hountas spring for the events 4/10/2021–14/10/2021, 1/11/2021–7/11/2021, and 20/11/2022–26/11/2022.

	EC (µS/cm)	Ca (mg/L)	Mg (mg/L)	HCO_3 (mg/L)	SO_4 (mg/L)	NO_3 (mg/L)	Cl (mg/L)	Na (mg/L)	K (mg/L)
Las Hountas spring 4/10/2021–14/10/2021									
TR	quarte hour	event based	event based	event based	event based	event based	event based	event based	event based
n	1005	65	65	65	65	65	65	65	65
Mean	340.6	60.2	5.6	192.4	16.5	3.3	1.4	1	0.4
SD	15	2.5	0.3	5.6	6.3	0.1	0.1	0.06	0.1
Min	316	54.1	5.1	182.4	10.9	3.1	1.3	0.9	0.3
Max	401.3	67.9	6.7	201.4	42.5	3.8	1.9	1.3	0.9
Las Hountas spring 1/11/2021–7/11/2021									
TR	quarte hour	event based	event based	event based	event based	event based	event based	event based	event based
n	633	77	77	77	77	77	77	77	77
Mean	355.9	70	5.4	210.4	22.1	3.8	2.3	1.1	1.3
SD	16.4	3.8	0.2	6.4	5.5	0.2	0.2	0.1	0.4
Min	328	63.6	5.1	189.2	15	3.6	2.2	1	0.5
Max	410	77	6.1	219.7	42	4.2	2.4	1.3	1.9
Las Hountas spring 20/11/2022–26/11/2022									
TR	quarte hour	event based	event based	event based	event based	event based	event based	event based	event based
n	619	103	103	103	103	103	103	103	103
Mean	352.2	62.2	5.5	198.4	21.2	5.1	1.8	1.1	0.5
SD	15.1	3.1	0.5	9.1	11	1.7	0.3	0.1	0.1
Min	319.	55.7	4.4	185.6	6.8	2.4	1.4	0.9	0.3
Max	418.7	70.8	7.1	230.5	50.8	8.9	2.7	1.5	1

The EC was measured in the field at the Kerschbaum spring using a conductivity meter (HT Hydrotechnik, Typ 575-LTC) and reported at 25 °C. During data preprocessing, the EC signal in 2018–2019 was corrected to compensate for an offset of the probe of 19 µS/cm. The solute concentration measurements were provided by the waterworks of Waidhofen a.d. Ybbs for the periods 2000–2016 and 2018–2019 at different temporal resolutions. During the event from 23/1/2022 to 28/1/2022, water samples were collected every 5 h by means of a 6712 ISCO sampler.

The EC at the perennial spring Las Hountas was measured continuously with a temporal resolution of 15 minutes using an In-Situ Aqua TROLL 200 device. To collect water samples for ionic measurements, a 6712 ISCO sampler was installed at the spring and connected to the EC probe. To enable an efficient sampling at the spring during storm conditions, the sampler was programmed to automatically start sampling above a given water level threshold (30 cm). In total, three precipitation events were gauged, the first from 4 October 2021 to 14 October 2021, the second from 1 November 2021 to 7 November 2021 and the third from 20 November 2022 to 26 November 2022. For all the events, the temporal resolution of the sampling was 1 h during the rising limb of the hydrograph, while it was set to 2 h during the recession phase. To record the baseflow following the end of each precipitation event, we collected composite samples, integrating 8 h samples each. All the collected samples were analyzed in terms of major solute concentrations. The specifications of the laboratory analysis for the datasets of

Kerschbaum and Las Hountas are reported in supplementary materials B.1.1 and B.1.2, respectively. During the preprocessing of the data of both the study areas, the charge balance of each sample was checked using the software PHREEQC (Parkhurst and Appelo, 2013) and the samples with an error larger than +/- 5% are considered too uncertain and eliminated from the datasets.

5.2.3 EC decomposition method

Our methodology aims to retrieve individual solute species concentrations at high temporal resolution for the specific case of karst springs starting from the work of Benettin and van Breukelen (2017), which we modify to consider complexation processes in the karstic environments of the springs. The observed EC signal is decomposed into the major solute species concentrations at the same temporal resolution as the available EC data, based on the results of ionic measurements of water samples collected at lower temporal resolution than EC. Due to sample preparation procedures, the total concentration of a solute species measured in the laboratory consists of the sum of that species as free ion and as part of aqueous complexes. The concentrations of each species occurring as free ions and as complexes are first computed separately, then summed together and compared to the total solute species concentrations obtained with laboratory analyses. The concentrations of the species present as free ions are computed based on the contributions of each ion to the total measured EC, whereas the concentrations of the species involved in complexes are derived with speciation calculations. The workflow is as follows:

1. Estimation of the contribution of each free ion to the total EC: The EC is a measure of the water´s capability to pass an electrical flow through the movement of charged ions and results from the total amount of dissolved solid (Massei et al., 2007). Consequently, the total EC (µS/cm) of water can be expressed as the sum of the contributions of each individual ionic species i (Eq. 5.1).

$$EC = \sum_i EC_i \qquad (5.1)$$

The contribution of the species i to the total electrical conductivity (EC_i) is computed from Eq. B.2–B.5 presented in the supplementary material B.1.3. As suggested by Benettin and van Breukelen (2017), the chemical properties of each ion i can be grouped in a single coefficient a_i ((µS/cm) /(mg/L)) as:

$$a_i = \frac{\Lambda_m^{\circ} * \gamma_{EC}}{M} \qquad (5.2)$$

with $\Lambda_{\mathrm{m}}^{\circ}$ the molar conductivity (µS m^2/mol), γ_{EC} the electrochemical activity coefficient (-) and M the solute molar mass (g/mol) of the individual ion.

Eq. B.1–B.6, which are reported in supplementary material B.1.3, can be implemented on PHREEQC to derive the EC_i of the free ions Ca^{2+}, Mg^{2+}, HCO_3^-, SO_4^{2-}, NO_3^-, Cl^-, Na^+ and K^+. The PHREEQC file containing the implemented equations to compute the EC_i and a_i of each ion is reported in the supplementary material B.1.4. In addition, for a more detailed explanation of the procedure, one can refer to the PHREEQC manual (Parkhurst and Appelo, 2013).

Following the approach of Benettin and van Breukelen (2017), for each free ion i is possible to define a "weight factor" $f_{i\,(-)}$ that describes how much the free ion contributes to the total EC based on its chemical properties and concentration:

$$f_i(t) = \frac{EC_i(t)}{EC(t)} = \frac{a_i(t) * C_i(t)}{EC(t)} \tag{5.3}$$

The weights f_i can only be measured at times t, when the ion concentration $C_i(\mathrm{t})$ is available.

2. Linear interpolation of the weights f_i to obtain high-resolution major free ion time series: The low-frequency weight factors f_i (Eq. 5.3)) are linearly interpolated to the same high-resolution time scale of the observed EC. Then, the high-frequency concentrations C_i time series of the individual solute species as free ions are computed with the inverse of Eq. 5.3.

$$C_i(t) = \frac{EC(t) * f_i(t)}{a_i(t)} \tag{5.4}$$

3. Computation of high-resolution time series of species involved in aqueous complexes: The concentrations of the species involved in complexes cannot be derived by applying the same method used for the species as free ions. Some complexes, such as $NaSO_4^-$ and $CaHSO_4^+$, involve more than one of the species of interest, that is Ca, Mg, HCO_3, SO_4, NO_3, Cl and Na. Thus, it is not possible to directly correlate the contribution of a complex to the total observed EC and the concentrations of the individual species. In addition, even if this correlation was possible, the low contribution of the complexes to the total measured EC would result in large errors in the computed concentrations. Indeed, Benettin and van Breukelen (2017) found out that species with small contribution to the total EC are prone to high relative errors on the estimation of the weight factors f_i and thus more difficult to isolate in the EC decomposition. Instead, the concentration of each individual species, which would form complexes under the given conditions, is derived at the resolution of the collected water samples by speciation calculations with PHREEQC as difference between the total molality of a species (mol/kgw) and the molality of the solution (mol/kgw). The PHREEQC file containing the implemented equations is reported in the supplementary material B.1.3. The derived low-resolution

concentrations of each complex are then linearly interpolated at the temporal resolution of the measured EC.

4. Finally, the total concentration time series at high resolution of each major solute species of interest, that is Ca, Mg, HCO_3, SO_4, NO_3, Cl, Na and K, is computed as the sum of the concentrations of that species as free ion and as involved in complexes.

5.2.4 Uncertainty quantification

In the present study, we investigate both the uncertainty on the individual solute concentrations resulting from the experimental error on f_i, and the uncertainty derived by considering f_i as random variables (Subsection 5.2.4.1). Moreover, we propose to use the described methodology not only to interpolate between the coarse samples, but also to reconstruct the ion content for periods in which only the EC data are available (Subsection 5.2.4.2). The presented analyses are done for both the Kerschbaum and Las Hountas. However, since for the Kerschbaum spring no ionic measurements were available at peak spring discharge conditions in January 2019, the results of the uncertainty quantification for Kerschbaum are reported in the supplementary material.

5.2.4.1 Uncertainty quantification of the weight factors f_i

Each value of $f_i\ (t)$ is affected by uncertainty that propagates from the $\mathrm{EC}(t)$ measurement error and from the error in the ion concentration obtained at the coarse temporal scale as shown in Eq. 5.3. We can then quantify the uncertainty $\delta f_i(t)$ on the weight factor $f_i\ (t)$, assuming that the uncertainty affecting $a_i(t)$ is negligible, according to (Fornasini 2008):

$$\delta f_i(t) \simeq \sqrt{\left[\left(\frac{\delta f_i(t)}{\delta C_i(t)}\right)_0^2 * \left(\delta C_i(t)\right)^2 + \left(\frac{\delta f_i(t)}{\delta \mathrm{EC}(t)}\right)_0^2 * \left(\delta \mathrm{EC}(t)\right)^2\right] * a_i(t)^2} \tag{5.5}$$

which results in:

$$\left(\delta f_i(t)\right)^2 \simeq \left[\left(\frac{\delta f_i(t)}{\delta C_i(t)}\right)_0^2 * \left(\delta C_i(t)\right)^2 + \left(\frac{\delta f_i(t)}{\delta \mathrm{EC}(t)}\right)_0^2 * \left(\delta \mathrm{EC}(t)\right)^2\right] * a_i(t) =$$
$$= \left[\frac{1}{\mathrm{EC}_0(t)^2} * \left(\delta C_i(t)\right)^2 + \frac{C_{i_0}(t)^2}{\mathrm{EC}_0(t)^4} * \left(\delta \mathrm{EC}(t)\right)^2\right] * a_i(t) \tag{5.6}$$

$$\left(\frac{\delta f_i(t)}{f_{i_0}(t)}\right)^2 \simeq \left[\left(\frac{\delta \mathrm{C}(t)}{C_{i_0}(t)}\right)^2 + \left(\frac{\delta \mathrm{EC}(t)}{\mathrm{EC}_0(t)}\right)^2\right] * a_i(t) \tag{5.7}$$

As shown in Eq. 5.7, we can further observe that the relative error in the weight factor f_i is always larger than the relative error in EC and C_i. Table 5.3 shows the values of $\delta\mathrm{EC}$ and δC_i which we consider for

the analysis, their measurement device/analysis and the reference used for the estimated measurement error.

Finally, we derive the experimental uncertainty on individual solute species concentrations by applying the EC decomposition method considering the measured weight factors f_i and their experimental error. In addition, the experimental uncertainty on the individual species concentrations is compared with the concentration's estimates obtained considering the weight factors f_i as random variables.

Table 5.3 Measurement errors used to quantify the uncertainty on the weight factor f_i, together with their value, measurement device/analysis and reference.

Measurement error	Value	Device/analysis	Reference
δEC	0.5% of reading +1 µS/cm	Aqua TROLL 200	In-Situ Inc. (2012)
$\delta C_{Ca^{2+}}$	1.22 mg/L	ICP-OES[a]	Report analysis GET[b]
$\delta C_{Mg^{2+}}$	0.08 mg/L	ICP-OES	Report analysis GET
$\delta C_{HCO_3^-}$	3 mg/L	Titration	Somridhivej and Boyd (2016)
$\delta C_{SO_4^{2-}}$	1.47 mg/L	Ion chromatography	Pfaff (1993)
$\delta C_{NO_3^-}$	0.36 mg/L	Ion chromatography	Pfaff (1993)
δC_{Cl^-}	0.29 mg/L	Ion chromatography	Pfaff (1993)
δC_{Na^+}	0.02 mg/L	ICP-OES	Report analysis GET
δC_{K^+}	0.01 mg/L	ICP-OES	Report analysis GET

[a]Laboratoire Gosciences Environnement Toulouse.
[b]Inductively coupled plasma optical emission spectrometry.

5.2.4.2 Predictive model based on the frequency of occurrence of the weight factors f_i

The ability of the method to determine high-resolution concentration time series of major solute species is investigated by computing the frequency of occurrence of the weight factors and applying them in a predictive manner. For Kerschbaum, the years 2000–2016 are used as period in which we estimate the frequency of occurrence of the weight factors (calibration period), while the year 2018–2019 and the event 23 January 2022–28 January 2022 are

used as validation periods; for Las Hountas, the first event in October 2021 is used as calibration period, the second event in November 2021 and the third event in November 2022 as validation periods. In the calibration step, the weight factors f_i are calculated by considering the solute concentrations and total EC both measured in the calibration period (Eq. B.1– B.6, Eq. 5.3). Then, in the validation step, to predict the concentration of each solute species as free ion (Eq. 5.4), the empirical frequency distribution of the weight factor of each free ion computed for the calibration period is combined with the total EC observed in the validation periods and a_i. The concentration of each species involved in complexes is first computed for the calibration period as described in Subsection 5.2.3 and then for the validation periods by assuming the same proportion between solutes as free ions and involved in complexes as observed in the calibration period. This assumption is done based on speciation calculations with PHREEQC, which show that the percentages of solutes as free ions and as part of complexes are constant, for each karstic spring, over the studied periods (Fig. 5.2a, c). This analysis evaluates the performance of the

method to estimate, based on historical data, high-resolution concentrations time series when only EC observations are available.

Fig. 5.2 Speciation of the spring discharge. **a, c** Solute species occurring as free ions (%) and as involved in aqueous complexes (%) expressed, for each species, as mean percentage of the total solute concentration, together with their percentage contribution to the total electrical conductivity EC, for the Kerschbaum spring (a) and for the Las Hountas spring (c). **b, d** Mean contribution to the total EC (%) of each free ion observed at the Kerschbaum spring (b) and at the Las Hountas spring (d). **e, f** Computed total concentration, computed concentration as free ion and observed concentration of SO_4, for the Kerschbaum spring (e) and for the Las Hountas spring (f).

5.2.5 Investigation of different water contributions

For the case of Las Hountas, we tested different approaches to investigate the water contributions from the different geological areas present in the Baget catchment (Fig. 5.1c).

The dissolution processes and stoichiometric relationships characterizing the calcareous rocks and black flysch are shown in the supplementary material B.1.5 (Fig. B.1). The sulfuric acid, which comes from the black flysch, results in an alkalinity lower than what we would have in case of only carbonate dissolution by carbonic acid. The percentage decrease in alkalinity can be estimated as shown in the following equation:

$$\Delta_{\mathrm{Alk}}(\%) = \frac{(\mathrm{Ca^{2+}} + \mathrm{Mg^{2+}}) - \mathrm{HCO_3^-}}{(\mathrm{Ca^{2+}} + \mathrm{Mg^{2+}})} \tag{5.8}$$

where the ion concentrations are expressed in meq/L (Ulloa-Cedamanos et al., 2020).
The computed alkalinity reduction is then correlated with the equivalent ratio SO_4^{2-} over HCO_3^- and with the performance of the method both when interpolating and predicting solute concentrations at high resolution.
In addition, the variation over time of the relative contributions to the total EC provides insights into the system functioning. More precisely, the correlation between EC, water level and weight factors of HCO_3^- and SO_4^{2-} makes it possible to investigate the water contributions from the calcareous rocks and black flysch under different discharge conditions.

5.3 Results

5.3.1 Speciation and total electrical conductivity calculations on PHREEQC

From the major solute concentrations, speciation calculations with PHREEQC provide the distribution of the aqueous species in each water sample. Fig. 5.2a, c show the average percentages of each solute species as free ion and as involved in aqueous complexes for both the Kerschbaum and Las Hountas springs. The results are consistent between the two studied areas. Among the investigated solutes, SO_4 is the one with the largest tendency to form complexes, with 16.3% (Kerschbaum) and 14.2% (Las Hountas) of its total concentration involved in the formation of $CaHSO_4^+$, $NaSO_4^-$ and HSO_4^-. Also, Ca, Mg and HCO_3 are involved in complexes ($CaOH^+$, $CaHSO_4^+$, $CaHCO_3^+$, $MgHCO_3^+$ and $MgOH^+$) and for Kerschbaum the percentages of Ca, Mg and HCO_3 are 5%, 4.5% and 3%, respectively, whereas for Las Hountas 6.1%, 5.5% and 5.2%, respectively. For both springs, only 0.2% of Na forms $NaSO_4^-$ and $NaCO_3^-$, while NO_3 and Cl are present only as free ions. Finally, K occurs in Kerschbaum only as free ions, whereas in Las Hountas 0.1% of it forms complexes. For the case of SO_4, Fig. 5.2e, f compare the computed free ion and total concentration time series and thus show the pivotal role of complexes when reconstructing the total solute concentration from the total *EC*.
As described in Subsection 5.2.3, the total EC is computed as the sum of the electrical conductivities EC_i of the charged individual solutes (Eq.B.1–B.5 in the supplementary material B.1.3). The individual free ions contribute to the total computed EC differently in the two studied areas (Fig. 5.2b, d), due to

the different geological formations of the watersheds. For the Kerschbaum spring, the contributions of HCO_3^-, Ca^{2+} and Mg^{2+} to the total EC are on average 42.1%, 30.5% and 20.1%, respectively, with about 92.7% of the total EC correlated to the dissolution of dolomite rocks. SO_4^{2-}, $NO3^-$ contributes with a percentage of 1.5% and 1.3%, respectively, and the total contribution of Cl^-, Na^+ and K^+ is approximately 4.1%. On the contrary, for Las Hountas, the dominance of limestone bedrocks leads to a larger contribution of Ca^{2+} (45.5%) and a lower contribution of Mg^{2+} (6.2%), while the contribution of HCO_3^- (39%) is comparable. Moreover, the black flysch formation releases SO_4^{2-}, which contributes with a percentage of 6.3% to the total EC. Finally, the total contribution of NO_3^-, Cl^-, Na^+ and K^+ is equal to 2.8%.

Fig. 5.3a, b and Fig. 5.3e, f present the EC and charge balance errors (%), respectively, computed by PHREEQC at the same temporal resolution as the measured water samples for the Kerschbaum (period 2018–2019) and Las Hountas (event 4 October 2021–14 October 2021) springs. The low frequency computed EC (dashed line) and the continuous observed EC (solid line) are plotted together in Fig. 3a, b. For the case of Kerschbaum, the computed EC does not fully capture the dynamic of the system due to the low temporal resolution. For example, in December 2018 and January 2019 no water samples were collected and hence the manual sampling does not cover the period with the highest EC values. Considering the Las Hountas dataset with a higher temporal resolution of hydrochemical measurements, the computed EC time series better matches the short dynamic of the system.

The relative error time series $\left(\frac{\mathrm{EC_{observed}} - \mathrm{EC_{PHREEQC}}}{\mathrm{EC_{observed}}}\right)$ and relative error probability distributions are shown in Fig. 5.3c, d and Fig. 5.3g, h, respectively. For Kerschbaum, the computed EC slightly underestimates the observations, with a relative error range between -0.01 and 0.05 and relative error mean of 0.02. Las Hountas shows computed EC slightly lower than the observations. The relative error ranges from 0.01 to 0.06 and has a mean value of 0.03. Overall, for both springs, the EC computed through Eq. B.1–B.5 by PHREEQC is satisfactory.

Finally, Fig. 5.3e, f presents the charge error (%) time series computed for each input water sample by means of built-in functions on PHREEQC. For Kerschbaum, the charge error ranges from -1.7% to 3.7% with a mean value of 0.5%, while, for Las Hountas, it ranges between -2.8% and -0.1% with mean value of -1.2%. For both the springs, the charge error indicates an overall respected charge balance.

5.3.2 Frequency of occurrence of the weight factors f_i

Fig. 5.4 shows the violin plots comparing the frequency of occurrence and boxplots of the weight factors f_i of each major free ion observed during the available data periods. Thus, we compared the f_i observed in 2000–2016, 2018–2019 and 23/1/2022–28/1/2022 for Kerschbaum and those observed during the events in October 2021, November 2021 and November 2022 for Las Hountas. Fig. 5.4 shows that, despite referring to two events close in time, the differences between the frequency of occurrence of the weight factors f_i observed in Las Hountas are more pronounced than those observed for Kerschbaum.

For Las Hountas, two events separated by a longer time interval, like the ones in October 2021 and November 2022, can display more similar distributions of the weight factors of some ions than two events closer in time (October 2021 and November 2021).

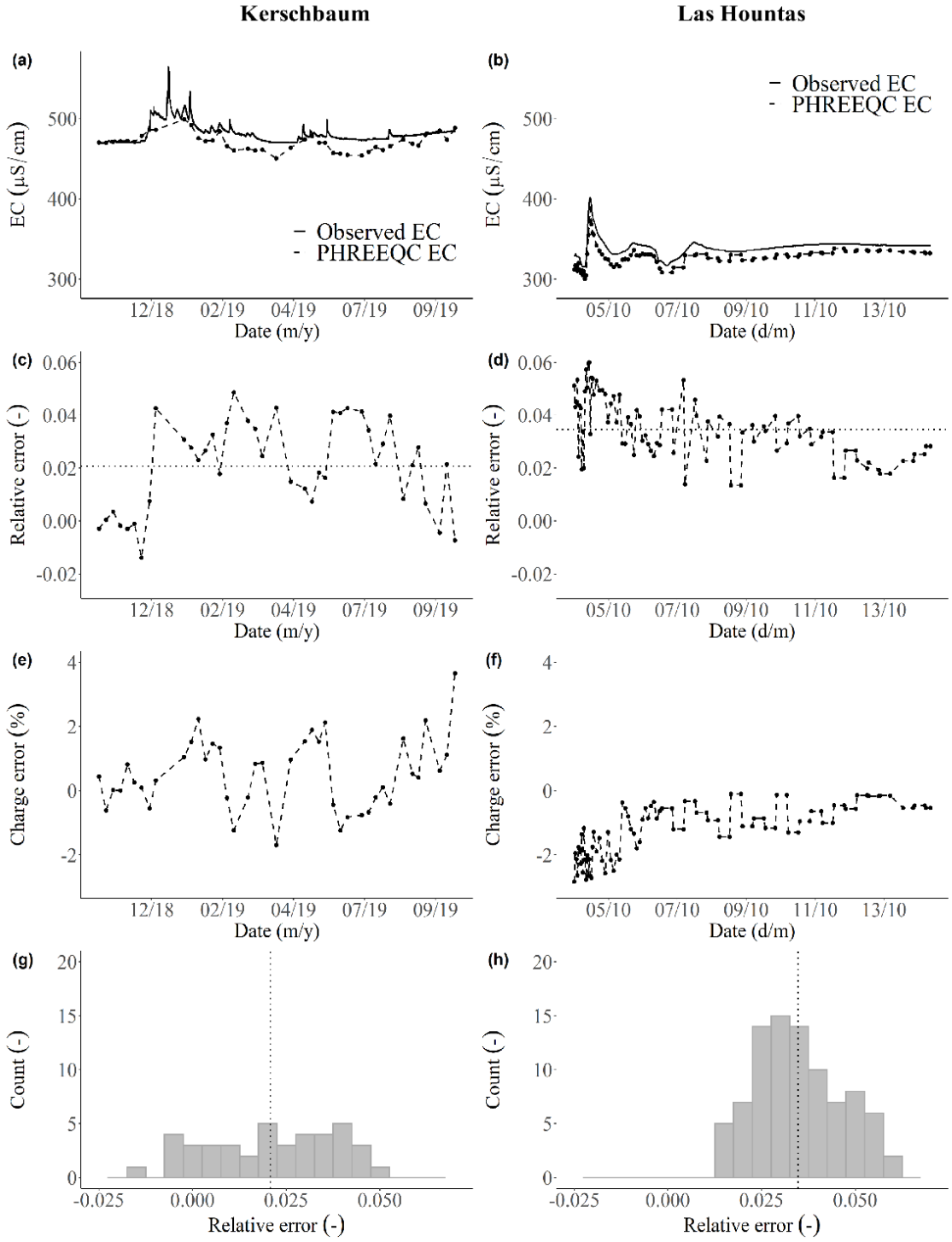

Fig. 5.3 Electrical conductivity EC (µS/cm) computed on PHREEQC at the same temporal resolution of the observed water samples given as input, for the Kerschbaum (period 2018–2019) and Las Hountas (events 4/10/2021–14/10/2021) springs. **a, b** Computed against observed total EC time series, **c, d** EC

relative error (-) time series, **e, f** charge error (%) time series and **g, h** probability distribution of the EC relative error (-).

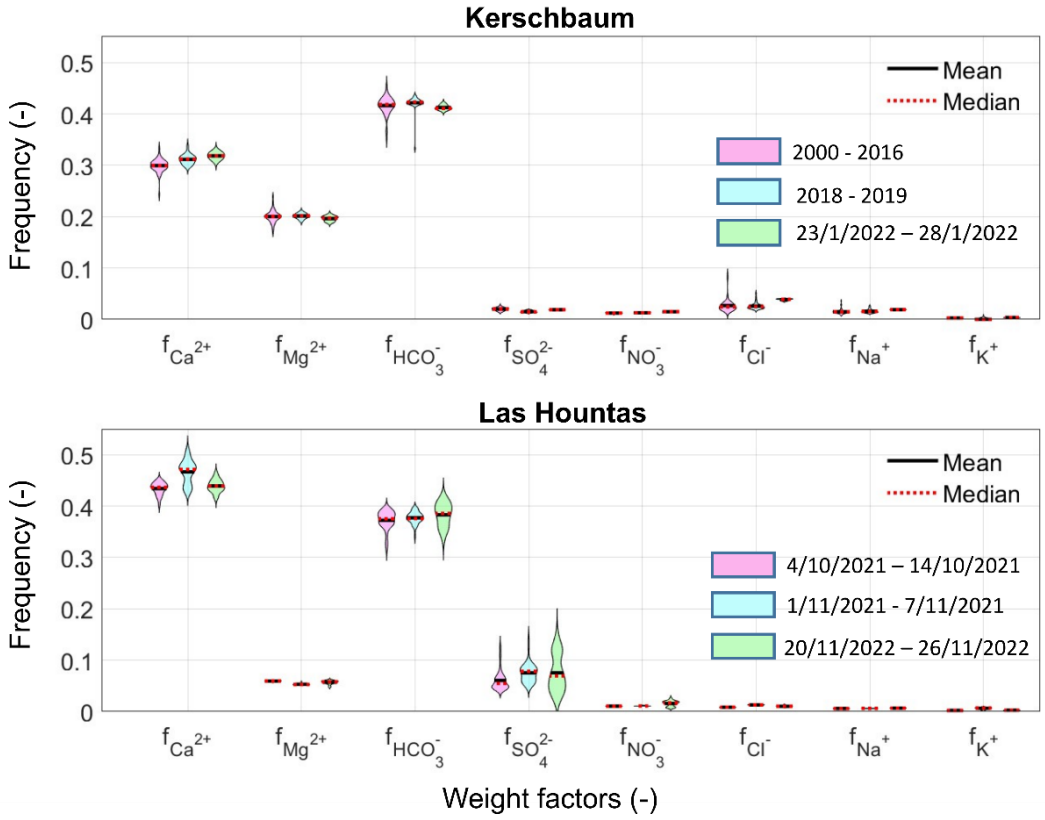

Fig. 5.4 Frequency of occurrence of the weight factors f_i of the individual free ions for both the springs and periods. For the Kerschbaum spring, the distributions refer to the periods 2000–2016 (pink), 2018–2019 (blue) and 23/01/2022 – 28/1/2022 (green); for the Las Hountas spring to the periods 4/10/2021–14/10/2021 (pink), 1/11/2021–7/11/2021(blue) and 20/11/2022 – 26/11/2022 (green).

5.3.3 Uncertainty quantification of the individual solute species concentrations in case of Interpolation

This subsection presents the uncertainty on the individual solute species concentrations resulting from the experimental error on f_i (Eq. 5.7), as well as the uncertainty derived by considering f_i as random variables when we apply the methodology for interpolation. Both the computed uncertainties are shown for each solute species in Fig. 5.5 for Las Hountas (4 October 2021–14 October 2021) together with the low-resolution observed solute concentrations (red points).

The error in the interpolated solute concentrations caused by the experimental error in the estimation of f_i is shown for Las Hountas in Fig. 5.5 and for Kerschbaum in Fig. B.2 (left side) and B.3 (left side) with dashed red lines. We can observe that the larger the concentration of a specific solute species the lower the related experimental error on f_i and consequently on the interpolated C_i. For instance, the concentration of Mg is much larger in Kerschbaum (Table 5.1) than in Las Hountas (Table 5.2) and consequently the error in the interpolated Mg values for Las Hountas (Fig. 5.5) is larger than for

Kerschbaum (Fig. B.2 (left side) and B.3 (left side)). On the contrary, Las Hountas shows a larger concentration of SO_4 and thus a lower experimental error than Kerschbaum.

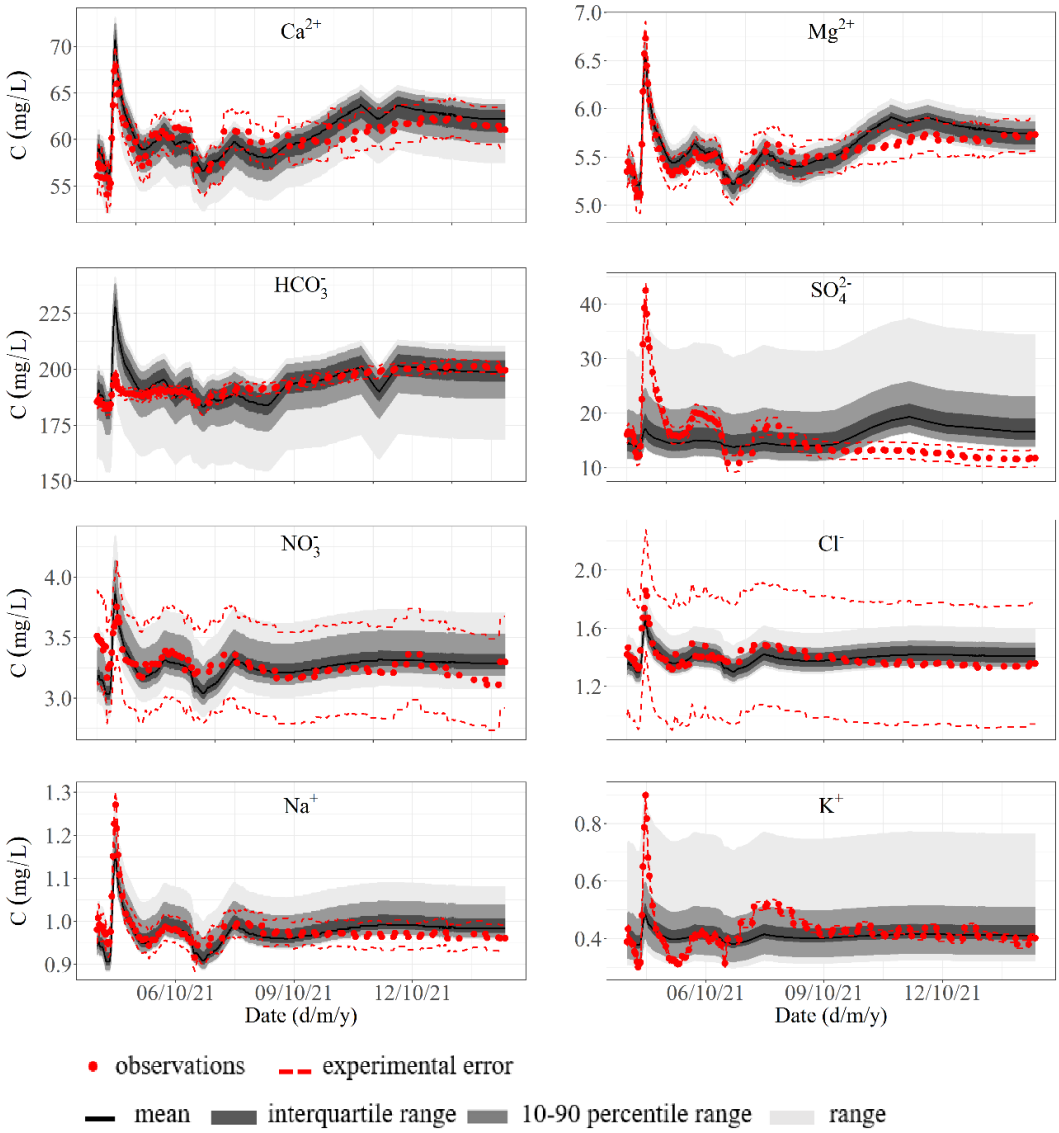

Fig. 5.5 Interpolated experimental uncertainty on the individual solute species concentrations (dashed red lines) together with their interpolated uncertainty based on the frequency of occurrence of the observed weight factors (gray bands). The black, gray and light gray areas of the bands represent the interquartile, the 10–90% percentile and full ranges of the computed solute species concentrations (mg/L), respectively. The red points are the observed solute concentrations (mg/L). The concentrations are computed at the Las Hountas spring for the period 4/10/2021–14/10/2021.

Fig. 5.5 also shows the uncertainty bands computed for Las Hountas considering f_i a random variable whose value is sampled from the frequency of occurrence shown in Fig. 5.4. The measured solute concentrations are indicated with red points and, for each solute species, fall within the full-range uncertainty band. The majority of the observed concentrations are included in the computed interquartile

ranges, with exception of HCO_3 and SO_4. As shown in Table B.1 in the supplementary material B.1.6, there is a positive correlation between the relative variation in measured concentrations and relative width of the uncertainty bands. The method shows low uncertainty in the estimation of Mg and Ca, followed in order by Na, Cl and NO_3. Whereas, the method is less accurate for HCO_3 and SO_4, for which it overestimates and underestimates, respectively, the peak concentrations observed on 4 October 2021 (Fig. 5.5). Finally, the large uncertainty in the estimates for K results from the large relative variation in the measured concentration (Table B.1).

Fig. B.2 (left side) and B.3 (left side) in the supplementary material show the same analyses for Kerschbaum for the period 2018–2019 and 23 January 2022–28 January 2022, respectively. The results show that the method provides a better interpolation of the observations than in Las Hountas. Moreover, the results are in line with what observed for Las Hountas spring, confirming that the method is more uncertain for those solute species contributing less to the total *EC* and with larger relative variability. Due to the lack of samples representing the variability at high flow conditions, the behaviour of the peak in January 2019 has to be interpreted as the probable behaviour considering the available information.

5.3.4 Predictive model based on the frequency of occurrence of the weight factors f_i

For most solute species, the use of f_i as a random variable allows us to reproduce quite well the observations when we apply the method for interpolation. Therefore, we test under which circumstances the method can be applied to predict the ion content for periods in which only the EC data are available. Fig. 5.6 shows the predicted high-resolution concentration time series of major solute species for Las Hountas (1 November 2021–7 November 2021 and 20 November 2022–26 November 2022). The weight factors distribution is taken from the event of October 2021, which we use as calibration event. The accuracy of the prediction is for each solute species correlated with changes in the frequency distribution of the related weight factor f_i. More precisely, the larger the difference between the frequency of occurrence of the weight factor observed in the calibration and validation periods (Fig. 4) the lower the accuracy of the estimations. The performance of the decomposition EC method in predicting solute concentrations is hence significantly different in the two validation periods due to the results described in Section 5.3.2.

The differences between the frequency of occurrence of the weight factors f_i observed for Las Hountas during the events in October and November 2021 are larger than those observed between October 2021 and November 2022 (Fig. 5.4), leading to a less accurate prediction. This is particularly evident for Ca, Mg, Cl and K, whose predicted uncertainty bands for November 2021 show a shift with respect to the observations (Fig. 5.6, left side). On the contrary, being the frequency of occurrence of the weight factors f_i similar between October 2021 and November 2022, the model well predicts the concentrations of Ca and Mg in November 2022 with most of the observations falling in the 10 - 90% percentile range (Fig. 5.6, right side).

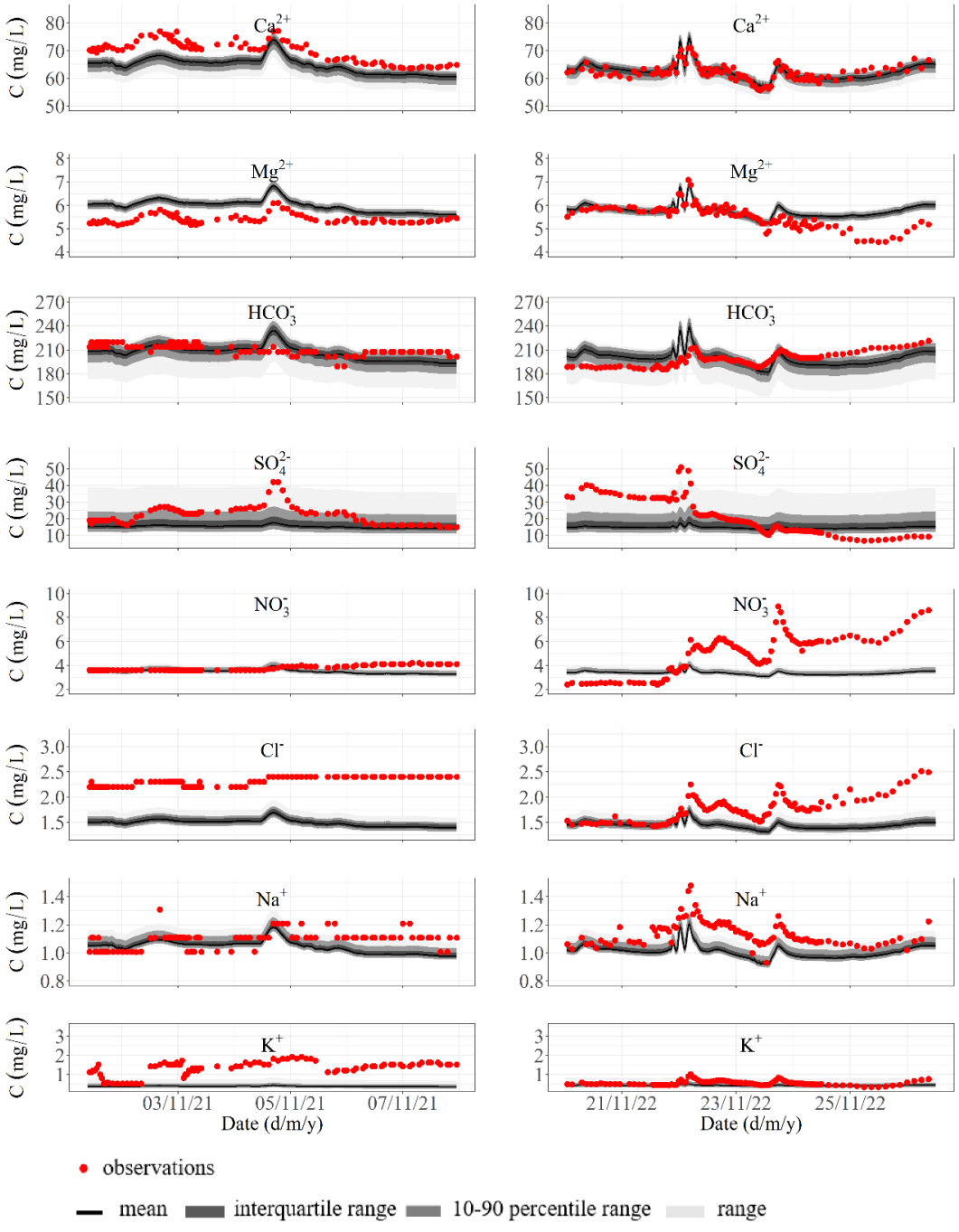

Fig. 5.6 Uncertainty bands for the predicted individual solute species (mg/L). The concentrations are computed at the Las Hountas spring for the periods 1/11/2021–7/11/2021 (left side) and for the period 20/11/2022–26/11/2022 (right side) based on the frequency of occurrence of the weight factors observed in 4/10/2021–14/10/2021. The black, gray and light gray areas of the bands represent the interquartile, the 10–90% percentile and full ranges of the computed solute species concentrations (mg/L), respectively. The red points are the observed solute concentrations (mg/L).

Regarding HCO_3 and SO_4, all observations fall in the full range of the predicted uncertainty bands for both the validation periods. However, the model overestimates the concentration of HCO_3 and

underestimated the concentration of SO_4 at peak conditions observed on 4 November 2021, and 22 November 2022. The not accurate prediction of NO_3 for November 2022 results from the fact that the distribution used as calibration period (October 2021) is characterized by a narrower variability, more similar to that observed in November 2021. The overestimation in the estimates of Cl and Na for November 2022 is due to a shift in the mean weight factors between the calibration and validation periods.

The same analyses were done for Kerschbaum considering the years 2000–2016 as calibration period. Fig. B.2 (rigth side) and B.3 (rigth side) show the prediction for the period 2018–2019 and 23 January 2022–28 January 2022, respectively. Overall, the prediction of the observed concentrations is accurate although the spring displays a small discharge variability and hence the variability in ion concentration is also small.

5.4 Discussion

When comparing the contributions of the solute species present as free ions and as part of complexes to the total concentration, complexation processes are particularly significant for SO_4, followed in order by Ca, Mg, HCO_3, and Na (Fig. 5.2a-c). As for the case of SO_4 (Fig. 5.2e, f), for some solute species complexes represent a significant percentage of the total concentration and therefore have a pivotal role when deriving the total solute species concentration from the measured EC. Being our aim to derive high resolution time series for the ion concentration from the EC measurements, and not vice versa, we can conclude that karst system studies require to account for the role of complexation processes when applying EC decomposition methods to retrieve the concentrations of those solute species which form complexes.

The uncertainty quantification was investigated for both watersheds. Due to the lack of EC and concentration measurements at high flow conditions for Kerschbaum, the analysis of this spring is to some extent limited. The inclusion of Kerschbaum in the present work was chosen to investigate the relevance of complexes in karst systems with different geologies. Moreover, the available data show that for catchments with stationary and homogeneous geology the method performs well both for interpolation and prediction purposes.

The results of both the uncertainty quantification during interpolation (Fig. 5.5 and B.2a, Table B.1 in the supplementary material) and of the predictive model (Fig 5.6 and B.2b) show a positive correlation between the width of the uncertainty band and the relative variation in concentration. As already observed by Benettin and van Breukelen. (2017), the information contained in continuous EC time series better represents the dynamics of those solute species with higher contribution to EC and lower relative variation in concentration. Indeed, due to the use of a linear interpolation for the weight factors f_i, the larger the relative variation of an ion the wider the frequency distribution of its weight factor (Eq. 5.3) and consequently the wider the uncertainty in the computed concentration (Eq. 5.4).

Further interpretations of the results need to consider the different geologies of the study areas, which lead to diverse ion content, temporal variability, and transport processes. Kerschbaum is a dolomitic karst system with a single water contribution to the spring and whose EC comes almost entirely from Ca^{2+}, Mg^{2+} and HCO_3^- (Fig. 5.2b). On the contrary, Baget is a limestone system (lower contribution of Mg^{2+}) characterized by an outcrop impermeable formation of black flysch (Fig. 5.1c), which affects the hydrochemistry of the spring discharge due to pyrite oxidation and thus increasing the concentration of SO_4^{2-} (Ulloa-Cedamanos et al. 2020). The area also includes a gypsum clay formation (Fig. 5.1c), which we do not consider significantly impacting the hydrochemistry of the system due to its minor extension. Due to the black flysch, Baget is not a completely karst system and shows varying contributions of water from different geological formations during different events. This leads to significant changes in the frequency distribution of the weight factors observed between successive events (Fig. 5.4) and consequently affects the performance of the EC decomposition method in both the interpolation and prediction of the individual solutes.

The discharge at Las Hountas shows large variability in solute species concentrations within a precipitation event and between successive events, due to the chemical compositions and response times of the different water contributions. This explains the relevant shifts in the frequency of occurrence of the weight factors f_i observed at the spring between the events in October 2021 and November 2022 on one side and November 2021 on the other (Fig. 5.4). Despite being close in time, the events in October 2021 and November 2021 show different hydrological and geochemical conditions (Fig. 5.7a, Fig. B4a) and thus different ion signatures. Consequently, as Fig. 5.6 shows for Ca, Mg and Cl, the dynamic behavior of the system causes the EC decomposition method to not satisfactory predict solute species concentrations for November 2021. On the contrary, being the frequency of occurrence of f_i similar between October 2021 and November 2022 (Fig. 5.4), the method well predicts Ca and Mg for November 2022 (Fig. 5.6). The similar frequency of occurrence of the weight factors results from the similar response of the system during the events in October 2021 and November 2022, which are characterized by a sharp increase in water level and piston effect (Fig. 5.7a, Fig. B.5a). This indicates that to sample the variability of the weight factors in catchments with heterogeneous geology, it is necessary to collect multiple events.

Fig. B.1 shows the dissolution processes characterizing the limestone and black flysch. According to the stoichiometry of the reactions, the dissolution of $CaCO_3$ by both H_2CO_3 and H_2SO_4 leads to a lower alkalinity than what we would observe in the case of only dissolution by H_2CO_3. The reduction in alkalinity explains why the method overestimates HCO_3 and underestimates SO_4 at flow peak conditions, both when used to interpolate (Fig. 5.5) and predict (Fig. 5.6) the major solute species concentrations. Fig. 5.8 correlates the percentage reduction in alkalinity (Eq. 5.8) with the tendency of the method to overestimate and underestimate HCO_3 and SO_4, respectively. The time series of the equivalent ratio SO_4 over HCO_3 follows the same behavior of the reduction in alkalinity (Fig. 5.8a), proving the correlation between the dissolution of $CaCO_3$ by H_2SO_4 and the decrease in HCO_3^-.

Fig. 5.8b, c show the concentrations of HCO_3 and SO_4 (black lines) obtained by running the model with only few input concentrations (red points) and using the remaining observations to evaluate the results (gray points). The computed concentrations do not represent properly the increase in HCO_3 and SO_4 on October 4, if no measured solute concentrations representing the peak condition are given as input. This results from the fact that during flow peak conditions the weight factors of HCO_3^- and SO_4^{2-} are not adequately predicted by the linear interpolation and consequently the model has no information about the increase in the alkalinity reduction and in the equivalent ratio SO_4 over HCO_3. Thus, the application of the EC decomposition method at peak conditions requires high-resolution ionic measurements or a better method to estimate the weight factors during such conditions. However, the linear interpolation of the weight factors of the other free ions seems to capture the peak conditions. This is the case for Ca (Fig. 5.8d), whose estimated peak concentration well represents the observations.

To investigate the contributions from calcareous rocks and black flysch at different flow conditions, we compare the EC, water level (m) and weight factors f_i of the free ions HCO_3^- and SO_4^{2-}, which were observed at Las Hountas during the event in October 2021 (Fig. 5.7), November 2021 (Fig. B.4) and November 2022 (Fig. B.5). As shown in Fig. 5.7a and B.5a, the first increase in water level on October 4 and on November 22, respectively, is characterized by piston and flushing effects, which come with the simultaneous increase in both EC and water level.

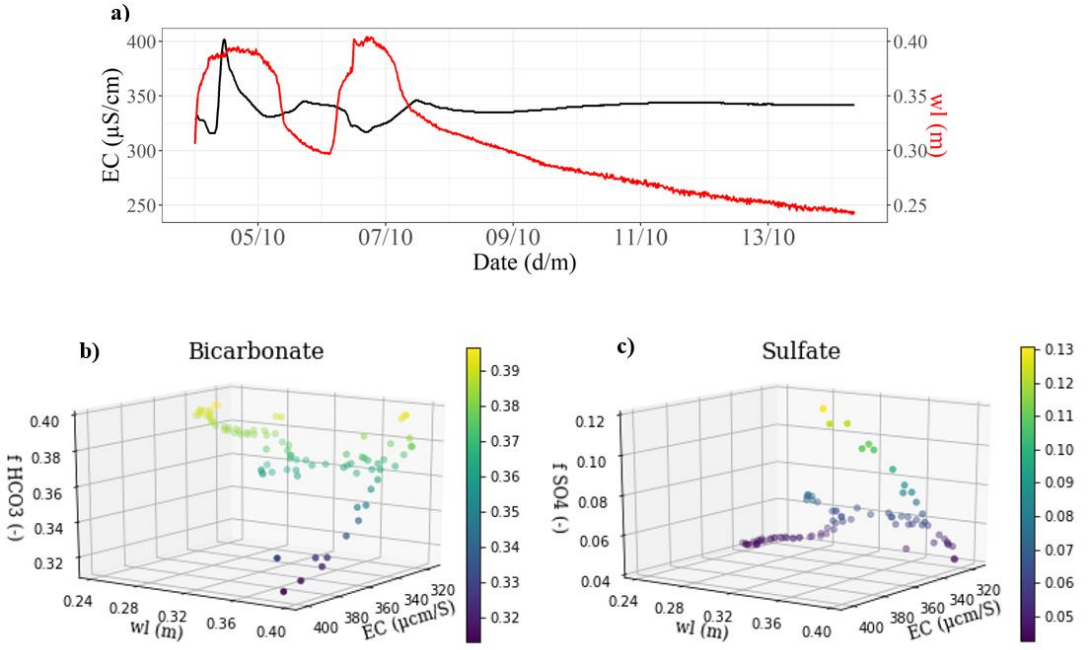

Fig. 5.7 Correlation between electrical conductivity EC (µS/cm), water level wl (m) and the weight factors f_i (-) of HCO_3^- and SO_4^{2-} observed at Las Hountas for the period 4/10/2021 – 14/10/2021. **a** Time series of EC (black line) and water level (red line). **b** 3D scatter plots of EC, water level and weight factor of HCO_3^-. **c** 3D scatter plots of EC, water level and the weight factors of SO_4^{2-}.

High values of EC and water levels correspond to low values of $f_{HCO_3^-}$ and large vales of $f_{SO_4^{2-}}$ (Fig. 5.7b, c, Fig. B.5b, c). Indeed, during high flow conditions, due to its faster response time, we

observe an increase in the relative contribution from the black flysch and a lower relative contribution from the calcareous rocks, which may even be under-estimated due to the existence of surface waters bypassing the spring during flood events (Mangin, 1975; Ulloa-Cedamanos et al., 2021). The second rise in water level on 6–7 October 2021 shows dilution processes and thus increase in water level and decrease in EC (Fig. 5.7a). The corresponding increase in $f_{HCO_3^-}$ and decrease in $f_{SO_4^{2-}}$ (Fig. 5.7b, c) are explained by the larger contribution of water coming from the karst calcareous formations, which had the time to get activated. Finally, during base flow conditions, the constant EC comes with high values of $f_{HCO_3^-}$ and low values of $f_{SO_4^{2-}}$ (Fig. 5.7b, c, Fig. B.5b, c), indicating that the water mainly comes from calcareous rocks. Therefore, from the comparison of $f_{HCO_3^-}$ and $f_{SO_4^{2-}}$we can understand the dynamics of the system. This allows us to predict when the method is not able to represent the temporal variability in alkalinity reduction. This is the case of 4 October 2021, when the increase in $f_{SO_4^{2-}}$ (Fig. 5.7c) indicates a larger contribution from the black flysch and a consequent increase in the alkalinity reduction, which is not captured by the method (Fig. 5.8).

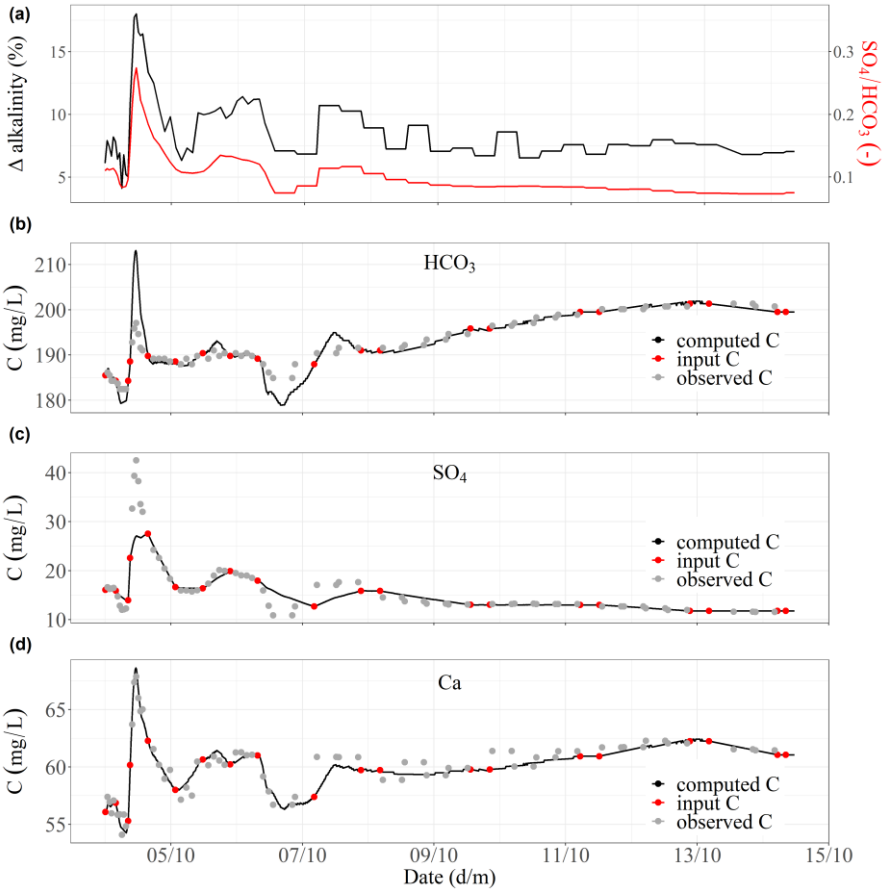

Fig. 5.8 Correlation between the reduction in alkalinity due to the carbonate dissolution by sulfuric acid and the model performance (overestimation and underestimation of HCO_3 and SO_4, respectively) at the Las Hountas spring for the event 4/10/2021 – 14/10/2021. **a** Time series of the reduction in alkalinity (%) (black line) and the equivalent molar ratio SO_4 /HCO_3 (-) (red line). **b, c, d** Concentrations of HCO_3, SO_4 and Ca (mg/L) obtained by running the model with only few input concentrations (red points).

5.5 Summary

This study investigates how a decomposition of electrical conductivity (EC) signals can be used to retrieve individual solute species concentrations time series in the case of karst systems. Starting from continuous EC and low-frequency water samples, the presented method estimates the concentrations of the major solute species at the same temporal resolution of the observed EC. Due to the large ionic content and complex speciation characterizing the discharge of karst springs, it was necessary to compute the distribution of solute species occurring as free ions and as part of aqueous complexes. The concentrations of the free ions, i.e. Ca^{2+}, Mg^{2+}, HCO_3^-, SO_4^{2-}, NO_3^-, Cl^-, Na^+ and K^+, are derived based on the linear interpolation of the weight factors f_i, which represent the relative contribution of each ion to the total measured EC. Conversely, the concentrations of the solute species involved in complexes are obtained by means of speciation calculations with PHREEQC as difference between the total molality of a solute (mol/kgw) and the molality of the solution (mol/kgw).

To investigate the relevance of complexation processes, we performed speciation calculations considering two karstic catchments with different geologies and temporal resolution of the available hydrochemical datasets, that is the Kerschbaum dolostone system in Austria and the Baget limestone system in France. The results of the uncertainty quantification performed within this work show that our method can successfully be applied in case of karst systems with a homogeneous geology, as in the case of Kerschbaum. For the latter the EC signal can be used to interpolate and predict with less uncertainty the temporal dynamics of those solute species with large contribution to the total EC and low variability of the weight factor f_i. In case of heterogeneous systems as Baget, the method cannot represent the mixing of the water contributions from the different geological areas of the catchment. The results further show that the correlation between EC, water level and the weight factors of HCO_3^- and SO_4^{2-} can support the investigation of the system functioning, allowing us to distinguish the response of the black flysch formation from that of the calcareous rocks.

The possibility to interpolate high-resolution solute species concentrations time series, without performing continuous -and costly- ionic measurements, has a huge potential in the improvement of hydrochemical data availability and, consequently, supports the understanding of internal transport processes mechanisms and temporal scales.

Chapter 6

High-resolution hydrochemical data to constrain event-based hydrological karst model concepts

Richieri, B., Bittner, D., Sivelle, V., Hartmann, A., Labat, D., and Chiogna, G. (2024). On the value of hydrochemical data for the interpretation of flow and transport processes in the Baget karst system, France. Hydrogeology Journal. https://doi.org/10.1007/s10040-024-02801-2

Abstract

Continuous hourly time series of hydrochemical data can provide insights into the subsurface dynamics and main hydrological processes of karst systems. This study investigates how high-resolution hydrochemical data can be used for the verification of robust conceptual event-based karst models. To match the high temporal variability of hydrochemical data, the LuKARS 2.0 model was developed on an hourly scale. The model concept considers the interaction between matrix and conduit components to allow a flexible conceptualization of binary karst systems characterized by a perennial spring and intermittent overflow as well as possible surface water bypassing the spring. The model was tested on the Baget karst system, France, featuring a recharge area defined by the coexistence of karst and non-karst areas. The Morris screening method was used to investigate parameter sensitivity, and to calibrate the model according to the Kling-Gupta Efficiency (KGE). Model verification was performed by considering additional hydrochemical constraints with the aim to represent the internal dynamics of the systems i.e., water contributions from the various compartments of the conceptual model. The hydrochemical constraints were defined based on high-temporal resolution time series of SO_4^{2-} and HCO_3^-. The results of this study show that the simulation with the highest KGE among 9000 model realizations well represents the dynamics of the spring discharge but not the variability of the internal fluxes. The implementation of hydrochemical constraints facilitates the identification of realizations reproducing the observed relative increase in the flow contribution from the non-karst area.

Keywords: Karst, conceptual models, rainfall-runoff, hydrochemistry, France

6.1 Introduction

Karst systems cover 10-15% of the Earth surface and 35% of the European continental area (Goldscheider et al., 2020), representing a major worldwide source of freshwater providing drinking water to 10-25% of the world´s population (Ford and Williams 2007; Stevanović, 2019). Hydrological models support the understanding of the system functioning and are fundamental to ensure the sustainable water management of karst water resources (Hartmann et al., 2014). However, modelling of karst systems is still a difficult task, due to the complex interaction between matrix and conduit domains (Hartmann et al., 2013a) and the difficulty in observing and measuring flow and transport processes in the subsurface (Berthelin and Hartmann, 2020). Sivelle et al. (2022b) investigated the relevance of excess air and thus hydrostatic pressure for the assessment of matrix-conduit exchange. As a result, large uncertainty characterizes the internal dynamics of karst systems i.e., fast discharge through the conduit, infiltration into the matrix and water contributions from different geological formations inside the recharge area (Chang et al., 2017).

Hence, hydrological models need to be calibrated due to the lack of knowledge in model parameter values and in process understanding (Le Moine et al., 2008). Moreover, model validation is necessary to assess model reliability and utility for further applications (Andréassian, 2023; Klemeš, 1986). Typically, model calibration and validation are done using measured discharge time series at a monitoring site and computing performance metrics. Among the several existing metrics (Bennett et al., 2013; Ferreira et al., 2020; Moriasi et al., 2007), the Kling-Gupta Efficiency (KGE) is considered suitable for capturing the entire flow regime (Gupta et al., 2009). However, a single metric is generally unable to properly evaluate all model characteristics and solely relying on optimal values of an objective function to assess a model has been criticized (Gupta et al., 2008; Leins et al., 2023). Indeed, acceptable values of a model performance indicator do not necessarily mean that the hydrological model is reliable due to the problem of equifinality (Cinkus et al., 2022), i.e., the existence of multiple optimal parameter sets that reproduce the observed values (Chiogna et al., 2024). Different models, characterized by different structures or parameter values, can result in satisfactory simulated spring discharge (Mudarra et al., 2019). Previous works have shown that models validated with a single spring monitoring site may not capture the internal functioning of karst system and result in large equifinality (Hartmann et al., 2017).

The use of hydrochemical data allows for a better understanding of the internal dynamics of karst systems. Beside the use of conservative tracers such as stable water isotopes (Wang et al., 2021; Winston and Criss, 2004), major ions and electrical conductivity (EC) are also used to investigate the spatial and temporal variability in the hydrological response of karts systems (Barbieri et al., 2005; Chang et al., 2021; Gil-Márquez et al., 2017; Hartman et al., 2013). However, to take full advantage of the benefits of hydrochemical data to better capture the variability of the internal response of a system, the hydrochemical data should be at a resolution at least as detailed as the resolution of discharge

observations, in particular for event-based models. Nevertheless, hydrochemical data are typically collected at weekly or coarser temporal resolutions due to high analysis cost and time constraints.

The aim of this study is to further contribute to ongoing research into the coupling of hydrological (e.g., spring discharge) and hydrochemical (e.g., high resolution ion concentration time series) information for the verification of conceptual event-based models. The method proposed by Richieri et al. (2023) is used to retrieve high resolution hydrochemical information from continuous measurements of electrical conductivity (EC). Moreover, the semi-distributed LuKARS 2.0 (Land use change modelling in KARSt systems) model, based on the original model from Bittner et al. (2018), is further developed by using it for the first time at an hourly timescale. LuKARS represents the discharge observed at the spring as the sum of water contributions draining different geological areas (hydrotopes) characterized by different response times. In this work, this approach is validated considering that different parts of the catchment can be characterized by different chemical signatures. The new version of the model represents the different compartments of a karst system as buckets, i.e., epikarst, matrix and conduits, and aims to provide an adaptable representation of binary karst systems with a perennial spring and intermittent overflow. In particular, the model provides an updated conceptualization of the interaction between matrix and conduit in comparison to Bittner et al. (2018) to allow a more flexible and consistent conceptualization of the subsurface system following the approach proposed in KarstMod (Mazzilli et al., 2019; Sivelle et al. 2023). To constrain model parameters, the KGE performance criteria is combined with the conceptual information derived from high-resolution hydrochemical data i.e., major ion concentrations. The hypothesis of the present work is that high temporal resolution hydrochemical data can support the verification of the conceptual model, whereas model structures simulating the spring discharge without consideration of hydrochemistry may feature a comparable KGE but may not match the internal dynamics of a system.

The model was tested on the Baget system, an intensively studied karst watershed in France (Labat et al., 1999; Sivelle et al., 2022a) which is characterized by an absence of interbasin groundwater flow (Mangin, 1975; AL Khoury et al., 2023). Baget shows a heterogeneous geology combining limestone bedrock and an extensive outcrop formation of black flysch (karst and non-karst areas) (Ulloa-Cedamanos et al., 2020). Time series at hourly resolution of the contributions of HCO_3^- and SO_4^{2-} to the total EC, called weight factors and derived by Richieri et al. (2023), contribute to the description of the internal dynamics of the Baget system, i.e., the response of water contributions from different geological areas in the catchment to different flow conditions.

The manuscript is structured as follows. First the study area and the available dataset are presented. Then the new features of LuKARST 2.0 are described in detail, whereas the components of the model that remain unchanged are provided in the supplementary material. Finally, the Morris method is used for the sensitivity analysis of the model parameters and an envelope of behavioral simulations is defined

based on KGE. Finally, this study shows that only a limited subset of behavioral simulations can explain the observed hydrochemical dynamics.

6.2 Materials and methods

This section provides information about the Baget karst watershed and the hydrochemical dataset used to select an appropriate conceptual model and parameter values. The hydrochemical data were collected at Las Hountas spring for the period 30/03/2022 – 7/04/2022. This section also describes the previous investigations into the internal dynamics of the Baget karst system based on hydrochemical data at high temporal resolution (Richieri et al., 2023).

6.2.1 Study area

The Baget karst system is a binary karst system characterized by a perennial spring and intermittent overflow, located 10 km southwest of the city of Saint-Girons, in the Ariege administrative department, France (Fig. 6.1a, b). It has a recharge area of approximately 13 km^2 and does not receive water from adjacent catchments (Mangin, 1975; AL Khoury et al., 2023). The vegetation of the recharge area is dominated by fir-beech forest, with only a small agricultural plot covering 3% of the recharge area (Sivelle et al., 2022a). Vegetation is particularly dense along the north-facing slope, whereas grassland occupies some of the south-facing slope. The Baget system is under the influence of the Atlantic oceanic climate with a mean annual air temperature of 12.3 °C, an average annual rainfall close to 1700 mm, and no influence of snow melt processes (Padilla et al., 1994). The annual precipitation distribution is bimodal, with peaks occurring in December and February (Ulloa-Cedamanos et al., 2020).

The catchment features heterogeneous geology, dominated by calcareous lithologies originating from the Jurassic and Lower Cretaceous. In addition to the limestone bedrock, a large outcrop of relatively impermeable black flysch partially covers the south-facing slope (Fig. 6.1c – Fig. 6.1e). The extent of the black flysch was obtained using the BD Charm-50 geology map (French Geological Survey) by measuring the corresponding covered area. Its estimation of approximately 30% of the catchment is comparable to the 25.2% estimated by Ulloa-Cedamanos et al. (2020). Spring flow contributions derived from different geological areas of the catchment have undergone different dissolution processes. Calcium carbonate ($CaCO_3$) associated with the limestone is dissolved by carbonic acid (H_2CO_3) resulting in water typified by elevated Ca^{2+} and HCO_3^-. The black flysch contains pyrite, where oxidation processes release sulfuric acid (H_2SO_4), which in turn dissolves $CaCO_3$ with the products SO_4^{2-}, Ca^{2+} and HCO_3^-. Consequently, the water contributions from the limestone bedrock and black flysch provide different components to the chemical signature at the spring (Richieri et al., 2023). A more detailed overview of the different sources affecting the chemical composition at the spring is given below in Subsection 6.2.3.

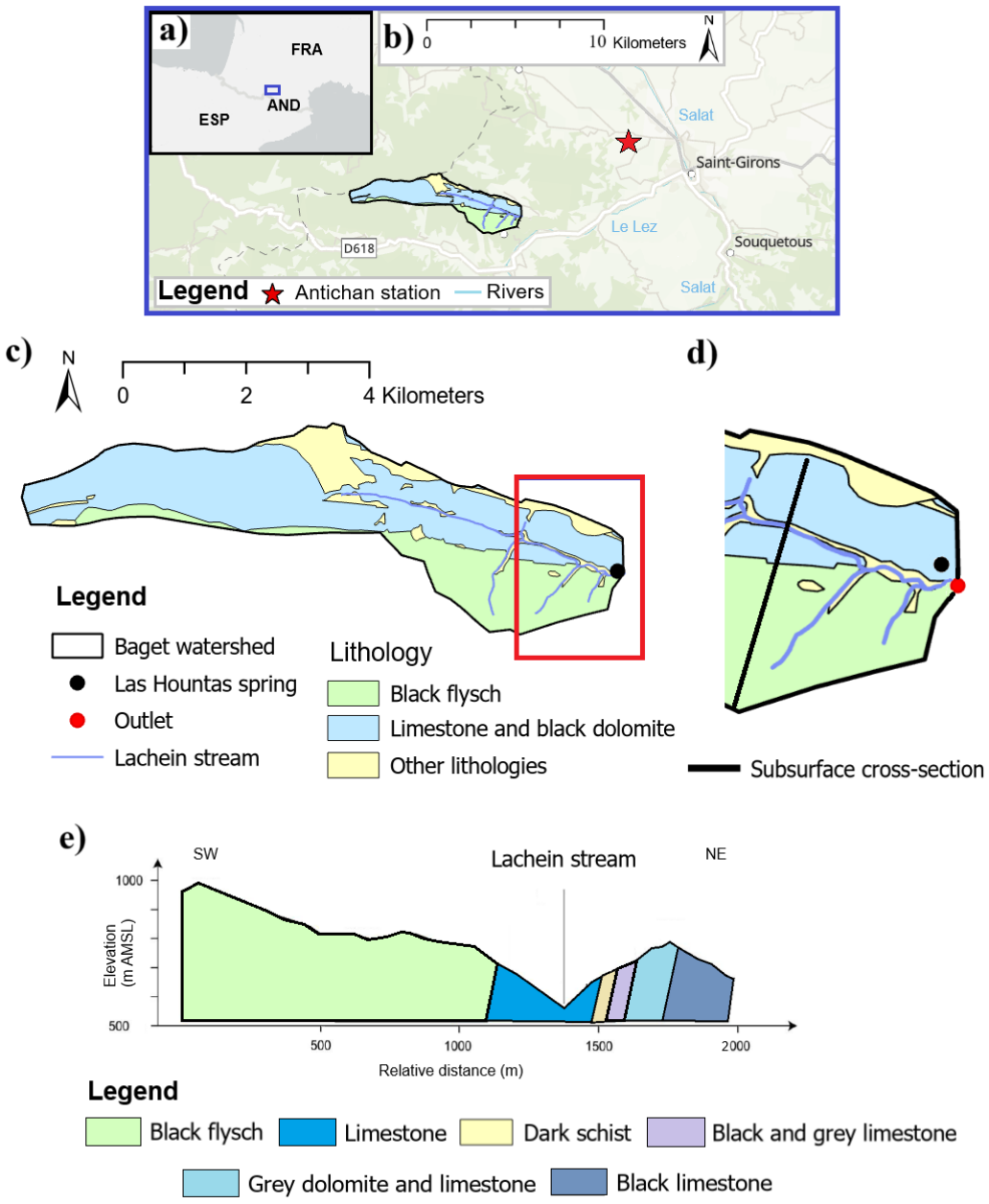

Fig. 6.1 Overview of the study site. **a** The location of the study area in Europe. **b** The location of the Antichan rain gauging station in relation to the study area. **c** Geological map of the Baget catchment with the location of the Las Hountas spring (modified after the BD Charm-50 geology map from the French Geological Survey). **d** Zoomed in area of the geological map showing the locations of the Las Hountas spring, at which the water samples were collected, and the outlet of the recharge area. **e** Geological subsurface cross-section in the location indicated in Fig. 1d with a black line. Elevation is provided in meters above mean sea level (m AMSL). Modified from Debroas (2009).

The karstic watershed is characterized by one perennial spring, called Las Hountas. Las Hountas is situated 110 m away from the outlet of the catchment (Fig. 6.1d) and is representative of a part of the total response of the system. During precipitation events, the downstream part of the Baget catchment

recharges the Las Hountas spring. Only during high flood events, the karst conduits in the upper part of the catchment start to discharge water to the surface, actively contributing to the streamflow generation in the Lachein stream, which is usually dry (Sivelle et al., 2020). Groundwater discharge to streamflow in the upper part of the surface channel occurs around 50 days per year (Mangin, 1975). The surface water of the Lachein stream bypasses the Las Hountas spring and directly reaches the outlet of the catchment (Ulloa-Cedamanos et al., 2021). This is evident by comparing the measured discharge at the outlet and at Las Hountas spring: the discharge at the spring shows a plateau at approximately 0.6 m^3/s (Fig. B.6 in supplementary material B.2.3).

6.2.2 Data collection

The hourly precipitation data used as an input for the model were recorded at the meteorological station of Antichan, approximately 8 km away from the spring (Fig. 6.1b). The observed discharge time series at the Las Hountas spring was derived by recording water level with an Aqua TROLL 200 device (In-Situ Inc., United States) and applying the rating curve from Mangin (1975), which was adjusted to represent the current state of the cross section during additional field measurements performed in 2021 and 2022. Evapotranspiration was not considered because this study focuses on the simulation of peak flows in response to intense precipitation events during which evapotranspiration effects are negligible.

Table 6.1 contains information about the temporal resolution, number of samples and the statistics of the specific EC (µS/cm), water temperature, pH and major solute species total concentration (i.e., each present both as free ion and as part of complexes as described in Richieri et al. (2023)), i.e., Ca, Mg, HCO_3, SO_4, NO_3, Cl, Na and K (mg/L), which were measured at Las Hountas spring during the event-based sampling campaign from 30/03/2022 to 7/04/2022. The specific EC was measured with a time interval of 15 minutes by means of the In-Situ Aqua TROLL 200 device and reported at the standard temperature of 25°C. The water samples were collected by a 6712 ISCO sampler (Teledyne ISCO, United States), which was connected to the EC probe to automatically start sampling above a water level threshold (30 cm). The sampling frequency was hourly during the rising curve of the hydrograph, every two hours during the recession curve and then every three hours near baseflow conditions. The ISCO sampler was installed inside a shelter that always provided shade. The samples were collected every day in plastic vials with zero headspace, filtered through a 0.22 µm membrane and stored in a refrigerator at 4 °C for approximately one week prior to analysis. For each sample, an aliquot for cation analysis was acidified with nitric acid (HNO_3) to prevent complexation and precipitation (Weiss, 2020; Ulloa-Cedamanos et al., 2020). The solute concentrations, provided at the standard temperature of 25°C, were analyzed by the laboratory Geosciences Environment Toulouse, France. The ICP – OES (inductively coupled plasma optical emission spectrometry) was used to quantify Ca, Mg, Na and K; ion chromatography was used to quantify NO_3, SO_4 and Cl; titration analysis was used to quantify HCO_3.

To verify the accuracy of chemical quantification, the charge balance of each sample was computed using the software PHREEQC. The charge mass balance error ranged from 0.8 to 4.9% with a median of 2.4%. Since all the samples show a charge error lower than ±5%, the results of the laboratory analysis were considered reliable (Parkhurst and Appelo, 2013). Fig. B.7 in supplementary material B.2.4 shows the time series of the computed charge balance (%) together with the sum of cations (TC) and anions (TA) (mEq/L).

Table 6.1 Statistics of the used datasets, including: temporal resolution (TR), number of samples (*n*), mean, standard deviation (SD), minimum (MIN) and maximum (MAX) values of the specific electrical conductivity EC *(*µS/cm*)*, major solute species (mg/L), pH and water temperature *T* (°C) measured at the Las Hountas spring for the events 30/03/2022–7/04/2022.

Statistic	**EC (µS/cm)**	**Ca (mg/L)**	**Mg (mg/L)**	**Na (mg/L)**	**K (mg/L)**	**HCO_3^- (mg/L)**	**SO_4 (mg/L)**	**NO_3 (mg/L)**	**Cl (mg/L)**	**pH**	***T* (°C)**
TR	quarter-hour	event-based	event-based	event-based	event-based	event-based	event-based	event-based	event-based	event-based	quarter-hour
n	830	122	122	122	122	122	122	122	122	122	830
mean	332.2	64.5	4.5	1.1	0.6	193.6	10.8	1.6	1.5	8.2	9.9
SD	7.6	1.9	0.3	0.1	0.1	4.4	2.5	0.2	0.08	0.2	0.2
MIN	316.5	61.1	3.7	0.9	0.3	185.5	7.9	1.2	1.3	7.2	5.7
MAX	358.2	68.9	5.2	1.4	1.0	205.6	19.4	1.9	1.9	8.3	10.2

6.2.3 Prior investigation into hydrochemical signals

Richieri et al. (2023) previously investigated the hydrological functioning of the Baget karst system by comparing continuous water level recordings and EC measurements, with high-temporal resolution major solute concentrations for multiple precipitation events, occurring in October 2021, November 2021 and November 2022. EC dynamics confirmed the complex hydrological response behavior of the Las Hountas spring, which is characterized by a simultaneous increase in water level and EC (flushing and piston effects) during precipitation events that followed dry periods, and by dilution processes during peak spring discharge periods. Richieri et al. (2023) also used the individual contributions of individual major ions *i* to the total observed EC, called weight factors f_i, to identify the varying contributions of water derived from different areas of the watershed, i.e., limestone and black flysch, at different flow conditions. The individual contributions of each ion to the total EC were computed for each sample with PHREEQC, by considering ion molar conductivity, molar concentration and the electrochemical activity coefficient as well as pH and temperature of the sample (Table 6.1). A complete description of the equations used to compute the weight factors is provided in Richieri et al. (2023). Eq. 6.1 describes the dissolution process characterizing the limestone formation. The dissolution of one mole

of calcium carbonate ($CaCO_3$) by carbonic acid (H_2CO_3) produces one mole of Ca^{2+} and two moles of HCO_3^-. Eq. 6.2 describes the dissolution process characterizing the black flysch containing pyrite, whose oxidation releases strong acids, i.e., sulfuric acid (H_2SO_4). The reaction between one mole of $CaCO_3$ and half mole of H_2SO_4 produces one mole of Ca^{2+}, one mole of HCO_3^- and half mole of SO_4^{2-}. Thus, the dissolution of $CaCO_3$ by both H_2CO_3 and H_2SO_4 leads to a lower alkalinity (HCO_3^-) than what we would observe in the case of only dissolution by H_2CO_3. Consequently, it was shown that the increase and decrease in the weight factors of SO_4^{2-} and HCO_3^- ($f_{SO_4^{2-}}$ and $f_{HCO_3^-}$), respectively, indicate a relative increase in the water draining the black flysch, which was observed to be simultaneous to flushing and piston effects. On the contrary, the increase in $f_{HCO_3^-}$ indicates a larger water contribution from the limestone bedrocks during dilution processes and baseflow conditions (Richieri et al., 2023).

$$CaCO_3 + H_2CO_3 \rightarrow Ca^{2+} + 2HCO_3^- \quad (6.1)$$

$$CaCO_3 + 0.5H_2SO_4 \rightarrow Ca^{2+} + HCO_3^- + 0.5SO_4^{2-} \quad (6.2)$$

It is pertinent to note, that despite the black flysch containing Na silicate minerals (Na_2SiO_3) (Ulloa-Cedamanos et al., 2021), the origin of HCO_3^- is considered to be dominated by $CaCO_3$ dissolution due to the low Na^+ content of water samples (Table 6.1). The variability in silicate weathering input could be further investigated by means of isotopes (Hagedorn and Whittier, 2015; Spence and Telmer, 2005), which were not available for the present study. The role of Na silicate weathering by H_2CO_3 (Ulloa-Cedamanos et al., 2021) is therefore considered negligible in the Baget catchment. In addition, a minor contribution of SO_4^{2-} might be related to a gypsum formation within the catchment. However, as the area of gypsum bedrock only represents 0.2% of the recharge area (Ulloa-Cedamanos et al., 2020), the present study considers the mass flux of SO_4^{2-} to be controlled by the discharge from the black flysch formation, which covers 30% of the catchment.

Despite being often considered a conservative tracer, Cl^- is not used in this study for the investigation of system dynamics for two reasons. Firstly, the computation of the weight factors f_i at high temporal resolution is affected by high uncertainty in case of ions with low concentration, such as Cl^- (Table 6.1) (Richieri et al., 2023). Second, this work focuses on the investigation of water draining different geological formations in the catchment, which does not contain any halite deposit or other geogenic sources of Cl^- (Ulloa-Cedamanos et al., 2021).

The Baget catchment is relatively unpolluted with an absence of SO_4^{2-}, NO_3^- and Cl^- originating from anthropogenic activities. NO_3^- was observed to be associated with organic decomposition and to increase in autumn. Indeed, the seasonal increase in precipitation causes the leaching of NO_3^- from the soil (Ulloa-Cedamanos et al., 2020); whereas the observed SO_4^{2-} and Cl^- are entirely derived from geogenic sources and precipitation, respectively (Ulloa-Cedamanos et al., 2021).

6.3 Model development

This section describes the LuKARS 2.0 model concept, together with the modifications done within this study with respect to the original model from Bittner et al. (2018). Subsequently, the Morris screening sensitivity analysis and the calibration procedure are presented. Finally, the use of high-resolution hydrochemical data for the selection of the model structure and parameters is described. The model was tested for the Las Hountas spring and calibrated and validated for the periods 1/03/2022– 29/03/2022 and 30/03/2022 – 30/04/2022, respectively.

6.3.1 Description of LuKARS 2.0 model concept

LuKARS is a semi-distributed model developed by Bittner et al. (2018). The model divides the catchment into hydrotopes, which are defined as independent units exhibiting similar hydrological behavior and soil characteristics. The original model from Bittner et al. (2018) was later modified by Sivelle et al. (2022) to be coupled with KarstMod (Mazzilli et al., 2019). In this study, LuKARS 2.0 was developed and applied to the Baget catchment starting from the original model (Bittner et al., 2018) considering two hydrotopes in the upper compartment, which represent the main geological formations within the studied catchment, i.e., limestone and black flysch. LuKARS 2.0 adds three new features to LuKARS: (1) the model was modified from a daily to an hourly time step and the parameters adjusted accordingly; (2) a transfer between the matrix and conduit was implemented in the lower compartment of the model; and (3) a drainage from the conduit was implemented to represent water bypassing the spring at high flow conditions (Fig. B.6 in supplementary material B.2.3). Fig. 6.2 and Table 6.2 show the model concept and provide a description of the model parameters, respectively. The model concept was developed based on the understanding of system functioning, more precisely on the dynamics of the water contributions draining the different geological formations (Richieri et al., 2023). Since the hydrological response of the contribution from the black flysch was observed to be fast with no apparent influence on the baseflow, hydrotope 2 was defined as such to provide only fast flow to the conduit but no infiltration to the matrix. On the contrary, hydrotope 1 represents the limestone karst formation, which contributes to both the discharge to the conduit and infiltration in the matrix. The fast flow Q_{hyd} (m^3/s) from a certain hydrotope gets active when the water level in that hydrotope reaches the upper storage threshold E_{max} (mm) and continues until the water level goes down to the lower storage threshold E_{min} (mm) (hysteresis). On the contrary, the infiltration Q_{is} (m^3/s) is always active and linearly correlated with the water level in the hydrotope. Finally, the water in the conduit will be transferred to the spring with the linear function from Mazzilli et al. (2019) (supplementary material B.2.2, Eq. B.13). The implemented modifications to LuKARS are described here, whereas the model equations from the original model (Bittner et al., 2018) are reported in the supplementary material B.2.1.

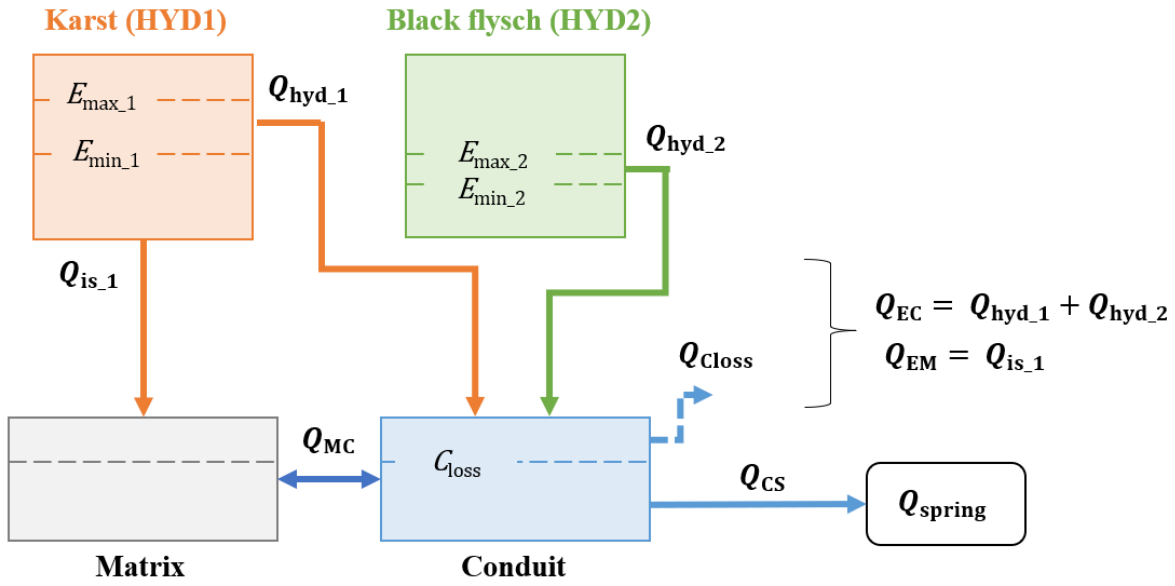

Fig. 6.2 LuKARS 2.0 model concept including the implemented transfer between the matrix bucket and the conduit bucket and the drainage from the conduit bucket for the case of Las Hountas spring. The two hydrotopes are defined based on the main geological formations present in the recharge area i.e., karst bedrock and black flysch, and their response to rainfall.

Transfer between matrix and conduit A transfer between matrix and conduit Q_{MC} (m^3/s) was implemented in the lower compartment of the model to represent the dual behavior typical of karst systems. The transfer was defined based on the approach of Mazzilli et al. (2023) as function of the recharge area Ra (km^2) the discharge coefficient k_{MC} (mm/h), exponent a_{MC} (-) and dimensionless water levels in the matrix *M* and conduit *C* (-). Q_{MC} (m^3/s) was implemented as shown in Eq. 6.3, with *t* indicating the current time step, abs the absolute value and sgn the sign of the subtraction of the dimensionless water level in the conduit *C* from that in the matrix M (-). Positive values of Q_{MC} (m^3/s) means that the current direction of flow is from the matrix to the conduit. To avoid numerical instabilities, Eq. 6.3 is solved using the analytical solution for the inter-compartment coupling (Mazzilli et al., 2023).

$$Q_{MC,t} = \text{Ra} \times k_{MC} \times \text{sgn}(M_t - C_t) \times \text{abs}(M_t - C_t)^{a_{MC}} \quad (6.3)$$

Discharge from the conduit A drainage Q_{Closs} (m^3/s) from the conduit was used to represent the plateau in discharge and the water bypassing the spring (Fig. B.6 in supplementary material B.2.3), which results from the natural drainage through the conduits at high flow conditions. The drainage was implemented to start when the water level in the conduit C_t (where the subscript *t* indicates the time step at which a quantity is computed) gets higher than the storage threshold C_{loss} (mm) and to remain active as long as the water level does not drop below it. Eq 6.4 shows the implementation of the drainage $Q_{Closs,t}$ (m^3/s),

with Ra (km^2) the recharge area and dt (h) the hourly time step. The water level is checked at each time step t and the excess water exits immediately from the system without reaching the spring.

$$\text{if } C_t > C_{\text{loss}}: \quad Q_{\text{Closs},t} = (C_t - C_{\text{loss}}) * \frac{\text{Ra}}{dt} \quad \text{and} \quad C_t = C_{\text{loss}},$$

$$\text{else}: Q_{Closs,t} = 0 \tag{6.4}$$

Table 6.2 Overview of the model parameters of LuKARS 2.0, including symbol, unit, description, and range used for the Morris analysis.

Area	**Symbol**	**Unit**	**Description**	**Range**
Catchment	Ra	(km^2)	Total recharge area	9 – 15
Karst (HYD1)	$l_{\text{hyd\_1}}$	(m)	Mean distance of hydrotope 1 to the spring	1500 – 6500
	$k_{\text{hyd\_1}}$	(mm^2/h)	Discharge coefficient for the fast flow from hydrotope 1 to the conduit ($Q_{\text{hyd\_1}}$)	1 – 10000
	$E_{\text{min\_1}}$	(mm)	Lower storage threshold for hydrotope 1	8 – 20
	$E_{\text{max\_1}}$	(mm)	Upper storage threshold for hydrotope 1	21 – 200
	$\alpha_{\_1}$	(-)	Exponent for the fast flow from hydrotope 1 to the conduit ($Q_{\text{hyd\_1}}$)	0 – 2
	$k_{\text{is\_1}}$	(1/h)	Discharge coefficient for the infiltration from hydrotope 1 to the matrix ($Q_{\text{is\_1}}$)	10^{-7}– 10^{-3}
Black flysch (HYD2)	$l_{\text{hyd\_2}}$	(m)	Mean distance of hydrotope 2 to the spring	1000 – 4000
	$k_{\text{hyd\_2}}$	(mm^2/h)	Discharge coefficient for the fast flow from hydrotope 2 to the conduit ($Q_{\text{hyd\_2}}$)	1 – 1000
	$E_{\text{min\_2}}$	(mm)	Lower storage threshold for hydrotope 2	1 – 5
	$E_{\text{max\_2}}$	(mm)	Upper storage threshold for hydrotope 2	6 – 30
	$\alpha_{\_2}$	(-)	Exponent for the fast flow from hydrotope 2 to the conduit ($Q_{\text{hyd\_2}}$)	0 – 2
Lower compartment	k_{MC}	(mm/h)	Discharge coefficient for the transfer between matric and conduit (Q_{MC})	10^{-5} – 10^{-1}
	a_{MC}	(-)	Exponent for the transfer between matric and conduit (Q_{MC})	1 – 3
	C_{loss}	(mm)	Storage threshold for the conduit	10^{-2} – 10^{0}
	k_{CS}	(mm/h)	Discharge coefficient for the flow from the conduit to the spring (Q_{CS})	10^{-3} – 10^{1}
	a_{CS}	(-)	Exponent for the flow from the conduit to the spring (Q_{CS})	1 – 4

6.3.2 Sensitivity analysis (Morris screening)

The identification of the most sensitive model parameters and potential nonlinear interactions was done with the elementary effects method, also known as Morris screening (Campolongo et al., 2007; Morris, 1991). The Morris screening is a one-at-a-time (OAT) method to perform global sensitivity analysis which is widely applied in literature and it is often used in case of models characterized by a large number of input parameters for which variance based sensitivity analysis would be computationally demanding (Campolongo et al., 2007; Jaxa-Rozen and Kwakkel, 2018; Merchán-Rivera et al., 2022; Smith, 2013). The Morris method considers that each model parameter set $\mathbf{q} = [q_1, \ldots, q_n]$ varies across a discrete number l of values, called levels, forming a n-dimensional l-level grid Γ_l. The method relies on the average of the elementary effects over the parameter space to provide a measure of global sensitivity. The elementary effect $d_i(q)$ of the i^{th} input parameter quantifies the approximate local sensitivity at the point q and is defined as in Eq. 6.5 (Smith, 2013)

$$d_i(q) = \frac{f(q_1, \ldots, q_{i-1}, q_i + \Delta, q_{i+1}, \ldots, q_n) - f(q)}{\Delta} = \frac{f(q + \Delta e_i) - f(q)}{\Delta} \tag{6.5}$$

where e_i is a vector of zeros with one on the i^{th} components and Δ is the stepsize which is chosen from the set shown in Eq. 6.6 (Smith, 2013)

$$\Delta \in \left\{\frac{1}{l-1}, \ldots, 1 - \frac{1}{l-1}\right\} \tag{6.6}$$

To obtain a global sensitivity measure, Campolongo et al. (2007) and Morris (1991) proposed the mean μ^* and variance σ, respectively, of the finite-dimensional distribution G_i associated with the absolute value of the elementary effect $d_i(q)$, which is derived from randomly sampling q within Γ_l. Considering r sampling trajectories, these metrics associated with the i^{th} parameter can be expressed, as shown in Eq. 6.7 and Eq. 6.8, as function of the elementary effect associated to each defined trajectory j.

$$\mu_i^* = \frac{1}{r}\sum_{j=1}^{r}\left|d_i^j(q)\right| \tag{6.7}$$

$$\sigma_i^2 = \frac{1}{r-1}\sum_{j=1}^{r}\left(d_i^j(q) - \mu_i\right)^2 \; with \; \mu_i = \frac{1}{r}\sum_{j=1}^{r} d_i^j(q) \tag{6.8}$$

Where d_i^j is the elementary effect associated with the i^{th} parameter and j^{th} trajectory.

High values of σ indicate possible interactions between the model parameters and/or of parameter nonlinearity. The parameters with σ/μ^* smaller than 0.1 or between 0.1 and 1 are almost linear or monotonic, respectively. The parameters with σ/μ^* larger than 1 are characterized by marked nonmonotonic nonlinearities or interactions with other parameters (Sanchez et al., 2012). μ^* and σ are constructed by considering r trajectories of n+1 points in the parameter space. The total number of

realizations accounted in the metrics calculations is defined by $(n+1)*r$. For a detailed explanation of the method, one can refer to the works of Morris (1991) and Campolongo et al. (2007) as well as to the book of Smith (2013).

In this study, Morris was run for the calibration period (1/03/2022 – 30/03/2022) by using the sensitivity analysis library in Python (SALib) and considering the 17 model parameters reported in Table 6.2, 500 trajectories and 100 grid levels, for a total of 9000 realizations. The length of the calibration period was selected considering the aim of building an event-based model. The number of realizations was considered sufficient since the method with 1000 trajectories and 200 grid levels showed convergence of the results. Table 6.2 shows the parameter ranges used for the Morris analysis. Since it was the first application of LuKARS at hourly scale, it was required to initially investigate the parameter ranges by means of an independent set of 10000 Monte Carlo simulations. In addition, the parameter ranges for the two hydrotopes were selected to be consistent with the observations of the water contribution from the two different geological formations. A lower upper storage threshold was set for the black flysch, i.e., hydrotope 2, to represent its faster activation and thus the relative increase in the water contribution at beginning of heavy precipitation events (Richieri et al., 2023). The extends of hydrotope 1 and hydrotope 2 were taken fixed and equal to 70% and 30% of the entire catchment, respectively. Each realization performed for the Morris method was evaluated by computing the Kling-Gupta Efficiency (KGE). Eq. 6.9 shows the equation for the computation of KGE, with r_c the linear correlation between the observations and simulations, σ_{sim} the standard deviation in simulations, σ_{obs} the standard deviation in observations, μ_{sim} the simulation mean and μ_{obs} the observation mean (Knoben et al., 2019).

$$\mathrm{KGE} = 1 - \sqrt{(r_c - 1)^2 + \left(\frac{\sigma_{sim}}{\sigma_{obs}} - 1\right)^2 + \left(\frac{\mu_{sim}}{\mu_{obs}} - 1\right)^2} \tag{6.9}$$

Among the 9000 model realizations used for the sensitivity analysis, the realization with the highest KGE was considered as the selected one, while the subset of realizations with a KGE larger than 0.5 was defined as behavioral (e.g., Beven and Freer, 2001). To assess the uncertainty of the model, each flow component (Q_{hyd_1}, Q_{hyd_2}, Q_{is_1}, Q_{MC}, Q_{Closs} and Q_{CS} (m^3/s)) derived by using the selected parameters values was compared to the distribution of the behavioral simulations, i.e., interquartile and 10-90 percentile envelopes.

6.3.3 Model selection considering hydrochemical constraints

Once the selected and behavioral parameter sets were found, they were used to validate the model for the period 30/03/2022 – 30/04/2022. Thereafter, it was necessary to check if the selected simulation represented not only the discharge at the spring but also the internal dynamics of the system, i.e., water contributions from the limestone and black flysch. For this purpose, the flows from hydrotope 1 (limestone) and 2 (black flysch) to the conduit together with the transfer between the matrix and conduit were compared to the observed hydrochemical data recorded during the increase in water level –

occurred in the two days 30/03 and 1/04/2023 – for the event 30/03/2022 – 7/04/2022. Therefore, three additional criteria were defined to constrain among the multiple Morris realizations with KGE larger than 0.5 those also matching the hydrochemical information. The criteria were identified based on the weight factors (Richieri et al., 2023) computed for the time series of HCO_3^- and SO_4^{2-} observed during the event in April 2022 (Table 6.1) and are described in detail in the result (Subsection 6.4.3). It is important to note that the weight factors were computed using PHREEQC by considering for each water sample the measured pH (Table 6.1). In addition, despite HCO_3^- not being a conservative species, the alkalinity in case of pH between 7.2 and 8.3 (Table 6.1) is typically considered to derive from HCO_3^- alone (Boyd, 2020). The hydrochemical constraints were defined based on HCO_3^- and SO_4^{2-} as these ions were previouslyused for the investigation of the internal dynamics of the Baget system (Richieri et al., 2023). In addition, both HCO_3^- and SO_4^{2-} were proved to be present at Las Hountas spring at sufficiently high concentration to be retrieved at high temporal resolution by applying the EC decomposition method from Richieri et al. (2023). Indeed, the EC decomposition method (Richieri et al., 2023) allows to retrieve accurate concentration time series at high temporal resolution for those solutes present with a sufficiently high concentration and thus significantly contributing (approximately >6%) to the total EC. Whereas the reconstructed time series of solutes with low concentration, e.g., Cl^- (Table 6.1), are subject to large uncertainty.

6.4 Results

This section presents the results of the investigation. Firstly, the results of the Morris analysis are presented both in terms of sensitivity and non-linear interaction among the model parameters. Secondly, the results of the model calibration and validation considering the KGE of the spring discharge are shown together with the respective uncertainty bands. Finally, it is shown how the hydrochemical criteria were used to further constrain the model by considering not only the discharge at the spring but also the expected internal flow dynamics.

6.4.1 Sensitivity analysis

The results of the sensitivity analysis based on the Morris screening method are evaluated by comparing the mean μ^* and standard deviation σ of the distribution function of each parameter. Fig. 6.3a shows the value of μ^* for each parameter in descending order, while Table 6.3 contains the corresponding sensitivity ranking. Among the model parameters, the discharge coefficient for the flow from the conduit to the spring k_{CS} is the most sensitive, followed in order by the upper storage threshold for hydrotope 1 E_{max_1} and by the storage threshold for the conduit C_{loss}. On the contrary, the discharge coefficient k_{MC} and the exponent a_{MC}, which are both related to the transfer between matrix and conduit (Q_{MC}), are the least sensitive. In between the most and least sensitive parameters, the parameters related to the flow components from the hydrotope 1, i.e., limestone, are more sensitive than those from the hydrotope 2, i.e., black flysch.

Fig. 6.3b shows the scatter plot of the computed σ and μ^*, delineating the areas of the graph corresponding to monotonic and/or linear interactions and nonlinear nonmonotonic interactions (Sanchez et al., 2012). Most of the parameters fall above the bisector, indicating strong nonlinear nonmonotonic interaction among most of the model parameters.

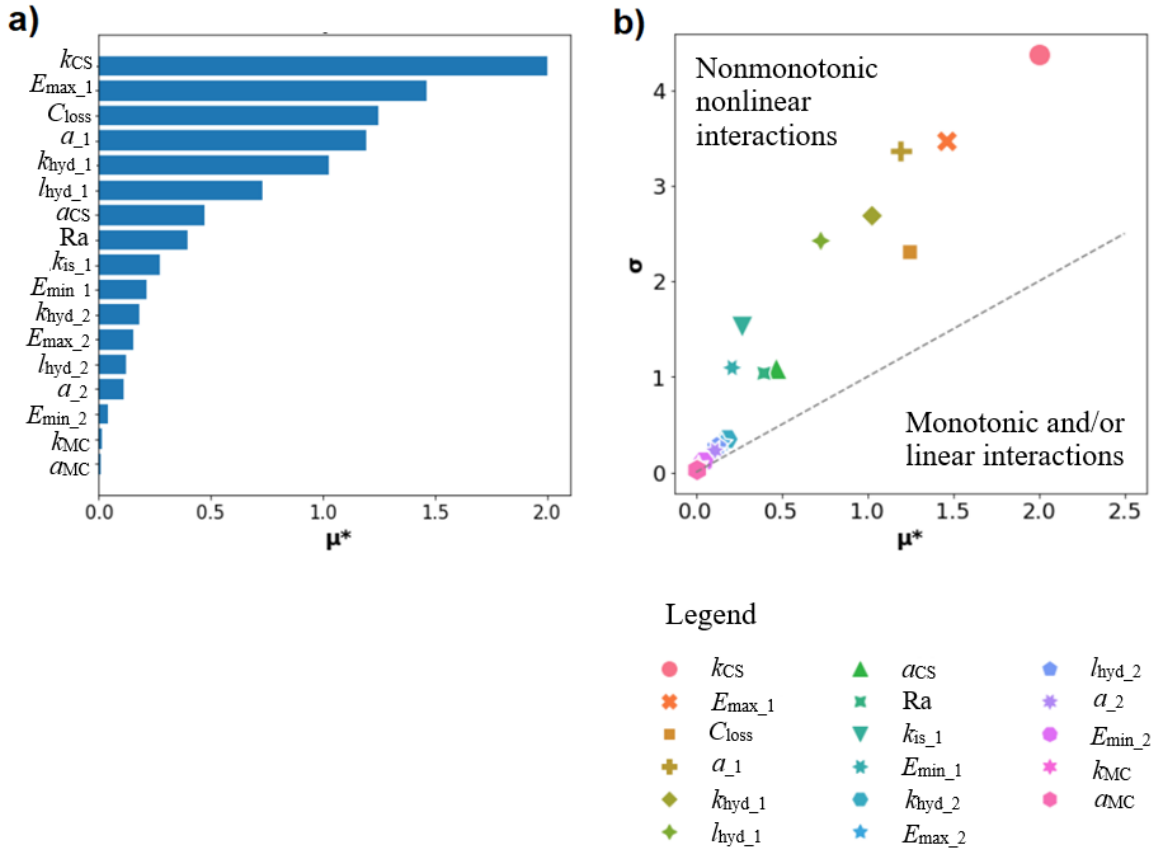

Fig. 6.3 Results of the Morris screening sensitivity analysis. **a** Mean of the absolute values of the elementary effects (μ^*) for each model parameter as index of their sensitivity. **b** Mean of the distribution of the absolute values (μ^*) against the standard deviation of the distribution (σ) for each model parameter; the areas of the graph corresponding to monotonic and/or linear interactions and nonlinear interactions (Sanchez et al. 2012) are shown with a dashed gray line.

Table 6.3 Overview of the results of the Morris analysis, including for each parameter the sensitivity ranking, the selected parameter value and the median and standard deviation for the behavioral simulations based on KGE.

Area	Parameter	Sensitivity ranking	Selected parameter value	Behavioral median	Behavioral stand.dev.
Catchment	Ra (km^2)	8	12.9	12.0	1.78
Karst (HYD1)	l_{hyd_1} (m)	6	6050	4430	1350
	k_{hyd_1} (mm^2/h)	5	4140	3640	2990
	E_{min_1} (mm)	10	8.24	12.5	3.54
	E_{max_1} (mm)	2	124	142	45
	$\alpha_{\_1}$ (-)	4	1.19	1.39	0.46
	Log(k_{is_1}) (1/h)	9	-5.34	-4.74	-3.65
Black flysch (HYD2)	l_{hyd_2} (m)	13	3300	2610	900
	k_{hyd_2} (mm^2/h)	11	274	405	287
	E_{min_2} (mm)	15	2.58	2.94	1.19
	E_{max_2} (mm)	12	27.8	18.61	6.46
	$\alpha_{\_2}$ (-)	14	1.8	1.03	0.58
Lower compartment	Log(k_{MC}) (mm/h)	16	-4.03	-3.14	-1.69
	a_{MC} (-)	17	2.33	2.01	0.59
	C_{loss} (mm)	3	0.37	0.69	0.6
	k_{CS} (mm/h)	1	0.56	1.42	2.46
	a_{CS} (-)	7	1.48	2.39	0.94

The sensitivity of the parameters was investigated by considering the distribution of the performance of the Morris model realizations over the parameter ranges (Table 6.2, Fig. 6.4).

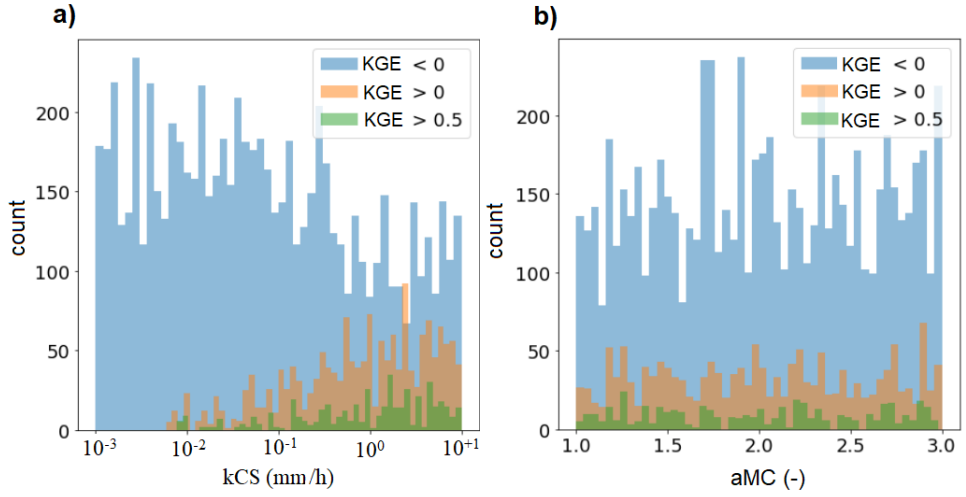

Fig. 6.4 Distribution of occurrence of the Kling-Gupta Efficiency (KGE) of the model realizations obtained by means of the Morris screening sensitivity analysis for **a** the most sensitive parameter i.e., the recession coefficient of the flow from the conduit to the spring (k_{CS}), and **b** for the least sensitive parameter i.e., the exponent of the flow transfer between the matric and the conduit (a_{MC}).

Fig. 6.4 shows the distribution of occurrence of the metric KGE of the model realizations for the most and least sensitive parameters, which are the discharge coefficient of the flow from the conduit to the spring k_{CS} and the exponent of the transfer between matrix and conduit a_{MC}, respectively (Fig. 6.3a, Table 6.3). The distribution of the realizations with KGE lower than zero, larger than zero and larger than 0.5 confirms the sensitivity rank obtained with the Morris analysis (Table 6.3). Indeed, for the exponent a_{MC}, all the three distributions of KGE are uniform over the parameter range (Fig. 6.4b). On the contrary, for the discharge coefficient k_{CS} the realizations with KGE larger than 0 and larger than 0.5 show a probability of occurrence skewed towards the right side of the parameter range (Fig 6.4a).

6.4.2 Model Calibration and validation

Among the 9000 Morris realizations, the parameter sample corresponding to the highest KGE was chosen as the selected parameter set and the corresponding realization as selected discharge. The selected parameters, calibrated for the period 1/03/2022 – 30/03/2022, are shown in Table 6.3 and lead to a KGE of 0.89. The model was then validated with the same selected parameter values for the period 30/03/2022 – 30/04/2022 leading to a KGE of 0.8. Fig. 6.5a shows the calibrated and validated discharge time series together with the observed discharge at the spring. Overall, the simulated discharge matches the rising and falling limbs of the observed hydrograph, with the exception of the recession phase between April 4 and April 18 which is underestimated by 0.08 m^3/s on average. For a better visualization, Fig. B.8 in supplementary material B.2.5 shows the time series of the observed discharge, selected discharge among the Morris´ realizations based on KGE and difference between the observed and selected discharges at the Las Hountas spring.

To account for the uncertainty in the model results, the distribution of the Morris behavioral simulations with a KGE greater than 0.5 were considered for both the calibration and the validation periods. Fig. 6.5 shows, for each flow component, i.e., Q_{spring}, Q_{hyd_1}, Q_{hyd_2}, Q_{is_1}, Q_{MC}, and Q_{Closs}, the interquartile and 10-90% percentile envelopes as well as the median of the 448 selected simulations. For each flow component, the selected simulated discharge falls inside the interquartile range. The simulated discharge at the spring Q_{spring} and the flow from the hydrotope 1 to the conduit Q_{hyd_1} show the lowest relative width of the interquartile uncertainty band (Fig. 6.5a, b, Table 6.4). On the contrary, the flow components characterized by larger uncertainty are the infiltration from hydrotope 1 to the matrix Q_{is_1} and the transfer between the matrix and conduit Q_{MC} (Fig. 6.5d, e , Table 6.4). The relative width of the 10-90% percentile ranges follows the same behavior as the interquartile ranges: Q_{spring} and Q_{hyd_1} show the narrowest bands (Fig. 6.5a, b, Table 6.4). Whereas Q_{is_1}, Q_{MC} and Q_{Closs} are characterized by the largest uncertainty (Fig. 6.5d-f, Table 6.4). The drainage from the conduit Q_{Closs} is active only during high peak discharges, whereas is null at low flow conditions (Fig. 6.5f).

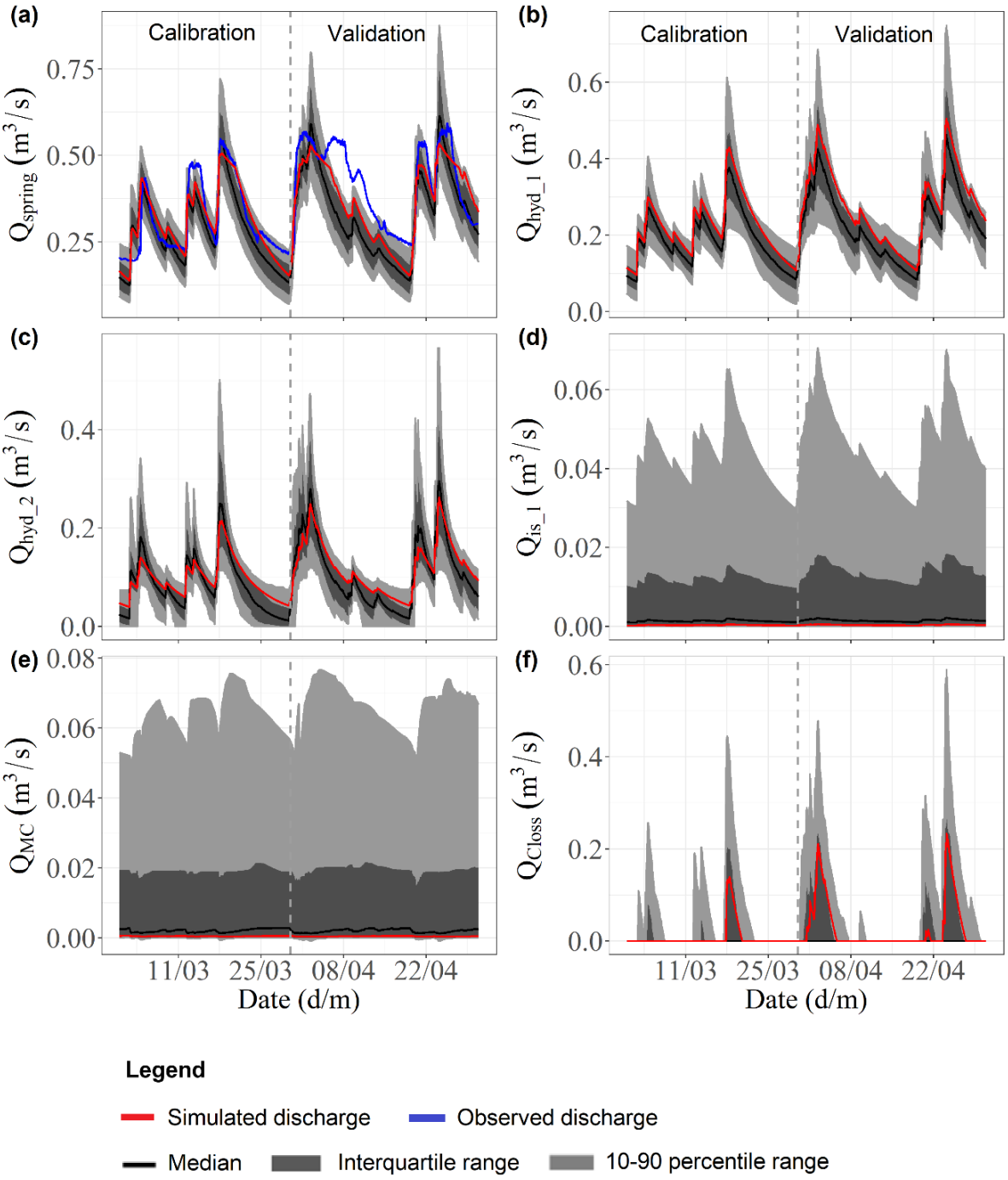

Fig. 6.5 Simulated (red lines) flow components (Q_{spring}, Q_{hyd_1}, Q_{hyd_2}, Q_{is_1}, Q_{MC} and Q_{Closs}) of the selected simulation together with their uncertainty bands computed from the distribution of the behavioral simulations with a KGE larger than 0.5 (gray bands). The dark grey and grey areas of the bands represent the interquartile and the 10-90% percentile ranges of the behavioral simulations, respectively, while the black line is the median of the distribution. The blue line is the discharge observed at the spring.

Table 6.4 Relative width of the uncertainty bands computed from the distribution of the behavioral simulations (KGE > 0.5) and of the constrained simulations (hydrochemical constrains) for the flow components Q_{spring}, Q_{hyd_1}, Q_{hyd_2}, Q_{is_1}, Q_{MC} and Q_{Closs}. Both the relative with of the interquartile and 10-90% percentile ranges were normalized considering the mean of the behavioral and constrained simulations.

Flow component	**Behavioral simulations**		**Constrained simulations**	
	Relative width interquartile range	**Relative width 10-90% percentile range**	**Relative width interquartile range**	**Relative width 10-90% percentile range**
Q_{spring}	0.345	0.613	0.185	0.555
Q_{hyd_1}	0.386	0.774	0.336	0.941
Q_{hyd_2}	0.822	1.44	0.396	0.844
Q_{is_1}	2.66	1.99	0.942	1.57
Q_{MC}	2.66	2.00	0.967	1.64
Q_{Closs}	0.39	2.41	0.962	3.1

6.4.3 Model selection using hydrochemical constraints

After validating the model by only considering the KGE metric, it was investigated whether the internal dynamics of the system, i.e., water contributions from the limestone and black flysch, were represented or not. The observed temporal dynamics of the system show high temporal variability, justifying the high-temporal resolution of hydrochemical data collection. Here, daily sampling frequencies or averaged daily values would be unsuitable to represent the variability of the water contributions. For this purpose, the high-temporal resolution hydrochemistry data collected in April 2022 (Table 6.1) were used together with the understanding of the system functioning. Richieri et al. (2023) found out that it is possible to distinguish the water contributions from the two main geological formation present in the Baget catchment by looking at the contribution to the total EC, called weight factor f_i, of HCO_3^- and SO_4^{2-}. More precisely, a simultaneous increase in $f_{SO_4^{2-}}$ and decrease in $f_{HCO_3^-}$ indicated an increase in the relative contribution from the black flysch (Richieri et al. 2023). Fig. 6.6 shows water level wl (m), EC (µcm/S) and weight factors $f_{HCO_3^-}$ (-) and $f_{SO_4^{2-}}$ (-) time series observed at the spring during the increase in water level, which occurred between 30/03 and 1/04/2023, for the event 30/03/2022 – 7/04/2022. Three peaks in $f_{SO_4^{2-}}$, simultaneous to low point in $f_{HCO_3^-}$ were observed on May 30 at 8pm, May 31 at 9.30am and May 31 at 10pm. However, the simulation selected among the 9000 Morris realizations (highest KGE) does not represent the observed varying relative water contributions. Indeed, the flow from the limestone to the conduit Q_{hyd_1} and the flow from the black flysch to the conduit Q_{hyd_2} are almost parallel lines with a null transfer between matrix and conduit Q_{MC} (Fig. 6.7a).

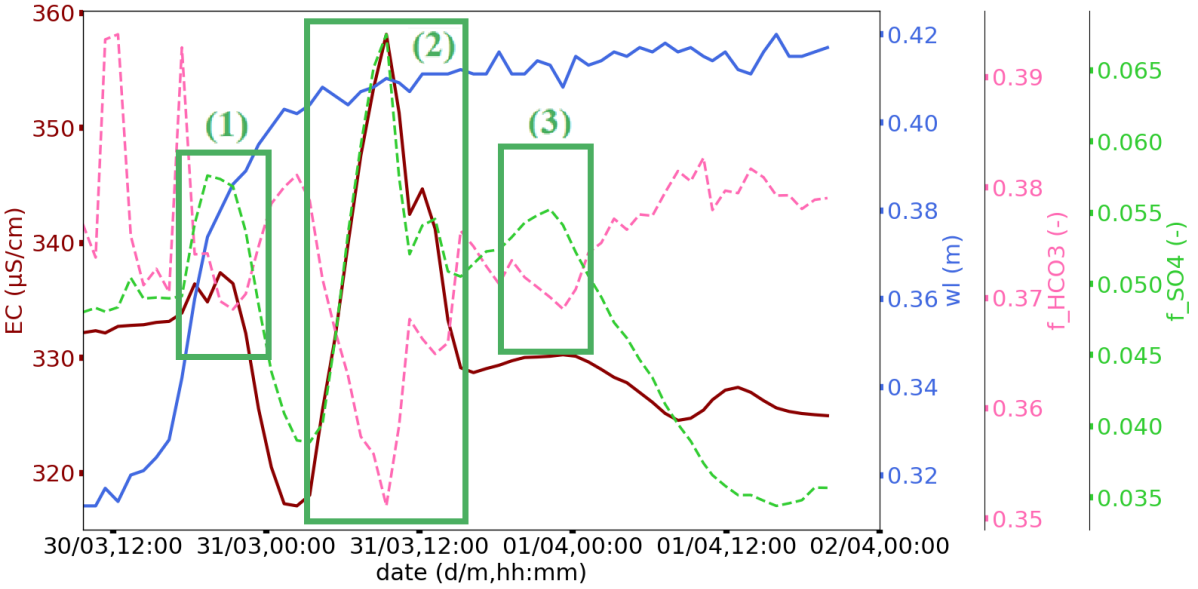

Fig. 6.6 Water level wl (m), electrical conductivity EC (µcm/S) and weight factors $f_{HCO_3^-}$ (-) and $f_{SO_4^{2-}}$ (-) time series observed at the Las Hountas spring during the increase in water level – occurred in the two days 30/03 and 1/04/2023 – for the event 30/03/2022 –7/04/2022. The weight factors are computed as the contribution of the individual free ion to the total EC (Richieri et al. 2023). The three green panels indicate the times at which there is a simultaneous increase in $f_{SO_4^{2-}}$ (-) and decrease in $f_{HCO_3^-}$ (-).

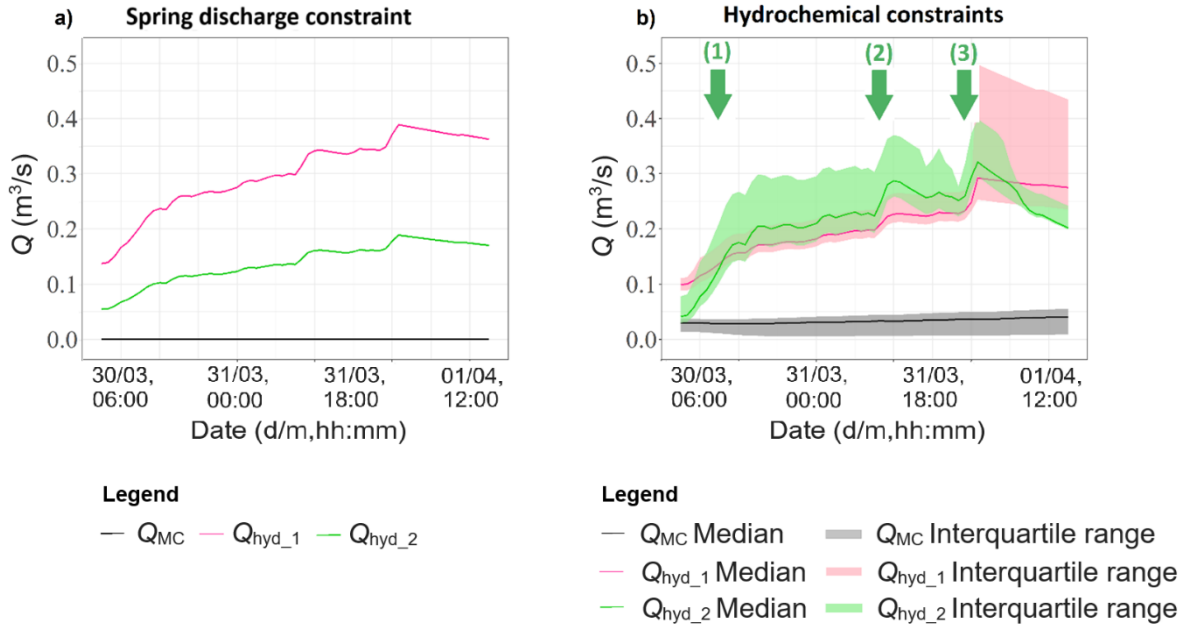

Fig. 6.7 Simulated discharge time series for the transfer between matrix and conduit Q_{MC}, the flow from hydrotope 1 (limestone) to conduit Q_{hyd_1} and the flow from hydrotope 2 (black flysch) to the conduit Q_{hyd_2} during the increase in water level – occurred in the two days 30/03 and 1/04/2023 – for the event 30/03/2022 –7/04/2022. **a** Discharge time series from the Morris´ simulation selected based on the KGE of the spring discharge. **b** Median and interquartile range of the behavioral Morris 'simulations respecting the three hydrochemical constraints. The three green arrows indicate the times at which the increase in the contribution from the black flysch Q_{hyd_2} is larger than that from the limestone Q_{hyd_1}.

Based on the observed hydrochemical data (Fig. 6.6), three hydrochemical constraints were used to identify among the Morris realizations with KGE larger than 0.5 those also respecting the internal dynamics of the system. The first criterion defines that the standard deviation of the transfer between matrix and conduit Q_{MC} needs to be significant. Here, the presented conceptual model requires that an exchange between matrix and conduit exists. To define a threshold value to consider significant the exchange, it is considered a standard deviation computed over the calibration period which has to be larger than the mean standard deviation of the behavioral Morris simulations (0.004). In fact, many behavioral simulations lead to zero or minimal exchange between the two compartments. Other thresholds for the minimum accepted standard deviation were also tested: smaller thresholds (e.g., 0.002) had limited impact on the selected simulations respecting all three criteria, whereas larger thresholds (e.g., 0.01) led to no simulation respecting all three criteria. The second criterion states that the increase in the flow from the black flysch to the conduit (Q_{hyd_2}) during the rising limb of the hydrograph must be larger than the increase in the flow from the limestone to the conduit (Q_{hyd_1}) in the same period. Finally, the third criterion defines that, on April 1, the flow from the black flysch to the conduit (Q_{hyd_2}) must be lower than the flow from the limestone to the conduit (Q_{hyd_1}). Fig. 6.7b shows the median and interquartile ranges of Q_{hy_1}, Q_{hyd_2} and Q_{MC} for the seven Morris realizations respecting the three defined hydrochemical constrains. The median of the flow from the limestone (Q_{hyd_1}) and black flysch (Q_{hyd_2}) to the conduit captures the relative increases in water contribution from the black flysch observed on May 30 at 8pm, May 31 at 9.30am and May 31 at 10pm, with the first peak anticipated of about 12 hours (Fig. 6.7b, Fig. 6.6). The median of the transfer between matrix and conduit (Fig. 6.7b) is positive during the entire rising limb of the hydrograph, indicating flow direction from the matrix to the conduit.

Fig. 6.8 shows the distribution of the constrained Morris simulations, i.e., the simulations respecting both the constraint on the spring discharge (acceptable simulations with KGE larger than 0.5) and the three hydrochemical constrains. The relative interquartile ranges of the constrained simulations (Table 6.4) are reduced in comparison to the distribution of the simulations considered behavioral based on the discharge KGE (Fig. 6.5) for all the flow components except Q_{Closs}. As observed in Fig. 6.5, Q_{spring} (Fig. 6.8a) and Q_{hyd_1} (Fig. 6.8b) are characterized by the lowest relative width of the interquartile band, whereas Q_{is_1} (Fig. 6.8d), Q_{MC} (Fig. 6.8e) and Q_{Closs} (Fig. 6.8f) by the largest (Table 6.4). The relative width of the 10-90% percentile ranges is less significantly reduced than the interquartile ranges (Fig. 6.5, Fig. 6.8). Q_{spring} (Fig. 6.8a) shows the lowest relative width of the percentile band, while Q_{MC} (Fig. 6.8e) and Q_{Closs} (Fig. 6.8f) show the largest (Table 6.4). Despite the reduction in the uncertainty bands, the median of the distribution of Q_{spring} does not respect the plateau of 0.6 m^3/s (Fig. B.6 in supplementary material B.2.3). Q_{hyd_1} and Q_{Closs} are the only flow components displaying larger relative width of the percentile band (Fig. 6.8b, Fig. 6.8f) in comparison to what observed without considering the hydrochemical constraints (Fig. 6.5, Table 6.4). Finally, the 10-90% percentile bands for Q_{hyd_2} and Q_{Closs} are characterized by a relative width which increases proportionally with the discharge.

Even if the 10-90% percentile range for Q_{spring} is overall decreased (Fig. 6.8a), the percentile band is reduced for the calibration and increased for the validation period (Fig. 6.5a, Fig. 6.8a). On the contrary of what was observed before applying the hydrochemical constraints (Fig. 6.5a), the observed discharge at the spring falls outside the 10-90% percentile band for the calibration and inside the percentile band for the validation period (Fig. 6.8a). This results from the fact that the 10-90% percentile range of Q_{spring} respecting the hydrochemical constraints (Fig. 6.8a) includes realizations which were excluded from the 10-90% percentile range of the realizations selected based only on KGE (Fig. 6.5a).

To compare the performance of the model in simulating the discharge at the spring before and after considering the hydrochemical constraints, Fig. B.8 in supplementary material B.2.5 shows the time series of the difference between observed discharge and constrained discharge. The constrained discharge corresponds to the realization with the highest KGE among the subset of realizations respecting the hydrochemical constraints.

6.5 Discussion

This section reports the novelties of the new LuKARS 2.0 conceptual model and on the use of hydrochemical criteria for the verification of model concept and parametrization.

6.5.1 New LuKARS conceptual model

LuKARS 2.0 was developed at hourly scale starting from the original LuKARS model at daily scale (Bittner et al., 2018). When comparing the values of the parameters which are in common to both models, the discharge coefficient of the fast flow k_{hy} and of the infiltration to the matrix k_{is} are the parameters showing the largest variation between daily (reported in Bittner et al., 2018) and hourly simulations (this study). This difference in magnitude can be explained by the fact that the karst system in which Bittner et al. (2018) tested LuKARS, i.e., Kesrchbaum, does not show relevant concentrated recharge processes and thus is characterized by a more pronounced infiltration than the Baget system, which shows a natural subsurface drainage rapidly recharged by sinkholes along the Lachein stream (Mangin, 1975; Sivelle and Labat, 2019). Thus, the response of Kerschbaum can be described by means of lower k_{hy} and larger k_{is} than the Baget system.

To represent the plateau in the discharge time series at the Las Hountas spring (Fig. B.6 in supplementary material B.2.3), a drain is implemented from the conduit out of the catchment. The sensitivity analysis indicates that the parameter controlling the activation of the drainage (C_{loss}) is the third most sensitive parameter (Table 6.3).

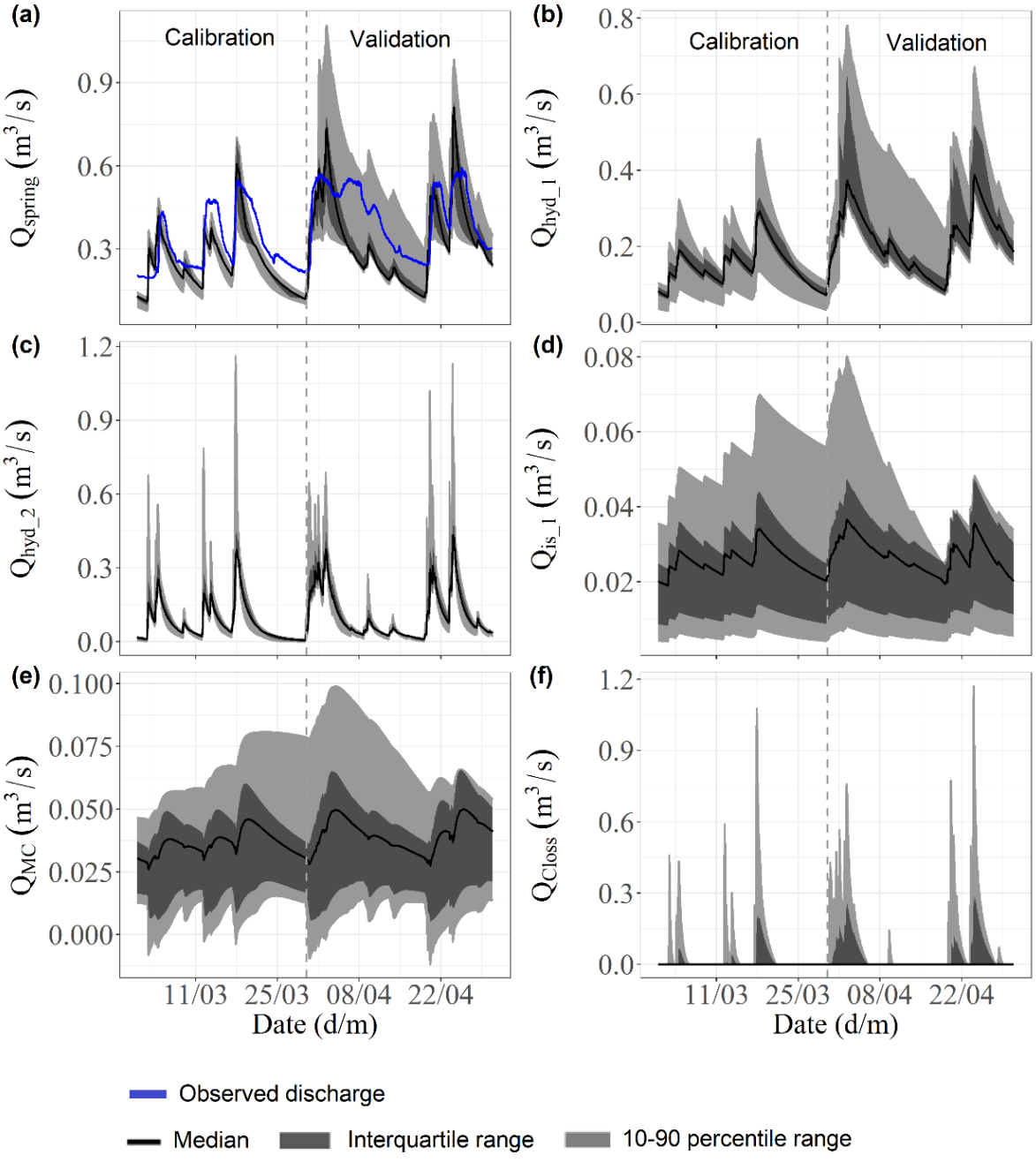

Fig. 6.8 Uncertainty bands computed from the distribution of the behavioral simulations with a KGE larger than 0.5 and respecting the three hydrochemical constrains for the flow components Q_{spring}, Q_{hyd_1}, Q_{hyd_2}, Q_{is_1}, Q_{MC} and Q_{Closs} (gray bands). The dark grey and grey areas of the bands represent the interquartile and the 10-90% percentile ranges of the behavioral simulations, respectively, while the black line is the median of the distribution. The blue line is the discharge observed at the spring

The selected Morris´ simulation as well as the interquartile range of the behavioral simulations (Fig. 6.5) confirm the relevance of the drain to discharge out of the system the excess water (Fig. 6.5f) and thus respect the maximum threshold of 0.6 m^3/s at the spring (Fig. B.6 in supplementary material B.2.3). However, the median of the behavioral simulations coincides with the 25% quartile and is constantly null throughout the calibration and validation periods, meaning that Q_{Closs} does not play a role

for 50% of the realizations (Fig. 6.5f). The behavioral simulation respecting the hydrochemical data show the same behavior (Fig. 6.8f): the median of the Q_{Closs} is constantly null while the interquartile and 10-90% percentile bands show the large impact that the drainage from the conduit has for a share of the realizations. This indicates, as discussed below, that further data at high temporal resolution, such as solutes and isotopes time series, should be considered to constrain the model parameters. In addition, time series collected in different points of the catchment would give more insight into the role of the conduits as natural drain as well as into the dynamics of the water draining from the different recharge areas.

To represent the characteristic dual response behavior of karst systems, the original LuKARS model (Bittner et al., 2018) was further modified by implementing two buckets in the lower compartment, i.e., matrix and conduit, and a transfer Q_{MC} between these two. The sensitivity analysis indicates that the parameters controlling the transfer between matrix and conduit Q_{MC}, i.e., the discharge coefficient k_{MC} and exponent a_{MC}, are the least sensitive parameters (Table 6.3, Fig. 6.3a). The selected Morris simulation and the median of the realizations with KGE larger than 0.5 are characterized by no and little influence of Q_{MC} on the simulated discharge at the spring, respectively (Fig. 6.5e). The role of the transfer between matrix and conduit becomes more relevant after applying the hydrochemical constraints: the realizations respecting the hydrochemical data (Fig. 6.6) present an increase in the width of the interquartile range and a median larger than the mean standard deviation of the behavioral Morris simulations i.e., 0.004 (Fig. 6.8e).

Overall, the selected Morris realization well represents the dynamics of the spring discharge Q_{spring} for both the calibration and validation, with exception for the period between April 4 and April 18 in which the simulated discharge is lower than the observed discharge (Fig. 6.5a). The model cannot represent the increase in discharge at the spring on April 4 due to the input data, which do not show significant precipitation on April 4 that could cause the increase in simulated discharge (Fig. B.6 in supplementary material B.2.3). The hourly precipitation data were recorded at the Antichan gauging station, approximately 8 km north-east from the Las Hountas spring, and used as spatially homogeneous input for the presented conceptual model. Due to the heterogeneity of the precipitation field, it might be that the data are not always accurate for the Baget catchment during this specific rainfall event. Consequently, the entire recession curve until April 18 systematically underestimates the observed discharge of 0.08 m^3/s on average. The raster daily E-OBS precipitation data (Cornes et al., 2018) were used as comparison with the Antichan gauging station and showed consistent observations. However, due to the daily temporal resolution and the coarse spatial resolution of the grid (0.25°) of E-OBS that dataset could not be used for the present study.

6.5.2 Sensitive parameters

The results of the sensitivity analysis can be qualitatively compared to those obtained by Bittner et al. (2020) by applying the active subspaces on the daily LuKARS. In the present paper, the parameters

related to hydrotope 1 i.e., limestone, are more sensitive than those from hydrotope 2 i.e., black flysch, probably since the limestone represents 70% of the entire catchment area and thus, assuming spatially homogeneous precipitation rate, contributes with a larger extent to the total recharge to the spring. This observation agrees with the results from Bittner et al. (2020), where the parameters related to the hydrotope with larger area are generally more sensitive. On the contrary, the sensitivity of the other parameters differs between the present study and the previous investigation, due to the different representation of the lower compartment in the model concept and the different study area. Indeed, according to Bittner et al. (2020), the discharge coefficient regulating the infiltration to the matrix k_{is} is the most sensitive parameter, whereas in the present study k_{is} shows a sensitivity ranking of 9 out of 17 (Table. 6.4).

The parameters regulating the transfer between matrix and conduit, i.e., discharge coefficient k_{MC} and exponent a_{MC}, are the least sensitive parameters of the presented model concept (Table 6.3, Fig. 6.3a). This is also due the model structure. In fact, the matrix-conduit interaction can be merged as a single compartment as for example in the original version of LuKARS. While this choice can be satisfactory to reproduce discharge time series, it can lead to erroneous hydrochemical interpretation of the results. Therefore, since the sensitivity is a function of the used objective function, the results of the sensitivity analysis performed with respect to KGE and only against the discharge at the spring may not capture the importance of all the parameters, especially when non-linearities are present (Fig. 6.3b). Indeed, the selection of the Morris´ realizations respecting the hydrochemical constrains show the relevance of the transfer between matrix and conduit. Those realizations characterized by a transfer between matrix and conduit Q_{MC} with a standard deviation larger than the mean standard deviation of the behavioral Morris´ simulations (Fig. 6.7b) well represent the observed hydrochemical dynamics (Fig. 6.6).

6.5.3 Impact of hydrochemical information on model selection

The model was calibrated and validated considering the discharge and the hydrochemical signal at the spring, respectively, over a time period of 9 days. The short period of time was chosen in line with the performed analyses such to have an event-based model. In addition, despite the limitations related to a calibration over a short period of time (Leins et al., 2023), the length of the calibration and validation periods were chosen based on the collected high-resolution hydrochemical data (Table 6.1). Indeed, the interpretation of the internal fluxes of a longer simulated period may require the consideration of reactive transport i.e., chemical reaction with soil and aquifer materials, seasonal variation in background concentrations, coexistence of water with different ages.

Based on the previous investigation into the system functioning of Richieri et al. (2023), the parameter ranges (Table 6.2) for the hydrotope 1 and hydrotope 2, i.e., limestone and black flysch, respectively, were defined to enhance a faster reaction of the black flysch in case of strong precipitation event. In fact, it was observed that when the water level at the spring rises simultaneously to the EC, the relative

contribution to EC of SO_4^{2-}, which originated from the pyrite contained in the black flysch (Eq. 6.2), increases. The faster response of the black flysch was considered by defining lower upper and lower threshold for the activation of the fast flow to the conduit (Table 6.2). However, when investigating the internal flow component of the selected Morris´ realization, the increase in fast flow from hydrotope 2, i.e., black flysch, observed during the precipitation event from 30/03/2022 to 7/04/2022 (Fig. 6) is not captured (Fig. 6.7a). Hydrochemical constraints were thus implemented to constrain those realizations respecting the dynamics of $f_{SO_4^{2-}}$ and $f_{HCO_3^-}$ (Fig. 6.6). The constrained simulations (Fig. 6.7b) capture the larger relative increases in the contribution from the black flysch and the lower relative increases in the contribution from the limestone occurred on May 30 at 8pm, May 31 at 9.30am and May 31 at 10pm. The first relative faster increase in black flysch on May 30 at 8pm (Fig. 6.7b) is anticipated respect to the observed hydrochemcial data (Fig. 6.6) of about 12 hours, probably due to the initial water content in the soil before the rise in water level and the need of a larger storage.

The verification of the model by considering hydrochemical constraints resulted in the overall reduction of the interquartile uncertainty bands respect to the case in which the Morris realizations were evaluated based only on the KGE (Fig. 6.5, Fig. 6.8). This is due to the application of the hydrochemical constraints, which reduce the selected simulations from 448 to 8. Therefore, the hydrochemical criteria may be too stringent for the validation of the parameter sets, but they can be used to verify whether the conceptual model applies to simulations and can therefore be used to test the plausibility of the conceptual model. Despite the reduction of the uncertainty bands, the median of the realizations respecting the hydrochemical constraints of Q_{spring} underestimates the baseflow and exceeds the plateau of 0.6 m^3/s (Fig. B.6 in supplementary material B.2.3), which is respected by both the selected Morris realizations and the median of the Morris realizations with a KGE larger than 0.5. Finally, the relevance of the hydrochemical constraints is also seen by the fact that the percentile range for Q_{spring} of the realizations selected based only on KGE (Fig. 6.5a) does not contain some realizations which are included in the percentiles of the realizations respecting the hydrochemical dynamics (Fig. 6.8a). Therefore, without considering the hydrochemical constraints, some parameter sets representing the hydrochemical dynamics would have been excluded.

An alternative to the approach demonstrated in this study, hydrochemical data could be used during the model calibration process. Here, the sensitive parameters of the simulations respecting the hydrochemical dynamics could be further investigated and constrained. Among the most sensitive parameters (Fig. 6.3, Table 6.3), patterns can be identified for $\alpha_{\_1}$ (-), k_{hyd_1} (mm^2/h), E_{max_1} (mm), k_{is_1}(1/h) and k_{hyd_2} (mm^2/h), whose values fall in ranges narrower than those initially defined for the Morris analysis (Table 6.2).

6.6 Conclusion

This study presents the development of LuKARS 2.0 on an hourly scale for the Baget karst catchment. The model concept was modified in comparison to the original daily LuKARS from Bittner et al. (2018) to represent the plateau of 0.6 m^3/s, which characterizes the discharge at Las Hountas spring. Thus, a drain from the conduit was implemented to discharge the excess water out of the system as soon as the water level in the conduit rises above a defined threshold. The interaction between matrix and conduit is here updated in comparison to Bittner et al. (2018) to allow a more flexible conceptualization of karst systems. The sensitivity analysis performed using the Morris method with a total of 9000 realizations was used to investigate the parameter sensitivity and to calibrate the model. The model was calibrated and validated for the periods 1/03/2022– 29/03/2022 and 30/03/2022 – 30/04/2022, respectively, considering KGE as performance metric. Among the Morris realizations, the behavioral simulations were first defined based on the KGE value of the simulated discharge at the spring. Then, three additional hydrochemical constraints were considered to represent the internal dynamics of the systems, i.e., water contributions from the limestone and black flysch present in the catchment. The hydrochemical constraints were defined based on SO_4^{2-} and HCO_3^- time series at high resolution and the previous work from Richieri et al. (2023).

The results of the present investigation show that the selected Morris realizations can represent the dynamics of the spring discharge but does not sufficiently account for the temporal variation of the contribution from the limestone and black flysch, which was observed during the rising limb of the event 30/03/2022–7/04/2022. The implementation of hydrochemical constraints leads to the representation of the relative increase in black flysch, while still providing a good match of the spring discharge. The uncertainty quantification performed on those realizations respecting the hydrochemical data show a reduction in the relative width of the interquartile bands in comparison to before the implementation of the hydrochemical constraints. The selected simulation and the interquartile range of the behavioral simulations show the relevance of the implemented drainage from the conduit to represent a plateau in the spring discharge. However, the 10-90% percentile range of the spring discharge exceed the defined threshold, indicating that further constrains in the parameter ranges would be required. In addition, further validation using other datasets would allow to investigate to which extent the information contained in hydrochemical data time series lead to a better representation of the system internal dynamics.

In conclusion, this study highlights the importance of considering the internal dynamics of a system when selecting hydrological models. Indeed, even if different model realizations simulated the spring discharge with a comparable KGE, not all of them were consistent with the dynamics of the measured SO_4^{2-} and HCO_3^- time series. Hence, hydrochemical data at high temporal resolution need to be collected to conceptualize and select hydrological models as well as to properly constrain the model parameter ranges.

Chapter 7

Conclusions, final remarks, and outlook

7.1 Summary and conclusions

In this dissertation, uncertainties in karst models were investigated by considering different sources of unknowns: input, structural, and parametric uncertainties. The research focused on hydrological conceptual karst models and potential multi-objective approaches to constrain model output uncertainties. Input uncertainties were examined through their propagation to the model output (Chapter 3). Structural uncertainties were addressed by analyzing the impact of model structures with different degrees of complexity on model performance (Chapter 4). Parametric uncertainties were addressed by using hydrochemical data, i.e., EC and major solutes, at hourly scale to constrain the parametrization of the hourly conceptual flow model LuKARS 2.0 (Chapter 6). To obtain high temporal resolution solute concentrations, a method was developed based on the decomposition of the EC signal measured at a karst spring (Chapter 5).

The first step of this dissertation was to investigate the temporal variability of input uncertainties for the LuKARS model (Chapter 3). To make possible the comparison between model input and parametric uncertainties, the study focused on the Kerschbaum karst system in Austria, for which parametric uncertainties had been previously investigated by Teixeira Parente et al. (2019). Being Kerschbaum a pre-alpine recharge area, interception, evapotranspiration, and snowmelt were identified as critical processes for groundwater recharge. A total of nine different input modelling approaches were considered, three for each considered hydrological process, i.e., interception (DVWK, Gash and Liu), evapotranspiration (Thornthwaite, Hamon and Oudin), and snowmelt (Martinec, Girons Lopez and Magnusson). To study the uncertainty propagating to the spring discharge, the groundwater recharge time series obtained by considering all possible model combinations were used as input for LuKARS. To focus on model input uncertainties, the parameters of the LuKARS model were taken constant and equal to those derived by Bittner et al. (2018), while varying the parameters of the input models. The uncertainties were analyzed considering both each individual process and the combination of more uncertain hydrological input time series. It was found out that the input uncertainties of evapotranspiration and snowmelt are higher than the interception uncertainties, and that uncertainties related to snow processes can be larger than parametric uncertainties. Moreover, the results highlight that input model uncertainties show a seasonal variability, while parametric uncertainties computed for the same model in previous studies do not show pronounced temporal variations. Input uncertainties vary over time as function of the importance of a specific process, such as snowmelt and evapotranspiration, for the groundwater recharge and thus spring discharge. This implies that the significance of a particular process for groundwater recharge can be inferred from its associated input

uncertainties. Finally, it was found out that including more uncertain hydrological input time series does not necessarily result in larger model output uncertainties, suggesting that uncertainties in different processes can offset each other.

The next step of this dissertation focused on structural model uncertainties, which were investigated by considering model structures with different levels of complexities (Chapter 4). More precisely, this investigation examined the impact on model performance of considering a semi-distributed recharge which is conceptualized with an increased number of land cover and land use (LCLU), and thus hydrotopes, in the upper model compartment (unsaturated zone). Hydrotopes are defined, following the definition of Bittner et al. (2018), as individual catchment units characterized by homogeneous LCLU and soil. Each hydrotope shows a specific response to precipitation events and thus contributes differently to the groundwater recharge and spring discharge. To account for different flow processes conceptualization, two hydrological conceptual models were selected, i.e., LuKARS and KarstMod, and a multi-model calibration was performed by testing different configurations in the upper level of the model structure (ranging from 1 to 4 hydrotopes). The study considered three recharge areas with similar LCLU (forest-dominated): Baget, Oeillal, and Kerschbaum. The performance of the model was first evaluated by considering the combination of seven numerical performance metrics, i.e., NSE, KGE, KGENP, BE, VE, Rp, and Rs (pag. 68). Then, following a multi-objective approach, the outputs of the different models were investigated by further analyzing the discharge time series. Therefore, as introduced in subsection 1.5.2, auto-correlation analysis, cross-correlation analysis and Wavelet multiresolution analysis were used to evaluate the ability of the models to capture different aspects and time scales of the hydrological processes. The results indicate that incorporating a semi-distributed recharge approach can reduce the uncertainty in quantifying internal fluxes between the upper and lower levels of the model structure. However, incorporating LCLU does not necessarily enhance the performance of hydrological conceptual models. Specifically, the semi-distributed recharge approach improved the performance of hydrological models for the Kerschbaum and Oeillal catchments, but not for the Baget catchment. The Kerschbaum and Oeillal karst springs exhibit slower recession dynamics compared to the Baget spring, which is characterized by a high degree of karstification, significant variability in spring discharge, and important matrix-conduit exchanges. The heterogeneities and high temporal variability in recharge processes at the Baget catchment are challenging to capture with a daily lumped parameter hydrological model. Therefore, a more detailed investigation using higher frequency data may be necessary to capture the dynamics of the recharge processes especially of heterogeneous and highly transient karst systems.

The subsequent steps of this dissertation focused on investigating the hydrological processes of karst systems at an hourly scale by integrating hydrological data (e.g., spring discharge) and hydrochemical data (e.g., high temporal resolution solute concentration time series). As discussed in subsection 1.3, solute concentrations are often unavailable at high temporal resolution due to the high analysis cost and

time requirements, whereas discharge and EC are commonly measured continuously at karst springs. To address the challenge of limited availability of hydrochemical data and to support the investigation of karst system dynamics at an hourly scale, this dissertation developed a method to retrieve high temporal resolution solute concentrations at a karst spring without the need for costly sampling campaigns and laboratory analyses (Chapter 5). The method is based on the decomposition of the EC signal measured at a karst spring into the individual solutes that conduct electrical current in water. Starting from continuous EC and point ionic measurements, the methods allows to obtain the concentrations of the major solutes (i.e., Ca, Mg, HCO_3, SO_4, NO_3, Cl, Na and K) at the same temporal resolution as the measured EC. Due to the high solute concentrations and complex speciation characterizing karst springs, the concentrations of each solute species occurring as free ion and as part of aqueous complexes need to be computed separately. The concentrations of the free ions, i.e., Ca^{2+}, Mg^{2+}, HCO_3^-, SO_4^{2-}, NO_3^-, Cl^-, Na^+ and K^+, were computed as linear interpolation of the relative contribution of each ion to the total measured EC, which are called weight factors *fi* and were derived using PHREEQC. On the contrary, the concentrations of species occurring as aqueous complexes were obtained from speciation calculations as difference between the total molality of a solute (mol/kgw) and the molality of the solution (mol/kgw). The method was tested in two karstic watersheds with different types of bedrock and temporal resolution of the available hydrochemical datasets, i.e. the Kerschbaum dolostone system in Austria and the Baget limestone system in France. The results show that complexation processes need to be considered for the solutes SO_4, Ca, Mg and HCO_3, whose neglection would lead to an underestimation of the total concentrations. The method was tested first by accounting for the uncertainty derived by considering the weight factors *fi* as random variables, then by applying it to reconstruct ion content for periods in which only EC data are available. The uncertainty quantification results demonstrate that the method can be effectively applied to karst systems with rather homogeneous geology, such as Kerschbaum. In such cases, the EC signal can be used to interpolate and predict the temporal dynamics of solutes that significantly contribute to the total EC and characterized by low temporal variability of weight factors *fi*, i.e., HCO_3, Ca and Mg. Conversely, in heterogeneous systems like Baget, the method fails to accurately represent the mixing of water contributions from different geological areas within the catchment. Furthermore, the results indicate that the correlation between EC, water level, and the weight factors of the free ions HCO_3^- and SO_4^{2-} can support the understanding of the system's functioning, more precisely the identification of the varying contributions of water draining different areas of the watershed, i.e., limestone and black flysch, at different flow conditions. Due to dissolution processes, water draining from limestone and black flysch impacts the chemical signature at the spring differently (Fig. B.1). For three sampling campaigns (October 2021, November 2021 and November 2022) it was observed that an increase in the weight factor of SO_4^{2-} ($f_{SO_4^{2-}}$) and a decrease in the weight factor of HCO_3^- ($f_{HCO_3^-}$), indicate a relative increase in water draining from the black flysch, simultaneous to flushing and piston effects. Conversely, an increase in $f_{HCO_3^-}$ suggests a larger contribution of water from the limestone bedrocks during dilution processes and baseflow conditions.

Understanding the internal flow dynamics of a karst system can contribute to reduce the problem of equifinality, by enhancing the development of hydrological model structures that accurately capture the functioning of specific recharge areas as well as constraining model parameters.

The final step of this dissertation focused on the use of hydrochemical data at high temporal resolution for the verification of consistent hydrological conceptual event-based karst models (Chapter 6). The study focused on the Baget karst systems and considered the understanding of the system functioning developed during the previous step of the dissertation, i.e., temporal variability of water contributions from different geological areas within the Baget catchment. Hourly solute concentrations were used for the selection of proper model parametrization, based on the observed transient water contributions from the different geological areas within the Baget recharge area. To represent the high temporal variability of the spring discharge and chemical signature at the Las Hountas spring, the LuKARS 2.0 model was developed on an hourly scale. The model concept was modified in comparison to the original LuKARS (Bittner et al., 2018) by implementing a transfer between the matrix and the conduit which allows a flexible representation of karst systems. Additionally, to represent the water bypassing the spring at high flow conditions, a drain was added to the conduit compartment to discharge excess water during high flow conditions, preventing the water level in the conduit from exceeding a certain threshold. LuKARS 2.0 was developed for the Baget karst system considering two hydrotopes in the upper compartment, which represent the main geological formations within the studied catchment, i.e., limestone and black flysch. The Morris screening was used to generate 9000 realizations, corresponding to 9000 parameter combinations, to perform a global sensitivity analysis and to calibrate the model. Calibration and validation of the model were carried out for the periods 1/03/2022– 29/03/2022 and 30/03/2022 – 30/04/2022, respectively, using the Kling-Gupta Efficiency (KGE) as the performance metric. Initially, behavioral simulations were identified from the Morris realizations based on the KGE values of the simulated spring discharge (KGE>0.5). The results show that the realization with the highest KGE accurately represents the dynamics of the spring discharge but fails in capturing the temporal variability of the observed internal fluxes. Therefore, three additional hydrochemical constraints (pag.126) were used to constrain those realizations capturing the temporal variability of the water contributions from the limestone and black flysch, which was observed during the rising limb of the event 30/03/2022– 7/04/2022. These hydrochemical constraints were derived from high-resolution time series of the weight factors $f_{SO_4^{2-}}$ and $f_{HCO_3^-}$. This approach successfully represents the relative increase in water contribution from the black flysch while still providing a good match of the spring discharge. The results of the uncertainty analysis show a reduction and increase in the interquartile and 10-90 percentile range, respectively, after applying the hydrochemical constraints. The increase in the percentile range highlights the importance of considering hydrochemical constraints: when selecting simulations based on only the computed spring discharge, there is the risk to exclude model parameter sets which would capture the internal fluxes of the system. The role of drainage from the conduit is evident from the selected simulations and the interquartile range of behavioral simulations. However, the 10-90%

percentile range of the spring discharge exceeds the defined threshold, indicating the need to further constrain the parameter range. In conclusion, although various model realizations produce similar KGE values, not all are consistent with the observed dynamics of the of $f_{SO_4^{2-}}$ and $f_{HCO_3^-}$. This highlights the significance of accounting for system's internal dynamics when selecting hydrological conceptual models.

In summary, this dissertation presents a comprehensive study of uncertainties in hydrological conceptual karst models and explores possible approaches to constrain them, with particular attention to the use of additional hydrochemical data at high temporal resolution. It was demonstrated that model input uncertainties exhibit seasonal variations and can be larger than parametric uncertainties. Furthermore, the significance of specific processes for groundwater recharge can be inferred from the respective input uncertainties. The study also found that considering a semi-distributed recharge does not necessarily enhance model performance. To address the issue of hydrochemical data availability, a method was developed to derive continuous solute concentrations from EC measurements. Additionally, to take full advantage of the information provided by high temporal resolution hydrochemical data, the LuKARS 2.0 model was developed at an hourly scale. The model parametrization of LuKARS 2.0 was successfully constrained using hourly solute concentration time series observed at the Baget karst system. Ultimately, the combined use of hydrological and hydrochemical data for the selection of appropriate model concepts for the Baget system highlighted the necessity of a more complex model structure, including the transfer between matrix and conduit compartments, although calibration based solely on spring discharge did not lead to this conclusion.

7.2 Outlook

7.2.1 Lower and Upper Benchmarks (LUB)

The investigation of the time dependency of model input uncertainties, which was the topic of Chapter 3, highlighted that the performance of hydrological models is strongly dependent on the input time series, and not only on the choice of the model parameters. It would be therefore required to quantitatively assess how much the model performance of a hydrological and hydrogeochemical lumped parameter karst model depends on the quality and quantity of the driving input boundary conditions, such as precipitation P and evapotranspiration ET. As discussed in subchapter 1.5, a single metric is not enough to consider different aspects of model performance (Cinkus et al., 2022). In addition, model results are affected also by limitation in data availability, such as precipitation data not representative of the specific area of interest due to sparse data collection. Therefore, when evaluating model results, bad performing and good performing reference models should be considered as Lower and Upper Benchmark (LUB), repectively. Despite the use of LUB have been already widely recommended (Pappenberger et al., 2015; Schaefli and Gupta, 2007; Seibert, 2001), hydrological model performance is still often solely assessed based on the value of some performance metrics (Seibert et al., 2018). The

upper benchmark represents what could be possible with a given model; the lower benchmark represents what should be expected given the available data (and their uncertainty) and the characteristics of the catchment (Seibert et al., 2018). To contribute to the discussion about the use of LUB, an evaluation of the performance of conceptual karst models could be done by accounting for LUB and their dependency on the quality and amount of available model input time series, without accounting for parametric uncertainties. In addition, it would be of relevance to extend the definition of LUB to hydrogeochemical time series, such as EC and major solutes, which are of fundamental importance for the investigation of karst systems (e.g., Wang et al., 2022, Winston and Criss, 2004). Fig. 7.1 provides an example of how uncertainties in precipitation time series (a) could affect the LUB of spring discharge Q (m^3/s) (b) and concentration of Ca (mg/L) (c). This example considers LuKARS 2.0 and its implementation for the Baget karst catchment (Chapter 6, Fig. 6.2).

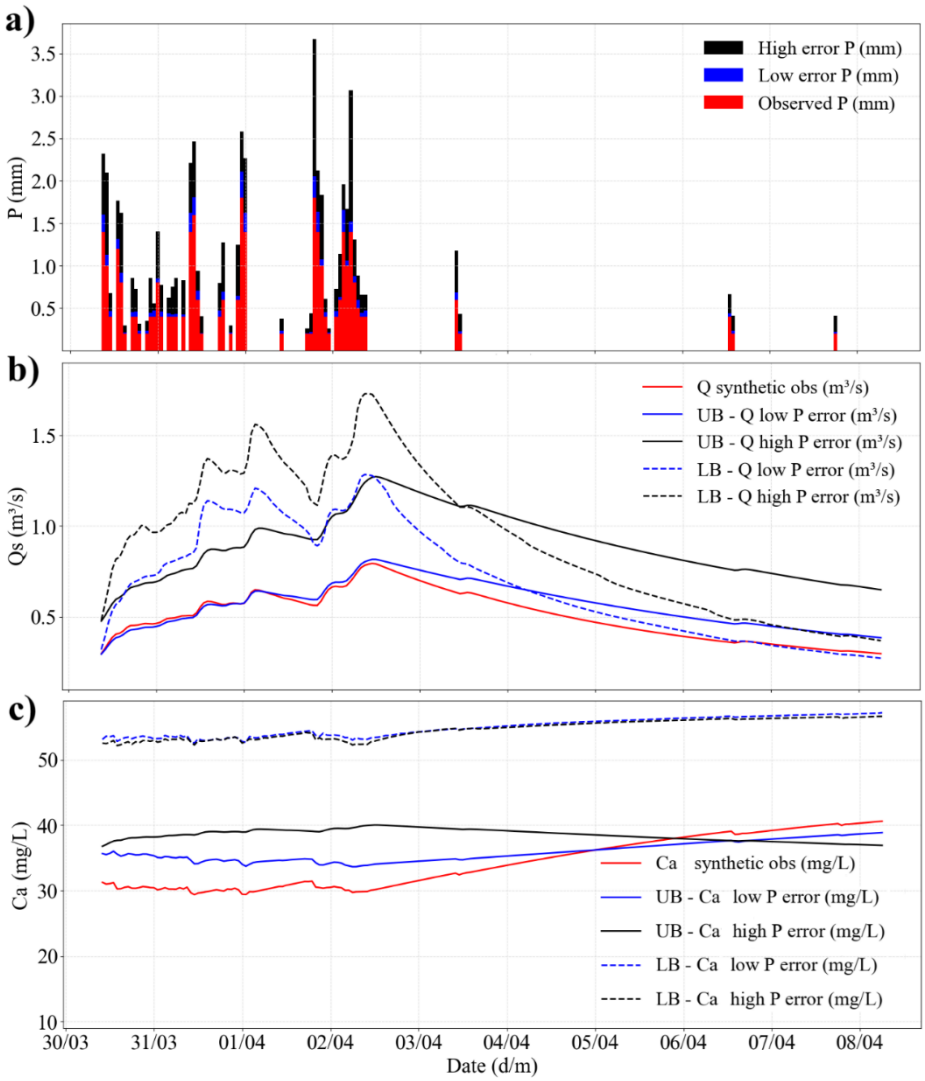

Fig.7.1 Example of how uncertainties in precipitation time series could affect the model LUB **a** Observed precipitation for the Baget karst catchment together with low (5-20%) and high error precipitation time series (30-120% of the observed precipitation). **b, c** Computed upper (UB) and lower (LB) benchmarks for discharge Q (b) and concentration Ca (c) for the case of low precipitation error

(blue) and high precipitation error (black). The UB and LB are compared with synthetic time series (red), which are obtained considering LuKARS model output.

To include different errors in the precipitation input, Fig. 7.1a shows two scenarios, i.e., low precipitation error and high precipitation error. The deviations from the observed precipitation were computed as random percentage of the observed precipitation: the deviations are in the range 5-20% and 30-120% for the low and high precipitation error scenario, respectively. For each scenario, 100 Monte Carlo realizations were run, by considering a model realization of LuKARS 2.0 with observed input precipitation as synthetic observed discharge. Fig. 7.1b shows the synthetic observed discharge together with the upper (UB) and lower (LB) benchmarks for the spring discharge (Q) for both the high and low error precipitations. The UB is defined as the Monte Carlo realization better representing the synthetic observed discharge (highest KGE), whereas the LB as the mean of the Monte Carlo realizations. Fig. 7.1.c shows the synthetic observed concentration Ca with the corresponding LUB for both the high and low error precipitations. Ca was derived from the computed internal fluxes of LuKARS 2.0, considering perfect mixing of the spring water contributions from different compartments of the model (Fig. 6.2). The percentage fluxes from hydrotope 1 (X_1), hydrotope 2 (X_2) and conduit (X_C) were obtained for each time *t* with Eq. (7.1 – 7.3) and considering null the loss of water from the conduit compartment.

$$X_{1,t} = \frac{Q_{\text{hyd\_1},t}}{Q_{\text{hyd\_1},t} + Q_{\text{hyd\_2},t} + Q_{\text{MC},t} + C_{t-1}\text{Ra}} \tag{7.1}$$

$$X_{2,t} = \frac{Q_{hyd\_2,t}}{Q_{\text{hyd\_1},t} + Q_{\text{hyd\_2},t} + Q_{\text{MC},t} + C_{t-1}\text{Ra}} \tag{7.2}$$

$$X_{\text{C},t} = \frac{C_{t-1}Ra}{Q_{\text{hyd\_1},t} + Q_{\text{hyd\_2},t} + Q_{\text{MC},t} + C_{t-1}\text{Ra}} \tag{7.3}$$

Where $Q_{\text{hyd_1}}$and $Q_{\text{hyd\_2}}$ (m^3/s) are the fast flow from hydrotope 1 and 2, respectively, to the conduit, Q_{MC} the transfer between matrix and conduit, C (m) the water level in the conduit, Ra (m^2) the recharge area and t the time.

The time series of Ca was then computed at each time t by mixing the water contributions (Eq. 7.4), assuming that each compartment is characterized by a constant chemical signature. The concentration of Ca for each compartment of the epikarst was computed by using PHREEQC and assuming instantaneous equilibrium between the rainwater and the specific solid phase representative for the corresponding geological formation. Therefore, the rainwater was assumed in equilibrium with calcite for hydrotope 1 (Ca = 44.61 mg/L) and in equilibrium with pyrite for hydrotope 2 (Ca = 0.22 mg/L). The mean Ca concentration observed during the baseflow in November 2022 was assigned to the water from the conduit (Ca = 60.51 mg/L).

$$Ca_t = 44.61\, X_{1,t} + 0.22\, X_{2,t} + 60.51\, X_{C,t} \quad (7.4)$$

For both the precipitation error scenarios, the UB for the Ca concentration was obtained by considering the X_1, X_2 and X_C corresponding to the Monte Carlo realization best representing the synthetic observed spring discharge, whereas the LB was computed by considering the mean X_1, X_2 and X_C of all the Monte Carlo realizations.

This example shows that the LUB can be significantly impacted by model input uncertainties, and thus underlines the need to further investigate how much the performance of conceptual karst models relies on the quality of input data. A comprehensive investigation considering different karst catchments with varying climate conditions and resolution of the available datasets is the objective of the RoCKaT-Bench project (project proposal under review).

7.2.2 Further develeopment of LuKARS REACT (coupling LuKARS 2.0 and IPHREEQC)

A coupled flow and transport model, called LuKARS REACT, is currently being implemented on Python by coupling LuKARS 2.0 and IPHREEQC, which is a python interface for the PHREEQC geochemical modeling software, developed by the U.S. Geological Survey (USGS). In the framework of the ROCKAT project, LuKARS REACT is being specifically applied to the Baget karst catchment. It consists of an instantaneous and complete mixing approach in each bucket based on equilibrium (similar to Hartmann et al., 2017), which could be extended with newly developed routines that conceptually account for advection and dispersion (Özdemir Calli et al., 2023). Fig. 7.2 shows the conceptual model of LuKARS (a) and of LuKARS REACT (b). Each bucket of LuKARS represents a solution on PHREEQC, whose chemical composition is updated at each time step by means of speciation calculations. The compartments representing the epikarst (PHREEQC SOLUTIONs 2 and 3) result from the equilibrium between rainwater (PHREEQC SOLUTION 1) and the specific solid phase representative for the corresponding geological formation. Thus, the limestone bedrock is represented by means of the equilibrium phase of rainwater with calcite (PHREEQC SOLUTION 2), while the black flysch by means of the equilibrium with pyrite (PHREEQC SOLUTION 3). At each time step, LuKARS provides the internal fluxes, which are then used to determine the mixing percentages of PHREEQC SOLUTIONs in each compartment. To represent dilution in each epikarst bucket, the water remaining from the previous time step (t-1) is mixed with the rainfall from the current time step (t). Then, based on the internal fluxes computed by LuKARS, a portion of this mixed water will move to the lower level of the model (before equilibrium), while the rest will stay in the bucket and go in equilibrium with the specific solid phase.

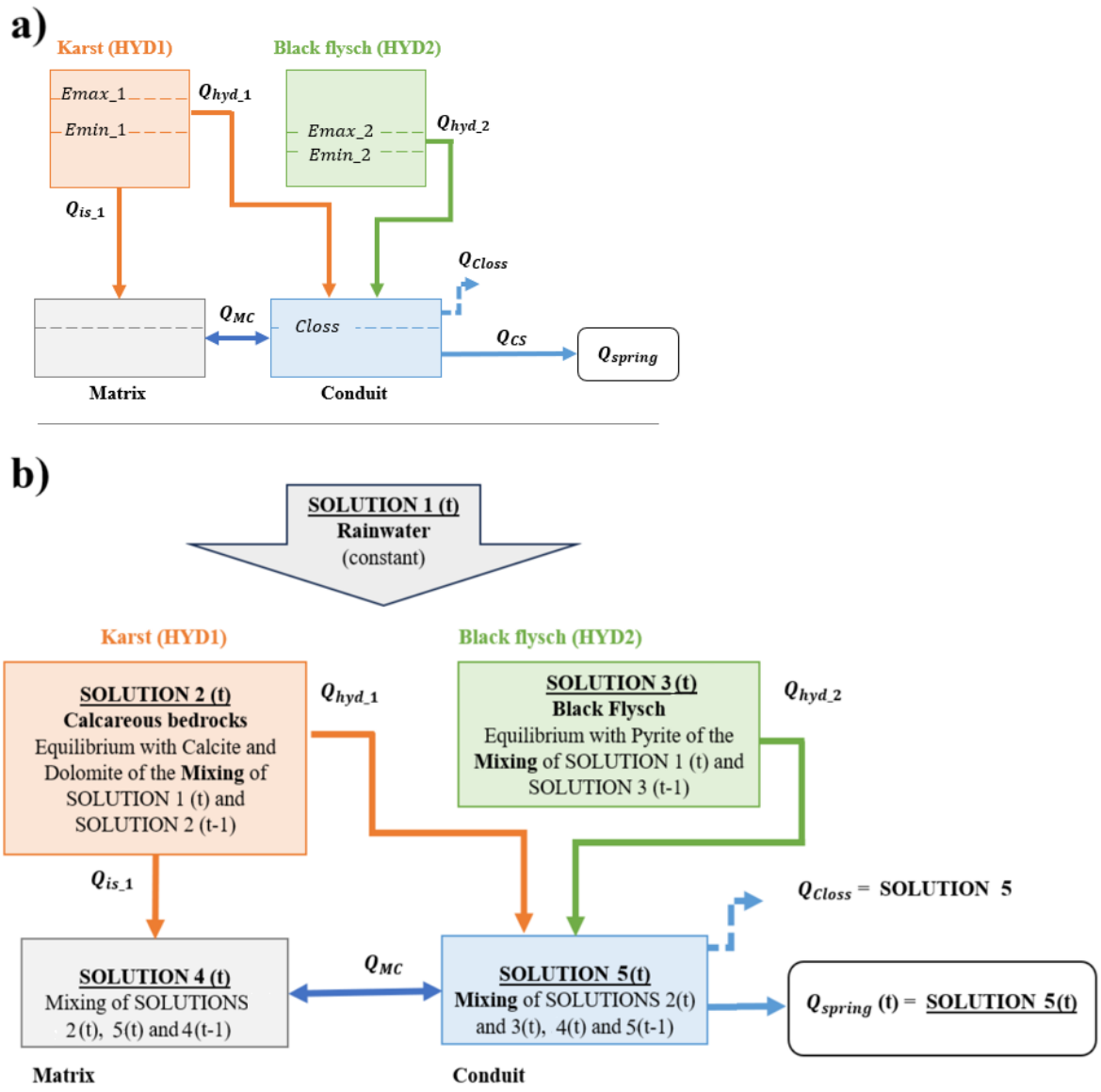

Fig. 7.2 Conceptual model of **a** LuKARS and **b** LuKARS REACT for the Baget catchment. SOLUTION refers to the PHREEQC software as defined in Parkhurst and Appelo (2013).

The water infiltrating from hydrotope 1 ($Q_{\mathrm{is\_1}}$) is mixed and routed through the matrix. When the water level in the epikarst reaches a certain threshold, there is the activation of the quickflow ($Q_{\mathrm{hyd\_1}}$ and $Q_{\mathrm{hyd\_2}}$), which results from the mixing (PHREEQC SOLUTION 5) of the water contributions from the different hydrotopes (PHREEQC SOLUTIONs 2 and 3). The water in the matrix and conduit buckets at the time step t results from the mixing between the flows from the upper level of the model concept at time step t, the water from the conduit and matrix at time step t, respectively, and the water left in the respective bucket from the previous time step t-1. Finally, the chemical composition at the spring results from the mixture between the baseflow a the mixed quickflow.

The evaluation of the coupled flow and transport model could be done by defining a new multi-objective function (MOF), which accounts for the residuals of both the computed discharge and chemical signature at the spring. An idea of possible multi-objective function is shown in Eq. 7.5.

$$\mathrm{MOF} = \sum_{i=1}^{n}(Q_i^{obs} - Q_i^{sim})^2 + \sum_{j=1}^{m} z_j \sum_{i=1}^{n}(C_{j,i}^{obs} - C_{j,i}^{sim})^2 \quad (7.5)$$

Where Q^{obs} is the observed discharge at the spring, Q^{sim} the computed discharge at the spring, C the solute concentration, n the total number of time steps, i the current time step, m the number of considered solute species, j the specific solute (e.g., Ca, Mg, HCO_3). For each solute j, the weight z_j allows to define the importance of that individual solute on the overall model performance.

After successfully implementing LuKARS REACT on Python based on perfect instantaneous mixing, other approaches will be tested. These include non-instantaneous equilibrium in the epikarst buckets and the implementation of the one-dimensional advection-diffusion equation.

Bibliography

Aeschbach-Hertig, W., and Gleeson, T. (2012). Regional strategies for the accelerating global problem of groundwater depletion. Nature Geosci 5, 853–861. https://doi.org/10.1038/ngeo1617

Ahmadi, A., Nasseri, M., and Solomatine, D.P. (2019). Parametric uncertainty assessment of hydrological models: coupling UNEEC-P and a fuzzy general regression neural network. Hydrological Sciences Journal 64:1080–1094. https://doi.org/10.1080/02626667.2019.1610565

AL Khoury, I., Boithias, L., Bailey, R. T., Ollivier, C., Sivelle, V., and Labat, D. (2023). Impact of land-use change on karst spring response by integration of surface processes in karst hydrology: the ISPEEKH model. J. Hydrol. 626(12), 130300. https://doi.org/10.1016/j.jhydrol.2023.130300

Alduchov, O.A., and Eskridge, R.E. (1996). Improved Magnus Form Approximation of Saturation Vapor Pressure. J. Appl. Meteor. 35:601–609. https://doi.org/10.1175/1520-0450(1996)035%3C0601:IMFAOS%3E2.0.CO;2

Almorox, J., Quej, V.H., and Martí, P. (2015). Global performance ranking of temperature-based approaches for evapotranspiration estimation considering Köppen climate classes. Journal of Hydrology 528:514–522. https://doi.org/10.1016/j.jhydrol.2015.06.057

Andréassian, V. (2023). On the (im)possible validation of hydrogeological models. Comptes Rendus. Géoscience 355, 1–9. https://doi.org/10.5802/crgeos.142

Aquilina, L., Ladouche, B., and Dörfliger, N. (2006). Water storage and transfer in the epikarst of karstic systems during high flow periods. Journal of Hydrology 327(3–4): 472–485. https://doi.org/10.1016/j.jhydrol.2005.11.054

Arnold, J.G., Srinivasan, R., Muttiah, R.S., and Williams, J.R. (1998). Large area hydrologic modeling and assessment part I: Model development. J Am Water Resources Assoc 34:73–89. https://doi.org/10.1111/j.1752-1688.1998.tb05961.x

Azimi, S., Massari, C., Formetta, G., Barbetta, S., Tazioli, A., Fronzi, D., Modanesi, S., Tarpanelli, A., and Rigon. R. (2023). On understanding mountainous carbonate basins of the Mediterranean using parsimonious modeling solutions, Hydrol. Earth Syst. Sci., 27, 4485–4503, https://doi.org/10.5194/hess-27-4485-2023

Bailly-Comte, V., Martin, J., and Screaton, E. (2011). Time variant cross correlation to assess residence time of water and implication for hydraulics of a sink-rise karst system. Water Resources Research, 47(5). https://doi.org/10.1029/2010WR009613

Bakalowicz, M. (2005). Karst groundwater: a challenge for new resources. Hydrogeology Journal, 13, 148–160. https://doi.org/10.1007/s10040-004-0402-9

Bancheri, M., Serafin, F., and Rigon, R. (2019). The representation of hydrological dynamical systems using Extended Petri Nets (EPN). Water Resources Research, 55, 8895–8921. https://doi.org/10.1029/2019WR025099

Barberá, J. A., and Andreo, B. (2012). Functioning of a karst aquifer from S Spain under highly variable climate conditions, deduced from hydrochemical records. Environ Earth Sciences 65(8), 2337–2349. https://doi.org/10.1007/s12665-011-1382-4

Barbieri, M., Boschetti, T., Petitta, M., and Tallini, M. (2005). Stable isotope (2H, 18O and 87Sr/86Sr) and hydrochemistry monitoring for groundwater hydrodynamics analysis in a karst aquifer (Gran Sasso, Central Italy). Applied Geochemistry, 20(11), 2063-2081, ISSN 0883-2927. https://doi.org/10.1016/j.apgeochem.2005.07.008

Batiot, C., Emblanch, C., and Blavoux, B. (2003). Total Organic Carbon (TOC) and magnesium (Mg2+): Two complementary tracers of residence time in karstic systems. Comptes Rendus Géoscience, 335(2), 205–214. https://doi.org/10.1016/S1361-0713(03)00027-0

Baudement, C., Arfib, B., Mazzilli, N., Jouves, J., Lamarque, T., and Guglielmi, Y. (2017). Groundwater management of a highly dynamic karst by assessing baseflow and quickflow with a rainfall-discharge model (Dardennes springs, SE France). Bull. Société Géologique Fr. 188, 40. https://doi.org/10.1051/bsgf/2017203

Bear, J. (1975). Dynamics of Fluids in Porous Media. Soil Science, 120, 162–163. https://doi.org/10.1097/00010694-197508000-00022

Berner, R. A., and Morse, J. W. (1974). Dissolution kinetics of calcium carbonate in sea water; IV, Theory of calcite dissolution. American Journal of Science, 274(2), 108–134. https://doi.org/10.2475/AJS.274.2.108

Bennett, N.D., Croke, B.F.W., Guariso, G., Guillaume, J.H.A., Hamilton, S.H., Jakeman, A.J., Marsili-Libelli, S., Newham, L.T.H., Norton, J.P., Perrin, C., Pierce, S.A., Robson, B., Seppelt, R., Voinov, A.A., Fath, B.D., Andreassian, V. (2013). Characterising performance of environmental models. Environmental Modelling and Software 40, 1–20. https://doi.org/10.1016/j.envsoft.2012.09.011

Benettin, P., and Van Breukelen, B. M. (2017). Decomposing the Bulk Electrical Conductivity of Streamflow to Recover Individual Solute Concentrations at High Frequency. Environmental Science and Technology Letters 4(12): 518-522. https://doi.org/10.1021/acs.estlett.7b00472

Berthelin, R., and Hartmann, A. (2020). The Shallow Subsurface of Karst Systems: Review and Directions. In C. Bertrand, S. Denimal, M. Steinmann, and P. Renard (Eds.), Advances in Karst Science

(Issue April, pp. 61–68). Springer International Publishing. https://doi.org/10.1007/978-3-030-14015-1_7

Beven, K.J., and Freer, J.E. (2001). Equifinality, data assimilation, and uncertainty estimation in mechanistic modelling of complex environmental systems using the GLUE methodology. Journal of Hydrology, 249, 11-29. https://doi.org/10.1016/S0022-1694(01)00421-8

Bhanja, S. N., Coon, E. T., Lu, D., and Painter, S. L. (2023). Evaluation of distributed process-based hydrologic model performance using only a priori information to define model inputs. Journal of Hydrology, 618, 129176. https://doi.org/10.1016/j.jhydrol.2023.129176

Birk, S., Geyer, T., Liedl, R., and Sauter, M. (2005). Process-based interpretation of tracer tests in carbonate aquifers, Ground Water, 43, 381–388. https://doi.org/10.1111/j.1745-6584.2005.0033.x

Bittner, D., Narany, T.S., Kohl, B., Disse, M., and Chiogna, G. (2018). Modeling the hydrological impact of land use change in a dolomite-dominated karst system. Journal of Hydrology 567:267–279. https://doi.org/10.1016/j.jhydrol.2018.10.017

Bittner, D. (2020). Uncertainty quantification in modeling karst water resources and the impacts of land use changes (Doctoral dissertation, Technische Universität München). https://nbn-resolving.de/urn/resolver.pl?urn:nbn:de:bvb:91-diss-20200528-1531295-1-2

Bittner, D., Rychlik, A., Klöffel, T., Leuteritz, A., Disse, M., and Chiogna, G. (2020a). A GIS-based model for simulating the hydrological effects of land use changes on karst systems – The integration of the LuKARS model into FREEWAT. Environmental Modelling and Software 127:104682. https://doi.org/10.1016/j.envsoft.2020.104682

Bittner, D., Parente, M.T., Mattis, S., Wohlmuth, B., Chiogna, G. (2020b). Identifying relevant hydrological and catchment properties in active subspaces: An inference study of a lumped karst aquifer model. Advances in Water Resources 135:103472. https://doi.org/10.1016/j.advwatres.2019.103472

Bittner, D., Richieri, B., and Chiogna, G. (2021). Unraveling the time-dependent relevance of input model uncertainties for a lumped hydrologic model of a pre-alpine karst system. Hydrogeol. J. https://doi.org/10.1007/s10040-021-02377-1

Bittner, D., Engel, M., Wohlmuth, B., Labat, D., and Chiogna, G. (2021b). Temporal scale-dependent sensitivity analysis for hydrological model parameters using the discrete wavelet transform and active subspaces. Water Resources Research, 57, e2020WR028511. https://doi.org/10.1029/2020WR028511

Blöschl, G., and Sivapalan, M., (1995). Scale issues in hydrological modelling: A review. Hydrol. Process. 9, 251–290. https://doi.org/10.1002/hyp.3360090305

Boyd, C.E. (2020). Carbon dioxide, pH, and alkalinity. In: Water quality. Springer, Cham. https://doi.org/10.1007/978-3-030-23335-8_9

Braun, L., and Renner, C. (1992). Application of a conceptual runoff model in different physiographic regions of Switzerland. Hydrological Sciences Journal 37:217–231. https://doi.org/10.1080/02626669209492583

Brehier, F. (2019). Horizon VerticalSaint Girons, France. Speleoglogic Investigations over the Baget Area. Personal Communication

Breinl, K. (2016). Driving a lumped hydrological model with precipitation output from weather generators of different complexity. Hydrological Sciences Journal 61:1395–1414. https://doi.org/10.1080/02626667.2015.1036755

Brenner, S., Coxon, G., Howden, N.J.K., Freer, J., and Hartmann, A. (2018). Process-based modelling to evaluate simulated groundwater levels and frequencies in a Chalk catchment in south-western England. Nat. Hazards Earth Syst. Sci. 18, 445–461. https://doi.org/10.5194/nhess-18-445-2018

Bussotti, F., Ferrini, F., Pollastrini, M., and Fini, A. (2014). The challenge of Mediterranean sclerophyllous vegetation under climate change: From acclimation to adaptation. Environ. Exp. Bot., Response to abiotic stresses of plants of Mediterranean-type ecosystems 103, 80–98. https://doi.org/10.1016/j.envexpbot.2013.09.013

Butscher, C., and Huggenberger, P. (2008). Intrinsic vulnerability assessment in karst areas: A numerical modeling approach. Water Resour. Res. 44. https://doi.org/10.1029/2007WR006277

Butts, M.B., Payne, J.T., Kristensen, M., and Madsen, H. (2004). An evaluation of the impact of model structure on hydrological modelling uncertainty for streamflow simulation. Journal of Hydrology 298:242–266. https://doi.org/10.1016/j.jhydrol.2004.03.042

Calder, I.R. (1996). Dependence of rainfall interception on drop size: 1. Development of the two-layer stochastic model. Journal of Hydrology 185:363–378. https://doi.org/10.1016/0022-1694(95)02998-2

Çallı K. Ö., Bittner, D., Liu, Y., Çallı, S. S., Melsen, L. A., Bense, V., and Hartmann, A. (2023). Revealing the positive influence of young water fractions derived from stable isotopes on the robustness of karst water resources predictions. Journal of Hydrology, 621, 129549. https://doi.org/10.1016/j.jhydrol.2023.129549

Calmels, D., Gaillardet, J., and François, L. (2014). Sensitivity of carbonate weathering to soil CO2 production by biological activity along a temperate climate transect. Chemical Geology, 390, 74–86. https://doi.org/10.1016/j.chemgeo.2014.10.010

Campolongo, F., Cariboni, J., and Saltelli, A. (2007). An effective screening design for sensitivity analysis of large models. Environmental Modelling and Software, Modelling, computer-assisted simulations, and mapping of dangerous phenomena for hazard assessment 22, 1509–1518. https://doi.org/10.1016/j.envsoft.2006.10.004

Cano-Paoli, K., Chiogna, G., and Bellin, A. (2019). Convenient use of electrical conductivity measurements to investigate hydrological processes in Alpine headwaters. Science of The Total Environment 685: 37-49. https://doi.org/10.1016/j.scitotenv.2019.05.166

Castany, G. (1968). Prospection et exploitation des eaux souterraines. Paris: Dunod.

Charlier, J. -B., Ladouche, B., Mar´echal, J. -C. (2015). Identifying the impact of climate and anthropic pressures on karst aquifers using wavelet analysis. J. Hydrol. 523, 610–623. https://doi.org/10.1016/j.jhydrol.2015.02.003

Chang, Y., Hartmann, A., Liu, L., Jiang, G., and Wu, J. (2021). Identifying more realistic model structures by electrical conductivity observations of the karst spring. Water Resources Research, 57, e2020WR028587. https://doi.org/10.1029/2020WR028587

Charlier, J.-B., Bertrand, C., and Mudry, J. (2012). Conceptual hydrogeological model of flow and transport of dissolved organic carbon in a small Jura karst system, J. Hydrol., 460–461, https://doi.org/10.1016/j.jhydrol.2012.06.043

Chen, Z., Grasby, S. E., and Osadetz, K. G. (2004). Relation between climate variability and groundwater levels in the upper carbonate aquifer, southern Manitoba, Canada. Journal of Hydrology, *290*(1-2), 43–62. https://doi.org/10.1016/j.jhydrol.2003.11.029

Chen, Z., Hartmann, A., and Goldscheider, N. (2017). A new approach to evaluate spatiotemporal dynamics of controlling parameters in distributed environmental models. Environmental Modelling and Software, 87. https://doi.org/10.1016/j.envsoft.2016.10.005

Chen, Z., Hartmann, A., Wagener, T., and Goldscheider, N. (2018). Dynamics of water fluxes and storages in an Alpine karst catchment under current and potential future climate conditions. Hydrol. Earth Syst. Sci. 22, 3807–3823. https://doi.org/10.5194/hess-22-3807-2018

Chiogna, G., Marcolini, G., Engel, M. and Wohlmuth, B. (2024). Sensitivity analysis in the wavelet domain: a comparison study. Stochastic Environmental Research and Risk Assessment. https://doi.org/10.1007/s00477-023-02654-3

Chiogna, G., Marcolini, G., Liu, W., Pérez Ciria, T., and Tuo, Y. (2018). Coupling hydrological modeling and support vector regression to model hydropeaking in alpine catchments. Science of The Total Environment, 633, 220–229. https://doi.org/10.1016/j.scitotenv.2018.03.162

Cinkus, G., Mazzilli, N., Jourde, H., Wunsch, A., Liesch, T., Ravbar, N., Chen, Z., and Goldscheider, N. (2022). When best is the enemy of good – critical evaluation of performance criteria in hydrological models, Hydrol. Earth Syst. Sci. Discuss. https://doi.org/10.5194/hess-2022-380

Colaizzi, P.D., Kustas, W.P., Anderson, M.C., Agam, N., Tolk, J.A., Evett, S.R., Howell, T.A., Gowda, P.H., and O'Shaughnessy, S.A. (2012). Two-source energy balance model estimates of

evapotranspiration using component and composite surface temperatures. Advances in Water Resources 50:134–151. https://doi.org/10.1016/j.advwatres.2012.06.004

Cornes, R., van der Schrier, G., van den Besselaar, E. J. M., and Jones, P.D. (2018). An Ensemble Version of the E-OBS Temperature and Precipitation Datasets. Journal of Geophysical Research: Atmospheres,123(17). https://doi.org/10.1029/2017JD028200

Criss, R.E., and Winston, W.E. (2008). Do Nash values have value? Discussion and alternate proposals. Hydrol. Process. 22, 2723–2725. https://doi.org/10.1002/hyp.7072

Cukier, R.I., Levine, H.B., and Shuler, K.E. (1978). Nonlinear sensitivity analysis of multiparameter model systems. Journal of Computational Physics 26:1–42. https://doi.org/10.1016/0021-9991(78)90097-9

Dagan, G. (1988). Time-dependent macrodispersion for solute transport in anisotropic heterogeneous aquifers. Water Resources Research, 24(9), 1491–1500. https://doi.org/10.1029/WR024I009P01491

Dal Soglio, L., Danquigny, C., Mazzilli, N., Emblanch, C., and Massonnat, G. (2020). Modeling the Matrix-Conduit Exchanges in Both the Epikarst and the Transmission Zone of Karst Systems. Water 12, 3219. https://doi.org/10.3390/w12113219

Darcy H., (1856). Les fontaines publiques de la ville de Dijon : exposition et application des principes `a suivre et des formules `a employer dans les questions de distribution d'eau, Paris, Victor Dalmont.

De Stefano, L., Duncan, J., Dinar, S., Stahl, K., Strzepek, K. M., and Wolf, A. T. (2012). Climate change and the institutional resilience of international river basins. J. Peace Res 49 (1), 193–209. https://doi.org/10.1177/0022343311427416

Debroas, É-J. (2009). Géologie du bassin versant du Baget (zone nord-pyrénéenne, Ariège, France): nouvelles observations et consequences. Strata, 3 (46), p.93. ISSN 0296-2055

Delbart, C., Valdes, D., Barbecot, F., Tognelli, A., Richon, P., and Couchoux, L. (2014). Temporal variability of karst aquifer response time established by the sliding-windows cross-correlation method. Journal of Hydrology, 511, 580-588. https://doi.org/10.1016/j.jhydrol.2014.02.008

Doherty, J. (2010). PEST, Model-Independent Parameter Estimation—User Manual. 5th Edition, with Slight Additions, Watermark Numerical Computing, Brisbane.

Doummar, J., Hassan, Kassem, A., and Gurdak, J.J. (2018). Impact of historic and future climate on spring recharge and discharge based on an integrated numerical modelling approach: Application on a snow-governed semi-arid karst catchment area. Journal of Hydrology 565:636–649. https://doi.org/10.1016/j.jhydrol.2018.08.062

Doummar, J., Sauter, M., and Geyer, T. (2012). Simulation of flow processes in a large scale karst system with an integrated catchment model (Mike She)—Identification of relevant parameters influencing spring discharge. J. Hydrol., 426–427, 112–123. https://doi.org/10.1016/j.jhydrol.2012.01.021

Dreybrodt, W. (1990). The Role of Dissolution Kinetics in the Development of Karst Aquifers in Limestone: A Model Simulation of Karst Evolution. The Journal of Geology, 98(5), 639–655. https://doi.org/10.1086/629431

Dreiss S. J. (1989). Regional scale transport in a Karst Aquifer: 1. Component separation of spring flow hydrographs. Water Resources Research 25(1): 117–125. https://doi.org/10.1029/wr025i001p00117

Duran, L., Massei, N., Lecoq, N., Fournier, M., and Labat, D. (2020). Analyzing multi-scale hydrodynamic processes in karst with a coupled conceptual modeling and signal decomposition approach. Journal of Hydrology, 583, 124625. https://doi.org/10.1016/j.jhydrol.2020.124625

Đurović, M. Ć, Petrič, M., Jemcov, I., Mulec, J., Grudnik, Z. M., Mayaud, C., Blatnik, M., Kogovšek, B., and Ravbar, N. (2022). Multivariate Statistical Analysis of Hydrochemical and Microbiological Natural Tracers as a Tool for Understanding Karst Hydrodynamics (The Unica Springs, SW Slovenia). Water Resources Research, 58(11). https://doi.org/10.1029/2021WR031831

DVWK. (1996). Ermittlung der Verdunstung von Land- und Wasserflächen (Determination of evaporation from land and water). DVWK-Merkblatt , 238/1996.

Eberhart, R., Kennedy, J. (1995). Particle swarm optimization, in: Proceedings of the IEEE International Conference on Neural Networks. Citeseer, pp. 1942–1948. https://doi.org/10.1109/ICNN.1995.488968

Efstratiadis, A. and Koutsoyiannis, D. (2010). One decade of multi-objective calibration approaches in hydrological modelling: a review. Hydrological Sciences Journal, 55(1), 58–78. https://doi.org/10.1080/02626660903526292

Ellison, D., N. Futter, M., and Bishop, K. (2012). On the forest cover–water yield debate: from demand-to supply-side thinking. Glob. Change Biol. 18, 806–820. https://doi.org/10.1111/j.1365-2486.2011.02589.x

Enemark, T., Peeters, L. J. M., Mallants, D., and Batelaan, O. (2019). Hydrogeological conceptual model building and testing: A review. Journal of Hydrology, 569. https://doi.org/10.1016/j.jhydrol.2018.12.007

Engelhardt, I., De Aguinaga, J. G., Mikat, H., Schüth, C., and Liedl, R. (2014). Complexity vs. simplicity: groundwater model ranking using information criteria. Groundwater, 52(4), 573-583. https://doi.org/10.1111/gwat.12080

Ewers, R. O., White, K. A. and Fuller, J. F. (2012). Contaminant plumes and pseudoplumes in karst aquifers. Carbonates Evaporites 27, 153–159. https://doi.org/10.1007/s13146-012-0099-0

Fandel, C., Ferré, T., Chen, Z., Renard, P., and Goldscheider, N. (2020). A model ensemble generator to explore structural uncertainty in karst systems with unmapped conduits. Hydrogeol J 414–415:516. https://doi.org/10.1007/s10040-020-02227-6

Faulkner, J., Hu, B. X., Kish, S., and Hua, F. (2009). Laboratory analog and numerical study of groundwater flow and solute transport in a karst aquifer with conduit and matrix domains. J Contam Hydrol, 110(1):34–44. https://doi.org/10.1016/j.jconhyd.2009.08.004

Ferreira, P. M. de L., Paz, A.R. da, and Bravo, J. M. (2020). Objective functions used as performance metrics for hydrological models: state-of-the-art and critical analysis. RBRH 25, e42. https://doi.org/10.1590/2318-0331.252020190155

Field, M.S. (2018). Investigating and Remediating Contaminated Karst Aquifers. In: White, W., Herman, J., Herman, E., Rutigliano, M. (eds) Karst Groundwater Contamination and Public Health. Advances in Karst Science. Springer, Cham. https://doi.org/10.1007/978-3-319-51070-5_11

Field, M. S., and Pinsky, P. F. (2000). A two-region nonequilibrium model for solute transport in solution conduits in karstic aquifers. Journal of Contaminant Hydrology, 44(3-4), 329-351. https://doi.org/10.1016/S0169-7722(00)00099-1

Field, M. S., & Leij, F. J. (2014). Combined physical and chemical nonequilibrium transport model for solution conduits. Journal of contaminant hydrology, 157, 37-46. https://doi.org/10.1016/j.jconhyd.2013.11.001

Filippini, M., Squarzoni, G., Waele, J., Fiorucci, A., Vigna, B., Grillo, B., Riva, A., Rossetti, S., Zini, L., Casagrande, G., Stumpp, C., and Gargini, A. (2018). Differentiated spring behavior under changing hydrological conditions in an alpine karst aquifer. Journal of Hydrology, 556, 572-584. https://doi.org/10.1016/j.jhydrol.2017.11.040

Fiorillo, F., and Guadagno, F. M. (2012). Long karst spring discharge time series and droughts occurrence in Southern Italy. Environ. Earth Sci. 65, 2273–2283. https://doi.org/10.1007/s12665-011-1495-9

Fleury, P., Plagnes, V., and Bakalowicz, M. (2007). Modelling of the functioning of karst aquifers with a reservoir model: Application to Fontaine de Vaucluse (South of France). Journal of Hydrology 345:38–49. https://doi.org/10.1016/j.jhydrol.2007.07.014

Foley, J. A., Ramankutty, N., Brauman, K. A., Cassidy, E. S., Gerber, J. S., Johnston, M., Mueller, N. D., O'Connell, C., Ray, D. K., West, P. C., Balzer, C., Bennett, E. M., Carpenter, S. R., Hill, J.,

Monfreda, C., Polasky, S., Rockström, J., Sheehan, J., Siebert, S., Tilman, D., and Zaks, D. P. (2011). Solutions for a cultivated planet. Nature, 478, 337–342. https://doi.org/10.1038/nature10452

Ford, D. C. and Williams, P. W. (2007). Karst Hydrogeology and Geomorphology, John Wiley and Sons, Wiley, Chichester, United Kingdom, 567 pp., ISBN:978-0-470-84996-5. https://doi.org/10.1002/9781118684986

Forkasiewicz, M. J., and Paloc, H. (1967). Régime de tarissement de la foux-de-la-vis (Gard) étude préliminaire. La Houille Blanche, 53(1), 29–36. https://doi.org/10.1051/lhb/1967002

Fornasini, P. (2008). The Uncertainty in Physical Measurements. An Introduction to Data Analysis in the Physics Laboratory. Springer. https://doi.org/10.1007/978-0-387-78650-6

Frank, S., Goeppert, N., Ohmer, M., and Goldscheider, N. (2019). Sulfate variations as a natural tracer for conduit-matrix interaction in a complex karst aquifer. Hydrological Processes 33(9): 1292-1303. https://doi.org/10.1002/hyp.13400

García-Ruiz, J.M., López-Moreno, J.I., Vicente-Serrano, S.M., Lasanta–Martínez, T., and Beguería, S. (2011). Mediterranean water resources in a global change scenario. Earth-Sci. Rev. 105, 121–139. https://doi.org/10.1016/j.earscirev.2011.01.006

Garrigues, S., Olioso, A., Calvet, J.C., Martin, E., Lafont, S., Moulin, S., Chanzy, A., Marloie, O., Buis, S., Desfonds, V., Bertrand, N., and Renard, D. (2015). Evaluation of land surface model simulations of evapotranspiration over a 12-year crop succession: impact of soil hydraulic and vegetation properties. Hydrol. Earth Syst. Sci. 19:3109–3131. https://doi.org/10.5194/hess-19-3109-2015

Gash, J.H.C., Lloyd, C.R., and Lachaud, G. (1995). Estimating sparse forest rainfall interception with an analytical model. Journal of Hydrology 170:79–86. https://doi.org/10.1016/0022-1694(95)02697-N

GBA. (2021). Geologische Bundesländerkarten (Geological maps of the federal states). Geologische Bundesanstalt Österreich

Geyer, T., Birk, S., Liedl, R., and Sauter, M. (2008). Quantification of temporal distribution of recharge in karst systems from spring hydrographs, Journal of Hydrology (348), 452–463. https://doi.org/10.1016/j.jhydrol.2007.10.015

Gil-Márquez, J. M., Barberá, J. A., Andreo, B., and Mudarra, M. (2017). Geochemical Evolution of Groundwater in an Evaporite Karst System: Brujuelo Area (Jaén, S Spain). Procedia Earth and Planetary Science, 17, 336–339. https://doi.org/10.1016/j.proeps.2016.12.085

Girons Lopez, M., Vis, M. J. P., Jenicek, M., Griessinger, N., and Seibert, J. (2020). Assessing the degree of detail of temperature-based snow routines for runoff modelling in mountainous areas in central Europe. Hydrol. Earth Syst. Sci. 24:4441–4461. https://doi.org/10.5194/hess-24-4441-2020

Gleeson, T., Wada, Y., Bierkens, M. F. P., and van Beek, L. P. H. (2012). Water balance of global aquifers revealed by groundwater footprint. Nature 488, 197–200. https://doi.org/10.1038/nature11295

Goldscheider, N., Chen, Z., Auler, A. S., Bakalowicz, M., Broda, S., Drew, D., Hartmann, J., Jiang, G., Moosdorf, N., Stevanovic, Z. and Veni, G. (2020). Global distribution of carbonate rocks and karst water resources. Hydrogeology Journal, 28, 1661–1677. https://doi.org/10.1007/s10040-020-02139-5

Goldscheider, N., and Drew, D. (Eds.). (2014). Methods in karst hydrogeology: IAH: International Contributions to Hydrogeology, 26. Crc Press. https://doi.org/10.1201/9781482266023

Goldscheider, N., Pronk, M., and Smart, C. (2008). Tracer tests in karst hydrogeology and speleology. International Journal of Speleology, 37, 27–40. https://doi.org/1 0.5038/1827-806X.37.1.3

Grossmann, A. and Morlet, J. (1984). Decomposition of Hardy Functions into Square Integrable Wavelets of Constant Shape. SIAM Journal on Mathematical Analysis, 15(4) :723–736. https://doi.org/10.1137/0515056

Guinot, V., Savéan, M., Jourde, H., and Neppel, L. (2015). Conceptual rainfall-runoff model with a two-parameter, infinite characteristic time transfer function. Hydrol. Process. 29:4756–4778. https://doi.org/10.1002/hyp.10523

Guo, Q., Wang, Y., Ma, T., and Li, L. (2005). Variation of karst spring discharge in the recent five decades as an indicator of global climate change: A case study at Shanxi, northern China. Sci. China Ser. Earth Sci. 48, 2001–2010. https://doi.org/10.1360/04yd0113

Gupta A., and Govindaraju, R. S. (2019). Propagation of structural uncertainty in watershed hydrologic models. Journal of Hydrology 575:66–81. https://doi.org/10.1016/j.jhydrol.2019.05.026

Gupta, H. V., Kling, H., Yilmaz, K. K., and Martinez, G. F. (2009). Decomposition of the mean squared error and NSE performance criteria: Implications for improving hydrological modelling. Journal of hydrology, 377(1–2), 80–91. https://doi.org/10.1016/j.jhydrol.2009.08.003

Gupta, H. V, Wagener, T., and Liu, Y. (2008). Reconciling theory with observations: elements of a diagnostic approach to model evaluation. Hydrological Processes, 22(18), 3802–3813. https://doi.org/10.1002/hyp.6989

Gutiérrez, F., Parise, M., De Waele, J., and Jourde, H. (2014). A review on natural and human-induced geohazards and impacts in karst. Earth-Science Reviews, 138, 61–88. https://doi.org/10.1016/j.earscirev.2014.08.002

Hacker, P. (2003). Hydrologisch-hydrogeologische Untersuchungen im Bereich des Glashüttenberges zur Frage des engeren Schutzgebietes für die Kerschbaumer-Quelle. ARC Seibersdorf research GmbH

Hagedorn, B., and Whittier, R.B. (2015). Solute sources and water mixing in a flashy mountainous stream (Pahsimeroi River, U.S. Rocky Mountains): Implications on chemical weathering rate and groundwater–surface water interaction. Chemical Geology. 391, 123 – 137. https://doi.org/10.1016/j.chemgeo.2014.10.031

Hall, R.L. (2003). Interception loss as a function of rainfall and forest types: stochastic modelling for tropical canopies revisited. Journal of Hydrology 280:1–12. https://doi.org/10.1016/S0022-1694(03)00076-3

Hamon, W.R. (1961). Estimating Potential Evapotranspiration. Journal of the Hydraulics Division, Proceedings of the American Society of Civil Engineers:107–120. https://doi.org/10.1061/JYCEAJ.0000599

Hansen, M. C., Potapov, P. V., Moore, R., Hancher, M., Turubanova, S. A., Tyukavina, A., Thau, D., Stehman, S. V., Goetz, S. J., Loveland, T. R., Kommareddy, A., Egorov, A., Chini, L., Justice, C. O., and Townshend, J. R. G. (2013). High-Resolution Global Maps of 21st-Century Forest Cover Change. Science 342, 850–853. https://doi.org/10.1126/science.1244693

Hao, Y., Liu, G., Li, H., Li, Z., Zhao, J., and Yeh, T.-C. J. (2012). Investigation of karstic hydrological processes of Niangziguan Springs (North China) using wavelet analysis. Hydrological Processes, 26(20), 3062-3069. https://doi.org/10.1002/hyp.8265

Hao, Y., Wang, Y., Zhu, Y., Lin, Y., Wen, J. -C., and Yeh, T. -C. -J. (2009). Response of karst springs to climate change and anthropogenic activities: the Niangziguan Springs. China. Prog. Phys. Geogr. Earth Environ. 33, 634–649. https://doi.org/10.1177/0309133309346651

Hariharan, G. (2019). Wavelet Analysis—An Overview. Forum for Interdisciplinary Mathematics. https://doi.org/10.1007/978-981-32-9960-3_2

Hartmann, A., Barberá, J. A., and Andreo, B. (2017). On the value of water quality data and informative flow states in karst modelling, Hydrol. Earth Syst. Sci., 21, 5971–5985, https://doi.org/10.5194/hess-21-5971-2017

Hartmann, A., Gleeson, T., Wada, Y., and Wagener, T. (2017b). Enhanced groundwater recharge rates and altered recharge sensitivity to climate variability through subsurface heterogeneity. Proc Natl Acad Sci U S A 114:2842–2847. https://doi.org/10.1073/pnas.1614941114

Hartmann, A., Goldscheider, N., Wagener, T., Lange, J., and Weiler, M. (2014). Karst water resources in a changing world: Review of hydrological modeling approaches. Reviews of Geophysics, 52, 218–242. https://doi.org/10.1002/2013RG000443

Hartmann, A., Lange, J., Vivó Aguado, À., Mizyed, N., Smiatek, G., and Kunstmann, H. (2012). A multi-model approach for improved simulations of future water availability at a large Eastern Mediterranean karst spring. J. Hydrol. 468–469, 130–138. https://doi.org/10.1016/j.jhydrol.2012.08.024

Hartmann, A., Mudarra, M., Andreo, B., Marín, A., Wagener, T., and Lange, J. (2014b). Modeling spatiotemporal impacts of hydroclimatic extremes on groundwater recharge at a Mediterranean karst aquifer. Water Resour Res 50:6507–6521. https://doi.org/10.1002/2014WR015685

Hartmann, A., Barberá, J. A., Lange, J., Andreo, B., and Weiler, M. (2013). Progress in the hydrologic simulation of time variant recharge areas of karst systems - Exemplified at a karst spring in Southern Spain. Advances in Water Resources, 54, 149–160. https://doi.org/10.1016/j.advwatres.2013.01.010

Hartmann, A., Wagener, T., Rimmer, A., Lange, J., Brielmann, H. and Weiler, M. (2013a). Testing the realism of model structures to identify karst system processes using water quality and quantity signatures. Water Resour. Res., 49, 3345–3358. https://doi.otg/10.1002/wrcr.20229

Hartmann, A., Weiler, M., Wagener, T., Lange, J., Kralik, M., Humer, F., Mizyed, N., Rimmer, A., Barberá, J. A., Andreo, B., Butscher, C., and Huggenberger, P. (2013b). Process-based karst modelling to relate hydrodynamic and hydrochemical characteristics to system properties, Hydrol. Earth Syst. Sci., 17, 3305–3321, https://doi.org/10.5194/hess-17-3305-2013

Hauduc, H., Neumann, M. B., Muschalla, D., Gamerith, V., Gillot, S., and Vanrolleghem, P. A. (2015). Efficiency criteria for environmental model quality assessment: A review and its application to wastewater treatment. Environ. Model. Softw. 68, 196–204. https://doi.org/10.1016/j.envsoft.2015.02.004

Hauns, M., Jeannin, P. Y., and Atteia, O. (2001). Dispersion, retardation and scale effect in tracer breakthrough curves in karst conduits. Journal of hydrology, 241(3–4), 177-193. https://doi.org/10.1016/S0022-1694(00)00366-8

Hayashi, M., Vogt, T., Machler, L., and Schirmer, M. (2012). Diurnal fluctuations of electrical conductivity in a pre-alpine river: Effects of photosynthesis and groundwater exchange. Journal of Hydrology 450: 93–104. https://doi.org/10.1016/j.jhydrol.2012.05.020

Henson, W.R., Rooij, R., and Graham, W. (2018). What Makes a First-Magnitude Spring?: Global Sensitivity Analysis of a Speleogenesis Model to Gain Insight into Karst Network and Spring Genesis. Water Resour. Res. 54:7417–7434. https://doi.org/10.1029/2017WR021950

Herrero, J., Polo, M. J., Moñino, A., and Losada, M. A. (2009). An energy balance snowmelt model in a Mediterranean site. Journal of Hydrology 371:98–107. https://doi.org/10.1016/j.jhydrol.2009.03.021

Hilberg, S., and Schneider, J. F. (2011). The aquifer characteristics of the dolomite formation a new approach for providing drinking water in the northern calcareous Alps region in Germany and Austria. Water Resour Manag 25(11):2705–2729. https://doi.org/10.1007/s11269-011-9834-x

Hottelet, C., Blažková, Š., and Bičík, M. (1994). Application of the ETH Snow Model to Three Basins of Different Character in Central Europe. Hydrology Research 25:113–128. https://doi.org/10.2166/nh.1994.0023

Hu, J., Chen, S., Behrangi, A., and Yuan, H. (2019). Parametric uncertainty assessment in hydrological modeling using the generalized polynomial chaos expansion. Journal of Hydrology 579:124158. https://doi.org/10.1016/j.jhydrol.2019.124158

Huo, J., and Liu, L. (2020). Evaluation Method of Multiobjective Functions' Combination and Its Application in Hydrological Model Evaluation. Comput. Intell. Neurosci. 2020, 8594727. https://doi.org/10.1155/2020/8594727

In-Situ Inc. (2012) Aqua TROLL operator´s manual: Aqua TROLL 100 – Aqua TROLL 200. https://www.geotechenv.com/Manuals/In-Situ_Manuals/AquaTroll_100-200_Manual.pdf

Jaxa-Rozen, M., and Kwakkel, J. (2018). Tree-based ensemble methods for sensitivity analysis of environmental models: A performance comparison with Sobol and Morris techniques. Environ. Modell. Software 107, 245–266. https://doi.org/10.1016/j.envsoft.2018.06.011

Jackson, E. K., Roberts, W., Nelsen, B., Williams, G. P., Nelson, E. J., and Ames, D. P. (2019). Introductory overview: Error metrics for hydrologic modelling – A review of common practices and an open source library to facilitate use and adoption. Environ. Model. Softw. 119, 32–48. https://doi.org/10.1016/j.envsoft.2019.05.001

Jeannin, P. -Y., Artigue, G., Butscher, C., Chang, Y., Charlier, J.-B., Duran, L., Gill, L., Hartmann, A., Johannet, A., Jourde, H., Kavousi, A., Liesch, T., Liu, Y., Lüthi, M., Malard, A., Mazzilli, N., Pardo-Igúzquiza, E., Thiéry, D., Reimann, T., Schuler, P., Wöhling, T., and Wunsch, A. (2021). Karst modelling challenge 1: Results of hydrological modelling. Journal of Hydrology, 600. https://doi.org/10.1016/j.jhydrol.2021.126508

Jódar, J., González-Ramón, A., Martos-Rosillo, S., Heredia, J., Herrera, C., Urrutia, J., Caballero, Y., Zabaleta, A., Antigüedad, I., Custodio, E., Lambán, L. J. (2020). Snowmelt as a determinant factor in the hydrogeological behaviour of high mountain karst aquifers: The Garcés karst system, Central Pyrenees (Spain). Sci Total Environ 748:141363. https://doi.org/10.1016/j.scitotenv.2020.141363

Jourde H, Massei N, Mazzilli N, Binet S, Batiot-Guilhe C, Labat D, et al. (2018). SNO KARST: A French network of observatories for the multidisciplinary study of critical zone processes in karst watersheds and aquifers. Vadose Zone Journal 17(1): 1-18. https://doi.org/10.2136/vzj2018.04.0094

Jourde, H., Mazzilli, N., Lecoq, N., Arfib, B., and Bertin, D. (2015). KARSTMOD: A Generic Modular Reservoir Model Dedicated to Spring Discharge Modeling and Hydrodynamic Analysis in Karst, in: Andreo, B., Carrasco, F., Durán, J.J., Jiménez, P., LaMoreaux, J.W. (Eds.), Hydrogeological and Environmental Investigations in Karst Systems. Springer Berlin Heidelberg, Berlin, Heidelberg, pp. 339–344. https://doi.org/10.1007/978-3-642-17435-3_38

Jourde, H., and Wang, X. (2023). Advances, challenges and perspective in modelling the functioning of karst systems: a review. Environ Earth Sci 82, 396. https://doi.org/10.1007/s12665-023-11034-7

Jukic, D., and V. Denic-Jukic. (2008). Estimating parameters of groundwater recharge model in frequency domain: Karst springs Jadro and Žrnovnica. Hydrological Processes, 22(23), 4532–4542. https://doi.org/10.1002/hyp.7057

Käss, W. (2004). Lehrbuch der Hydrogeologie, Bd. 9, Geohydrologische Markierungstechnik. Verlag Gebrüder Borntraeger, Berlin

Katz, B. G. (2019). Chapter 91 - Nitrate contamination in karst groundwater. In Encyclopedia of caves (Third Edition), 756-760. Academic Press. https://doi.org/10.1016/B978-0-12-814124-3.00091-1

Katz, B., McBride, W., Hunt, A., Crandall, C., Metz, P., Eberts, S., and Berndt, M. (2009). Vulnerability of a public supply well in a karstic aquifer to contamination, Ground Water, 47 (3), 438–452. https://doi.org/10.1111/j.1745-6584.2008.00504.x

Kavetski, D., Kuczera, G., and Franks, S. W. (2006). Bayesian analysis of input uncertainty in hydrological modeling: 2. Application. Water Resour. Res. 42:1015. https://doi.org/10.1029/2005WR004376

Kavousi, A., Reimann, T., Liedl, R., and Raeisi, E. (2020). Karst aquifer characterization by inverse application of MODFLOW-2005 CFPv2 discrete-continuum flow and transport model. Journal of Hydrology, 587, 124922. https://doi.org/10.1016/j.jhydrol.2020.124922

Khatami, S., Peel, M. C., Peterson, T. J., Western, A. W. (2019). Equifinality and flux mapping: A new approach to model evaluation and process representation under uncertainty Water Resour. Res., 55 (11), 8922-8941. https://doi.org/10.1029/2018WR023750

Kiraly, L. (1998). Modelling karst aquifers by the combined discrete channel and continuum approach. Bulletin du Centre d'hydrogéologie, 16, 77–98.

Klausmeyer, K. R., and Shaw, M. R. (2009). Climate Change, Habitat Loss, Protected Areas and the Climate Adaptation Potential of Species in Mediterranean Ecosystems Worldwide. PLOS ONE 4, e6392. https://doi.org/10.1371/journal.pone.0006392

Klemeš, V. (1986). Dilettantism in hydrology: Transition or destiny? Water Resources Research, 22(9S), 177S-188S. https://doi.org/10.1029/WR022i09Sp0177S

Klimchouk, A. (2000). The formation of epikarst and its role in vadose speleogenesis. Speleogenesis: evolution of karst aquifers. National Speleological Society, Huntsville

Knoben, W. J. M., Freer, J. E., and Woods, R. A. (2019). Technical note: Inherent benchmark or not? Comparing Nash–Sutcliffe and Kling–Gupta efficiency scores, Hydrol. Earth Syst. Sci., 23, 4323–4331, https://doi.org/10.5194/hess-23-4323-2019

Kordilla, J., Sauter, M., Reimann, T., and Geyer, T. (2012). Simulation of saturated and unsaturated flow in karst systems at catchment scale using a double continuum approach, Hydrol. Earth Syst. Sci., 16(10), 3909–3923. https://doi.org/ 10.5194/HESS-16-3909-2012

Kovács, A. and Sauter, M. (2007). Modelling karst hydrodynamics. In Goldscheider, N and Drew, D (Eds.), Methods in Karst Hydrogeology (pp. 200–222). https://doi.org/10.1201/9781482266023

Kresic, N., and Stevanovic, Z. (Eds.). (2009). Groundwater hydrology of springs: engineering, theory, management and sustainability. Butterworth-Heinemann. https://doi.org/10.1016/C2009-0-19145-6

Kuniansky, E. L. (2016). Simulating groundwater flow in karst aquifers with distributed parameter models—Comparison of porous-equivalent media and hybrid flow approaches: U.S. Geological Survey Scientific Investigations Report 2016–5116, 14 p., http://dx.doi.org/10.3133/sir20165116

Kuniansky, E. L., Bellino, J. C., and Dixon, J. (2012). Transmissivity of the upper Floridan aquifer in Florida and parts of Georgia, South Carolina, and Alabama. US Department of the Interior, US Geological Survey. https://pubs.usgs.gov/sim/3204

Kurtuluş, B., and Razack, M. (2007). Evaluation of the ability of an artificial neural network model to simulate the input-output responses of a large karstic aquifer: the La Rochefoucauld aquifer (Charente, France). Hydrogeology Journal, 15, 241-254. https://doi.org/10.1007/S10040-006-0077-5

Labat, D. (2005). Recent advances in wavelet analyses: Part 1. A review of concepts. Journal of Hydrology, 314(1-4), 275-288. https://doi.org/10.1016/j.jhydrol.2005.04.003

Labat, D. (2010). Cross wavelet analyses of annual continental freshwater discharge and selected climate indices. Journal of Hydrology, 385(1-4), 269-278. https://doi.org/10.1016/j.jhydrol.2010.02.029

Labat, D., Ababou, R., and Mangin, A. (1999). Linear and nonlinear input/output models for karstic springflow and flood prediction at different time scales. Stochastic Environmental Research and Risk Assessment, 13(5), 337–364. https://doi.org/10.1007/s004770050055

Labat, D., Ababou, R., and Mangin, A. (2000a). Rainfall–runoff relations for karstic springs. Part I: convolution and spectral analyses. Journal of Hydrology, 238(3), 123–148. https://doi.org/10.1016/S0022-1694(00)00321-8

Labat, D., Ababou, R., and Mangin, A. (2000b). Rainfall–runoff relations for karstic springs. Part II: continuous wavelet and discrete orthogonal multiresolution analyses. J. Hydrol. 238, 149–178. https://doi.org/10.1016/S0022-1694(00)00322-X

Labat, D., Ababou, R., and Mangin, A. (2001). Introduction of Wavelet Analyses to Rainfall/Runoffs Relationship for a Karstic Basin: The Case of Licq-Atherey Karstic System (France). Groundwater, 39(4), 605–615. https://doi.org/10.1111/j.1745-6584.2001.tb02348.x

Labat, D., and Mangin, A. (2015). Transfer function approach for artificial tracer test interpretation in karstic systems. J. Hydrol. 529, 866–871. https://doi.org/10.1016/j.jhydrol.2015.09.011

Ladouche, B., Maréchal, J., and Dörfliger, N. (2014). Semi-distributed lumped model of a karst system under active management. Journal of Hydrology, 509(13), 215–230. https://doi.org/10.1016/j.jhydrol.2013.11.017

Larocque, M., Mangin, A., Razack, M., and Banton, O. (1998). Contribution of correlation and spectral analyses to the regional study of a large karst aquifer (Charente, France). J. Hydrol. 205, 217–231. https://doi.org/10.1016/S0022-1694(97)00155-8

Lauber, U., and Goldscheider, N. (2014). Use of artificial and natural tracers to assess groundwater transit-time distribution and flow systems in a high-alpine karst system (Wetterstein Mountains, Germany). Hydrogeology Journal, 22(8), 1807. https://doi.org/10.1007/s10040-014-1173-6

Le Moine, N., Andréassian, V., and Mathevet, T. (2008). Confronting surface- and groundwater balances on the La Rochefoucauld-Touvre karstic system (Charente, France). Water Resources Research, 44(3), 1–10. https://doi.org/10.1029/2007WR005984

Le Moine, N., Andréassian, V., Perrin, C., and Michel, C. (2007). How can rainfall-runoff models handle intercatchment groundwater flows? Theoretical study based on 1040 French catchments. Water Resources Research, 43, W06428. https://doi.org/10.1029/2006WR005608

Lechuga-Crespo J. L, Ruiz-Romera E, Probst J.-L, Unda-Calvo J, Cuervo-Fuentes Z. C, Sánchez-Pérez J. M (2020). Combining punctual and high frequency data for the spatiotemporal assessment of main geochemical processes and dissolved exports in an urban river catchment. Science of The Total Environment 727, 138644. https://doi.org/10.1016/j.scitotenv.2020.138644

Lee, A. (2014). pyswarm: Particle swarm optimization (PSO) with constraint support.

Lee, G., Tachikawa, Y., and Takara, K. (2011). Comparison of model structural uncertainty using a multi-objective optimisation method. Hydrol. Process. 25:2642–2653. https://doi.org/10.1002/hyp.8006

Leins, T., Liso, I. S., Parise, M., and Hartmann, A. (2023). Evaluation of the predictions skills and uncertainty of a karst model using short calibration data sets at an Apulian cave (Italy). Environmental Earth Sciences, 82(14), 351. https://doi.org/10.1007/s12665-023-10984-2

Leibundgut, C., Maloszewski, P., and Kulls, C. (2009). Tracers in Hydrology, 1st ed., 415 pp., Wiley-Blackwell, Chichester, U. K. https://doi.org/10.1002/9780470747148

Li, G., Chen, X., Zhang, Z., Wang, L., and Soulsby, C. (2022). Effects of passive-storage conceptualization on modeling hydrological function and isotope dynamics in the flow system of a cockpit karst landscape. Hydrol. Earth Syst. Sci., 26 (21), 5515-5534. https://doi.org/10.5194/hess-26-5515-2022

Li, Z., Xu, X., Liu, M., Li, X., Zhang, R., Wang, K., and Xu, C. (2017). State-space prediction of spring discharge in a karst catchment in southwest China. Journal of Hydrology, 549, 264-276. https://doi.org/10.1016/j.jhydrol.2017.04.001

Liedl, R., Sauter, M., Hückenhaus, D., Clemens, T., and Teutsch, G. (2003). Simulation of the development of karst aquifers using a coupled continuum pipe flow model, Water Resour. Res., 39(3), 1057. https://doi.org/10.1029/2001WR001206

Liu, S. (2001). Evaluation of the Liu model for predicting rainfall interception in forests world-wide. Hydrol. Process. 15:2341–2360. https://doi.org/10.1002/hyp.264

Liu Z, Groves C, Yuan D, Meiman J (2004) South China Karst aquifer storm-scale hydrochemistry. Ground Water 42(4): 491–499. https://doi.org/10.1111/j.1745-6584.2004.tb02617.x

Liu, Z., Li, Q., Sun, H., and Wang, J. (2007). Seasonal, diurnal and storm-scale hydrochemical variations of typical epikarst springs in subtropical karst areas of SW China: Soil CO2 and dilution effects, Journal of Hydrology, 337(1–2), 207–223. https://doi.org/10.1016/j.jhydrol.2007.01.034

Liu, M., Xu, X., Sun, A. Y., Luo, W., and Wang, K. (2018). Why do karst catchments exhibit higher sensitivity to climate change? Evidence from a modified Budyko model. Advances in Water Resources 122:238–250. https://doi.org/10.1016/j.advwatres.2018.10.013

Liu, Y., Wagener, T., and Hartmann, A. (2021). Assessing Streamflow Sensitivity to Precipitation Variability in Karst-Influenced Catchments With Unclosed Water Balances. Water Resour. Res. 57:177. https://doi.org/10.1029/2020WR028598

Lóaiciga, H. A., Maidment, D. R., and Valdes, J. B. (2000). Climate-change impacts in a regional karst aquifer, Texas. USA. J. Hydrol. 227, 173–194. https://doi.org/10.1016/S0022-694(99)00179-1

Long, A. J., and Putnam, L. D. (2004). Linearmodel describing three components of flow in karst aquifers using 18O data, Journal of Hydrology, 296, 254–270. https://doi.org/10.1016/J.JHYDROL.2004.03.023

Llorens, P., and Domingo, F. (2007). Rainfall partitioning by vegetation under Mediterranean conditions. A review of studies in Europe. J. Hydrol. 335, 37–54. https://doi.org/10.1016/j.jhydrol.2006.10.032

Lorette, G., Lastennet, R., Peyraube, N., Denis, A., (2018). Groundwater-flow characterization in a multilayered karst aquifer on the edge of a sedimentary basin in western France. J. Hydrol. 566, 137–149. https://doi.org/10.1016/j.jhydrol.2018.09.017

Lucianetti, G., Penna, D., Mastrorillo, L., and Mazza, R. (2020). The Role of Snowmelt on the Spatio-Temporal Variability of Spring Recharge in a Dolomitic Mountain Group, Italian Alps. Water 12:2256. https://doi.org/10.3390/w12082256

Luhmann, A., Covington, M., Alexander, S., Chai, S., Schwartz, B., Groten, J., and Alexander, E. (2012). Comparing conservative and nonconservative tracers in karst and using them to estimate flow path geometry. Journal of Hydrology, 448–449, 201–211. https://doi.org/10.1016/j.jhydrol.2012.04.044

Luo, K., Tao, F., Moiwo, J. P., and Xiao, D. (2016). Attribution of hydrological change in Heihe River Basin to climate and land use change in the past three decades. Sci Rep 6, 33704. https://doi.org/10.1038/srep33704

Ma, T., Wang, Y., and Guo, Q. (2004). Response of carbonate aquifer to climate change in northern China: a case study at the Shentou karst springs. J. Hydrol. 297, 274–284. https://doi.org/10.1016/j.jhydrol.2004.04.020

Magnusson, J., Gustafsson, D., Hüsler, F., and Jonas, T. (2014). Assimilation of point SWE data into a distributed snow cover model comparing two contrasting methods. Water Resour. Res. 50:7816–7835. https://doi.org/10.1002/2014WR015302

Mallat, S.G., (1989). A theory for multiresolution signal decomposition: the wavelet representation. IEEE Trans. Pattern Anal. Mach. Intell. 11, 674–693. https://doi.org/10.1109/34.192463

Mallat, S. (1999). A Wavelet Tour of Signal Processing. Elsevier. Google-Books-ID : hbVOfWQNtB8C.

Mangin, A., (1984). Pour une meilleure connaissance des syste`mes hydrologiques a` partir des analyses corre´latoires et spectrales. Journal of Hydrology, 67, 25–43. https://doi.org/10.1016/0022-1694(84)90230-0

Mangin, A. (1975). Contribution à l'étude hydrodynamique des aquifères karstiques (Theses). Université de Dijon.

Maréchal, J. C., Ladouche, B., Doerfliger, N., and Lachassagne, P. (2008). Interpretation of pumping tests in a mixed flow karst system, Water Resour. Res., 44, W05401. https://doi.org/10.1029/2007WR006288

Markart, G., Kohl, B., and Perzl, F. (2006). Der Bergwald und seine hydrologische Wirkung - eine unterschätzte Größe? (The mountain forest and its hydrological effect - an underestimated variable?)LWF Wissen. Wald - Schutz vor Hochwasser? Beiträge zum Symposium am 27. April 2006:34–43.

Marks, D., Domingo, J., Susong, D., Link, T., and Garen, D. (1999). A spatially distributed energy balance snowmelt model for application in mountain basins. Hydrol. Process. 13:1935–1959. https://doi.org/10.1002/(SICI)1099-1085(199909)13:12/13%3C1935::AID-HYP868%3E3.0.CO;2-C

Marsaud, B. (1996). Structure et fonctionnement de la zone noyee des karsts a partir des resultats experimentaux (thesis). Paris 11. https://www.sudoc.fr/049573411

Mathevet, T., Michel, C., Andréassian, V., and Perrin, C. (2006). A bounded version of the Nash-Sutcliffe criterion for better model assessment on large sets of basins. IAHS PUBLICATION, 307, 211.

Martinec, J. (1960). The degree-day factor for snowmelt runoff forecasting. IUGG General Assembly of Helsinki, IAHS Commission of Surface Waters:468–477.

Martín-Rodríguez, J. F., Mudarra, M., De la Torre, B., and Andreo, B. (2023). Towards a better understanding of time-lags in karst aquifers by combining hydrological analysis tools and dye tracer tests. Application to a binary karst aquifer in Southern Spain. Journal of Hydrology, 621, 129643. https://doi.org/10.1016/j.jhydrol.2023.129643

Massei, N., Mahler, B. J., Bakalowicz, M., Fournier, M., and Dupont, J. P. (2007). Quantitative interpretation of specific conductance frequency distributions in karst. Ground Water 45(3): 288–293. https://doi.org/10.1111/j.1745-6584.2006.00291.x

Mazzilli, N., Guinot, V., and Jourde, H. (2012). Sensitivity analysis of conceptual model calibration to initialisation bias. Application to karst spring discharge models. Adv. Water Resour. 42, 1–16. https://doi.org/10.1016/j.advwatres.2012.03.020

Mazzilli, N., Guinot, V., Jourde, H., Lecoq, N., Labat, D., Arfib, B., Baudement, C., Danquigny, C., Dal Soglio, L., and Bertin, D. (2019). KarstMod: A modelling platform for rainfall - discharge analysis and modelling dedicated to karst systems. Environ. Model. Softw. 122, 103927. https://doi.org/10.1016/j.envsoft.2017.03.015

Mazzilli, N., Sivelle, V., Cinkus, G., Jourde, H., and Bertin, D. (2023). KarstMod User Guide - version 3.0. hal-01832693v2

McMillan, H., Krueger, T., and Freer, J. (2012). Benchmarking observational uncertainties for hydrology: rainfall, river discharge and water quality. Hydrol. Process. 26:4078–4111. https://doi.org/10.1002/hyp.9384

Menció, A., Mas-Pla, J., Otero, N., Regàs, O., Boy-Roura, M., Puig, R., Bach, J., Domènech, C., Zamorano, M., Brusi, D., and Folch, A. (2016). Nitrate pollution of groundwater; all right…, but nothing else?. Science of The Total Environment, 539, 241–251. https://doi.org/10.1016/j.scitotenv.2015.08.151

Merchán-Rivera, P., Geist, A., Disse, M., Huang, J., and Chiogna, G. (2022). A Bayesian framework to assess and create risk maps of groundwater flooding. Journal of Hydrology, 610, 127797. https://doi.org/10.1016/j.jhydrol.2022.127797

Meus, P., Moureaux, P., Gailliez, S., Flament, J., Delloye, F., Nix, P. (2014). In situ monitoring of karst springs in Wallonia (southern Belgium). Environmental Earth Sciences 71(2): 533–541. https://doi.org/10.1007/s12665-013-2760-x

Mewes, B., Oppel, H., Marx, V., and Hartmann, A. (2020). Information-based machine learning for tracer signature prediction in karstic environments. Water Resources Research 56, e2018WR024558. https://doi.org/10.1029/2018WR024558

Miao, J., Liu, G., Cao, B., Hao, Y., and Chen, J. (2014). Identification of strong karst groundwater runoff belt by cross wavelet transform. Water resources management, 28(10), 2903-2916. https://doi.org/10.1007/s11269-014-0645-8

Mizukami, N., Rakovec, O., Newman, A. J., Clark, M. P., Wood, A. W., Gupta, H. V., and Kumar, R. (2019). On the choice of calibration metrics for "high-flow" estimation using hydrologic models, Hydrol. Earth Syst. Sci., 23, 2601–2614, https://doi.org/10.5194/hess-23-2601-2019

Mohanty, B.P., Cosh, M.H., Lakshmi, V. and Montzka, C. (2017). Soil Moisture Remote Sensing: State-of-the-Science. Vadose Zone Journal, 16(1), 1–9. https://doi.org/10.2136/vzj2016.10.0105

Monteil, C., Zaoui, F., Le Moine, and N., Hendrickx, F. (2020). Multi-objective calibration by combination of stochastic and gradient-like parameter generation rules – the caRamel algorithm. Hydrol. Earth Syst. Sci. 24, 3189–3209. https://doi.org/10.5194/hess-24-3189-2020

Morales, T., Uriarte, J. A., Olazar, M., Antigüedad, I., and Angulo, B. (2010). Solute transport modelling in karst conduits with slow zones during different hydrologic conditions. Journal of Hydrology, 390(3-4), 182-189. https://doi.org/10.1016/J.JHYDROL.2010.06.041

Moriasi, D.N., Arnold, J.G., Liew, M., Bingner, R.L., Harmel, R.D., and Veith, T.L. (2007). Model Evaluation Guidelines for Systematic Quantification of Accuracy in Watershed Simulations. Transactions of the ASABE, 50, 885–900. https://doi.org/10.13031/2013.23153

Morris, M.D. (1991). Factorial Sampling Plans for Preliminary Computational Experiments. Technometrics 33, 161–174. https://doi.org/10.1080/00401706.1991.10484804

Moussu, F. (2012). Prise en compte du fonctionnement hydrodynamique dans la modélisation pluie débit des systèmes karstiques (Thèse de Doctorat). Université Pierre et Marie Curie, Paris. https://www.sudoc.fr/165620153

Moussu, F., Oudin, L., Plagnes, V., Mangin, A., and Bendjoudi, H. (2011). A multi-objective calibration framework for rainfall-discharge models applied to karst systems. Journal of Hydrology, 400(3–4), 364–376. https://doi.org/10.1016/j.jhydrol.2011.01.047

Mudarra, M., and B. Andreo (2011). Relative importance of the saturated and the unsaturated zones in the hydrogeological functioning of karst aquifers. The case of Alta Cadena (Southern Spain), J. Hydrol., 397(3–4), 263–280. https://doi.org/10.1016/j.jhydrol.2010.12.005

Mudarra, M., Andreo, B., Marín, A. I., Vadillo, I., and Barberá, J. A. (2014). Combined use of natural and artificial tracers to determine the hydrogeological functioning of a karst aquifer: the Villanueva del Rosario system (Andalusia, southern Spain). Hydrogeology Journal, 22(5), 1027. https://doi.org/10.1007/s10040-014-1117-1

Mudarra, M., Hartmann, A., and Andreo, B. (2019). Combining experimental methods and modeling to quantify the complex recharge behavior of karst aquifers. Water Resources Research, 55(2), 1384-1404. https://doi.org/10.1029/2017WR021819

Munson, B.R., Young, D.F., Okiishi, T.H., Hollars, S., and Johnson, K. (2021). Fundamentals Of Fluid Mechanics. Aerodynamics for Engineers. https://doi.org/ 10.1142/9789812774828_0003

Narany, T. S., Bittner, D., Disse, M., and Chiogna, G. (2019). Spatial and temporal variability in hydrochemistry of a small-scale dolomite karst environment. Environmental Earth Sciences, 78(9). https://doi.org/10.1007/s12665-019-8276-2

Nash, J. E., and Sutcliffe, J. V. (1970). River flow forecasting through conceptual models. Part I: A discussion of principles, Jornal of Hydrology, 10(3), 282–290. https://doi.org/10.1016/0022-1694(70)90255-6

Nerantzaki, S. D., Hristopulos, D. T., and Nikolaidis, N. P. (2020). Estimation of the uncertainty of hydrologic predictions in a karstic Mediterranean watershed. Sci. Total Environ. 717, 137131. https://doi.org/10.1016/j.scitotenv.2020.137131

Odeh, T., Salameh, E., Schirmer, M., and Strauch, G. (2009). Structural control of groundwater flow regimes and groundwater chemistry along the lower reaches of the Zerka River, West Jordan, using remote sensing, GIS, and field methods. Environ Geol 58: 1797–1810. https://doi.org/10.1007/s00254-008-1678-1

Oehlmann, S., Geyer, T., Licha, T., and Sauter, M. (2015). Reducing the ambiguity of karst aquifer models by pattern matching of flow and transport on catchment scale, Hydrol. Earth Syst. Sci., 19, 893–912, https://doi.org/10.5194/hess-19-893-2015

Olarinoye, T., Gleeson, T., Marx, V., Seeger, S., Adinehvand, R., Allocca, V., Andreo, B., Apaéstegui, J., Apolit, C., Arfib, B., Auler, A., Bailly-Comte, V., Barberá, J. A., Batiot-Guilhe, C., Bechtel, T., Binet,

S., Bittner, D., Blatnik, M., Bolger, T., Brunet, P., Charlier, J.-B., Chen, Z., Chiogna, G., Coxon, G., Vita, P. de, Doummar, J., Epting, J., Fleury, P., Fournier, M., Goldscheider, N., Gunn, J., Guo, F., Guyot, J. L., Howden, N., Huggenberger, P., Hunt, B., Jeannin, P.-Y., Jiang, G., Jones, G., Jourde, H., Karmann, I., Koit, O., Kordilla, J., Labat, D., Ladouche, B., Liso, I. S., Liu, Z., Maréchal, J.-C., Massei, N., Mazzilli, N., Mudarra, M., Parise, M., Pu, J., Ravbar, N., Sanchez, L. H., Santo, A., Sauter, M., Seidel, J.-L., Sivelle, V., Skoglund, R. Ø., Stevanovic, Z., Wood, C., Worthington, S., and Hartmann, A. (2020). Global karst springs hydrograph dataset for research and management of the world's fastest-flowing groundwater. Scientific data 7:59. https://doi.org/10.1038/s41597-019-0346-5

Ollivier, C., Mazzilli, N., Olioso, A., Chalikakis, K., Carrière, S. D., Danquigny, C., and Emblanch, C. (2020). Karst recharge-discharge semi distributed model to assess spatial variability of flows. Science of The Total Environment,703, 134368. https://doi.org/10.1016/j.scitotenv.2019.134368

Ollivier, C., Olioso, A., Carrière, S. D., Boulet, G., Chalikakis, K., Chanzy, A., Charlier, J.-B., Combemale, D., Davi, H., Emblanch, C., Marloie, O., Martin-StPaul, N., Mazzilli, N., Simioni, G., and Weiss, M. (2021). An evapotranspiration model driven by remote sensing data for assessing groundwater resource in karst watershed. Science of The Total Environment 781:146706. https://doi.org/10.1016/j.scitotenv.2021.146706

Oudin, L., Hervieu, F., Michel, C., Perrin, C., Andréassian, V., Anctil, F., and Loumagne, C. (2005). Which potential evapotranspiration input for a lumped rainfall–runoff model? Journal of Hydrology 303:290–306. https://doi.org/10.1016/j.jhydrol.2004.08.026

Oudin, L., Perrin, C., Mathevet, T., Andréassian, V., and Michel, C. (2006). Impact of biased and randomly corrupted inputs on the efficiency and the parameters of watershed models. Journal of Hydrology, 320(1–2), 62–83. https://doi.org/10.1016/j.jhydrol.2005.07.016

Padilla, A., and Pulido-Bosch, A. (1995). Study of hydrographs of karstic aquifers by means of correlation and cross-spectral analysis. J. Hydrol. 168, 73–89. https://doi.org/10.1016/0022-1694(94)02648-U

Padilla, A., Pulido-Bosch, A. and Mangin, A. (1994). Relative Importance of Baseflow and Quickflow from Hydrographs of Karst Spring. Groundwater, 32: 267-277. https://doi.org/10.1111/j.1745-6584.1994.tb00641.x

Padilla, I. Y., and Vesper, D. J. (2018). Fate, transport, and exposure of emerging and legacy contaminants in karst systems: state of knowledge and uncertainty. Karst groundwater contamination and public health: beyond case studies, 33–49. https://doi.org/10.1007/978-3-319-51070-5_5

Panagopoulos, G., and Lambrakis, N. (2006). The contribution of time series analysis to the study of the hydrodynamic characteristics of the karst systems: Application on two typical karst aquifers of Greece

(Trifilia, Almyros Crete). Journal of Hydrology, 329(3–4), 368-376, https://doi.org/10.1016/j.jhydrol.2006.02.023

Pappenberger, F., Ramos, M. H., Cloke, H. L., Wetterhall, F., Alfieri, L., Bogner, K., Mueller, A., and Salamon, P. (2015). How do I know if my forecasts are better? Using benchmarks in hydrological ensemble predictions. Journal of Hydrology, 522, 697-713. https://doi.org/10.1016/j.jhydrol.2015.01.024

Parkhurst, D. L., and Appelo C. A. J. (2013). Description of input and examples for PHREEQC version 3-A computer program for speciation, batch-reaction, one-dimensional transport, and inverse geochemical calculations. U.S. Geological Survey Techniques and Methods, book 6, chap. A43, 497 p. http://pubs.usgs.gov/tm/06/a43/

Patil, A., Deng, Z.-Q., and Malone, R. F. (2011). Input data resolution-induced uncertainty in watershed modelling. Hydrol. Process. 25:2302–2312. https://doi.org/10.1002/hyp.8018

Peely, A. B., Mohammadi, Z., and Raeisi, E. (2021). Breakthrough curves of dye tracing tests in karst aquifers: Review of effective parameters based on synthetic modeling and field data. Journal of Hydrology, 602, 126604. https://doi.org/10.1016/j.jhydrol.2021.126604

Pfaff, J.D. (1993). Method 300.0 - Determination of Inorganic Anions by Ion Chromatography. https://www.epa.gov/sites/default/files/2015-08/documents/method_300-0_rev_2-1_1993.pdf

Penman, H. L. (1948). Natural evaporation from open water, hare soil and grass. Proc R Soc Lond A Math Phys Sci 193:120–145. https://doi.org/10.1098/rspa.1948.0037

Perrin, J., Jeannin, P. -Y., and Zwahlen, F. (2003). Epikarst storage in a karst aquifer: a conceptual model based on isotopic data, Milandre test site, Switzerland. Journal of Hydrology, 279(1–4), 106–124. https://doi.org/10.1016/S0022-1694(03)00171-9

Perrin, C., Michel, C., and Andréassian, V. (2001). Does a large number of parameters enhance model performance? Comparative assessment of common catchment model structures on 429 catchments. J. Hydrol. 242, 275–301. https://doi.org/10.1016/S0022-1694(00)00393-0

Pianosi, F., Sarrazin, F., and Wagener, T. (2015). A Matlab toolbox for Global Sensitivity Analysis. Environmental Modelling and Software 70:80–85. https://doi.org/10.1016/j.envsoft.2015.04.009

Pinault, J.-L., Plagnes, V., Aquilina, L., and Bakalowicz, M. (2001). Inverse modeling of the hydrological and the hydrochemical behavior of hydrosystems: Characterization of Karst System Functioning. Water Resour. Res. 37, 2191–2204. https://doi.org/10.1029/2001WR900018

Pinza, J. G., Katsanou, K., Lambrakis, N., and Stigter, T. Y. (2024). Temporal variations of spring hydrochemistry as clues to the karst system behaviour: an example of Louros Catchment. Environmental Monitoring and Assessment, 196(7), 624. https://doi.org/10.1007/s10661-024-12744-6

Piper, A. M. (1944). A Graphic Procedure in the Geochemical Interpretation of Water-Analyses. Transactions of the American Geophysical Union, 25(6), 914–928. https://doi.org/10.1029/TR025i006p00914

Pölz, A., Blaschke, A. P., Komma, J., Farnleitner, A. H., and Derx, J. (2024). Transformer versus LSTM: A comparison of deep learning models for karst spring discharge forecasting. Water Resources Research, 60, e2022WR032602. https://doi.org/10.1029/2022WR032602

Pool, S., Vis, M., and Seibert, J. (2018). Evaluating model performance: towards a non-parametric variant of the Kling-Gupta efficiency. Hydrol. Sci. J. 63, 1941–1953. https://doi.org/10.1080/02626667.2018.1552002

Plummer, L. N., and Wigley, T. M. L. (1976). The dissolution of calcite in CO2-saturated solutions at 25°C and 1 atmosphere total pressure. Geochimica et Cosmochimica Acta, 40(2), 191–202, https://doi.org/10.1016/0016-7037(76)90176-9

Quinn, J. J., Tomasko, D., and Kuiper, J. A. (2006). Modeling complex flow in a karst aquifer. Sedimentary Geology, 184(3-4), 343-351. https://doi.org/10.1016/j.sedgeo.2005.11.009

Rathinasamy, M., Khosa, R., Adamowski, J., Ch, S., Partheepan, G., Anand, J., and Narsimlu, B. (2014). Wavelet-based multiscale performance analysis: An approach to assess and improve hydrological models. Water Resources Research, 50(12), 9721–9737. https://doi. org/10.1002/2013wr014650

Ravbar, N., Engelhardt, I., and Goldscheider, N. (2011). Anomalous behavior of specific electrical conductivity at a karst spring induced by variable catchment boundaries: The case of the Podstenjšek spring, Slovenia. Hydrological Processes 25(13): 2130–2140. https://doi.org/10.1002/hyp.7966

Reimann, T., Rehrl, C., Shoemaker, W. B., Geyer, T., and Birk, S. (2011). The significance of turbulent flow representation in single-continuum models. Water Resour. Res., 47(9), W09503, https://doi.org/10.1029/2010WR010133

Reimann, T., Giese, M., Geyer, T., Liedl, R., Maréchal, J. C., and Shoemaker, W. B. (2014). Representation of water abstraction from a karst conduit with numerical discrete-continuum models. Hydrology and Earth System Sciences, 18(1), 227-241. https://doi.org/10.5194/hess-18-227-2014

Reberski, J. L., Terzić, J., Maurice, L. D., and Lapworth, D. J. (2022). Emerging organic contaminants in karst groundwater: A global level assessment. Journal of Hydrology, 604, 127242. https://doi.org/10.1016/j.jhydrol.2021.127242

Richieri, B., Bittner, D., Hartmann, A., Benettin, P., van Breukelen, B. M., Labat, D., and Chiogna, G. (2023). Using continuous electrical conductivity measurements to derive major solute concentrations in karst systems. Hydrological Processes, 37:e14929. https://doi.org/10.1002/hyp.14929

Richieri, B., Bittner, D., Sivelle, V., Hartmann, A., Labat, D., and Chiogna, G. (2024). On the value of hydrochemical data for the interpretation of flow and transport processes in the Baget karst system, France. Hydrogeology Journal. https://doi.org/10.1007/s10040-024-02801-2

Rimmer, A., and Hartmann, A. (2012). Simplified conceptual structures and analytical solutions for groundwater discharge using reservoir equations, in Water Resources Management and Modeling, edited by D. P. C. Nayak, pp. 217–238, InTech, Kakinada, India. https://doi.org/10.5772/34803

Rimmer, A., and Salingar, Y. (2006). Modelling precipitation-streamflow processes in karst basin: The case of the Jordan River sources. Israel, Journal of Hydrology, 331(3–4), 524–542. https://doi.org/10.1016/j.jhydrol.2006.06.003

Rodríguez, L., Vives, L., and Gomez, A. (2013). Conceptual and numerical modeling approach of the Guarani Aquifer System, Hydrol. Earth Syst. Sci., 17(1), 295–314. https://doi.org/ 10.5194/hess-17-295-2013

Rojas, R., Feyen, L., and Dassargues, A. (2008). Conceptual model uncertainty in groundwater modeling: Combining generalized likelihood uncertainty estimation and Bayesian model averaging. Water Resour. Res. 44:655. https://doi.org/10.1029/2008WR006908

Rudolph, M. G., Collenteur, R. A., Kavousi, A., Giese, M., Wöhling, T., Birk, S., Hartmann, A., and Reimann, T. (2023). A data-driven approach for modelling Karst spring discharge using transfer function noise models. Environ Earth Sci 82, 339. https://doi.org/10.1007/s12665-023-11012-z

Sanchez, D. G., Lacarrière B., Musy M., and Bourges, B. (2014). Application of sensitivity analysis in building energy simulations: Combining first- and second-order elementary effects methods. Energy and Buildings, 68, 741-750. https://doi.org/10.1016/j.enbuild.2012.08.048Sivelle, V., Cinkus, G., Mazzilli, N., Labat, D., Arfib, B., Massei, N., Cousquer, Y., Bertin, D., and Jourde, H. (2023). Improvement of the KarstMod modeling platform for a better assessment of karst groundwater resources. Hydrology and Earth System Sciences Discussions 1–26. https://doi.org/10.5194/hess-2023-17

Sarrazin, F., Hartmann, A., Pianosi, F., Rosolem, R., and Wagener, T. (2018). V2Karst V1.1: a parsimonious large-scale integrated vegetation–recharge model to simulate the impact of climate and land cover change in karst regions. Geosci. Model Dev. 11:4933–4964. https://doi.org/10.5194/gmd-11-4933-2018

Sarrazin, F. J., Kumar, R., Basu, N. B., Musolff, A., Weber, M., Van Meter, K. J., and Attinger, S. (2022). Characterizing Catchment-Scale Nitrogen Legacies and Constraining Their Uncertainties. Water Resources Research, 58. https://doi.org/10.1029/2021WR031587

Sauter, M. (1992). Quantification and forecasting of regional groundwater flow and transport in a karst aquifer (Gallusquelle, Malm, SW. Germany). (PhD thesis). Tübinger Geowissenschaftliche Arbeiten (TGA). http://nbn-resolving.de/urn:nbn:de:bsz:21-opus-20398

Sauter, M. (2000). A numerical approach to simulating mixed flow in karst aquifers. In: Sasowsky I, Wicks C (eds) Groundwater Flow and Contaminant Transport in Carbonate Aquifers. A.A. Balkema, Rotterdam, Holland, pp. 147–156.

Savio, D., Stadler, P., Reischer, G. H., Kirschner, A. K., Demeter, K., Linke, R., Blaschke, A. P., Sommer, R., Szewzyk, U., Wilharitz, I. C., Mach, R. L., Stadler, H. and Farnleitner, A. H. (2018). Opening the black box of spring water microbiology from alpine karst aquifers to support proactive drinking water resource management. Wiley Interdisciplinary Reviews: Water, 5(3), e1282. https://doi.org/10.1002/wat2.1282

Schaefli, B., and Gupta, H. V. (2007). Do Nash values have value?. Hydrological Processes, 21(15), 2075–2080. https://doi.org/10.1002/hyp.6825

Schaefli, B., and Zehe, E. (2009). Hydrological model performance and parameter estimation in the wavelet-domain. Hydrology and Earth System Sciences, 13(10), 1921–1936. https://doi.org/10.5194/hess-13-1921-2009

Schmidt, S., Geyer, T., Guttman, J., Marei, A., Ries, F., and Sauter, M. (2014). Characterisation and modelling of conduit restricted karst aquifers – Example of the Auja spring, Jordan Valley. J. Hydrol. 14. https://doi.org/10.1016/j.jhydrol.2014.02.019

Schoeller H (1962). Les eaux souterraines (ed.) Masson, Paris: 642 p. https://doi.org/10.1002/iroh.19640490118

Schuler, P., Cantoni, È., Duran, L., Johnston, P., and Gill, L. (2021). Using Wavelet Coherence to Characterize Surface Water Infiltration into a Low-Lying Karst Aquifer. Groundwater, 59, 71-79. https://doi.org/10.1111/gwat.13012

Seibert, J. (1997). Estimation of Parameter Uncertainty in the HBV Model. Hydrology Research 28:247–262. https://doi.org/10.2166/nh.1998.15

Seibert, J. (2001). On the need for benchmarks in hydrological modelling. Hydrological Processes, 15(6), 1063–1064. https://doi.org/10.1002/hyp.446

Seibert, J., and McDonnell, J.J. (2002). On the dialog between experimentalist and modeler in catchment hydrology: Use of soft data for multicriteria model calibration. Water Resources Research, 38 (11). https://doi.org/10.1029/2001WR000978

Seibert, J., Vis, M. J. P., Lewis, E., and van Meerveld, H. J. (2018). Upper and lower benchmarks in hydrological modelling. Hydrological Processes, 32(8), 1120-1125. https://doi.org/10.1002/hyp.11476

Selak, A., Reberski, J. L., and Klobučar, G. (2023). Assessing the persistence, mobility and toxicity of emerging organic contaminants in Croatian karst springs used for drinking water supply. Science of The Total Environment, 903, 166240. https://doi.org/10.1016/j.scitotenv.2023.166240

Shoemaker, W. B., Kuniansky, E. L., Birk, S., Bauer, S., and Swain, E. D. (2008). Documentation of a Conduit Flow Process (CFP) for MODFLOW-2005, US Department of the Interior, US Geological Survey, Reston, Va. https://doi.org/10.3133/tm6A24

Siebert, S., Burke, J., Faures, J. M., Frenken, K., Hoogeveen, J., Döll, P., and Portmann, F. T. (2010). Groundwater use for irrigation – a global inventory. Hydrology and Earth System Sciences, 14(10), 1863–1880. https://doi.org/10.5194/hess-14-1863-2010

Sinreich, M., (2011). Towards developing conceptual models for reactive contaminant transport in karst. IAHS Publ, 342, 473-476.

Sinreich, M. (2014). Contaminant attenuation in karst aquifers: a paradigm shift. H2Karst research in limestone hydrogeology, Environmental Earth Sciences, Springer, 175–184. https://doi.org/10.1007/978-3-319-06139-9_13

Sivelle, V., (2019). Couplage d'approches conceptuelles, syst´emiques et distribu´ees pour l'interpr´etation de traçages artificiels en domaine karstique. Implications Pour La D´etermination De La Structure Interne Des Aquif`eres Karstiques. (These de Doctorat). Universite Paul Sabatier, Toulouse. https://www.sudoc.fr/244792240

Sivelle, V., and Jourde, H. (2020). A methodology for the assessment of groundwater resource variability in karst catchments with sparse temporal measurements. Hydrogeology Journal, 29 (1), 137–157. https://doi.org/10.1007/s10040-020-02239-2

Sivelle, V., Jourde, H., Bittner, D., Mazzilli, N., and Tramblay, Y. (2021). Assessment of the relative impacts of climate changes and anthropogenic forcing on spring discharge of a Mediterranean karst system. J. Hydrol. 598, 126396. https://doi.org/10.1016/j.jhydrol.2021.126396

Sivelle, V., Jourde, H., Bittner, D., Richieri, B., Labat, D., Hartmann, A., and Chiogna, G. (2022). Considering land cover and land use (LCLU) in lumped parameter modeling in forest dominated karst catchments, Journal of Hydrology, 612(C), 128264. https://doi.org/10.1016/j.jhydrol.2022.128264

Sivelle, V., and Labat, D. (2019). Short-term variations in tracer-test responses in a highly karstified watershed. Hydrogeol. J. 27, 2061–2075. https://doi.org/10.1007/s10040-019-01968-3

Sivelle, V., Labat, D., Mazzilli, N., Massei, N., and Jourde, H. (2019). Dynamics of the Flow Exchanges between Matrix and Conduits in Karstified Watersheds at Multiple Temporal Scales. Water 11:56. https://doi.org/10.3390/w11030569

Sivelle, V., Pérotin, L., Ladouche, B., de Montety, V., Bailly-Comte, V., Champollion, C., and Jourde, H. (2022b). Alumped parameter model to evaluatethe relevance of excess air as a tracerof exchanged flows betweentransmissive and capacitivecompartments of karst systems.Front. Water 4:930115. https://doi.org/10.3389/frwa.2022.930115

Sivelle, V., Renard, P., and Labat, D. (2020). Coupling SKS and SWMM to Solve the Inverse Problem Based on Artificial Tracer Tests in Karstic Aquifers. Water 12, 1139. https://doi.org/10.3390/w12041139

Smiatek, G., Kaspar, S., and Kunstmann, H. (2013). Hydrological Climate Change Impact Analysis for the Figeh Spring near Damascus. Syria. J. Hydrometeorol. 14, 577–593. https://doi.org/10.1175/JHM-D-12-065.1

Smith, R.C. (2013). Uncertainty Quantification: Theory, Implementation, and Applications. SIAM, Computational Science and Engineering. https://doi.org/10.1137/1.9781611973228

Smith, M., Cross, K., Paden, M., and Laban, P. (2016). Spring-managing groundwater sustainability. IUCN, Gland, Switzerland. https://doi.org/10.2305/IUCN.CH.2016.WANI.8.en

Somridhivej, B., and Boyd, C.E. (2016). An assessment of factors affecting the reliability of total alkalinity measurements. Aquaculture 459: 99-109. https://doi.org/10.1016/j.aquaculture.2016.03.032

Spence, J., and Telmer, K. (2005). The role of sulfur in chemical weathering and atmospheric CO2 fluxes: Evidence from major ions, δ13CDIC, and δ34SSO4 in rivers of the Canadian Cordillera. Geochimica et Cosmochimica Acta. 69 (23), 5441 - 5458. https://doi.org/10.1016/j.gca.2005.07.011

Spiessl, S. M., Prommer, H., Licha, T., Sauter, M., and Zheng, C. (2007). A process-based reactive hybrid transport model for coupled discrete conduit–continuum systems. Journal of hydrology, 347(1-2), 23-34. https://doi.org/10.1016/j.jhydrol.2007.08.026

Stefano, L. D., Duncan, J., Dinar, S., Stahl, K., Strzepek, K. M., and Wolf, A. T. (2012). Climate change and the institutional resilience of international river basins: J. Peace Res. https://doi.org/10.1177/0022343311427416

Stevanović, Z. (2018). Global distribution and use of water from karst aquifers. Geological Society, London, Special Publications, 466(1), 217–236. https://doi.org/10.1144/SP466.17

Stevanović, Z. (2019). Karst waters in potable water supply: a global scale overview. Environmental Earth Sciences, 78, 662. https://doi.org/10.1007/s12665-019-8670-9

Summerfield, M. (2010). Programming in Python 3: A Complete Introduction to the Python Language. Addison-Wesley Professional.

Taylor, G.I. (1954). The dispersion of matter in turbulent flow through a pipe. Proceedings of the Royal Society of London. Series A. Mathematical and Physical Sciences, 223, 446–468. https://doi.org/10.1098/rspa.1954.0130

Taylor, R. G., Scanlon, B., D¨oll, P., Rodell, M., van Beek, R., Wada, Y., Longuevergne, L., Leblanc, M., Famiglietti, J. S., Edmunds, M., Konikow, L., Green, T. R., Chen, J., Taniguchi, M., Bierkens, M. F. P., MacDonald, A., Fan, Y., Maxwell, R. M., Yechieli, Y., Gurdak, J. J., Allen, D. M., Shamsudduha, M., Hiscock, K., Yeh, P. -J. -F., Holman, I., and Treidel, H. (2013). Ground water and climate change. Nat. Clim. Change 3, 322–329. https://doi.org/10.1038/nclimate1744

Teixeira Parente, M., Bittner, D., Mattis, S. A., Chiogna, G., and Wohlmuth, B. (2019). Bayesian Calibration and Sensitivity Analysis for a Karst Aquifer Model Using Active Subspaces. Water Resour. Res. 55:7086–7107. https://doi.org/10.1029/2019WR024739

Thenkabail, P. S., Lyon, J. G., and Huete, A. (2011). Advances in hyperspectral remote sensing of vegetation and agricultural crops. In Hyperspectral remote sensing of vegetation (pp. 1-34). CRC Press. https://doi.org/10.13140/2.1.2985.3127

Thornthwaite, C.W. (1948). An approach toward a rational classification of climate. Geographical review:55–94. http://dx.doi.org/10.2307/210739

Torresan, F., Fabbri, P., Piccinini, L., Dalla Libera, N., Pola, M., and Zampieri, D. (2020). Defining the hydrogeological behavior of karst springs through an integrated analysis: A case study in the Berici Mountains area (Vicenza, NE Italy). Hydrogeology Journal 28: 1229–1247. https://doi.org/10.1007/s10040-020-02122-0

Tramblay, Y., Koutroulis, A., Samaniego, L., Vicente-Serrano, S. M., Volaire, F., Boone, A., Le Page, M., Llasat, M. C., Albergel, C., Burak, S., Cailleret, M., Kalin, K. C., Davi, H., Dupuy, J.-L., Greve, P., Grillakis, M., Hanich, L., Jarlan, L., Martin-StPaul, N., Martínez-Vilalta, J., Mouillot, F., Pulido-Velazquez, D., Quintana-Seguí, P., Renard, D., Turco, M., Türkeş, M., Trigo, R., Vidal, J.-P., Vilagrosa, A., Zribi, M., and Polcher, J. (2020). Challenges for drought assessment in the Mediterranean region under future climate scenarios. Earth-Sci. Rev. 210, 103348. https://doi.org/10.1016/j.earscirev.2020.103348

Tritz, S., Guinot, V., and Jourde, H. (2011). Modelling the behaviour of a karst system catchment using non-linear hysteretic conceptual model. J. Hydrol., 397(3–4), 250–262. https://doi.org/10.1016/j.jhydrol.2010.12.001

Ulloa-Cedamanos, F., Probst, J.-L., Binet, S., Camboulive, T., Payre-Suc, V., Pautot, C., Bakalowicz, M., Beranger, S., and Probst, A. (2020). A Forty-Year Karstic Critical Zone Survey (Baget Catchment, Pyrenees-France): Lithologic and Hydroclimatic Controls on Seasonal and Inter-Annual Variations of

Stream Water Chemical Composition, pCO2, and Carbonate Equilibrium. Water 12(5):1227. https://doi.org/10.3390/w12051227

Ulloa-Cedamanos, F., Probst, A., Dos-Santos, V., Camboulive, T., Granouillac, F., and Probst, J.-L. (2021). Stream Hydrochemical Response to Flood Events in a Multi-Lithological Karstic Catchment from the Pyrenees Mountains (SW France). Water 13–1818. https://doi.org/10.3390/w13131818

Vilhar, U., Kermavnar, J., Kozamernik, E., Petrič, M., and Ravbar, N. (2022). The effects of large-scale forest disturbances on hydrology–An overview with special emphasis on karst aquifer systems. Earth-Science Reviews, 235, 104243. https://doi.org/10.1016/j.earscirev.2022.104243

Vrugt, J. A., ter Braak, C. J. F., Clark, M. P., Hyman, J. M., and Robinson, B. A. (2008). Treatment of input uncertainty in hydrologic modeling: Doing hydrology backward with Markov chain Monte Carlo simulation. Water Resour. Res. 44:937. https://doi.org/10.1029/2007WR006720

Wada, Y., de Graaf, I. E. M., and van Beek, L. P. H. (2016). High-resolution modeling of human and climate impacts on global water resources. J. Adv. Model. Earth Syst. 8, 735–763. https://doi.org/10.1002/2015MS000618

Wagener, T., and Gupta, H. V. (2005). Model identification for hydrological forecasting under uncertainty, Stoch. Environ. Res. Risk Assess., 19(6), 378–387. https://doi.org/10.1007/s00477-005-0006-5

Wagener, T., McIntyre, N., Lees, M.J., Wheater, H. S., and Gupta, H. V. (2003). Towards reduced uncertainty in conceptual rainfall-runoff modelling: dynamic identifiability analysis. Hydrol. Process. 17:455–476. https://doi.org/10.1002/hyp.1135

Wang, F., Chen, H., Lian, J., Fu, Z., and Nie, Y. (2020). Seasonal recharge of spring and stream waters in a karst catchment revealed by isotopic and hydrochemical analyses. Journal of Hydrology, 591, 125595. https://doi.org/10.1016/j.jhydrol.2020.125595

Wang, Z., Guo, X., Kuang, Y., Chen, Q., Luo, M., and Zhou, H. (2021). Recharge sources and hydrogeochemical evolution of groundwater in a heterogeneous karst water system in Hubei Province, Central China. Applied Geochemistry, 136, 105165. https://doi.org/10.1016/j.apgeochem.2021.105165

Wang, L., van Meerveld, H. J., and Seibert, J. (2017). When should stream water be sampled to be most informative for event-based, multi-criteria model calibration?. Hydrology Research, 48(6), 1566-1584. https://doi.org/10.2166/nh.2017.197

Weiss, J. (2020). Basics of ion chromatography. Separation Mechanisms, Stationary Phases, Detection Methods, and Applications. Dreieich, Germany: Thermo Fisher Scientific GmbH.

White, W. B. (2002). Karst hydrology: recent developments and open questions, Engineering Geology, 65(2–3), 85-105. https://doi.org/10.1016/S0013-7952(01)00116-8

White, W. B. (2019). Chapter 64 - Hydrogeology of karst aquifers. In Encyclopedia of caves, Third Edition, 537-54, Academic Press. https://doi.org/10.1016/B978-0-12-814124-3.00064-9

Williams, P. W. (2008). The role of the epikarst in karst and cave hydrogeology: A review. Geology, Environmental Science, International Journal of Speleology, 37(1), 1–10. https://doi.org/10.5038/1827-806X.37.1.1

Winston, W. E., and Criss, R. E. (2004). Dynamic hydrologic and geochemical response in a perennial karst spring. Water Resources Research, 40(5). https://doi.org/10.1029/2004WR003054

Worthington, S. R. (2009). Diagnostic hydrogeologic characteristics of a karst aquifer (Kentucky, USA), Hydrogeol. J., 17(7), 1665–1678. https://doi.org/ 10.1007/s10040-009-0489-0

Worthington, S. R., and D. C. Ford (2009). Self-organized permeability in carbonate aquifers, Ground Water, 47(3), 326–336. https://doi.org/10.1111/j.1745-6584.2009.00551.x

Wu, L., Wang, S., Bai, X., Luo, W., Tian, Y., Zeng, C., Luo, G., and He, S. (2017). Quantitative assessment of the impacts of climate change and human activities on runoff change in a typical karst watershed. SW China. Sci. Total Environ. 601–602, 1449–1465. https://doi.org/10.1016/j.scitotenv.2017.05.288

Zhang, Z., Chen, X, Cheng, Q., and Soulsby, C. (2021). Using StorAge Selection (SAS) functions to understand flow paths and age distributions in contrasting karst groundwater systems. J. Hydrol., 602, 126785. https://doi.org/10.1016/j.jhydrol.2021.126785

Zhang, J., Liesch, T., Chen, Z., and Goldscheider, N. (2023). Global analysis of land-use changes in karst areas and the implications for water resources. Hydrogeol J 31, 1197–1208. https://doi.org/10.1007/s10040-023-02650-5

Zhao, J., Li, G., Duan, Y., Hu, Y., Li, B., and Liang, Z. (2023). A karst runoff generation module based on the near-surface critical zone structure and threshold behaviors. Hydrology Research, 54 (5): 686–702. https://doi.org/10.2166/nh.2023.135

Zhao, S., Pereira, P., Wu, X., Zhou, J., Cao, J., and Zhang, W. (2020). Global karst vegetation regime and its response to climate change and human activities. Ecol. Indic. 113, 106208. https://doi.org/10.1016/j.ecolind.2020.106208

Zipper, S. C., Keune, J., and Kollet, S. J. (2019). Land use change impacts on European heat and drought: remote land-atmosphere feedbacks mitigated locally by shallow groundwater. Environmental Research Letters, 14(4), 044012. https://doi.org/10.1088/1748-9326/ab0db3

Article appendices

A.1 Appendix to Chapter 3

Table A.1 Overview of all model parameters used for the LuKARS model in the Kerschbaum spring recharge area (Bittner et al. 2018). Parameters highlighted with an asterisk (*) indicate those parameters which were considered in the parameter uncertainty study in Teixeira Parente et al. (2019).

Parameter	**Hyd 1**	**Hyd 2**	**Hyd 3**	**Hyd 4**	**Parameter description**
Hydrotope-specific parameters					
E_{ini} [mm]	0	1	1	1	Initial value of hydrotope storage
E_{min} [mm]*	0	23	60	90	Hydrotope storage under dry conditions
E_{max} [mm]*	1	31	120	200	Hydrotope storage under saturated conditions
E_{sec} [mm]*	0	35	180	380	Activation level for secondary springs
k_{hyd} [m^2d^{-1}]*	0	90	85	77	Discharge parameter for quickflow
k_{is} [m $mm^{-1}d^{-1}$]*	0	0.02	0.0055	0.0025	Discharge coeff. for recharge
k_{sec} [m $mm^{-1}d^{-1}$]*	0.9	0.095	0.026	0.022	Secondary spring discharge coeff.
α [-]*	0	0.9	0.8	0.55	Quickflow exponent
l_{hyd} [m]	550	1600	900	960	Mean hydrotope distance to spring
F [mm $d^{-1}{}^{\circ}C^{-1}$]	4	4	4	4	Melt factor in degree-day method
T_f [°C]	0.5	0.5	0.5	0.5	Temerature. threshold for snow melt
I_{max} [mm]	0	5	5	5	Max. interception of land use
Baseflow storage parameters					
k_b [m $mm^{-1}d^{-1}$] = 0.00043					Baseflow discharge coefficient
E_{b_ini} [mm] = 2900					Initial value of baseflow storage

A.2 Appendix to Chapter 4

A.2.1 LuKARS model

In a LuKARS model, areas with homogeneous infiltration conditions are implemented as distinct hydrological response units, called hydrotopes. A hydrotope is analogous to a bucket that has three discharge components: the quickflow component (Q_{hyd} [L^3T^{-1}]), a secondary spring discharge (Q_{sec} [L^3T^{-1}]), and the recharge (Q_{is} [L^3T^{-1}]). Q_{hyd} is considered a hydrotope-specific quickflow occurring in preferential flow paths (e.g., subsurface conduits). The quickflow bypasses the baseflow storage B and is directly transferred to the spring outlet. The quickflow starts, once a hydrotope-specific storage threshold (E_{max}) has been reached and stops after the hydrotope storage fall below a lower storage

threshold (E_{min}). Q_{sec} integrates all flow components that do not arrive at the simulated karst spring and that are transferred outside the regarded recharge area, i.e. secondary spring discharge and overland flow (Tritz et al., 2011). Q_{is} is the discharge from one hydrotope to the underlying baseflow storage B that represents the process of groundwater recharge. Each hydrotope has 7 physical parameters, with length units *L* and time units *T*, that are as follows:

- k_{hyd} [L^2T^{-1}] is the discharge parameter for Q_{hyd},
- E_{min} [L] is the minimum storage capacity of a hydrotope,
- E_{max} [L] is the maximum storage capacity of a hydrotope,
- α [-] is the hydrotope-specific quickflow exponent,
- k_{is} [LT^{-1}] is the discharge parameter for Q_{is},
- k_{sec} [LT^{-1}] is the discharge parameter for Q_{sec},
- E_{sec} [L] is the activation level for Q_{sec}

Following the conceptual sketch from Bittner et al., (2018), the model solves the following discrete balance equations for each hydrotope *i* and for each time step *n* :

$$E_{i,n+1} = max\left[0, E_{i,n} + \left(S_{i,n} - \frac{Q_{hyd,i,n} + Q_{sec,i,b} + Q_{is,i,n}}{a_i}\right)\Delta t\right] \quad \text{(A. 1)}$$

Where E_i indicates the water level [L] in hydrotope i. S_i is the hydrotope-specific sink and source term as a mass balance of precipitation, evapotranspiration, and interception. Then, evapotranspiration is considered using the formula from Oudin et al., (2005). $Q_{hyd,i}$ [L^3T^{-1}] represents the quickflow component (e.g., conduit flow), $Q_{sec,i}$ [L^2T^{-1}] refers to the secondary spring discharge, and $Q_{is,i}$ [L^2T^{-1}] is the groundwater recharge. The absolute area covered by a respective hydrotope is given by a_i [L^2].

$$E_{b,n+1} = max\left[0, E_{b,n} + \left(\frac{\sum(Q_{is,i,n}) - Q_{b,n} - Q_{pumpB,n}}{A}\right)\Delta t\right] \quad \text{(A. 2)}$$

is the balance equation for the baseflow storage B, where E_b indicates the water level [L] in the baseflow storage, $\sum(Q_{is,i,n})$ [L^3T^{-1}] indicates the cumulative flows from all hydrotopes to the baseflow storage, Q_b [L^3T^{-1}] indicates water that is transferred from the storage B to the spring, hence simulates the baseflow contribution from the phreatic aquifer system to the spring discharge, and Q_{pumpB} [L^3T^{-1}] indicates the groundwater abstraction in the aquifer. The variable A [L^2] stands for the entire recharge area. The discharge terms are computed as follows:

$$Q_{hyd,i,n} = a_i \frac{k_{hyd,i}}{l_{hyd,i}} \varepsilon_n \left[\frac{max(0, E_{i,n} - E_{min,i})}{E_{max,i} - E_{min,i}}\right] \alpha_i \quad \text{(A.3)}$$

$$Q_{sec,i,n} = a_i k_{sec,i} max(0, E_{i,n} - E_{sec,i}) \quad \text{(A.4)}$$

$$Q_{is,i,n} = a_i k_{is,i} E_{i,n} \tag{A.5}$$

$$Q_{b,n} = \begin{cases} \left[k_b * E_{b,n} + 0.2 * k_b * \left(E_{b,n} - ceil_B\right)\right] * Aif E_{b,n} \geq ceil_B \\ k_b * E_{b,n} * Aif E_{b,n} < ceil_B \end{cases} \tag{A.6}$$

$E_{max,i}$ [L] and $E_{min,i}$ [L] represent the upper and lower storage thresholds of the hydrotope i. $E_{sec,i}$ [L] is the hydrotope-specific activation level for a secondary spring discharge. $k_{sec,i}$ [LT^{-1}], $k_{is,i}$ [LT^{-1}] and k_b [LT^{-1}] are the specific discharge parameters for $Q_{sec,i}$ [L^3T^{-1}], $Q_{is,i}$ [L^3T^{-1}] and Q_b [L^3T^{-1}], respectively. $k_{hyd,i}$ [L^2T^{-1}] represents the specific discharge parameter for the quickflow of a hydrotope and $l_{hyd,i}$ [L] is the mean distance of hydrotope i to the adjacent spring, thus accounting for the relative location of the same hydrotope types in a specific recharge area. The ratio between $k_{hyd,i}$ and $l_{hyd,i}$ represents the hydrotope discharge coefficient and α_i is a hydrotope-specific exponent of the quickflow. The dimensionless connectivity/activation indicator ε is defined as follows:

$$\varepsilon_{n+1} = 0 if \{\varepsilon_n = 0 \wedge \varepsilon_{i,n+1} < E_{max,i} \vee \varepsilon_n = 1 \wedge \varepsilon_{i,n+1} \leq E_{min,i} \tag{A.7}$$

$$\varepsilon_{n+1} = 1 if \{\varepsilon_n = 0 \wedge \varepsilon_{i,n+1} \geq E_{max,i} \vee \varepsilon_n = 1 \wedge \varepsilon_{i,n+1} > E_{min,i} \tag{A.8}$$

To account for groundwater abstraction, the original equation for the baseflow compartment in the LuKARS model is modified as follows:

$$B_{n+1} = max\left[0, B_n + \left(\frac{Q_{is,n} - Q_{b,n} - Q_{pumpB}}{A}\right) * \Delta t\right] \tag{A.9}$$

$$Q_{b,n} = \begin{cases} \left[k_{b_{down}} * E_{b,n} + k_{b_{up}} * \left(E_{b,n} - threshold_B\right)\right] * Aif E_{b,n} \geq threshold_B \\ k_{b_{down}} * E_{b,n} * Aif E_{b,n} < threshold_B \end{cases} \tag{A.10}$$

where B_n is the water level [L] in the baseflow compartment at the time step *n*, $Q_{is,n}$ is the total flow from all hydrotropes to the baseflow compartment [L^3T^{-1}], $Q_{b_{down}}$ is the flow from the linear baseflow compartment to the spring [L^3T^{-1}],$Q_{b_{up}}$ is the flow from the linear baseflow compartment corresponding to the overflow when the water level $B_n \geq threshold_B$, Q_{pumpB} is the groundwater abstraction discharge [L^3T^{-1}], A is the total recharge area [L^2].

A.2.2 KarstMod model

The model is based on a structure available within the KarstMod modeling platform (Jourde et al., 2015; Mazzilli et al., 2019). The model consists of a two-level structure: (1) compartment E (higher level) and

(2) compartments M and C (lower level). The mass-balance equations provided by Mazzilli et al. (2019) are applied.

$$\frac{dE}{dt} = P - ET - Q_{EM} - Q_{EC} \;\; if \;\; E \geq 0 \tag{A.11}$$

$$\frac{dC}{dt} = Q_{EC} + Q_{MC} \tag{A.12}$$

$$\frac{dM}{dt} = Q_{EM} - Q_{MC} \tag{A.13}$$

where

$$Q_{EM} \; = \; k_{EM} \; \times \; E(t)^{a_{EM}} \; if \; E(t) \; > \; 0, otherwise \; Q_{EM} \; = \; 0 \tag{A.14}$$

$$Q_{EC} \; = \; k_{EC} \; \times \; E(t)^{a_{EC}} \; if \; E(t) \; > \; 0, otherwise \; Q_{EC} \; = \; 0 \tag{A.15}$$

$$Q_{MC} \; = \; k_{MC} \; \times \; [M(t) \; - \; C(t)]^{a_{MC}} \tag{A.16}$$

$$Q_{CS} \; = \; k_{CS} \; \times \; C(t)^{a_{CS}} \tag{A.17}$$

Where P and ET are respectively rainfall and evapotranspiration [L], E(t), M(t) and C(t) are the water levels in the compartments E (epikarst), M (matrix) and C (conduit), k_{AB} is the recession coefficient associated with the flow from compartment A (either E, M, or C) to compartment B (either M, C, or L) or to the outlet S and Q_{AB} [L^3T^{-1}] is the discharge from A to B. Discharge in [L^3T^{-1}] is computed by the product of Q_{AB} [L^3T^{-1}] with the total surface of the recharge area [L^2]. To reproduce the different flow behavior between epikarst (E) and the deeper compartments conduit (C) and matrix (M), emptying exponents are fixed as a_{EM} = a_{MC} = 1, a_{EC} = 2 and a_{CS} = 4 (Sivelle et al., 2019).

Article supplementary material

B.1 Supplementary material to Chapter 5

B.1.1 Specification of laboratory analysis for the Kerschbaum spring

According to the information provided by the waterworks of Waidhofen a.d. Ybbs, for the years 2000–2016 and 2018–2019, the sampling analysis methods and detection limits changed over the investigated period. However, since 2005, the ionic chromatography method (ISO 14911:1998) was applied to

analyze Ca^{2+}, Mg^{2+}, Na^{+} and K^{+}, with a minimum detection limit of 0.5 mg/L for Ca^{2+} and Mg^{2+}, and of 0.1 mg/L for Na^{+} and K^{+}. Additionally, NO_3^-, SO_4^{2-}, and Cl^- were analyzed via dissolved anions by ion chromatography (ISO 10304–1:2007), with a minimum detection limit of 0.1 mg/L (Narany et al. 2019). Finally, the concentration of HCO_3^- was calculated from the carbonate hardness by subtracting the contribution of water dissociation between pH values of 7 and 4.3. The carbonate hardness, in turn, was computed from the results of the acid capacity analysis according to DIN 38409-7. The samples collected during the event 23/1/2022–28/1/2022 were analyzed in the Erftverband laboratory, Bergheim, Germany. The concentrations were obtained with the ionic chromatography method ISO 11885: 2009 for Ca^{2+} and Mg^{2+}, ISO 10304 - 1: 2009 for Na^{+} and K^{+} and ISO 10304 - 1: 2009 for NO_3^-, SO_4^{2-}, and Cl^-. Finally, HCO_3^- was derived from the acid capacity (DIN 38409 - 7: 2005).

B.1.2 Specification of laboratory analysis for the Las Hountas spring

The analyses of the solute concentrations of the three recorded events were done in two different laboratories. The samples collected during the first event (4/10/2021–14/10/2021) and third event (20/11/2022–26/11/2022) were analyzed at the Laboratoire Gosciences Environnement Toulouse, France. The ICP – OES (inductively coupled plasma optical emission spectrometry) was used to quantify Ca^{2+}, Mg^{2+}, Na^{+} and K^{+} with a minimum detection limit of 0.168 mg/L for Ca^{2+}, 0.003 mg/L for Mg^{2+}, 0.017 mg/L for Na^{+} and 0.035 mg/L for K^{+}. NO_3^-, SO_4^{2-}, and Cl^- were analyzed via ion chromatography (ISO 10304–1:2007), with a minimum detection limit of 0.1 mg/L, and HCO_3^- was derived by means of titration analyses. The samples of the second event (1/11/2021–7/11/2021) were analyzed in the Erftverband laboratory, Bergheim, Germany. The ionic chromatography method was used to derive the concentrations of Ca^{2+} and Mg^{2+} (ISO 11885: 2009), Na^{+} and K^{+} (ISO 10304 - 1: 2009), NO_3^-, SO_4^{2-}, and Cl^- (ISO 10304 - 1: 2009). Finally, HCO_3^- was obtained from the acid capacity (DIN 38409 - 7: 2005).

B.1.3 Calculation of the contribution of the solute i to the total EC

The total electrical conductivity EC (µS/cm) of water results from the sum of the contributions EC_i (µS/cm) of the individual solutes i and can be derived using the following equations (Parkhurst and Appelo 2013):

$$EC = \sum_{i} \mathrm{EC_i} \tag{B.1}$$

$$EC_i = \Lambda_m^{\circ} * m * \gamma_{EC} \tag{B.2}$$

with $\Lambda^{\circ}_{\mathrm{m}}$ the molar conductivity (μS m^2/mol), m the molar concentration (mol/m^3) and γ_{EC} the electrochemical activity coefficient (-) of the individual solute. The molar conductivity of a solute species and its diffusion coefficient D_{W} (m^2/s) at 25 °C can be related through:

$$\Lambda^{\circ}_{\mathrm{m}} = \frac{z^2 * \mathrm{F}^2}{\mathrm{R} * T} D_{\mathrm{W}} \quad (\mathrm{B}.3)$$

where z is the charge number (-) of the ion, F the Faraday´s constant (96485.333 Coulomb/mol), R the gas constant (8.315 J/°K/mol) and T the absolute temperature (°K).
For temperatures different from 25 °C, the diffusion coefficient needs to be corrected based on the viscosity of water η (Pa s) at the specific temperature:

$$(D_{\mathrm{W}})_T = (D_{\mathrm{W}})_{298} * \frac{T}{298} * \frac{\eta_{298}}{\eta_T} \quad (\mathrm{B}.4)$$

The electrochemical activity coefficient γ_{EC} (-) of the individual ionic species *i* is function of the charge number z (-) and the Debye-Hückel activity coefficient γ_{DH} (-). PHREEQC calculates γ_{EC} considering an ionic strength $I < 0.36\,|z|$, as:

$$\log(\gamma_{\mathrm{EC}}) = \log(\gamma_{\mathrm{DH}}) * \frac{0.6}{|z|^{0.5}} \quad (\mathrm{B}.5)$$

To remove the temperature effect on $\Lambda^{\circ}_{\mathrm{m}}$ and γ_{EC}, EC measurements are normally given at the standard temperature of 25°C.
The chemical properties of each solute i can be grouped in a single coefficient a_i ((μS/cm) /(mg/L)) as:

$$a_i = \frac{\Lambda^{\circ} * \gamma_{\mathrm{EC}}}{M} \quad (\mathrm{B}.6)$$

where M indicates the solute molar mass (g/mol). a_i is function of time since $\Lambda^{\circ}_{\mathrm{m}}$ and γ_{EC} can change in time. In our case, $\Lambda^{\circ}_{\mathrm{m}}$ is constant because all computations are referred to a fixed temperature of 25 °C, whereas γ_{EC} changes with the ionic strength I of the solution (EC decreases for increasing I). However, as typical in natural freshwater systems, the total ion concentration varies within a relatively narrow range of values, which makes γ_{EC} to only have minor variations in time. Therefore, the coefficients a_i can be approximated to be constant (Benettin and van Breukelen 2017).
Eq (B.1) and (B.2) can be written as function of the coefficients a_i, concentration C_i (mg/L) and time t as:

$$EC(t) = \sum_i EC_i(t) = \sum_i a_i(t) * C_i(t) \quad \text{(B. 7)}$$

B.1.4 PHREEQC file

DATABASE C:\Program Files (x86)\USGS\Phreeqc Interactive 3.6.2-15100\database\phreeqc.dat
#DATABASE C:\(path to phreeqc.dat file)

PHREEQC file to compute
1) the Electrical Conductivity (*EC*) of the individual solute species present as free ions
2) the Electrical Conductivity (*EC*) of the individual solute species as aqueous complexes
3) the chemical coefficients ai
4) concentration of each solute species as aqueous complexes (= the difference between the total concentration of each solute species and its concentration as free ion)
The solute concentrations are given as input in the SOLUTION_SPREAD block
Outputs are printed to file as defined in the SELECTED_OUTPUT and USER_PUNCH blocks
----

SOLUTION_SPREAD #Offers a matrix-type input format for solute concentrations
default temperature is 25 °C
-units mg/l

Description	Ca	Mg	Alkalinity as HCO3	S(6)	N(5)	Cl	Na	K	pH
A1	56.06	5.349	185.49	16.10	3.51	1.42	0.98	0.38	8.31
A2	57.38	5.44	186.10	16.60	3.49	1.42	1.01	0.43	8.27

...
An

SELECTED_OUTPUT 1 # this block allows writing an output file. Here we print the result of *EC* computed for the major free ions
-reset false
-file output_EC_freeions.dat
USER_PUNCH 1 # print user-defined quantities to the selected_output file
-headings Sample_ID EC_freeions EC_Ca EC_Mg EC_HCO3 EC_SO4 EC_NO3 EC_Cl EC_Na EC_K charge_error[%]

```
-start

# definition of constants
10 F = 96485.33289 # Faraday´s constant (C/mol)
20 R = 8.3144621 # gas constant (J/K/mol)
30 ff1 = 0.6 / 1^0.5 # group together some constants
40 ff2 = 0.6 / 2^0.5 # group together some constants
50 temp25_corr = 1 # no temperature correction required for default EC at 25 °C
#50 temp25_corr = TK/298 * (viscosity298) / (viscosityTK) # temperature correction required for TK different from 25 °C

# EC computation for each free ion
# lg("species") is the log10 of the Debye-Huckel activity coefficient (-)
# DIFF_C("species") is the diffusion coefficient at 25 °C (m2/s)
# since the molar conductivity is in S/m / (mol/m3 = mmol/L), multiply mol("species") by 1000 to get mmol/L
# multiply by 10000 to get EC is in uS/cm
120 EC_Ca = ((2^2 * F^2)/(R*TK)) * (DIFF_C("Ca+2") * temp25_corr) * mol("Ca+2") * 1000 *10^(lg("Ca+2") * ff2) * 10000
130 EC_Cl = ((1^2 * F^2)/(R*TK)) * (DIFF_C("Cl-") * temp25_corr) * mol("Cl-") * 1000 *10^(lg("Cl-") * ff1) * 10000
140 EC_K = ((1^2 * F^2)/(R*TK)) * (DIFF_C("K+") * temp25_corr) * mol("K+") * 1000 * 10^(lg("K+") * ff1) * 10000
150 EC_NO3 = ((1^2 * F^2)/(R*TK)) * (DIFF_C("NO3-") * temp25_corr) * mol("NO3-") * 1000 *10^(lg("NO3-") * ff1) * 10000
160 EC_Na = ((1^2 * F^2)/(R*TK)) * (DIFF_C("Na+") * temp25_corr) * mol("Na+") * 1000 *10^(lg("Na+") * ff1) * 10000
170 EC_Mg = ((2^2 * F^2)/(R*TK)) * (DIFF_C("Mg+2") * temp25_corr) * mol("Mg+2") * 1000 *10^(lg("Mg+2") * ff2) * 10000
180 EC_SO4 = ((2^2 * F^2)/(R*TK)) * (DIFF_C("SO4-2") * temp25_corr) * mol("SO4-2") * 1000* 10^(lg("SO4-2") * ff2) * 10000
190 EC_HCO3 = ((1^2 * F^2)/(R*TK)) * (DIFF_C("HCO3-") * temp25_corr) * mol("HCO3-") * 1000 * 10^(lg("HCO3-") * ff1) * 10000
195 EC_freeions = EC_Ca + EC_Cl + EC_K + EC_NO3 + EC_Na + EC_Mg + EC_SO4 + EC_HCO3

# print results to output
198 PUNCH DESCRIPTION
```

205 PUNCH EC_freeions #total *EC* by considering major free ions
220 PUNCH EC_Ca
230 PUNCH EC_Mg
240 PUNCH EC_HCO3
250 PUNCH EC_SO4
260 PUNCH EC_NO3
270 PUNCH EC_Cl
280 PUNCH EC_Na
290 PUNCH EC_K
300 PUNCH PERCENT_ERROR # Percent charge-balance error: 100*(cations-|anions|)/(cations+|anions|)
-end

SELECTED_OUTPUT 2 # this block allows writing an output file. Here we print the result of *EC* computed for the aqueous complexes
-reset false
-file output_EC_solution_complexes.dat

USER_PUNCH 2 # print user-defined quantities to the selected_output file
-headings Sample_ID EC_complexes EC_CaOH EC_CaHSO4 EC_CaHCO3 EC_NaSO4 EC_NaCO3 EC_MgHCO3 EC_MgOH EC_HSO4 EC_CO3
-start

define some useful constant for the computations
10 F = 96485.33289 # Faraday´s constant (C/mol)
20 R = 8.3144621 # gas constant (J/K/mol)
30 ff1 = 0.6 / 1^0.5 # group together some constants
40 ff2 = 0.6 / 2^0.5 # group together some constants
50 temp25_corr = 1 # no temperature correction required for default 25 °C
#50 temp25_corr = TK/298 * (viscosity298) / (viscosityTK) # temperature correction required for TK different from 25 °C

EC computation for solute species as aqueous complexes
lg("species") is the log10 of the Debye-Huckel activity coefficient (-)
DIFF_C("species") is the diffusion coefficient at 25 °C (m2/s)

```
# since the molar conductivity is in S/m / (mol/m3 = mmol/L), multiply mol("species") by 1000 to get mmol/L
# multiply by 10’000 to get EC is in uS/cm
110 EC_CaOH = ((1^2 * F^2)/(R*TK)) * (DIFF_C("CaOH+") * temp25_corr) * mol("CaOH+") * 1000 * 10^(lg("CaOH+") * ff1) * 10000
120 EC_CaHSO4 = ((1^2 * F^2)/(R*TK)) * (DIFF_C("CaHSO4+") * temp25_corr) * mol("CaHSO4+") * 1000 *10^(lg("CaHSO4+") * ff1) * 10000
130 EC_CaHCO3 = ((1^2 * F^2)/(R*TK)) * (DIFF_C("CaHCO3+") * temp25_corr) * mol("CaHCO3+") * 1000 *10^(lg("CaHCO3+") * ff1) * 10000
140 EC_NaSO4 = ((1^2 * F^2)/(R*TK)) * (DIFF_C("NaSO4-") * temp25_corr) * mol("NaSO4-") * 1000 * 10^(lg("NaSO4-") * ff1) * 10000
150 EC_NaCO3 = ((1^2 * F^2)/(R*TK)) * (DIFF_C("NaCO3-") * temp25_corr) * mol("NaCO3-") * 1000 *10^(lg("NaCO3-") * ff1) * 10000
160 EC_MgHCO3 = ((1^2 * F^2)/(R*TK)) * (DIFF_C("MgHCO3+") * temp25_corr) * mol("MgHCO3+") * 1000 *10^(lg("MgHCO3+") * ff1) * 10000
170 EC_MgOH = ((1^2 * F^2)/(R*TK)) * (DIFF_C("MgOH+") * temp25_corr) * mol("MgOH+") * 1000 *10^(lg("MgOH+") * ff1) * 10000
180 EC_HSO4 = ((1^2 * F^2)/(R*TK)) * (DIFF_C("HSO4-") * temp25_corr) * mol("HSO4-") * 1000* 10^(lg("HSO4-") * ff1) * 10000
190 EC_CO3 = ((2^2 * F^2)/(R*TK)) * (DIFF_C("CO3-2") * temp25_corr) * mol("CO3-2") * 1000 * 10^(lg("CO3-2") * ff2) * 10000
195 EC_complexes = EC_CaOH + EC_CaHSO4 + EC_CaHCO3 + EC_NaSO4 + EC_NaCO3 + EC_MgHCO3 + EC_MgOH + EC_HSO4 + EC_CO3

# print results to output
198 PUNCH DESCRIPTION
205 PUNCH EC_complexes #total EC by considering aqueous complexes only
210 PUNCH EC_CaOH
220 PUNCH EC_CaHSO4
230 PUNCH EC_CaHCO3
240 PUNCH EC_NaSO4
250 PUNCH EC_NaCO3
260 PUNCH EC_MgHCO3
270 PUNCH EC_MgOH
280 PUNCH EC_HSO4
290 PUNCH EC_CO3
-end
```

```
# ----------------------

SELECTED_OUTPUT 3 # this block allows writing an output file. Here we print the result of the computed chemical coefficients
USER_PUNCH 3 # print user-defined quantities to the selected_output file
-headings Sample_ID a_Ca a_Mg a_HCO3 a_SO4 a_NO3 a_Cl a_Na a_K
-start

# define some useful constant for the computations
10 F = 96485.33289 # Faraday´s constant (C/mol)
20 R = 8.3144621 # gas constant (J/K/mol)
30 ff1 = 0.6 / 1^0.5 # group together some constants
40 ff2 = 0.6 / 2^0.5 # group together some constants
50 temp25_corr = 1 # no temperature correction required for default 25 °C
#50 temp25_corr = TK/298 * (viscosity298) / (viscosityTK) # temperature correction required for TK different from 25 °C

# calculate the variable a = molar_conductivity*electrochemical_activity_coefficient/ molar_mass [uS/cm / (mg/L)] for the individual species
# lg("species") is the log10 of the Debye-Huckel activity coefficient (-)
# GFW("species") is the molar mass (g)
# DIFF_C("species") is the diffusion coefficient at 25 °C (m2/s)
# multiply by 10'000 to get EC is in uS/cm
120 a_Ca = ((2^2 * F^2)/(R*TK)) * (DIFF_C("Ca+2") * temp25_corr) * 10^(lg("Ca+2") * ff2)/ GFW("Ca+2") * 10000
130 a_Cl = ((1^2 * F^2)/(R*TK)) * (DIFF_C("Cl-") * temp25_corr) * 10^(lg("Cl-") * ff1) /GFW("Cl-") * 10000
140 a_K = ((1^2 * F^2)/(R*TK)) * (DIFF_C("K+") * temp25_corr) * 10^(lg("K+") * ff1) / GFW("K+") * 10000
150 a_NO3 = ((1^2 * F^2)/(R*TK)) * (DIFF_C("NO3-") * temp25_corr) * 10^(lg("NO3-") * ff1)/ GFW("NO3-") * 10000
160 a_Na = ((1^2 * F^2)/(R*TK)) * (DIFF_C("Na+") * temp25_corr) * 10^(lg("Na+") * ff1) /GFW("Na+") * 10000
170 a_Mg = ((2^2 * F^2)/(R*TK)) * (DIFF_C("Mg+2") * temp25_corr) * 10^(lg("Mg+2") * ff2)/ GFW("Mg+2") * 10000
180 a_SO4 = ((2^2 * F^2)/(R*TK)) * (DIFF_C("SO4-2") * temp25_corr) * 10^(lg("SO4-2") *ff2) / GFW("SO4-2") * 10000
```

```
190 a_HCO3 = ((1^2 * F^2)/(R*TK)) * (DIFF_C("HCO3-") * temp25_corr) * 10^(lg("HCO3-") *ff1)
/ GFW("HCO3-") * 10000

# print results to output
198 PUNCH DESCRIPTION
220 PUNCH a_Ca
230 PUNCH a_Mg
240 PUNCH a_HCO3
250 PUNCH a_SO4
260 PUNCH a_NO3
270 PUNCH a_Cl
280 PUNCH a_Na
290 PUNCH a_K
-end
# ----------------------

SELECTED_OUTPUT 4 # this block allows writing an output file. Here we print the difference between
the total concentration of each solute species and its concentration as free ion
-file Diff_mol_tot.dat

USER_PUNCH 4 # print user-defined quantities to the selected_output file
-headings Sample_ID     gl_Ca gl_Mg gl_HCO3 gl_SO4 gl_NO3 gl_Cl gl_Na gl_K
-start

# computation of concentration of each solute species as aqueous complexes
# tot() returns the total molality (mol/kgw) of a solute
# mol() return the molality (mol/kgw) of a SOLUTION
# tot() - mol() represents the difference between the total concentration of each solute and its
concentration as free ion (= concentration of each species as aqueous complexes)
10 A = mol("HCO3-") + mol("CaHCO3+") + mol("MgHCO3+") + 2*(mol("CO3-2") + mol("CaCO3")
+ mol("MgCO3"))

110 gl_Ca = (tot("Ca") - mol("Ca+2")) * GFW("Ca+2") *1000
120 gl_Mg = (tot("Mg") - mol("Mg+2")) * GFW("Mg+2") *1000
130 gl_SO4 = (tot("S(6)") - mol("SO4-2")) * GFW("SO4-2") *1000
140 gl_HCO3 = (A - mol("HCO3-")) * GFW("HCO3-") *1000
150 gl_Cl = (tot("Cl") - mol("Cl-")) * GFW("Cl-") *1000
```

```
160 gl_K = (tot("K") - mol("K+")) * GFW("K+") *1000
170 gl_NO3 = (tot("N(5)") - mol("NO3-")) * GFW("NO3-") *1000
180 gl_Na = (tot("Na") - mol("Na+")) * GFW("Na+") *1000

200 PUNCH DESCRIPTION
210 PUNCH gl_Ca
220 PUNCH gl_Mg
230 PUNCH gl_HCO3
240 PUNCH gl_SO4
250 PUNCH gl_NO3
260 PUNCH gl_Cl
270 PUNCH gl_Na
280 PUNCH gl_K
  -end
END
```

B.1.5 Dissolution processes in the Baget catchment

The dissolution of one mole of calcium carbonate ($CaCO_3$) by carbonic acid (H_2CO_3) produces one mole of Ca^{2+} and two moles of HCO_3^-. The black flysch formation contains pyrite, whose oxidation release strong acids, i.e., sulfuric acid (H_2SO_4). The reaction between one mole of $CaCO_3$ and half mole of H_2SO_4 produces one mole of Ca^{2+}, one mole of HCO_3^- and half mole of SO_4^{2-}. Consequently, the dissolution of $CaCO_3$ by both H_2CO_3 and H_2SO_4 leads to a lower alkalinity than what we would observe in the case of only dissolution by H_2CO_3.

Limestone and calcareous rock → carbonate dissolution by carbonic acid → **1** $CaCO_3$: **2** HCO_3^-

$$Ca_{1-x}Mg_xCO_3 + H_2CO_3 \rightarrow (1-x)Ca^{2+} + (x)Mg^{2+} + 2HCO_3^-$$

Black flysch → carbonate dissolution by sulfuric acid → **1** $CaCO_3$: **1** HCO_3^- + **0.5** SO_4^{2-}

$$2CaCO_3 + H_2SO_4 \rightarrow 2Ca^{2+} + 2HCO_3^- + SO_4^-$$

Fig. B.1 Dissolution processes and stochiometric relationships characterizing the two main geological areas of the Baget springshed, i.e., calcareous rocks and black flysch.

B.1.6 Additional supplementary material

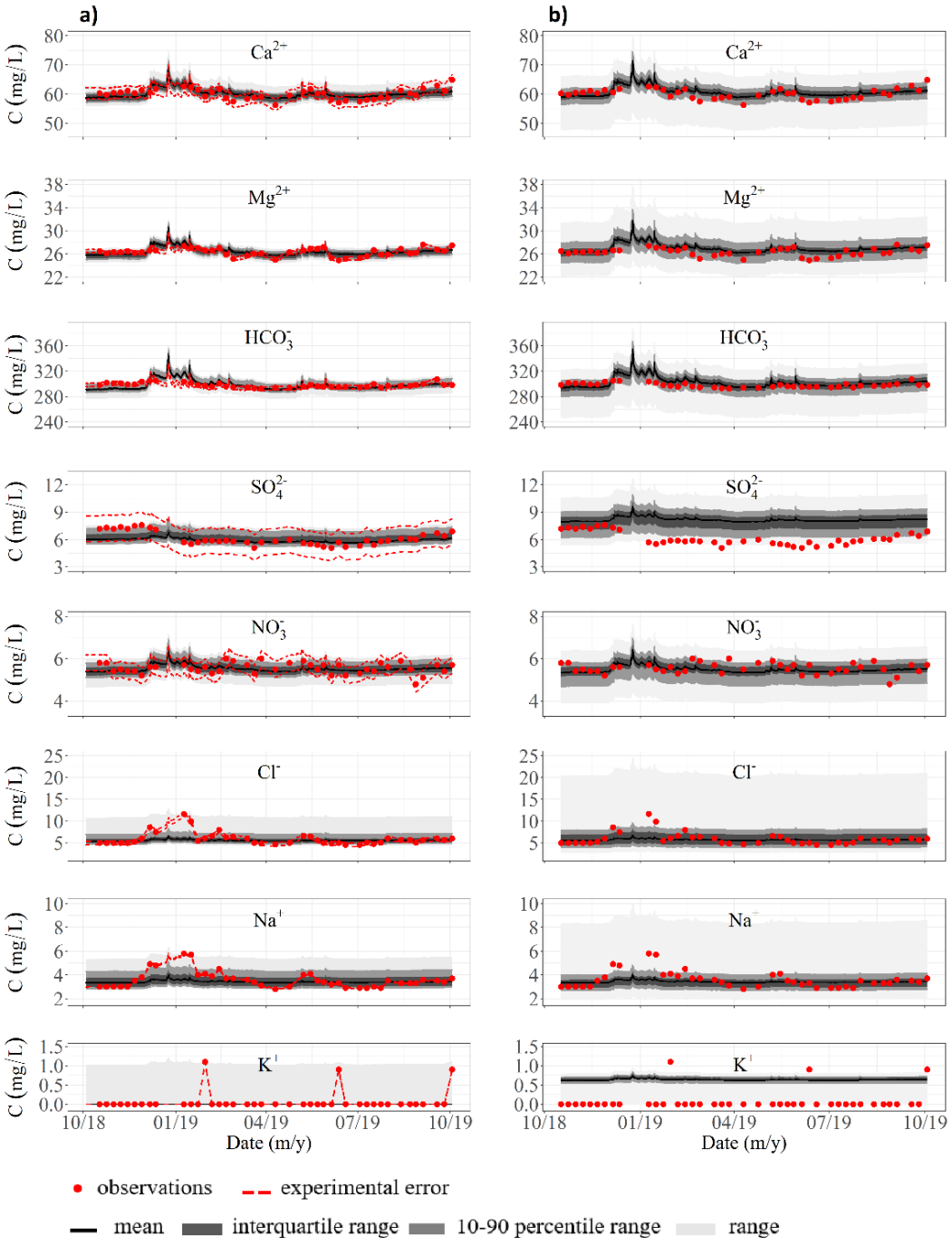

Fig. B.2 Interpolated and predictive uncertainties for the Kerschbaum spring for the period 2018–2019. **a** Interpolated experimental uncertainty on the individual solute species concentrations (dashed lines) together with their interpolated uncertainty based on the frequency of occurrence of the weight factors observed in the period 2018–2019. **b** Uncertainty bands for the predicted individual solute species based on the frequency of occurrence of the weight factors observed in 2000–2016. The black, gray and light gray areas of the bands represent the interquartile, the 10–90% percentile and full ranges of the computed solute species concentrations (mg/L), respectively. The red points are the observed solute concentrations (mg/L).

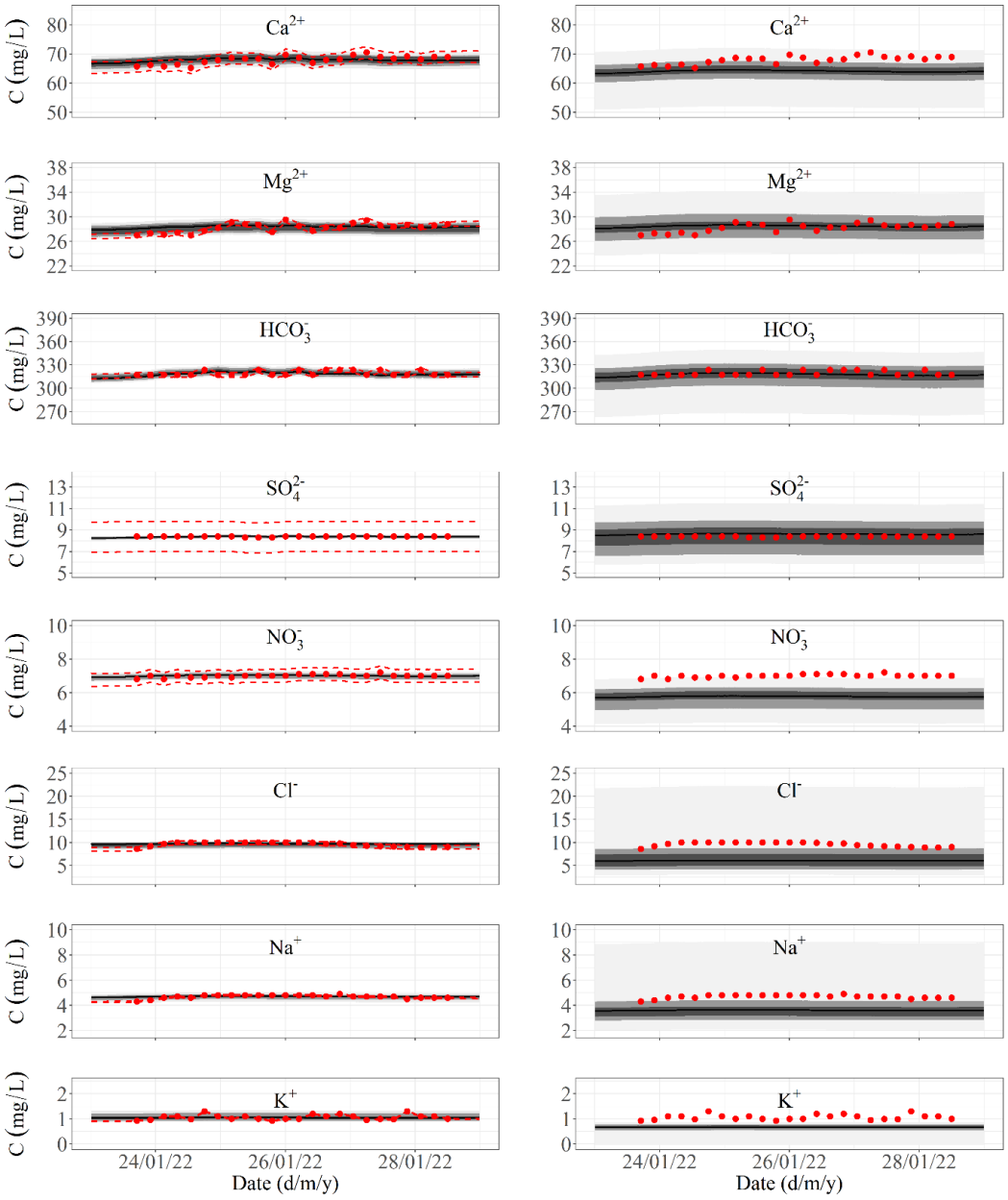

Fig. B.3 Interpolated and predictive uncertainties for the Kerschbaum spring for the period 23/1/2022–28/1/2022. **a** Interpolated experimental uncertainty on the individual solute species concentrations (dashed lines) together with their interpolated uncertainty based on the frequency of occurrence of the weight factors observed in the period 23/1/2022–28/1/2022. **b** Uncertainty bands for the predicted individual solute species based on the frequency of occurrence of the weight factors observed in 2000–2016. The black, gray and light gray areas of the bands represent the interquartile, the 10–90% percentile and full ranges of the computed solute species concentrations (mg/L), respectively. The red points are the observed solute concentrations (mg/L).

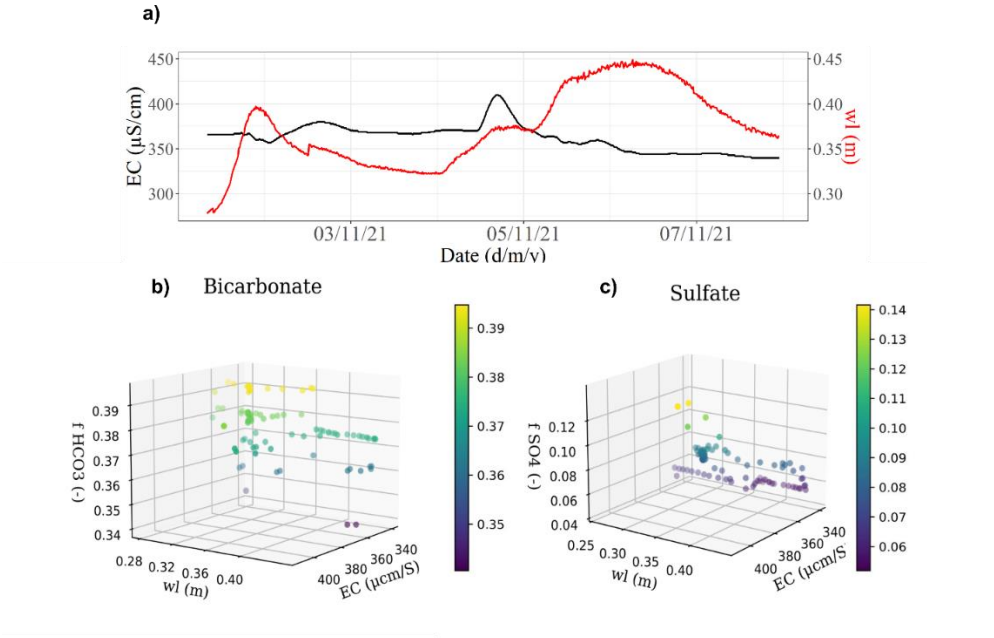

Fig. B.4 Correlation between *EC* (µS/cm), water level wl (m) and the weight factors f_i (-) of HCO_3^- and SO_4^{2-} observed at Las Hountas for the period 1/11/2021–7/11/2021. **a** Time series of *EC* (black line) and water level (red line). **b** 3D scatter plot of *EC*, water level and weight factor of HCO_3^-. **c** 3D scatter plot of *EC*, water level and the weight factor of SO_4^{2-}.

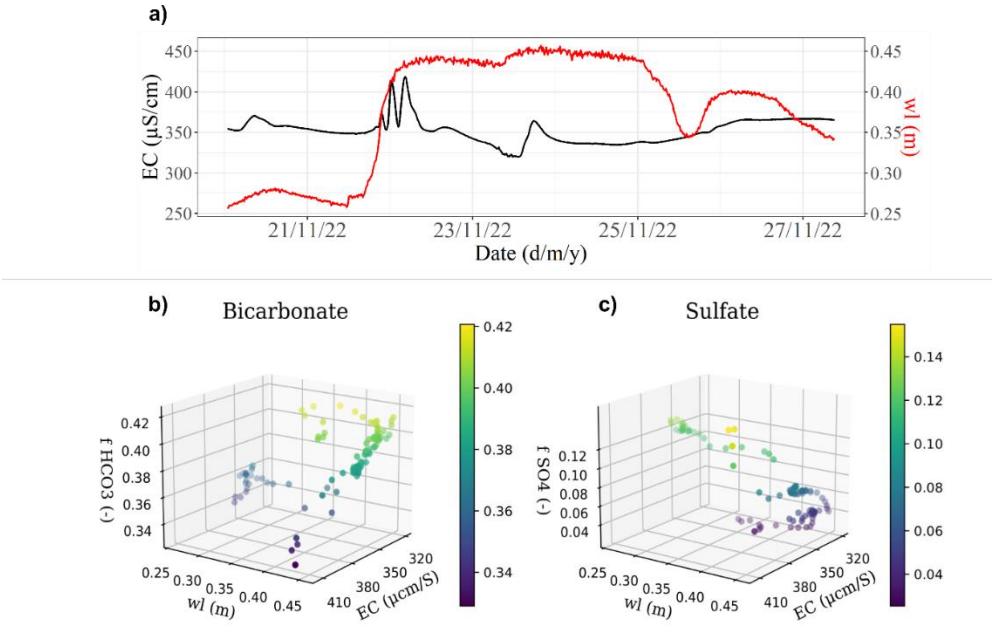

Fig. B.5 Correlation between *EC* (µS/cm), water level wl (m) and the weight factors f_i (-) of HCO_3^- and SO_4^{2-} observed at Las Hountas for the period 20/11/2022–26/11/2022. **a** Time series of *EC* (black line)

and water level (red line). **b** 3D scatter plot of *EC*, water level and weight factor of HCO_3^-. **c** 3D scatter plot of *EC*, water level and the weight factor of SO_4^{2-}.

Table B.1 Relative variation in measured concentrations (-) and relative width of the uncertainty bands (-) for Kerschbaum (2018–2019) and Las Hountas (4/10/2021–14/10/2021).

	Kerschbaum		**Las Hountas**	
	Relative variation in measured concentration (-)	**Relative width of the uncertainty band (-)**	**Relative variation in measured concentration (-)**	**Relative width of the uncertainty band (-)**
Ca	0.14	0.11	0.23	0.1
Mg	0.1	0.08	0.3	0.07
HCO_3	0.05	0.08	0.1	0.21
SO_4	0.41	0.34	1.93	1.19
NO_3	0.22	0.23	0.2	0.19
Cl	1.2	1.07	0.38	0.19
Na	0.84	0.72	0.36	0.12
K^+	15.5	15.46	1.39	1.02

B.2 Supplementary material to Chapter 6

B.2.1 LuKARS model from Bittner et al. (2018)

The modifications done within this study respect to the original version of LuKARS (Bittner et al. 2018) are presented in the text (Subsection 6.3). The equation from Bittner et al. (2018) which were directly applied without further adjustments are here presented.

LuKARS (Bittneret et al. 2018) solves the following discrete balance equation (Eq. B.8) for each hydrotope *i* and for each time step *t*.

$$E_{i,t+1} = \max\left[0,\ E_{i,t} + \left(S_{i,t} - \frac{Q_{\mathrm{hyd},i,t} + Q_{is,i,t}}{a_i}\right) \times dt\right] \quad \text{(B. 8)}$$

Where E_i (mm) is the water level in hydrotope *i*, S_i (mm) the hydrotope-specific sink and source term, $Q_{\mathrm{hyd},i}$ (m^3/s) the fast flow from hydrotope *i*, $Q_{\mathrm{is},i}$ (m^3/s) the groundwater recharge from hydrotope *i*, a_i the area of hydrotope *i* and *dt* the time step. In the present study, the evapotranspiration is not considered

and thus the sink and source term S_i is equal to the precipitation. The discharge term $Q_{hyd,i}$ is computed as shown in Eq. B.9.

$$Q_{\mathrm{hyd},i,t} = \varepsilon_t * \left[\frac{\max\left(0, E_{i,t} - E_{\min,i}\right)}{E_{\max,i} - E_{\min,i}}\right]^{\alpha_i} * \frac{k_{\mathrm{hyd},i}}{l_{\mathrm{hyd},i}} * a_i \quad \text{(B. 9)}$$

Where $E_{max,i}$ and $E_{min,i}$ (mm) are the upper and lower storage threshold of hydrotope i, α_i (-) is an exponent, $k_{hyd,i}$ (mm²/h) the discharge coefficient, and $l_{hyd,i}$ (m) the mean distance of hydrotope i from the spring. ε (-) specifies whether the fast flow component from a hydrotope is active at time step t (B.10, B.11).

$$\varepsilon_{t+1} = 0 \text{ if } \left\{ \varepsilon_t = 0 \;\&\; E_{i,t+1} < E_{\max,i} \text{ or } \varepsilon_t = 1 \;\&\; E_{i,t+1} \leq E_{\min,i} \right\} \quad \text{(B. 10)}$$

$$\varepsilon_{t+1} = 1 \text{ if } \left\{ \varepsilon_t = 0 \;\&\; E_{i,t+1} \geq E_{\max,i} \text{ or } \varepsilon_t = 1 \;\&\; E_{i,t+1} > E_{\min,i} \right\} \quad \text{(B. 11)}$$

The discharge term $Q_{is,i}$ is computed as function of the discharge coefficient $k_{is,i}$ (1/h) (Eq. B.12).

$$Q_{\mathrm{is},i,t} = k_{\mathrm{is},i} * E_{i,t} * a_i \quad \text{(B. 12)}$$

B.2.2 KarstMod model from Mazzilli et al. (2019)

In the present study, the flux from to conduit to the spring Q_{cs} is computed with the linear function from Mazzilli et al. (2019) as function of the dimensionless water level in the conduit C (-), the discharge coefficient k_{CS} (mm/h), the exponent a_{CS} (-) and the recharge area Ra (km²) (Eq. B.13).

$$Q_{\mathrm{cs},t} = Ra * k_{\mathrm{cs}} * {C_t}^{a_{\mathrm{CS}}} \quad \text{(B. 13)}$$

B.2.3 Hydrographs at Las Hountas spring and at the outlet of the catchment

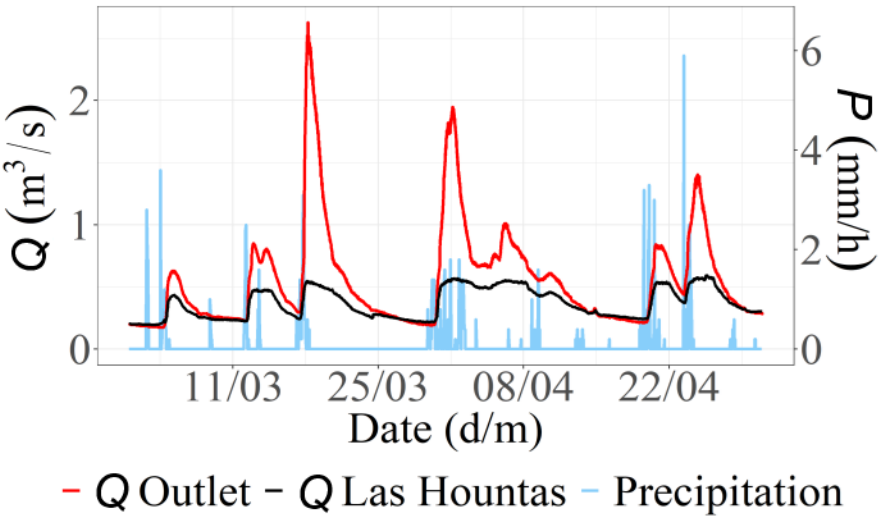

Fig.B.6 Precipitation time series and discharge hydrograph showing the different responses observed at the Las Hountas spring (black) and at the outlet of the Baget catchment (red) in March-April 2022.

B.2.4 Water samples collected at Las Hountas spring

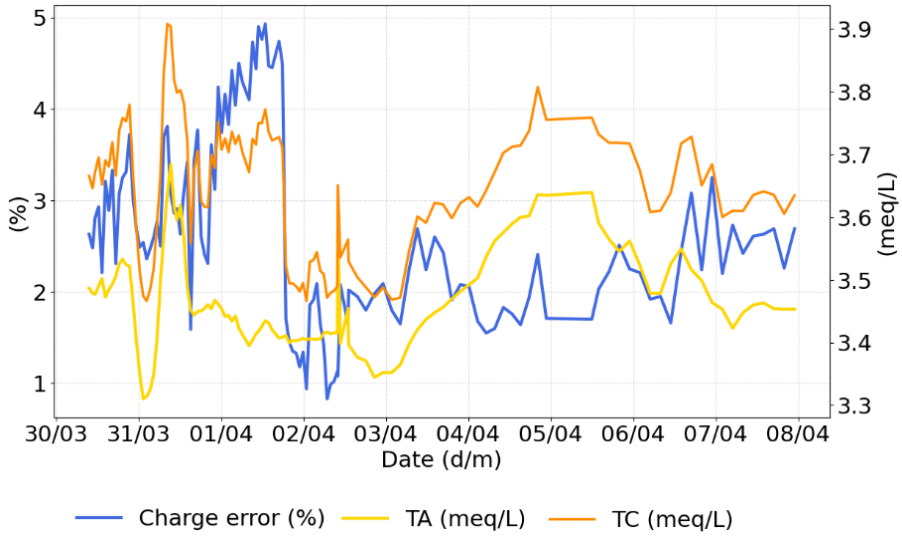

Fig. B.7 Time series of the charge balance (%), sum of cations TC and anions TA (meq/L) of the samples collected at the Las Hountas spring for the period 30/03/2022–7/04/2022. The charge balance was computed by using the software PHREEQC.

B.2.5 Observed and selected discharge time series at Las Hountas spring

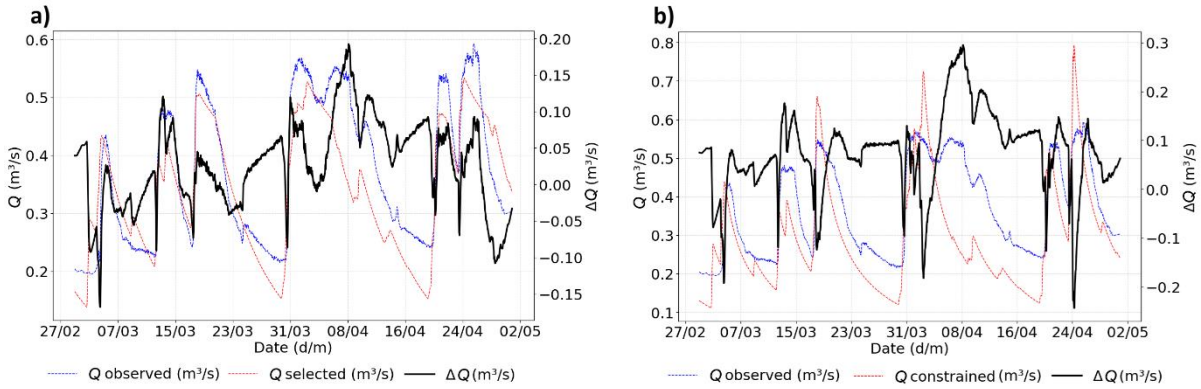

Fig. B.8 Time series at Las Hountas spring for the period 30/03/2022–7/04/2022. **a** Observed discharge (*Q* observed), selected discharge among the Morris realizations (*Q* selected) and difference between the observed and selected discharges (Δ*Q*). **b** Observed discharge (*Q* observed), discharge constrained by hydrochemical observations (*Q* constrained) and difference between the observed and constrained discharges (Δ*Q*). The constrained discharge corresponds to the realization with the highest KGE among the subset of realizations respecting the hydrochemical constraints.